UNIVERSITY OF OKLAHOMA

GRADUATE COLLEGE

TYPE-II QUANTUM WELL HOT CARRIER SOLAR CELLS

A DISSERTATION

SUBMITTED TO THE GRADUATE FACULTY

in partial fulfillment of the requirements for the

Degree of

DOCTOR OF PHILOSOPHY

By

HAMIDREZA ESMAIELPOUR
Norman, Oklahoma
2018

TYPE-II QUANTUM WELL HOT CARRIER SOLAR CELLS

A DISSERTATION APPROVED FOR THE
HOMER L. DODGE DEPARTMENT OF PHYSICS AND ASTRONOMY

BY

Dr. Ian R. Sellers, Chair

Dr. Rui Q. Yang

Dr. Michael B. Santos

Dr. Bruno U. Barboza

Dr. Eric R. I. Abraham

"*To My Beloved Country, IRAN*"

Acknowledgments

Over the last five years, I have been fortunate to work on a topic about renewable energies, photovoltaic solar cells, that I have been interested in since I was in high school. When I started my research I could not imagine how nice my journey would be during my PhD program. Thanks God, I have had a very enjoyable time to expand my knowledge in science and technology. I hope my achievements in the field will be helpful for future discoveries.

First I would like to express my sincere appreciation to my supervisor, ***Dr. Ian R. Sellers***, who has introduced me to the field and provided me everything, from scientific and technical prospective, to pursuit my enthusiasm in the field.

Then, I would like to acknowledge ***Dr. Vincent R. Whiteside*** for his valuable support during my PhD program. His patient, intellectual, and friendly characteristics have always been a source of inspiration for me that I will try to emulate them for the rest of my career.

I also would like to thank all my doctoral committee members, *Dr. Michael B. Santos, Dr. Bruno U. Barboza, Dr. Eric R. I. Abraham,* and *Dr. Rui Q. Yang* for their generous support during my program.

Thanks to all my former and current colleagues in the PV group at OU, *Mr. Hadi (Shahram) Afshari, Dr. Yang Cheng, Mr. Jinfeng Tang, Ms. Miwa Fukuda, Mr. Anthony J. Meleco, Mr. Collin R. Brown, Mr. Shashi Sourabh,* and *Mr. Kyle Doorman.* My collaborations with them have been extremely valuable to me.

I would like to thank all my friends in Iran and in the United States that have been supporting me during my program. There are too many names to mention here, however, I would like to specifically mention some of my best friends: *Mr. Salman Jafarie, Mr. Behzad Hemami, Mrs. Parastoo Imantallab, Mr. Seyyed Javad Robatjazi, Mr. David Nagi, Mr. Javad Dowran, Ms. Delaram Nematollahi, Mr. Akbar Jahangiri, Ms. Mina Mahdaviparsa, Mr. Moslem Parvin, Mrs. Elnaz Homayounmehr, Mr. Amir Tayebi, Mr. Amirhossein Kamali, Mr. Farzad Mottaghi, Mr. Jeremy A. Messengale, Mr. Matthew W. Holtfrerich*. I would also like to express my deepest appreciation to *Ms. Sedigheh Shiran, Mr. Morteza Farzaneh, Dr. Meysam Pournik, Mrs. Sandy Moore-Furneaux*, and their families for generous support they gave during my stay in the United States.

My *mother* and *father*, my beloved sisters: *Mahkameh* and *Mona*, my nephews and niece: *Arshia, Tania, and Daria*, and my brothers-in-law: *Ali Dolatshahi* and *Dr. Seyyed Youssef Torabian* with their endless encouragement have helped me to pursue my dream. Without their support, I could have never made this achievement in my life.

Table of Contents

List of Figures

List of Tables

Abstract

Hot carrier solar cells are a third generation photovoltaic technology, which aims to increase power conversion efficiency of solar cells beyond the fundamental Shockley-Queisser limit (33%). A major source of loss in conventional solar cells is thermalization loss (heat generation), which occurs when photogenerated hot carriers lose their excess kinetic energy by interacting with phonons. Hot carrier solar cells have been proposed to reduce such thermalization losses if electron-phonon interactions can be inhibited. Despite significant recent progress in the field, there are still two significant challenges to overcome in order to design a practical hot carrier solar cell: 1) designing an efficient hot carrier absorber to inhibit hot carrier-phonon interactions; 2) develop energy selective contacts to extract hot carriers before thermalization occurs.

Here, type-II InAs/AlAsSb quantum well (QW) structures are investigated as a promising candidate for hot carrier absorbers. Continuous wave power and temperature dependent photoluminescence spectroscopy and ultrafast transient absorption spectroscopy show evidence of robust hot carrier effects at low excitation powers and room temperature, which are significant properties when designing practical hot carrier solar cells. In addition, we have investigated accurate determination of the carrier temperature and phononic properties in the QW structures to provide a better understanding and fuller picture of the nature of hot carrier effects in these systems. Furthermore, we have designed and fabricated p-i-n diodes to study the electrical properties of hot carriers within practical InAs QW structures. As a result, through determination of the origin of hot carrier thermalization processes in the system it is

possible to find ways to manipulate and/or control the hot carrier loss mechanisms for hot carrier solar cell or other optoelectronic applications. Finally, we have also investigated the optical spectroscopy of 2D hybrid lead halide perovskite structures for potential hot carrier solar cells.

*Chapter **1***

Introduction: Hot carrier solar cells

1.1 Motivation

The amount of solar energy striking the Earth from the Sun in only one and half hours can fulfill the global energy consumption for one year! [1] In our modern world it is inevitable to seek cheap, reliable, and sustainable energy resources. Over recent decades, there has been a lot of interest utilizing renewable energy such as solar energy to generate electricity. One technology, which can convert sunlight directly into electricity, is a photovoltaic solar cell. This technology has the potential to generate a considerable amount of power directly from sun and to be utilized in most regions of the Earth. However, there remain issues regarding this technology, which limits its large-scale deployment. The main issues regarding photovoltaic solar cell technologies are economic competitiveness and power conversion efficiency. Therefore, it is essential to reduce solar cell fabrication costs and to improve their power conversion efficiency, all of which requires having a more fundamental understanding of their operation in order to expand their implementation.

Most solar cells are formed using p-n junctions. The advantage of a p-n junction is associated with their capability to separate photogenerated electron-hole pairs due to the existence of an internal electric field within the depletion region of the diode. As a result, photogenerated carriers can be extracted and produce electricity in an external circuit.

[2, 3] A schematic of a p-n junction is shown in Figure 1.1. It is observed that several different processes can occur upon the p-n junction's exposure to light. [4]

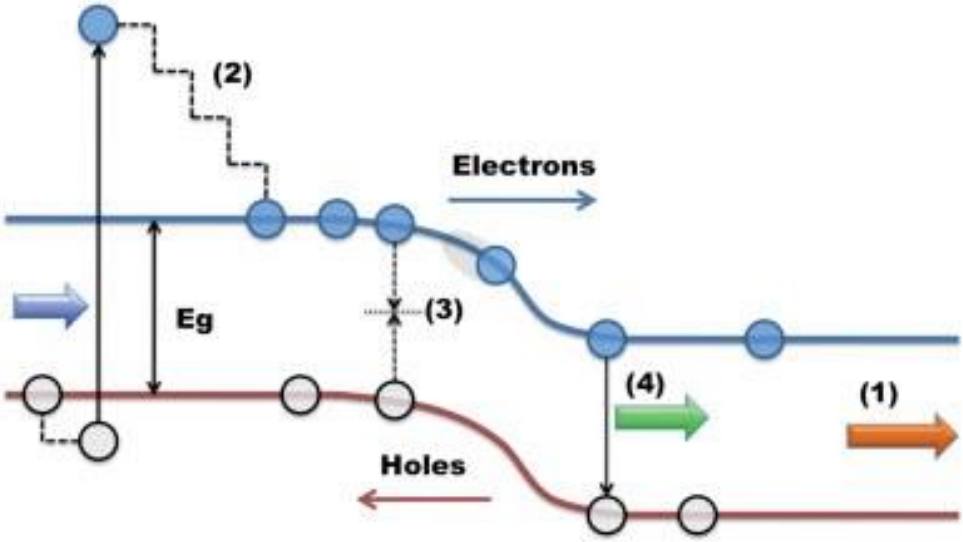

Figure 1. 1. Schematic of a p-n junction with major loss mechanisms: 1) transmission loss, 2) thermalization loss, 3) non-radiative recombination, 4) radiative-recombination. [Reproduced from: *Brown, Gregory F., et al. "Third generation photovoltaics." Laser & Photonics Reviews 3, no. 4 (2009): 394-405.*] [4]

As is the case for all thermodynamic systems, solar cells suffer from several fundamental energy loss mechanisms. One of the major loss mechanisms for solar cells is transmission loss (1) in Figure 1.1. This effect derives from the transmission of low-energy photons that are not absorbed by the system at energies less than the band gap of the absorber. Another major loss mechanism in solar cells is thermalization loss (process labeled 2 in Figure 1.1), which occurs when high-energy photons are absorbed. In a semiconductor when a photon with energy above the band gap is absorbed, it creates carriers with excess kinetic energy, which are often referred to as: hot carriers. In most

types of solar cells, photogenerated hot carriers lose their excess kinetic energy through interaction with phonons in the system. This thermalization loss occurs extremely quickly after absorption (in a few picoseconds) and causes the relaxation of hot carriers to the fundamental band edge of the absorber, (2) in Figure 1.1. [3, 4]

Other loss mechanisms, such as (3) and (4) in Figure 1.1, are related to non-radiative and radiative recombination processes. These loss processes limit the amount of current that can be extracted from the system. Through these processes, the energy of the charges is lost via radiative recombination (photon emission) or non-radiative recombination (defects or phononic interactions). [3, 4]

In general, it is possible to increase the total light absorption in a solar cell by using a lower band gap semiconductor; however, this causes an increase in thermalization loss. On the other hand, utilizing a wider band gap semiconductor reduces the thermalization loss at the expense of absorption. In other words, there is a trade-off between reducing thermalization loss and increasing the absorption in the solar cell. Therefore, to optimize power conversion efficiency in a single junction solar cell, it is required to find a balance between the thermalization and transmission loss. In 1961 Shockley and Queisser proposed a model to determine the maximum power conversion efficiency for a single junction solar cell. [5] According to this model, all photogenerated carriers above the solar cell's band gap relax down and occupy energy levels at the band edge of the semiconductor in both the conduction and valence bands. Hence, extracted carriers will have an energy difference equal to the semiconductor's band gap. By optimizing the extracted power, the maximum conversion efficiency for a single junction solar cell (without concentration) is ~ 33%, which is achieved for an absorber with a band gap of

~ 1.4 eV. [4] This value sets the upper limit for power conversion efficiency in a single junction solar cell and is known as the Shockley-Queisser limit.

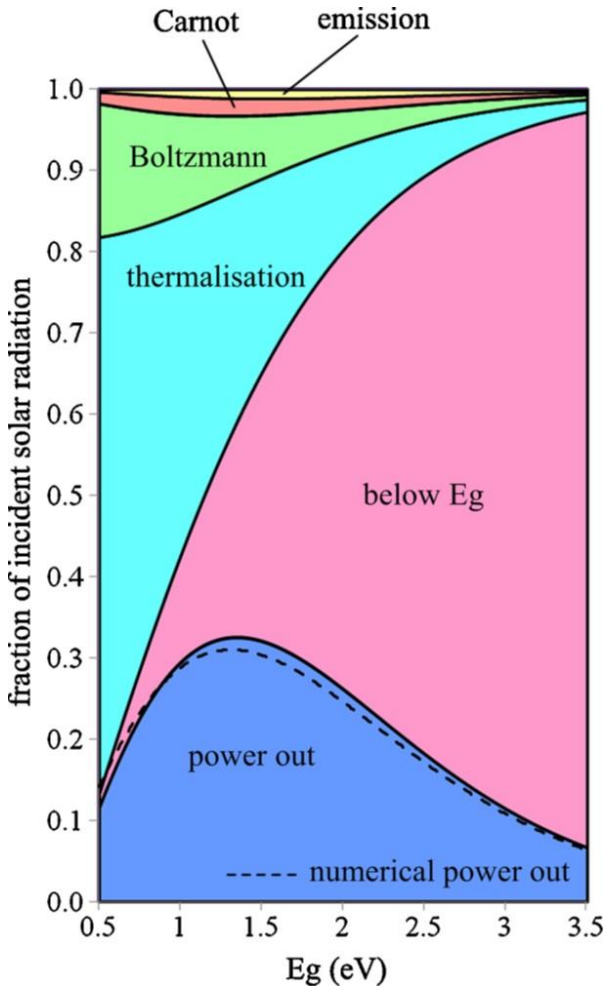

Figure 1. 2. The amount of power conversion efficiency and different fundamental loss processes as a function of solar cell absorber band gap. [Reproduced from: Hirst, Louise C., *et al.* "Fundamental losses in solar cells." Progress in Photovoltaics: Research and Applications 19, no. 3 (2011): 286-293.] [6]

It is possible to determine the contribution of different loss mechanisms for a range of band gap energies, as shown in Figure 1.2. These loss mechanisms are intrinsic for solar cells, regardless of material quality, operation condition, and parasitic resistances within

the system. The dark blue area in Figure 1.2 shows the region where usable power can be extracted in a single gap solar cell. The various colored regions (other than the blue regime) represent different loss mechanisms in the system. As described above, the two major losses incurred by the system are due to transmission of below band gap photons (magenta color) and thermalization (cyan color). The Boltzmann loss (green color) is due to the mismatch between the light absorption and emission angle and the subsequent increase in entropy this loss invokes. However, by concentrating light on the cell, it is possible to reduce this mismatch; consequently, lowering the contribution of this entropic loss mechanism. The Carnot loss is the thermodynamic loss, which limits the amount of power conversion for engines working between hot and cold reservoirs. [6]

Designing photovoltaic solar cells with low dollar per Watt ($/W) ratio and high power conversion efficiency is essential for the implementation of emerging photovoltaic technologies. Three generations of solar cells have been developed, which have been aimed at improving conversion efficiency and reducing the production costs. Figure 1.3 shows an efficiency map – and the parameter space for these three generations of solar cell. First generation (green region) solar cells are based on a single bulk semiconductor p-n junction. [2, 3] In the first generation, silicon solar cells have achieved efficiencies of 26.3%, which is very close to its maximum theoretical efficiency (29.1%) for such systems. [7, 8] One of the main *historical* challenges associated with first generation solar cells are costs related to material consumption. Therefore, second generation (yellow region in Figure 1.3) solar cells (which are based on thin film technologies) have been proposed to reduce material usage. Thin film solar cells, such as CdTe and $Cu(In,Ga)Se_2$ (CIGS), reduce production costs due to the

reduced material consumption of the modules. However, their power conversion efficiency is still somewhat less than first generation solar cells. [3]

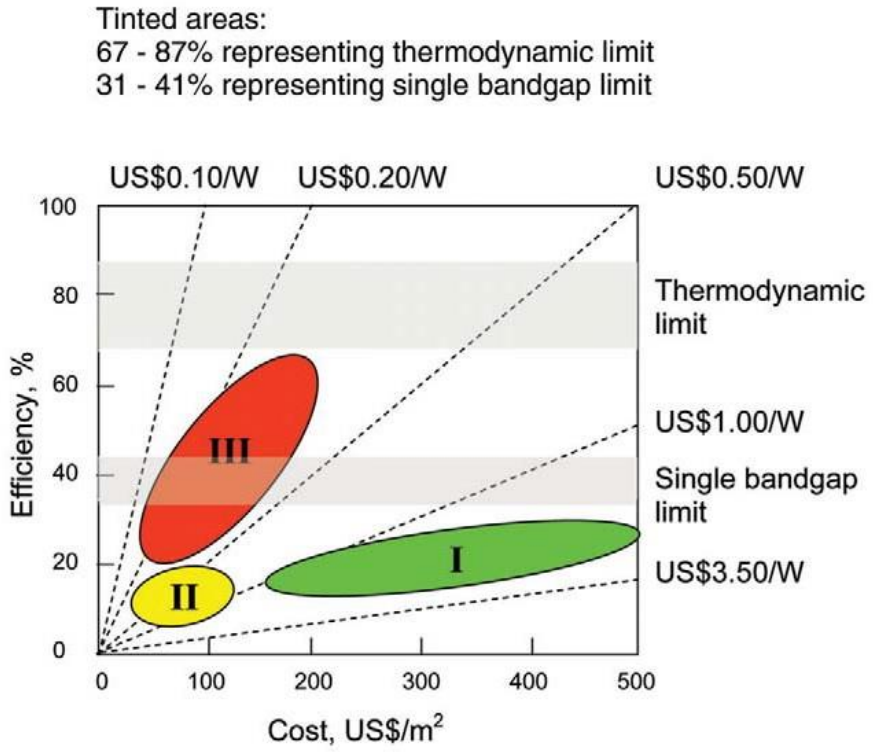

Figure 1. 3. Efficiency-cost graph of three generations of photovoltaic solar cells. First generation is about bulk systems, second generation is for thin films, and third generation is about advanced thin-film systems. [Reproduced from: *Conibeer, Gavin. "Third-generation photovoltaics." Materials today 10.11 (2007): 42-50.*] [9]

Although reducing the module fabrication cost is important for solar cell technology, there are other basic costs, like wiring, inverters, and/or batteries (amongst others), which are still considerable and increase final module costs. So, further reducing the module (solar cell) production costs will have a limited impact on the overall power

generation costs. Therefore, third generation (green region in Figure 1.3) solar cells have attracted considerable recent attention due to their potential to the increase power conversion efficiency, in tandem with reducing fabrication costs. [4, 9]

As discussed, only photons with the energy values of the absorber are optimally converted to electron hole pair generation. Photons with energies below the cell band gap are not absorbed and the excess energy of photons above the band gap is lost via thermalization. Therefore, to enhance power conversion efficiency there is two main strategies: 1) increasing the amount of low energy light absorption, and 2) reducing thermalization loss mechanisms. Third generation technologies are focused on using novel concepts to increase the conversion efficiency of solar cells beyond the Shockley-Queisser limit (33%). Several systems have been proposed as third generation solar cells such as: 1) multi-junction solar cells; 2) intermediate band solar cells; 3) up-conversion systems; 4) down-conversion techniques; 5) hot carrier solar cells; and 6) multi-exciton generation solar cells. The photovoltaic devices described from 1 to 4 are mainly concerned with solar spectral splitting to optimize access to the solar spectrum using several solar cell absorbers. However, the last two technologies (5 and 6) target inhibiting (or circumventing) the thermalization loss mechanisms. [3, 4, 9]

Multi-junction solar cells (MJSC) are third generation solar cells, which have achieved the highest power conversion efficiency to date (~ 46%). [8, 10] These solar cells consist of multiple semiconductors (with different band gap energies) stacked on top of one other. Materials with optimal band gap energies are selected in order to cover the whole solar spectrum range. Thus, the solar spectrum is decomposed to multiple energy ranges and absorbed by several solar cells. In these solar cells, the layer with the

largest band gap is placed on top of the MJSC – to absorb UV light – and the material with the lowest band gap is placed at the bottom to absorb low(er) energy IR photons. Through this strategy, it is possible to optimize solar cell absorption and increase power conversion efficiency. [4] MJSCs layers are connected in series, therefore, all layers are required to generate the same amount of current (so-called current matching) otherwise the extra current generated by one junction will be lost. [2]

Intermediate band solar cells (IBSCs) are photovoltaic devices that have been proposed to absorb sub-band gap energy photons (while sustaining the operating voltage of the matrix) establishing an intermediate energy level in the solar cell absorber. [11] Up-conversion and down-conversion techniques, which are based purely on optical processes, have been proposed to optimize the absorbed photon energy of the solar cell band gap in order to improve light absorption. In the up-conversion technique, low energy infrared (IR) photons are converted to higher energy photons (the opposite mechanism happens for the down conversion technique) so that: the amount of transmission losses will be reduced. [4, 12, 13] In multi-exciton generation (MEG) solar cells, photogenerated hot carriers (generated by high energy photons) promote several electron-hole pairs. Through this process, one high-energy photon generates multiple excitons via impact ionization, which results in an enhancement of the extracted current. [14]

Another attractive concept for third generation solar cells is a ***hot carrier solar cell***. This type of solar cell (the main topic of this thesis) has been proposed to increase power conversion efficiency beyond the Shockley-Queisser limit for a single junction solar cell via inhibiting thermalization loss. [15] In the absence of thermalization loss it is

possible to reduce the solar cell band gap in order to increase absorption. Through this technique, the maximum (ideal) achievable power conversion efficiency is predicted to be ~ 66% and ~ 85% for a single junction solar cell under 1-Sun AM 1.5G and full solar concentration, respectively. [15, 16]

1.2. Hot Carrier Solar Cells

As discussed, in a semiconductor when a photon with energy above the band gap is absorbed, it creates carriers with excess kinetic energy, so-called hot carriers, which are at an elevated temperature with respect to the lattice. However, these photogenerated hot carriers lose their excess kinetic energy via electron-phonon interactions a few picoseconds after generation. Figure 1.4 shows the dynamics of hot carriers from generation to radiative recombination (full thermalization).

Before photo-absorption occurs (see region (1) in Figure 1.4), electrons and holes are at equilibrium with the lattice. (1) Immediately after absorption (t = 0 s, region (2)), the photogenerated carriers occupy narrow energy levels. (2) Then, within sub-picoseconds, (elastic) carrier-carrier scattering occurs and photogenerated carriers redistribute energy amongst themselves as shown schematically in (3) and (4). Therefore, photogenerated electrons (and holes) achieve a global non-thermal "hot carrier" distribution in the conduction (and valence) band with an associated carrier temperature that is higher than the equilibrium temperature of the lattice (4). A few picoseconds after light absorption, however, photogenerated hot carriers interact with phonons, which thermalize the system. As a result, the energy of the carrier distribution reduces and they cool, see (5) and (6) in Figure 1.4. Finally, thermalized electrons and holes recombine and

equilibrium is restored. [3] The associated heat dissipation cannot be harnessed as useful power in a solar cell.

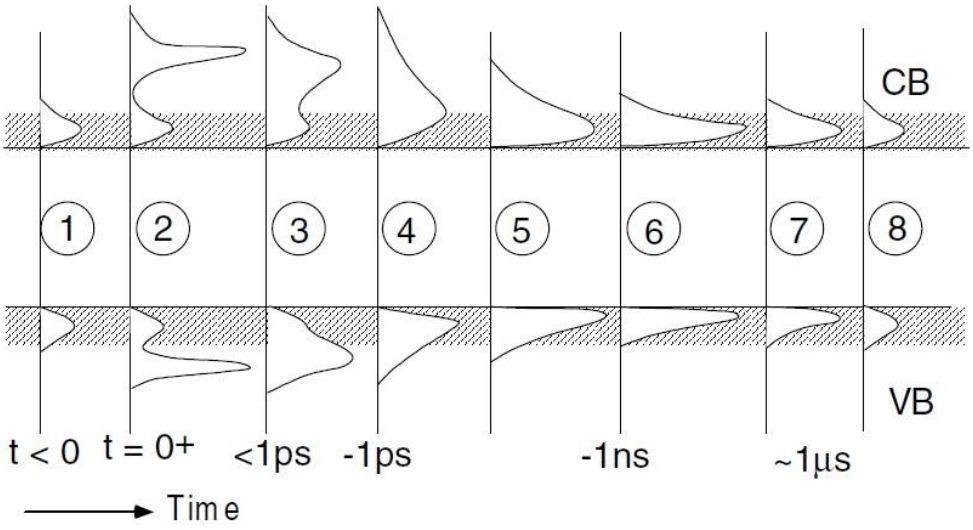

Figure 1. 4. Time evolution of hot carriers from generation to radiative recombination. [Reproduced from: *Green, Martin A. "Third generation photovoltaics: advanced solar energy conversion." Physics Today 57, no. 12 (2004): 71-72.*] [3]

It is observed by increasing excitation power, the photogenerated carrier density increases and consequently carrier-carrier scattering reduces. At this condition a steady state hot carrier distribution can be created if the photo-excitation rate is higher than the cooling rate and lower than carrier-carrier scattering. Therefore, the density of photogenerated hot carriers increases and electron-phonon interactions become less efficient; *i.e.*, the creation of a phonon bottleneck effect. [17, 18] Although a steady state hot carrier distribution has the potential to create a condition for increased conversion efficiency, it is still essential to extract the photogenerated hot carriers on an ultrafast timescale, otherwise hot carriers will *eventually* dissipate their excess kinetic energy via

electron-phonon interactions with no impact on enhancing power conversion efficiency. [19, 20, 21, 22]

Since the first proposal of the hot carrier solar cell concept by Ross and Nozik in 1982, [15] no *practical* hot carrier solar cells have been demonstrated. Despite significant progress in the field, there are still two main challenges that need to be overcome: 1) to design a hot carrier absorber, which can significantly inhibit hot carrier thermalization; [23] and 2) to extract hot carriers adiabatically before they thermalize. [24] Figure 1.5 shows a schematic of a proposed mechanism for operation of hot carrier solar cells using energy selective contacts to extract hot carriers. [25]

The hot carrier solar architecture shown in Figure 1.5 has two main components: 1) a hot carrier absorber; and 2) energy selective contacts for both electron and hole extraction. In Figure 1.5, T_L, T_{eh}, E_g, E_{eh}, and μ are lattice temperature, carrier temperature, absorber band gap, extraction energy, and *quasi* Fermi level splitting, respectively. In the hot carrier absorber, a steady state hot equilibrium distribution is established via inhibiting hot carrier-phonon interactions. [19, 20, 25] Therefore, carriers are at elevated temperature with respect to the lattice. Then, photogenerated hot carriers are extracted resonantly through an energy selective contact designed either for electrons or holes. The selectivity of the resonant tunneling structure is preferred to be narrow in order to minimize entropy exchange between the hot (the hot carrier absorber) and cold (ambient) reservoirs; thus, reducing hot carrier thermalization during the extraction process.

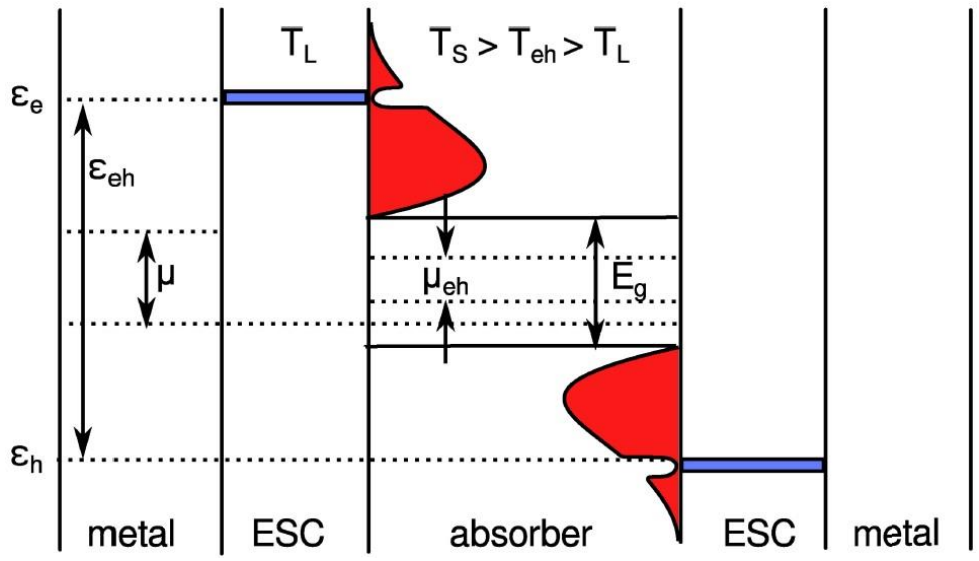

Figure 1. 5. Schematic of a hot carrier solar cell with a hot carrier absorber and energy selective contacts. [Reproduced from: *Hirst, L. C., et al. "Hot carriers in quantum wells for photovoltaic efficiency enhancement" IEEE Journal of Photovoltaics, 4(1), (2014): 244-252.*] [25]

By adiabatic extraction of hot carriers through narrow energy range membranes, the excess kinetic energy of hot carriers is then converted to potential energy. As shown in Figure 1.5, both electrons and holes are extracted through energy selective contacts. The energy difference between electrons and holes determines E_{eh}, which is larger than the absorber band gap energy. As a result, the output voltage, V, as proposed by Würfel *et al.* [26] for hot carrier solar cells with extracted energy, E_{eh}, and quasi Fermi level splitting, $\Delta\mu$, is given by:

$$q\,V = \left(1 - \frac{T_L}{T_{eh}}\right) E_{eh} + \Delta\mu\,\frac{T_L}{T_{eh}}. \tag{1.1}$$

1.3. Hot carrier absorbers

One important objective regarding hot carrier absorbers is (obviously) to determine the photogenerated carrier temperature. Steady state photoluminescence spectroscopy is a practical technique for the determination of the carrier temperature. It is possible to model the emitted PL spectrum of a sample utilizing an equilibrium based generalized Planck's radiation law, as given by: [27, 28]

$$I_{PL}(E) = \frac{A(E)\,(E)^2}{4\pi^2 h^3 c^2}\left[exp\left(\frac{E-\Delta\mu}{k_B T_H}\right) - 1\right]^{-1}, \tag{1.2}$$

where I_{PL} is the PL intensity, E is the photon energy, $\Delta\mu$ is the quasi Fermi level splitting, h is Planck's constant, c is the speed of light, k_B is Boltzmann constant, $\Delta\mu$ is the chemical potential difference (quasi-Fermi level splitting), T_H is the carrier temperature, and $A(E)$ is the absorptivity of the sample. By fitting the emitted PL spectrum of the sample with Equation 1.2, information regarding the carrier temperature and chemical potential difference can be extracted. The advantage of this analysis is to determine a quasi-Fermi level splitting, which is related to the open circuit voltage (V_{OC}) for a *contact-less* sample. [28]

Another method to extract the carrier temperature from a PL spectrum without doing a complicated analysis through fitting the whole PL spectrum using Equation 1.2 is to simply perform linear fitting on the high-energy side of natural logarithm of PL spectrum. By taking the natural logarithm of PL intensity in Equation 1.2, the equation is written: [20, 22, 25, 29]

$$\ln\big(I_{PL}(E)\big) = \ln\big(\varepsilon(E)\big) - \frac{E}{k_B T_H}, \tag{1.3}$$

where $\varepsilon(E)$ is emissivity. It is observed that the natural logarithm of the PL intensity is inversely proportional with carrier temperature. This method is a practical technique to extract carrier temperature from PL spectroscopy.

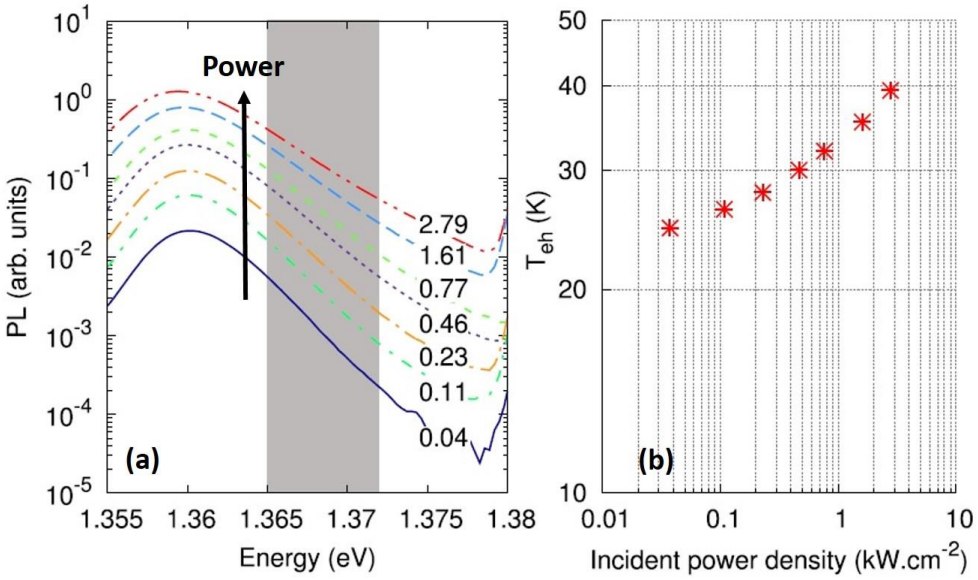

Figure 1. 6. (a) Excitation power dependent photoluminescence spectra at 10 K. (b) Extracted carrier temperature from the power dependent data in panel (a) versus excitation power at 10 K. [Reproduced from: *Hirst, L. C., et al. "Experimental demonstration of hot-carrier photo-current in an InGaAs quantum well solar cell." Applied Physics Letters 104, no. 23 (2014): 231115.*] [30]

Figure 1.6 (a) shows the PL spectrum (in a logarithm scale in the y-axis) of an InGaAs QW structure as a function of photon energy at various excitation powers, reproduced from Ref [30]. As discussed, it is possible to extract carrier temperature via linear fitting to the high-energy side of the PL spectrum, the extracted slope being inversely proportional to carrier temperature. It is observed by increasing the excitation power the

slope on the high-energy side of PL spectrum becomes shallower, see Figure 1.6 (a). The reduction in extracted slope, as shown in Equation 1.3, is indicative of an increase in carrier temperature at higher excitation powers, see Figure 1.6 (b). [20, 22, 29]

The above-mentioned technique therefore makes it possible to determine carrier temperature and investigate hot carrier behavior in solar cell absorbers using simple spectroscopy. However, to evaluate quantitatively the performance of a hot carrier absorber candidate system and to have a comparison with other designs, Le Bris *et al.*, [20] proposed a semi-empirical model to characterize hot carrier properties of the samples. The model is governed by the following equation:

$$P_{th} = \frac{t\, n_q\, E_{LO}}{\tau_{th}} \exp\left(-\frac{E_{LO}}{K_B T_H}\right) = Q(T_H - T) \exp\left(-\frac{E_{LO}}{K_B T_H}\right), \tag{1.4}$$

where P_{th} is thermalized power, n_q number of phonon modes, E_{LO} LO-phonon energy, and τ_{th} LO-phonon scattering lifetime. At open circuit voltage when there is no charge extraction (which is similar to steady state PL experiment) the absorbed power is considered to be equal to thermalized power (P_{th}). [18, 20] According to Equation 1.4, plotting absorbed power (divided by the exponential factor) versus the temperature difference between carriers (T_H) and the lattice (T) results in an extracted slope that provides the thermalization coefficient (Q) of the sample. The phonon mediated thermalization coefficient (Q) in Equation 1.4 represents how efficiently LO-phonon channels in the system thermalize hot carriers. In other words, an absorber with a large thermalization coefficient value is *not a good candidate* as a hot carrier absorber.

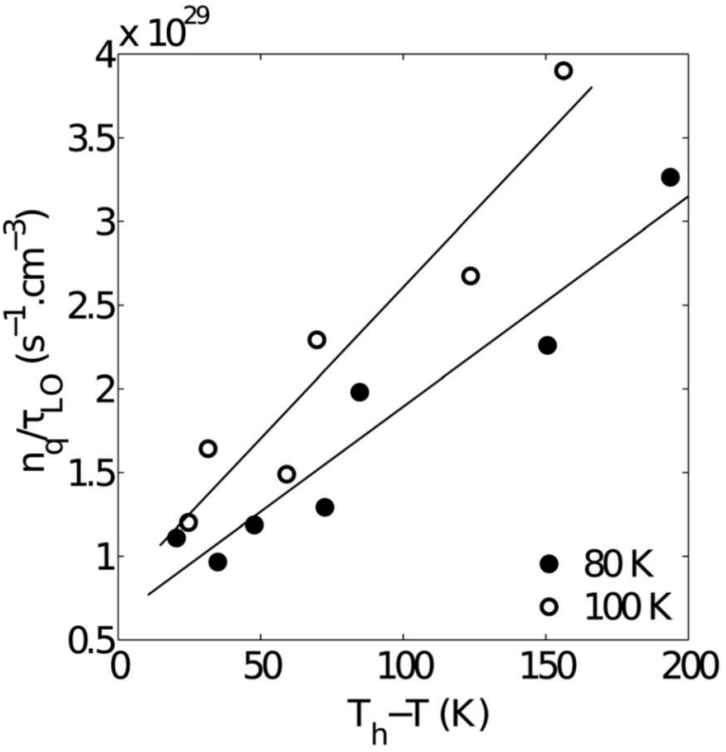

Figure 1. 7. Change in $^{n_q}/_{\tau_{LO}}$ ratio versus temperature difference between carrier and lattice at 80 K and 100 K. The extracted slopes show thermalization coefficient of the GaInAsSb QW structure. [Reproduced from: *Le Bris, A., et al. "Thermalisation rate study of GaSb-based heterostructures by continuous wave photoluminescence and their potential as hot carrier solar cell absorbers" Energy & Environmental Science, 5(3), (2012):6225-6232.*] [20]

Figure 1.7 shows the change in the $^{n_q}/_{\tau_{LO}}$ ratio determined from the power dependent PL of an InGaAsSb QW structure versus the temperature difference between the carriers and lattice at 80 K and 100 K (reproduced from Ref. [20]). [20] The extracted slopes in Figure 1.7 are related to the carrier cooling rates, in other words – equal to the thermalization coefficient values of the sample at 80 K and 100 K. It is observed that by increasing the lattice temperature, the thermalization coefficient increases, which

indicates that at a higher (100 K) lattice temperatures hot carrier thermalization via LO-phonon emission is a more efficient process. [20]

For hot carrier solar cell applications, it is important to design a hot carrier absorber with a low thermalization coefficient. There has been significant recent research with respect to finding materials with low hot carrier thermalization coefficients. Materials such as InN, [31] BSb, [32] AlSb [33] have all shown lower thermalization effects as compared with other bulk materials. The slow carrier cooling in these systems is due predominantly to a large band gap between optical and acoustic phonons that reduces anharmonic coupling and slows heat dissipation created by the large difference in mass of cations and anions. [23] In compounds with large 'so-called' phononic band gaps, the Klemens mechanism is inhibited. [34] In the Klemens process a high energy LO-phonon decays into two low energy acoustic phonons with the same energy value and opposite momenta. Through this Klemens process (which dominates in III-V semiconductors) the energy of LO-phonons is dissipated as heat in the system. [23, 34]

In addition, it is observed that carrier-cooling rates in nanostructure absorbers are also significantly slower than their bulk counterparts. [23] The comparison between cooling rates of bulk GaAs and a GaAs/AlGaAs MQW structure using time resolved transient spectroscopy by Rosenwaks *et al.* [35] revealed that a hot carrier distribution can be established for a longer period of time in a MQW structure than a bulk system, even at low injection levels. Similar studies have been performed on a number of different nanostructures, such as QWs, [36] QDs, [37] and quantum wires [38] to compare their carrier cooling rates with bulk systems. It was confirmed that there is a significant reduction in carrier cooling rates when carriers are confined in regions with dimensions

less than their de Broglie wavelength; i.e. in the quantum confined regime. [39, 40] This effect is attributed to the creation of a phonon bottleneck in nanostructures, although the exact origin of this behavior (or mechanisms involved) remains under debate. One proposed hypothesis is that the photogenerated carriers do not diffuse significantly in the lattice – which is not the case in bulk systems. This effect causes an increase in the local density of (hot) carrier concentration in nanostructures and consequently an increase in their average carrier temperature. [18, 23] In addition, the local density of the LO-phonons emitted by confined hot carriers within the QW becomes larger due to the increase in carrier localization within the QW. As a result, the probability of energy reabsorption of hot LO-phonons by hot carriers increases due to hot carrier screening effects. In other words, although there are phonons in the system, they less efficiently thermalize hot carriers (than bulk systems) via heat dissipation. As a result, it is expected that a more stabilized hot carrier distribution (even at lower excitation intensities) can be achieved, as compared with bulk systems. [21, 23]

Another proposed reason for the creation of the phonon bottleneck effect in nanostructures is the potential to engineer the phononic properties of compounds. In designing a nanostructure, it is possible to combine layers with very little overlap at their LO-phonon energies at the interface between the well and the barrier. Hence, LO-phonons generated during hot carrier cooling processes cannot propagate effectively through the interface and are therefore reflected. As a result, the local density of LO-phonons increases and the probability of energy reabsorption by hot carriers becomes larger (i.e., a phonon bottleneck). This provides the potential for a condition for the creation of a stabilized hot carrier distribution. [21, 23, 41]

1.4. Energy selective contacts

So far, the importance of reducing the carrier-cooling rate to keep hot carriers at higher temperatures than the lattice has been discussed. However, it is still essential to extract carriers quickly before they thermalize. With no efficient hot carrier extraction mechanism, hot carriers will eventually lose their excess kinetic energy via thermalization. Extraction of hot carriers requires an adiabatic process to reduce entropy within the system. Energy selective contacts (ESCs) have been proposed to extract carriers within a specific range of energy. To reduce the amount of entropy exchange with the environment, it is required to create a narrow energy selective (δE) contact. [16, 18] On the other hand, narrow energy selectivity has less electrical conductivity as compared to wider energy designs. Therefore, there is a trade-off between reducing entropy exchange and increasing the electrical conductivity in optimum hot carrier solar cells especially, at high solar concentration, which generates high carrier densities.

There have been several different proposed approaches to extract hot carriers with minimal entropy exchange with the ambient reservoir; such as resonant tunneling structures utilizing double-barrier QWs, [42] QDs, [24] and barrier oxide layers incorporating impurities or defects states. [19] In the above mentioned structures, wide band gap materials are typically used in order to separate the hot carrier distribution from a cold reservoir (ambient). Therefore, hot carriers can tunnel through the barrier material and be extracted. The energy selectivity of ESC structures is determined by the energy confinement in the nanostructures; only carriers with energy values equal to the confined states can tunnel through the barrier material resonantly.

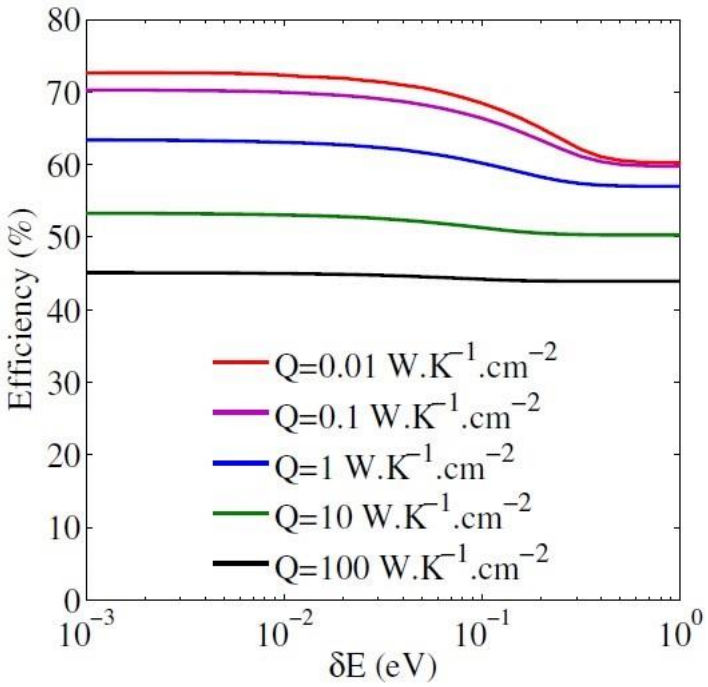

Figure 1. 8. Calculated efficiency for a hot carrier absorber with 1 eV band gap versus energy selectivity ranging from 1 meV to 1 eV for various thermalization coefficient values. [Reproduced from: *Le Bris, A. (2011). Feasibility study of a hot carrier photovoltaic device (Doctoral dissertation, Ecole Centrale Paris).*] [18]

Figure 1.8 shows the change in solar cell conversion efficiency versus energy selectivity of a resonant tunneling structure for various thermalization coefficients. Although designing ESCs with narrow energy selectivity reduces the entropy exchange with an ambient reservoir, a theoretical study of energy selective contacts with different energy selectivity has shown that the difference in power conversion efficiency for energy selectivity at the range of energy values between 1 meV to 1 eV is at most 12% under full solar concentration – for a system with a very low thermalization coefficient, see red line in Figure 1.8. In addition, as shown in Figure 1.8, it is observed that by utilizing wide band selective contacts (~ 1 eV) the total conversion efficiency does not

change considerably for a hot carrier absorber that has a thermalization coefficient in the range of a few W $K^{-1}cm^{-2}$. In other words, the results indicate that semi-selective contacts ($\delta E > 0.5\ eV$), which are desirable for enhancing electrical conductivity are also promising for hot carrier extraction – especially, at a condition with high solar concentrations. [18]

1.5. Recent progress in the hot carrier solar cells

The simultaneous demonstration of hot carrier photocurrent and photoluminescence recently published on an $In_{0.16}Ga_{0.84}As$/GaAs QW solar cell at 10 K by Hirst *et al*. [30] Figure 1.9 (a) shows *J*-*V* characteristics of the QW structure under a monochromatic laser source (1.41 eV, pumped below the GaAs barrier band gap energy) excitation at 10 K (red line) and at 1-sun illumination at 295 K (dashed line). It is evident that in reverse bias the *J*-*V* curve has a constant photocurrent density, which is indicative of extraction of all photo-excited carriers from the solar cell. However, by increasing bias voltage (moving towards positive values), the *J*-*V* curve develops an inflection, which is indicative of a barrier effect inhibiting carrier transport. Indeed, in Figure 1.9(a) it is observed that in the range 1.1 V – 1.4 V, the extracted current density from the QW structure is zero. At elevated temperature (295 K, dashed line) the *J*-*V* curve does not show any evidence of barrier effects.

The reason for zero extracted current in the bias regime between 1.1 V and 1.4 V is due to the strong confinement of photogenerated carriers within the InGaAs QW. Under these conditions, photogenerated carriers cannot readily escape the QW and are not effectively extracted as current. However, the *J*-*V* characteristic at 295 K does not show

such effects of localization of charges within the QW. This behavior is due to enhanced thermionic emission and the escape of photogenerated carriers from the QW at higher temperatures. [30]

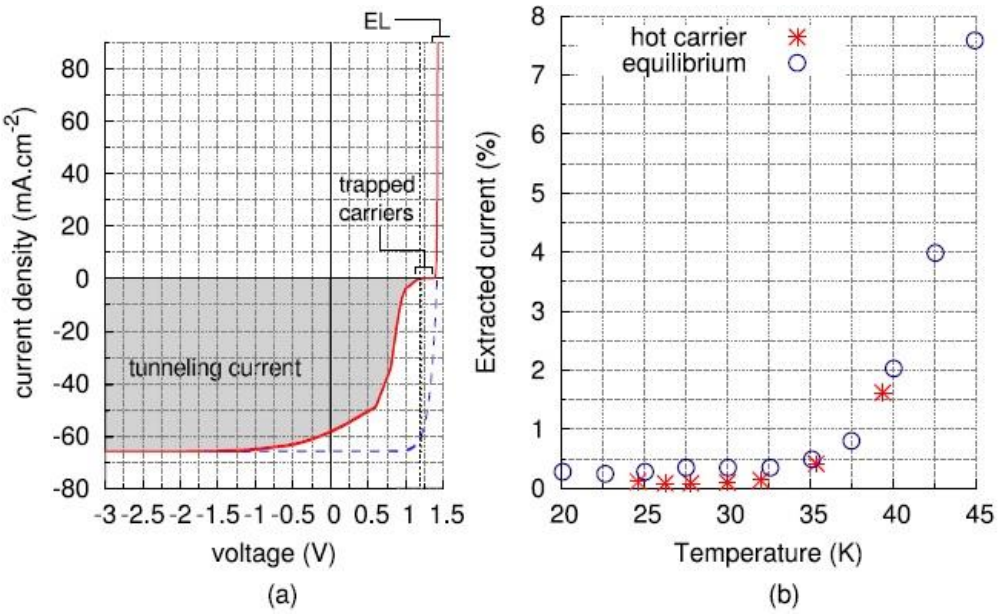

Figure 1. 9. (a) Current-voltage characteristic of the InGaAs QW at two conditions: 1) under a monochromatic laser source (1.4 eV) at 10 K, see the solid red line, 2) under a solar simulator (AM 1.5) illumination at 295 K, see the dashed line. (b) Extracted current percentage (the ratio between photo-excited current at 1.2 V and reverse bias saturation current) versus carrier temperature. Red stars and black circles show the values for non-equilibrium hot carriers and thermal equilibrium carrier with lattice, respectively. [Reproduced from: *Hirst, L. C., et al. "Experimental demonstration of hot-carrier photo-current in an InGaAs quantum well solar cell." Applied Physics Letters 104, no. 23 (2014): 231115.*] [30]

To investigate the presence of hot carrier derived photocurrent in the QW structure, PL spectroscopy of the sample at 10 K was performed while the sample is under a fixed

bias at 1.2 V. At this condition and under low excitation power, it is expected that the photogenerated carriers are strongly localized in the InGaAs QW. Therefore, by increasing the excitation power, any enhancement in photogenerated current is expected to be associated with an increase in the hot carrier distribution, which facilitates tunneling and/or thermionic emission processes through the barrier material. [30] This hypothesis is supported by the simultaneous determination of the carrier temperature from the high energy tail of the emitted PL spectra. Figure 1.9 (b) shows the percentage of current extracted (the ratio between photo-excited current at 1.2 V and reverse bias saturation current) versus temperature. The red stars in Figure 1.9 (b) show the amount of extracted current (%) at 10 K for various excitation powers. It is seen by increasing the non-equilibrium hot carrier temperature (or associated excitation powers), there is an increase in extracted current (%) in the system. In addition, a similar trend is observed for extracted current (%) when the lattice temperature increases while carriers remain at equilibrium with the lattice. The increase in extracted current (%) indicates that when the hot carrier distribution increases (either by an increase in excitation power or increase in lattice temperature) more photogenerated hot carriers (escape) are extracted the QW. [30]

Another recent demonstration of hot carrier solar operation was presented by Dimmock *et al.*, [42] incorporating a double barrier resonant tunneling structure, as shown in Figure 1.10 (a). In this design, hot carriers are generated within a narrow band gap material and then collected via a resonant tunneling process through a double-barrier structure into a wider band gap collector. The resonant tunneling structure in the system acts as an energy selective contact, which allows only carriers with a particular

range of energy to propagate through the system and finally be collected at the metallic contact. Through this mechanism, photogenerated hot carriers are extracted with minimal energy loss. In addition, electrons with different energy values are reflected back into the absorber and their energy redistributed amongst the other electrons. [42]

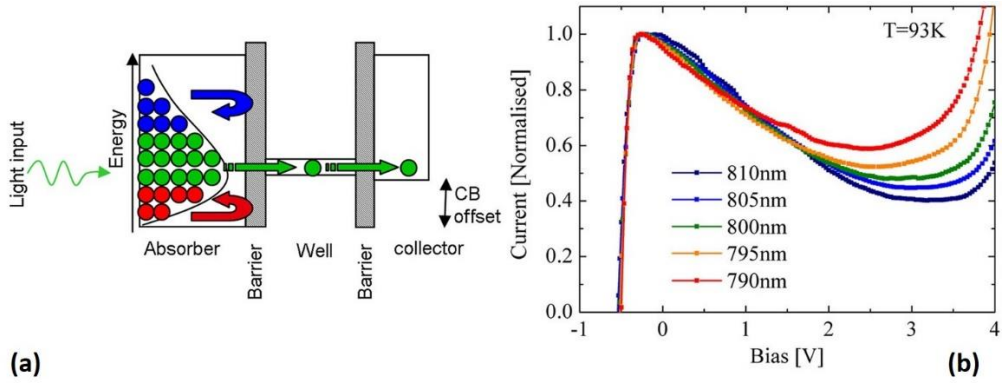

Figure 1. 10. (a) Schematic of a double-barrier resonant tunneling structure as a hot carrier solar cell. (b) Current-voltage characteristic of the device at 93 K under various wavelength excitations. [Reproduced from: *Dimmock, J., et al. "Demonstration of a hot-carrier photovoltaic cell." Progress in Photovoltaics: Research and Applications 22, no. 2 (2014): 151-160.*] [42]

The QW structure in this study consists of GaAs as a narrow band gap absorber embedded between two AlAs layers as the barrier regions. The collector material is $Al_{0.07}Ga_{0.93}As$ (a wide band gap material), which is undoped in order to improve the tunneling process from the absorber into the collector. The absorber region is *also* undoped to reduce the thermalization loss of hot carriers through interactions with pre-existing electrons, which are in equilibrium with the lattice. The driving force in this structure is attributed to the temperature difference between the photogenerated carriers

within the absorber and collector. Therefore, hot carriers in the absorber can tunnel through the barrier material and reach the collector. [42]

The device is illuminated using several different wavelengths from 790 nm to 810 nm to investigate the properties of the photogenerated carriers. It is expected under a short wavelength excitation that the photogenerated carriers will be at higher temperature with a broader carrier distribution, than when the system is excited with longer wavelength (lower energy) light. Consequently, shorter wavelength photons are expected to create a broader carrier distribution than those excited by longer wavelength light. As a result, by pumping the sample with shorter wavelength (790 nm) – higher energy – excitation, the peak position of the current-voltage (I-V) characteristic is expected to be at a lower voltage as compared with the I-V when excited with the other (longer) wavelength sources. In addition, the peak to valley current ratio (PVR) becomes less in the presence of an energetically wide electron distribution created by short wavelength light. The reduction in PVR is associated with tunneling of more hot carriers through the resonant tunneling structure. [42]

Figure 1.10 (b) shows the current-voltage characteristic for various wavelength excitations at 93 K. First, it is evident that peak current shifts to lower values under short wavelength excitation. Secondly, it is seen that the PVR decreases with increasing (decreasing) excitation photon energy (wavelength), which is indicative of a change in the linewidth broadening of the photogenerated carrier distribution as a function of the wavelength of excitation. [42] These characteristics are strong evidence of the creation of hot carriers and energy selective extraction in the simple QW system proposed.

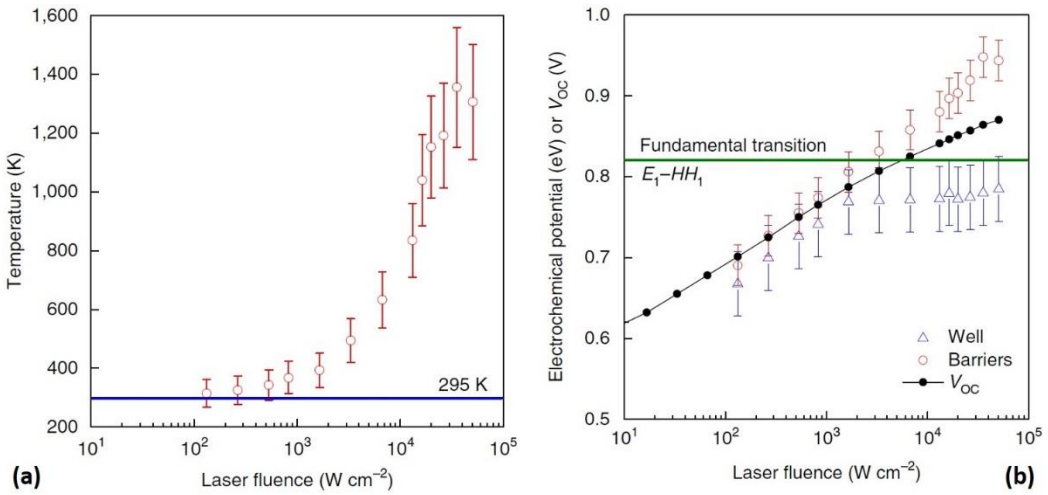

Figure 1. 11. (a) Extracted carrier temperature versus the laser excitation. (b) Extracted electrochemical potential for electrons in the QW (green triangles), the barrier (red circles), and the extracted open circuit voltage (black circles) versus laser excitation. The solid green line shows the lowest energy transition within the QW. [Reproduced from: *Nguyen, D., et al. "Quantitative experimental assessment of hot carrier-enhanced solar cells at room temperature." Nature Energy 3, no. 3 (2018): 236.*] [43]

Recently, an InP/InGaAsP single quantum well structure was designed to operate as a hot carrier solar cell at room temperature. [43] Continuous wave power dependent photoluminescence up to 1650 W/cm^2 (equivalent to 55,000 Suns) was performed to investigate the thermodynamic properties of the device. [44] The emitted PL spectra were fit with Planck's radiation law, and the results of the fitting of the carrier temperature and chemical potentials of both the QW and surrounding barrier material are shown in Figure 1.11. It is evident in (a) that the carrier temperature in the QW increases as a function of excitation power and it reaches a temperature greater than 1000 K above room temperature. [43]

The electrochemical potential of electrons in the QW (green triangles) and in the barrier (red circle), along with the open circuit voltage as a function of excitation power are plotted in Figure 1.11 (b). The solid green line shows the lowest energy value for the interband transition in the QW (E_1-HH_1). It is evident that by increasing excitation power, the open circuit voltage increases and at certain value it exceeds the lowest energy transition in the QW (0.82 eV).

This behavior is consistent with an increase in the chemical potential of electrons in the QW and the barrier, as well as a hot carrier distribution, as shown in Figure 1.11 (b). In addition, it is seen that at lower excitation powers, the difference between the electron chemical potential in the QW and barrier is small, but as the illumination intensity increases, this separation becomes larger. Moreover, the electron chemical potential in the QW does not go beyond the lowest transition of the QW; while, the electron chemical potential in the barrier increases beyond the lowest transition in the QW. This effect, which is associated with temperature gradient between electrons in the QW and those in the barrier, can be manipulated to increase the operating voltage of the solar cell by transferring hot electrons from the hot QW into the cold barrier (pseudo-Seebeck effect). [45]

The results presented in this recent Nature Energy article are strong evidence for the existence of hot carriers in the operation of a device at ambient conditions!

Outline of the thesis

This thesis presents a details investigation of the potential of type-II quantum wells and low-dimensional systems as candidate materials as the absorber for hot carrier solar

cells. This includes a comprehensive investigation of the InAs/AlAsSb system; in addition to optical spectroscopy of InGaAsP quaternary QWs and 2-dimentional (2D) hybrid lead halide perovskites ($MAPbI_3$). The thesis is organized into eight chapters.

Chapter 1 presents introductory material that describes hot carrier solar cells, along with current trends, perspectives, and techniques in this field of research. Chapter 2 describes the information regarding the experimental setups and characterization techniques used. Optical and electrical measurements performed in the PV group at OU are: photoluminescence spectroscopy, transmission spectroscopy, current-voltage characterization, and external quantum efficiency (EQE) measurements (amongst others).

The results of the optical characterization (continuous wave excitation power and temperature dependent photoluminescence spectroscopy) of the type-II InAs MQW structure are discussed in Chapter 3. In addition, methods for the extraction of the carrier temperature and phonon-mediated thermalization coefficient are also discussed in this chapter.

In Chapter 4, a detailed discussion of the methodology of extracting the hot carrier quantum wells is presented. Specifically, several methods are proposed and presented; as well as, potential issues related to the contribution of the higher order confined states and valence band degeneracy. This study focusses on the optical spectroscopy of an InGaAsP QW and type-II InAs QWs with supporting simulations calculated by NRL's MultiBands® software tool.

In Chapter 5, the origin of enhanced hot carrier effects in the InAs MQW structure is further investigated specifically, the origin of the *robust* hot carrier distributions

measured in these systems. The results of time-resolved transient absorption spectroscopy of the QW structure are discussed; as well as, an investigation of the phononic properties of the system, which is supported by Raman spectroscopy.

The results of the electrical characterization of type-II InAs/AlAsSb MQW p-i-n diodes with different barrier thicknesses, along with the details of the device fabrication techniques developed during this process are discussed in Chapter 6. Current-voltage characterization of the devices under 1-sun solar illumination (under concentration also), resonant and non-resonant monochromatic excitation, along with external quantum efficiency (EQE) measurements of the QW at various lattice temperatures.

The effects of the *typically-used* InP capping layer on the PL spectrum in standard InGaAsP QW structures are presented in Chapter 7. These results are disseminated by comparing QW structures with and without this InP layer. The origin of non-idealities in the system derived using temperature, power, and polarization dependent photoluminescence.

In Chapter 8, 2D and 3D $MAPbI_3$ hybrid lead halide perovskite structures are investigated using continuous wave photoluminescence and transmission measurements at various lattice temperatures. This study reveals several crystal phase transitions in these materials as a function of temperature. In addition, analysis of the temperature dependent PL is used to reveal contribution/roles of phonons and impurities in the PL linewidth broadening of these interesting new systems.

References

[1] https://www.sandia.gov/~jytsao/Solar%20FAQs.pdf

[2] Nelson, Jenny. The physics of solar cells. World Scientific Publishing Company, 2003.

[3] Green, Martin A. "Third generation photovoltaics: advanced solar energy conversion." Physics Today 57, no. 12 (2004): 71-72.

[4] Brown, Gregory F., and Junqiao Wu. "Third generation photovoltaics." Laser & Photonics Reviews 3, no. 4 (2009): 394-405.

[5] Shockley, William, and Hans J. Queisser. "Detailed balance limit of efficiency of p-n junction solar cells." Journal of applied physics 32, no. 3 (1961): 510-519.

[6] Hirst, Louise C., and Nicholas J. Ekins-Daukes. "Fundamental losses in solar cells." Progress in Photovoltaics: Research and Applications 19, no. 3 (2011): 286-293.

[7] Yoshikawa, Kunta, Hayato Kawasaki, Wataru Yoshida, Toru Irie, Katsunori Konishi, Kunihiro Nakano, Toshihiko Uto *et al.* "Silicon heterojunction solar cell with interdigitated back contacts for a photoconversion efficiency over 26%." Nature Energy 2, no. 5 (2017): 17032.

[8] https://www.nrel.gov/pv/assets/pdfs/pv-efficiencies-07-17-2018.pdf

[9] Conibeer, Gavin. "Third-generation photovoltaics." Materials today 10, no. 11 (2007): 42-50.

[10] Fraunhofer, I. S. E. "New world record for solar cell efficiency at 46% French-German cooperation confirms competitive advantage of European photovoltaic industry." Press release 26.1 (2014).

[11] Luque, Antonio, and Antonio Martí. "Increasing the efficiency of ideal solar cells by photon induced transitions at intermediate levels." Physical Review Letters 78, no. 26 (1997): 5014.

[12] Trupke, T., M. A. Green, and P. Würfel. "Improving solar cell efficiencies by up-conversion of sub-band-gap light." Journal of Applied Physics 92, no. 7 (2002): 4117-4122.

[13] Trupke, T., M. A. Green, and P. Würfel. "Improving solar cell efficiencies by down-conversion of high-energy photons." Journal of applied physics 92, no. 3 (2002): 1668-1674.

[14] Hanna, M. C., and A. J. Nozik. "Solar conversion efficiency of photovoltaic and photoelectrolysis cells with carrier multiplication absorbers." Journal of Applied Physics 100, no. 7 (2006): 074510.

[15] Ross, Robert T., and Arthur J. Nozik. "Efficiency of hot-carrier solar energy converters." Journal of Applied Physics 53, no. 5 (1982): 3813-3818.

[16] Würfel, Peter. "Solar energy conversion with hot electrons from impact ionisation." Solar Energy Materials and Solar Cells 46, no. 1 (1997): 43-52.

[17] Nozik, Arthur J., Gavin Conibeer, and Matthew C. Beard, eds. Advanced concepts in photovoltaics. Royal Society of Chemistry, 2014.

[18] Le Bris, Arthur. "Feasibility study of a hot carrier photovoltaic device." PhD diss., Ecole Centrale Paris, 2011.

[19] Conibeer, Gavin, Nicholas Ekins-Daukes, Jean-François Guillemoles, Dirk Kőnig, Eun-Chel Cho, Chu-Wei Jiang, Santosh Shrestha, and Martin Green. "Progress on hot carrier cells." Solar Energy Materials and Solar Cells 93, no. 6-7 (2009): 713-719.

[20] Le Bris, A., L. Lombez, S. Laribi, G. Boissier, P. Christol, and J-F. Guillemoles. "Thermalisation rate study of GaSb-based heterostructures by continuous wave photoluminescence and their potential as hot carrier solar cell absorbers." Energy & Environmental Science 5, no. 3 (2012): 6225-6232.

[21] Esmaielpour, Hamidreza, Vincent R. Whiteside, Herath P. Piyathilaka, Sangeetha Vijeyaragunathan, Bin Wang, Echo Adcock-Smith, Kenneth P. Roberts *et al.* "Enhanced hot electron lifetimes in quantum wells with inhibited phonon coupling." Scientific reports 8, no. 1 (2018): 12473.

[22] Esmaielpour, Hamidreza, Vincent R. Whiteside, Jinfeng Tang, Sangeetha Vijeyaragunathan, Tetsuya D. Mishima, Shayne Cairns, Michael B. Santos, Bin Wang, and Ian R. Sellers. "Suppression of phonon-mediated hot carrier relaxation in type-II InAs/$AlAs_xSb_{1-x}$ quantum wells: a practical route to hot carrier solar cells." Progress in Photovoltaics: Research and Applications 24, no. 5 (2016): 591-599.

[23] Conibeer, Gavin, Santosh Shrestha, Shujuan Huang, Robert Patterson, Hongze Xia, Yu Feng, Pengfei Zhang *et al.* "Hot carrier solar cell absorber prerequisites and

candidate material systems." Solar Energy Materials and Solar Cells 135 (2015): 124-129.

[24] Conibeer, G. J., C-W. Jiang, D. König, S. Shrestha, T. Walsh, and M. A. Green. "Selective energy contacts for hot carrier solar cells." Thin Solid Films 516, no. 20 (2008): 6968-6973.

[25] Hirst, Louise C., Hiromasa Fujii, Yunpeng Wang, Masakazu Sugiyama, and Nicholas J. Ekins-Daukes. "Hot carriers in quantum wells for photovoltaic efficiency enhancement." IEEE Journal of Photovoltaics 4, no. 1 (2014): 244-252.

[26] Würfel, P., A. S. Brown, T. E. Humphrey, and M. A. Green. "Particle conservation in the hot-carrier solar cell." Progress in Photovoltaics: Research and Applications 13, no. 4 (2005): 277-285.

[27] Wurfel, Peter. "The chemical potential of radiation." Journal of Physics C: Solid State Physics 15, no. 18 (1982): 3967.

[28] Gibelli, François, Laurent Lombez, and Jean-François Guillemoles. "Accurate radiation temperature and chemical potential from quantitative photoluminescence analysis of hot carrier populations." Journal of Physics: Condensed Matter 29, no. 6 (2016): 06LT02.

[29] Shah, Jagdeep. "Hot carriers in quasi-2-D polar semiconductors." IEEE Journal of Quantum electronics 22, no. 9 (1986): 1728-1743.

[30] Hirst, L. C., R. J. Walters, M. F. Führer, and N. J. Ekins-Daukes. "Experimental demonstration of hot-carrier photo-current in an InGaAs quantum well solar cell." Applied Physics Letters 104, no. 23 (2014): 231115.

[31] Aliberti, P., Y. Feng, Y. Takeda, S. K. Shrestha, M. A. Green, and G. Conibeer. "Investigation of theoretical efficiency limit of hot carriers solar cells with a bulk indium nitride absorber." Journal of Applied Physics 108, no. 9 (2010): 094507.

[32] Yao, Yao, Dirk König, and Martin Green. "Investigation of boron antimonide as hot carrier absorber material." Solar Energy Materials and Solar Cells 111 (2013): 123-126.

[33] Yao, Yao, and Dirk König. "Comparison of bulk material candidates for hot carrier absorber." Solar Energy Materials and Solar Cells 140 (2015): 422-427.

[34] Klemens, P. G. "Anharmonic decay of optical phonons." Physical Review 148, no. 2 (1966): 845.

[35] Rosenwaks, Y., M. C. Hanna, D. H. Levi, D. M. Szmyd, R. K. Ahrenkiel, and A. J. Nozik. "Hot-carrier cooling in GaAs: Quantum wells versus bulk." Physical Review B 48, no. 19 (1993): 14675.

[36] Pelouch, W. S., R. J. Ellingson, P. E. Powers, C. L. Tang, D. M. Szmyd, and A. J. Nozik. "Comparison of hot-carrier relaxation in quantum wells and bulk GaAs at high carrier densities." Physical Review B 45, no. 3 (1992): 1450.

[37] Conibeer, Gavin, Martin Green, Richard Corkish, Young Cho, Eun-Chel Cho, Chu-Wei Jiang, Thipwan Fangsuwannarak *et al.* "Silicon nanostructures for third generation photovoltaic solar cells." Thin solid films 511 (2006): 654-662.

[38] Rota, L., F. Rossi, S. M. Goodnick, P. Lugli, Elisa Molinari, and W. Porod. "Reduced carrier cooling and thermalization in semiconductor quantum wires." Physical Review B 47, no. 3 (1993): 1632.

[39] Nozik, Arthur J. "Spectroscopy and hot electron relaxation dynamics in semiconductor quantum wells and quantum dots." Annual review of physical chemistry 52, no. 1 (2001): 193-231.

[40] Conibeer, G. J., D. König, M. A. Green, and J. F. Guillemoles. "Slowing of carrier cooling in hot carrier solar cells." Thin solid films 516, no. 20 (2008): 6948-6953.

[41] König, D., Y. Takeda, and B. Puthen-Veettil. "Technology-compatible hot carrier solar cell with energy selective hot carrier absorber and carrier-selective contacts." Applied Physics Letters 101, no. 15 (2012): 153901.

[42] Dimmock, James AR, Stephen Day, Matthias Kauer, Katherine Smith, and Jon Heffernan. "Demonstration of a hot-carrier photovoltaic cell." Progress in Photovoltaics: Research and Applications 22, no. 2 (2014): 151-160.

[43] Nguyen, Dac-Trung, Laurent Lombez, François Gibelli, Soline Boyer-Richard, Alain Le Corre, Olivier Durand, and Jean-François Guillemoles. "Quantitative experimental assessment of hot carrier-enhanced solar cells at room temperature." Nature Energy 3, no. 3 (2018): 236.

[44] Delamarre, Amaury, Laurent Lombez, and Jean-François Guillemoles. "Characterization of solar cells using electroluminescence and photoluminescence hyperspectral images." Journal of Photonics for Energy 2, no. 1 (2012): 027004.

[45] Rodière, Jean, Laurent Lombez, Alain Le Corre, Olivier Durand, and Jean-François Guillemoles. "Experimental evidence of hot carriers solar cell operation in multi-quantum wells heterostructures." Applied Physics Letters 106, no. 18 (2015): 183901.

Chapter **2**

Experimental setups and characterization methods

2.1. Standard solar spectra

An important measurement to evaluate the performance of a solar cell is current density-voltage (*J*-*V*) characterization. In this experiment, the solar cell is illuminated with a simulated solar spectrum to assess the power conversion efficiency of the device. Via this experiment several important parameters can be deduced such as: the open circuit voltage (V_{OC}), the short circuit current (J_{SC}), and the aforementioned power conversion efficiency (η).

In order to be able to compare the measured results with solar cells from different laboratories, a standard reference for illumination is required. Moreover, it is important to evaluate solar cells under practical conditions within the laboratory. [1, 2] The temperature of the Sun is ~ 5700 K, therefore, its radiation can be simulated as a blackbody emitting at ~ 5800 K. The solid black line in Figure 2.1 shows the spectrum emitted by a blackbody at 5777 *K*, which is well matched to the solar spectrum above yellow – AM0) and below (orange – AM 1.5) the earth's atmosphere.

The solar irradiation that reaches the earth above the atmosphere is referred to AM0 (air mass zero) spectrum, which is shown in yellow in Figure 2.1. The AM0 spectrum is appropriate for photovoltaics systems in space, where atmospheric absorption is negligible. [3] However, when the solar irradiation passes through the atmosphere some of the photons are absorbed by the constituent different gases in the atmosphere –

therefore, the spectrum that reaches the earth surface is attenuated by molecular absorption. The AM1.5 spectrum (shown in orange in Figure 2.1) is a global standard that represents the solar flux incident on the earth at an angle of 42^{o} elevation under clear sky conditions. [4] The total integrated irradiance of the AM1.5 spectrum is ~ 1000 W m^{-2}.

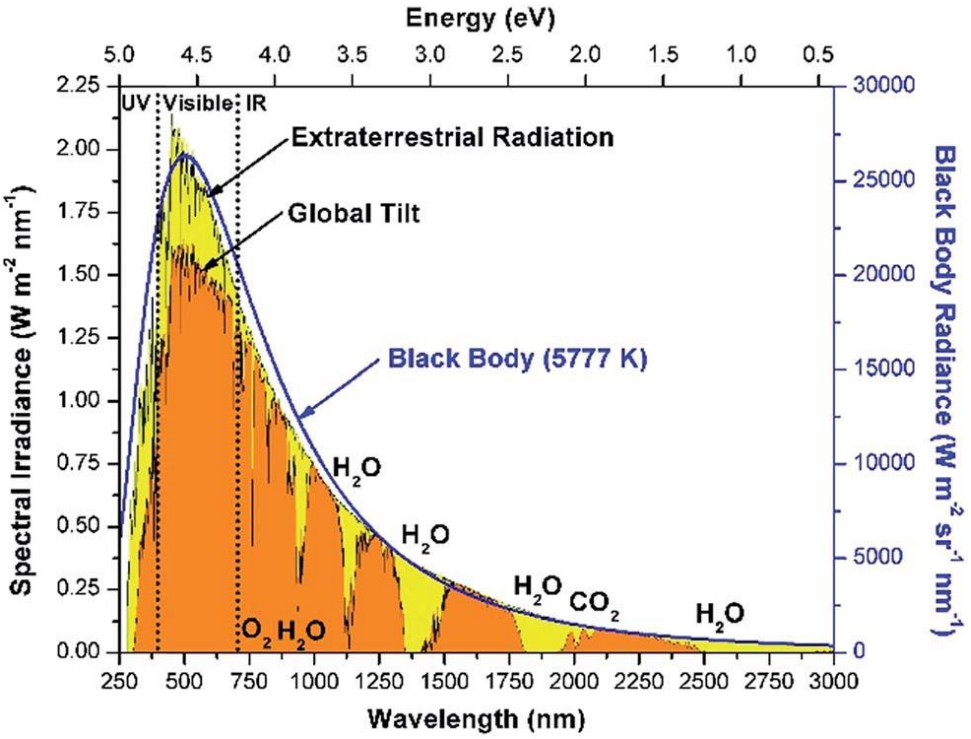

Figure 2. 1. Solar spectrum above (AM0; yellow region) and below (AM1.5; tangerine region) atmosphere. Solid black line shows the radiation of a blackbody at 5777 *K* (temperature of the Sun). Atmospheric gases responsible for sunlight absorption in AM1.5 solar spectrum are shown. [Reproduced from: *Herron, J., et al. "A general framework for the assessment of solar fuel technologies." Energy & Environmental Science 8, no. 1 (2015): 126-157.*] [3]

2.2. Current Density-Voltage Analysis

2.2.1. Theory and equations

Solar cells produce electricity when they are illuminated. As such, it is possible to determine the power conversion efficiency (η_{pc}) of the solar cell by dividing their maximum extracted power (P_{max}) (electricity) by the incident power (P_{max}) upon the device by:

$$\eta_{pc} = \frac{P_{max}}{P_{in}}. \tag{2.1}$$

Figure 2.2 shows current density-voltage (*J*-*V*) characteristic of a solar cell under illumination. The blue and red lines show how the extracted current density and operating power change versus bias voltage, respectively. In Figure 2.2, at zero bias (V = 0 V), the extracted current density is non-zero, this current density value is called the short circuit current density (J_{SC}), which reflects the amount of current generated in the device. By increasing the bias voltage, the amount of extracted current density does not change significantly until a certain value (here it is about V = 0.45 V); above that voltage (V > 0.45 V), the extracted current density drops abruptly. In addition, it is evident that at a particular bias voltage, known as the open circuit voltage (V_{OC}), the extracted current density is zero. The operating power of a solar cell is determined by multiplying the optimum photocurrent density by the optimum photo-voltage. At the zero bias open circuit voltage condition, the operating power is zero. Within the photovoltaic regime (displayed in black in Figure 2.2), there is a point at which the operating power is maximized (P_m) when considering the value of the maximum extracted current density

(J_m) and maximum bias voltage (V_m); this is the power considered in the calculation of power conversion efficiency, as described by Equation 2.1.

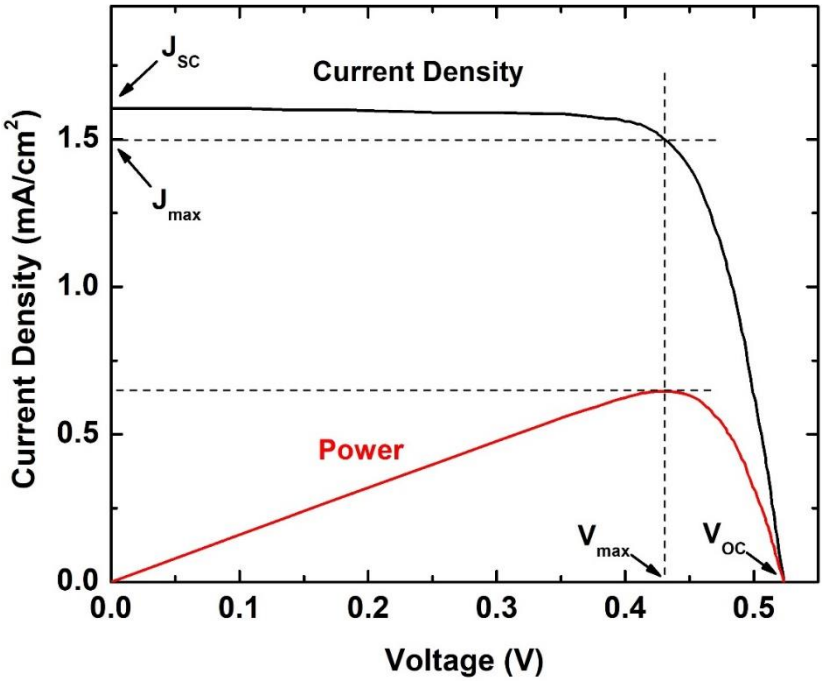

Figure 2. 2. Current density-voltage characteristic of a solar cell under illumination.

Another useful parameter for solar cell characterization is the so-called fill factor (*FF*), which represents how "square" of an ideal solar cell is the *J-V* response. The fill factor is determined by the ratio of the maximum operating power (P_m) divided by the product of the V_{OC} and J_{SC}. The equation for the solar cell *FF* is given by:

$$FF = \frac{V_{max}\, J_{max}}{V_{oc}\, J_{sc}}. \tag{2.2}$$

As a result, the power conversion efficiency of a solar cell can be written as:

$$\eta_{pc} = \frac{P_{max}}{P_{in}} = \frac{J_{max} V_{max}}{P_{in}} = \frac{V_{oc}\, J_{sc}\, FF}{P_{in}}. \tag{2.3}$$

In dark conditions (under no illumination) a solar cell works as a conventional p-n diode. Therefore, it is possible to determine the *J-V* characteristics of a solar cell via the ideal diode equation ($J_{dark}(V)$):

$$J_{dark}(V) = J_0\left(e^{qV/m\,k_BT} - 1\right), \tag{2.4}$$

where J_0, q, k_B, m, and T are the dark saturation current density, coulomb charge, Boltzmann constant, diode ideality factor, and lattice temperature, respectively. By illuminating the solar cell, its current density-voltage equation is the superposition of a constant photogenerated current density (which is usually J_{SC}) and the ideal diode equation, as given by:

$$J(V) = J_{dark} - J_{sc} = J_0\left(e^{qV/m\,k_BT} - 1\right) - J_{sc}. \tag{2.5}$$

2.2.2. Experimental setup

To characterize solar cell properties under the AM1.5 (or AM0) solar spectrum in the laboratory at OU, a Newport Oriel Sol2A solar simulator is utilized. The applied bias on test solar cells are supplied using a Keithley 2400 multimeter, which concurrently measures the extracted current from the device. Via this system, current density-voltage characteristics of solar cells are determined in the temperature range 77 K to 350 K using a Linkam THMS600E cryostat connected to a Linkam LNP95 cooling system.

2.3. External Quantum Efficiency (EQE) Analysis

2.3.1. Theory and equations

External quantum efficiency (EQE) is a standard characterization technique for solar cells, which considers the absorption of the solar cell as a function of excitation wavelength. Specifically, the EQE of a device represents how many electrons (or holes) are generated *and* extracted (as electrical current) per photon absorbed by the system. In addition, EQE characterization provides information about the absorption profile of the device. The EQE of a solar cell is: [4]

$$EQE\ (\lambda) = \frac{Number\ of\ extracted\ electrons}{Number\ of\ incident\ photons} = \frac{current/q}{P_{in}/hv}\ (\lambda). \tag{2.6}$$

The EQE of a device depends on two main parameters: 1) optical absorption; and 2) charge collection/transport efficiency. Hence, if one charge is collected per photon with a wavelength (λ): the EQE of the device will be 100% at that wavelength. As suggested, carrier extraction is also important for the EQE of solar cells. In a device, if photogenerated carriers cannot be extracted or recombine before extraction – the EQE of the sample will drop.

As discussed above, EQE determines the wavelength dependent behavior of charge extraction per incident photon for a solar cell. Therefore, the total charge extraction under illumination (J_{SC}) of a solar cell can be determined by integrating the device EQE multiplied by the incident photon flux (the solar spectrum). The relationship between J_{SC} and EQE is therefore:

$$J_{sc} = q\ \int \Phi(\lambda)\ EQE(\lambda)\ d\lambda, \tag{2.7}$$

where q is coulomb charge and Φ (λ) is the wavelength dependent photon flux. [4]

2.3.2. Experimental Setup

The EQE of a solar cell is measured in the laboratory at OU using an Oriel Cornerstone 260 monochromator and an Oriel Merlin digital lock-in amplifier radiometry system, as shown in Figure 2.3.

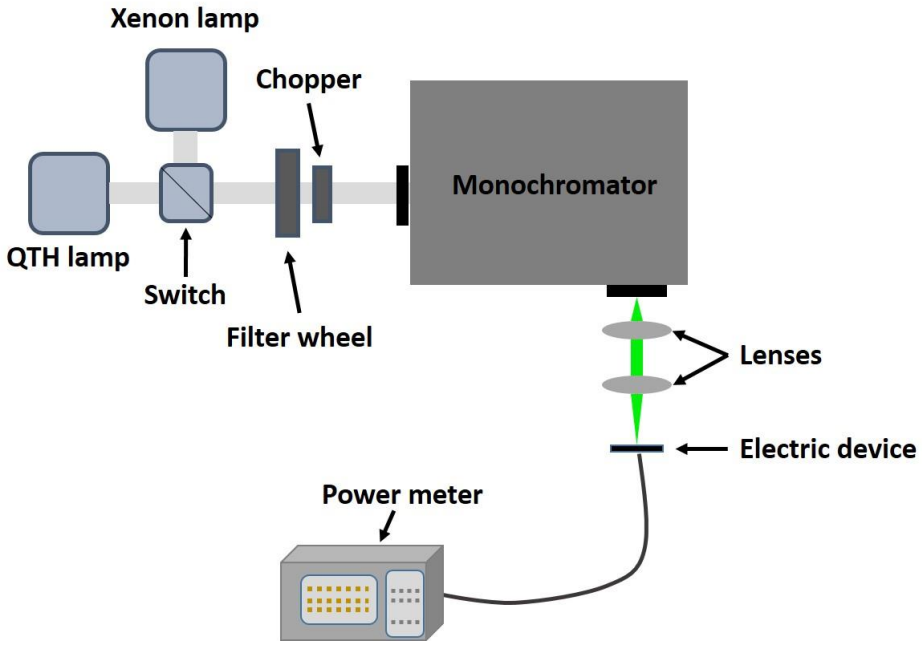

Figure 2. 3. Schematic of an EQE setup to study the wavelength dependence of solar cells.

The light sources used to characterize the EQE of solar cells are either a quartz tungsten halogen (QTH) bulb or a Xenon lamp, which radiate over the solar spectrum between the infrared (IR) and the ultra-violet (UV). A Si detector or a Ge detector is used to measure the incident light intensity between 300 nm to 1100 nm or 700 nm to 1800 nm, respectively. In addition, the temperature dependence of the EQE can also be studied

from 77 K to 350 K using the same Linkam cryostat setup described previously (Section 2.3.1) for the *J-V* measurements.

2.4. Photoluminescence (PL) Spectroscopy

2.4.1. Theory

Photoluminescence (PL) is a powerful technique, which can provide useful information about the optical properties of materials such as: optical transition levels, radiative recombination mechanisms, and general material qualities. [5] When a semiconductor absorbs a photon it excites an electron from the valence band to the conduction band. Quickly after photogeneration, these charges relax to the energy level minima and after a few nanoseconds the electron-hole pairs recombine radiatively or non-radiatively. As such, PL provides information regarding the properties of the band gap and/or localized states in the semiconductor. Figure 2.4 shows the schematic of a radiative recombination (photoluminescence) mechanism in a semiconductor. First, a photon with energy above the band gap is absorbed and excites an electron from the valence band to the conduction band. Then, photogenerated carriers in both the conduction and valence bands occupy the minimum energy levels after relaxation. Finally, the photogenerated carriers recombine and re-emit a photon. Therefore, by detecting and dispersing the emitted photons, it is possible to study the PL spectrum of the sample.

As such, continuous wave (CW) power and temperature dependent PL spectroscopy provide comprehensive information about the behavior of photogenerated carriers in semiconductor materials and structures, which provides significant physical information

for the development and assessment of solar cells (and other devices). The various methods to analyze PL spectrum data are discussed in detail in the following chapters.

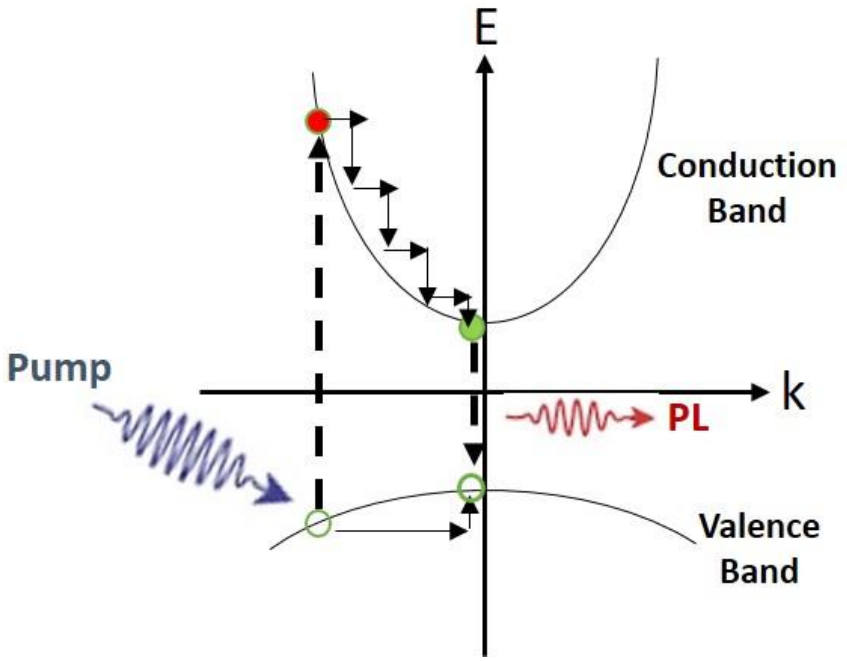

Figure 2. 4. Schematic of laser excitation of a semiconductor. A photon (blue arrow) excites an electron from valence band into conduction band, then photogenerated carriers relaxes to the minima of conduction and valence bands. Finally, they recombine radiatively (PL emission) and emit a photon (PL emission; red arrow).

2.4.2. Photoluminescence: Experimental Setup

Photoluminescence spectroscopy is performed using laser sources with various excitation wavelengths: a He-Cd (325 or 442 nm) laser, a He-Ne (632.8 nm) laser, and a 1064 nm diode pumped solid state (DPSS) laser to investigate materials with different band gap energies. As shown in Figure 2.5, the emitted PL spectra is dispersed using a Princeton Instrument Acton SP2500 spectrometer and detected with either an air cooled-

Si charge coupled device (2 dimensional CCD array) – for shorter wavelengths (300 nm to 1100 nm) – or a liquid N_2 cooled InGaAs linear array for longer wavelengths (750 nm to 1600 nm).

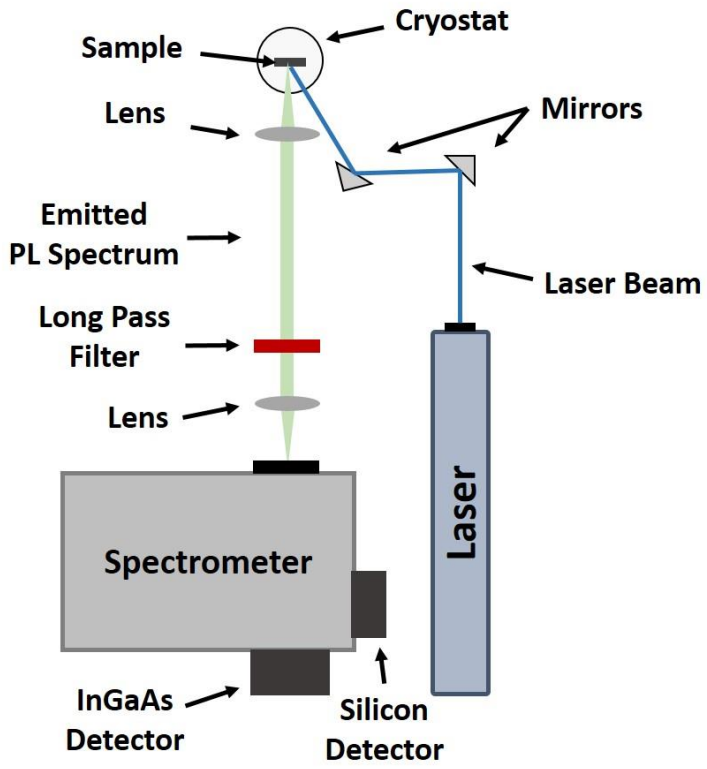

Figure 2. 5. Schematic of a photoluminescence spectroscopy setup.

Power dependent measurements were performed using an array of neutral density filters placed in the optical path of the laser beam. As a result, it is possible to change excitation power by up to three orders of magnitude. Temperature dependent PL spectroscopy was performed in a Janis closed-cycle Helium system with active temperature control provided by a Lake Shore® Cryogenics temperature controller (Model 335) from 4.2 K to 300 K.

References

[1] ASTM E490-00a(2014) Standard Solar Constant and Zero Air Mass Solar Spectral Irradiance Tables, ASTM International, West Conshohocken, PA, 2014, https://doi.org/10.1520/E0490-00AR14

[2] ASTM G173-03(2012) Standard Tables for Reference Solar Spectral Irradiances: Direct Normal and Hemispherical on 37° Tilted Surface, ASTM International, West Conshohocken, PA, 2012, https://doi.org/10.1520/G0173-03R12

[3] Herron, Jeffrey A., Jiyong Kim, Aniruddha A. Upadhye, George W. Huber, and Christos T. Maravelias. "A general framework for the assessment of solar fuel technologies." Energy & Environmental Science 8, no. 1 (2015): 126-157.

[4] Nelson, Jenny. The physics of solar cells. World Scientific Publishing Company, 2003.

[5] Gfroerer, Timothy H. "Photoluminescence in analysis of surfaces and interfaces." Encyclopedia of analytical chemistry: applications, theory and instrumentation (2006).

Chapter **3**

Analysis of hot carrier temperature

3.1. Introduction

Hot carrier solar cells have been proposed to increase the power conversion efficiency of solar cells beyond the fundamental limit (33%). One of the main challenges regarding practical hot carrier solar cells is to design a hot carrier absorber that inhibits electron-phonon interactions, or thermalization loss, and to generate stabilized hot carrier distributions in the absorber. [1] Several designs have been proposed to reduce phonon mediated thermalization loss in solar cells. [2] One technique is to utilize nanostructures in order to reduce carrier-cooling rates. [2, 3, 4] Slowed carrier cooling was first observed in a GaAs/AlGaAs QW [5] followed by several other QW systems, [6] QDs, [7] and nano-wires. [8] One proposed hypothesis for suppressing the phonon-mediated thermalization process in nanostructures is attributed to an increase in the local density of photogenerated hot carriers in the system, which can cause screening of optical (LO) phonons – thus, inhibiting LO-phonon decay to low energy acoustic (LA) phonons (heat), i.e., a phonon bottleneck effect. [2, 9] As a result of inhibiting thermalization loss, it is possible to establish photogenerated hot carrier distributions at elevated temperatures with respect to the lattice.

An accurate determination of the carrier temperature is extremely important in studying the hot carrier dynamics in a system. [1, 10, 11, 12, 13] One simple, practical technique is to use continuous wave photoluminescence (PL) spectroscopy. It is

possible to model a PL spectrum via Planck's radiation law through modeling developed by Lasher and Stern (1964), [14] De Vos and Pauwels (1981), [15] and Wurfel (1982). [16] The relevant equation is:

$$I_{PL}(E) = \frac{A(E)\,(E)^2}{4\pi^2 h^3 c^2}\left[exp\left(\frac{E-\Delta\mu}{k_B T}\right) - 1\right]^{-1}, \tag{3.1}$$

where I_{PL} is PL intensity, h Planck's constant, c the speed of light, k_B Boltzmann's constant, $\Delta\mu$ the difference in chemical potentials for electrons μ^e and holes μ^h (i.e., quasi-Fermi level splitting), T the carrier temperature and $A(E)$ the absorptivity of the sample. The absorptivity is described by the following relationship:

$$A(E) = 1 - \exp(-(A_{lh}\, exp\left(-\frac{(E-E_{lh})^2}{\Gamma_{lh}^2}\right) + \\ + A_{hh}\, exp\left(-\frac{(E-E_{hh})^2}{\Gamma_{hh}^2}\right) + A_{Cont.}\, \frac{1}{1+exp\left(-\frac{(E-E_{Cont.})}{\Gamma_{Cont.}}\right)} \frac{2}{1+exp\left(-2\pi\sqrt{\frac{E_{Cont.}-E_{lh}}{|E-E_{Cont.}|}}\right)})\, d\,(f_V^e - f_C^e)\,), \tag{3.2}$$

where d is the thickness, f_V^e and f_C^e are Fermi-Dirac distribution for transitions in valence band and conduction band states, respectively. A_{lh}, A_{hh} and $A_{Cont.}$ are amplitude of light holes, heavy holes, and continuum states transitions, respectively. E_{lh}, E_{hh} and $E_{Cont.}$ are the energy of light holes, heavy holes, and continuum states, respectively. Finally, Γ_{lh}, Γ_{hh} and $\Gamma_{Cont.}$ are broadening of light holes, heavy holes, and continuum states transitions, respectively. [17, 18, 19, 20]

To apply this model there are several different methods. One technique is to apply a linear fit to the high-energy side of the natural logarithm of the intensity of the PL spectrum: [10, 11, 12, 21]

$$\ln\left(I_{PL}(E)\right) = \ln\left(\varepsilon(E)\right) - \frac{E}{k_B T}, \tag{3.3}$$

where $\varepsilon(E)$ is effective emissivity of the sample. E is energy, and $k_B T$ is the thermal energy. As indicated in Equation 3.3, by taking the natural logarithm of the PL intensity, the equation becomes inversely proportional to carrier temperature, *T*. This is a simple method to determine carrier temperature, however in extracting carrier temperature, it does not include subtle contributions from state filling and/or phonon mediated line-width broadening. A comprehensive study involving the limitations of this technique is discussed in Chapter 4, Section 4.3.2. [22, 23]

An alternative technique to extract the carrier temperature is to fit the whole PL spectrum by applying Equation 3.1. [17, 18] To extract a carrier temperature via this method, it is necessary to determine the absorptivity of the sample. Doing a best fit by applying Equations 3.1 and 3.2 enables one to extract both the carrier temperature and the chemical potential difference for electrons and holes from the CW PL spectra.

The determination of the carrier temperature via fitting whole PL spectrum using Equation 3.1 is a powerful technique to determine optical properties of a sample. In addition, it excludes the effects of phonon mediated PL line-width broadening from the extracted carrier temperatures, which improves the accuracy of the extracted results. Another advantage of this technique is to determine the chemical potential difference (quasi-Fermi level splitting), which is proportional with open circuit voltage (V_{OC}), using a *contact-less* method. [18] However, there are several variables in Equation 3.2, which need to be determined. In addition, this technique does not include the

contribution of state filling effects, which have an important contribution to linewidth broadening in nanostructures.

Recently, the generalized Planck's radiation law was further developed by the hot carrier community to aid extracting individual (electron and/or hole) carrier temperatures and chemical potentials for both charge carriers in the semiconductor. The modified equation is given by: [17, 18]

$$I_{PL}(E) = \frac{A(E)\,(E)^2}{4\pi^2 h^3 c^2}\left[exp\left(\begin{array}{c}\frac{1}{k_B}\left(\frac{1}{T_H^e}-\frac{1}{T_H^h}\right)\times\left[\left(\frac{m^e}{m^e+m^h}\right)\left(\frac{E_G}{2}+E_c^i\right)-\left(\frac{m^h}{m^e+m^h}\right)\left(\frac{E_G}{2}+\left|E_v^j\right|\right)\right] \\ +\frac{E}{k_B(m^e+m^h)}\left(\frac{m^h}{T_H^e}+\frac{m^e}{T_H^h}\right)-\frac{\mu_H^e}{k_B T_H^e}-\frac{\mu_H^h}{k_B T_H^h}\end{array}\right)-1\right]^{-1}, \quad (3.4)$$

where E_G is the band edge of semiconductor, E_c^i and E_v^i confinement energies for electrons in the conduction band and holes in the valence band, respectively. m^e and m^h are effective mass of electrons in the conduction band and holes in the valence band, respectively. T_H^e and μ_H^e are the conduction band electron's temperature and chemical potential. T_H^h and μ_H^h are the valence band hole temperature and chemical potential, respectively.

As has been discussed, one of the main advantages of Equation 3.4 is its ability to extract information for both electrons and holes through a fit of the PL spectrum. This is significant because at a non-equilibrium condition, the temperature of electrons and holes may be different due to the difference in effective mass of these carriers, typical for most systems. It is expected that the thermalization process for holes is faster than electrons due to holes larger effective mass. [24] The determination of carrier

temperatures via this technique however, can be tedious – due to the various variables, which are needed in order to do the best fit.

In this chapter, the results of extracting the carrier temperature through applying the various methods described will be presented.

3.2. Description of InAs/$AlAs_xSb_{1-x}$ multi-quantum well structure

The sample studied is an InAs/$AlAs_{0.16}Sb_{0.84}$ multi-quantum well (MQW) grown by molecular beam epitaxy (MBE) on a GaAs (001) substrate. To improve the quality of sample growth and to remove native oxide layer on the surface, the substrate was heated to 580 ºC. This was followed by growth of a thin GaAs layer to planarize the growth front. Due to the large lattice mismatch (7%) between InAs and GaAs material, a 2000 nm InAs buffer layer was grown prior to the growth of the active structure to improve the quality of the succeeding InAs/AlAsSb layers. The active region consists of 30 repetitions of 2.4 nm InAs QWs and 10 nm $AlAs_{0.16}Sb_{0.84}$ barriers grown at 450 ºC and 510 ºC, respectively. Finally, a 50 nm InAs cap layer was grown to isolate the MQW structure from the effects of oxidation.

The quantum well structure presented has several interesting characteristics as a potential hot carrier absorber. First, there is a large conduction band offset between InAs and AlAsSb, promoting significant absorption of the solar irradiation within the InAs QWs. As shown in Figure 3.1 (b), there is a large confinement potential for electrons in the QW with a low confinement for holes in the valence band – it is expected that holes will escape more readily from the valence band at elevated lattice temperatures while electrons will be strongly confined in the conduction band. This will reduce the

recombination losses typically problematic in QWSCs, despite strong direct absorption in the InAs QW. Moreover, this system offers the potential to use superlattice designs to aid hot carrier extraction by resonant tunneling structures in future hot carrier solar cell designs. [21, 25]

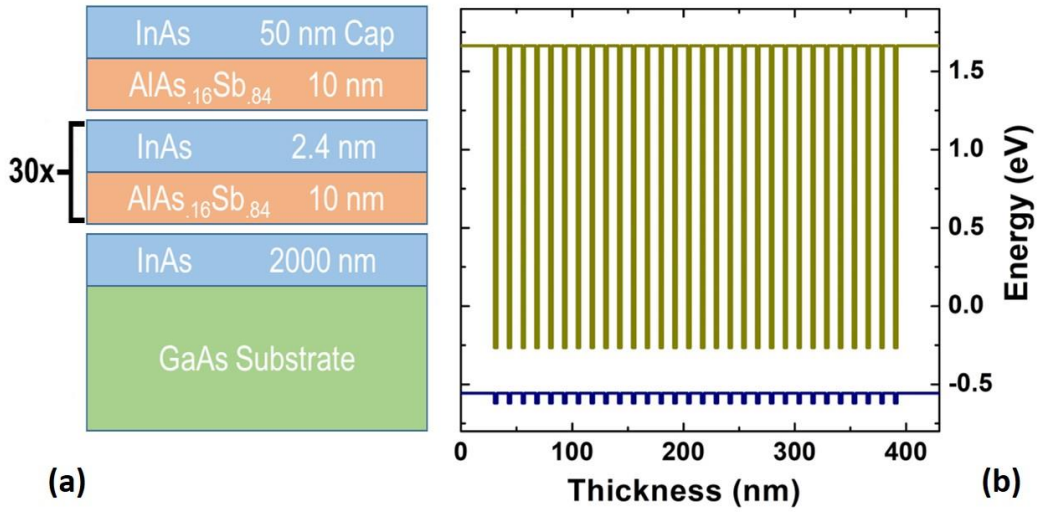

Figure 3. 1. Schematic (a) and band structure (b) of InAs/AlAsSb multi-quantum well (MQW) structure. [Reproduced from: *Esmaielpour, H., et al. "Suppression of phonon-mediated hot carrier relaxation in type-II InAs/AlAsSb quantum wells". Progress in Photovoltaics: Research and Applications, 24(5), (2016): 591-599.*] [27]

The InAs QW structure shown in Figure 3.2 (a) has a type-II band alignment, which results in the rapid spatial separation of the photogenerated electrons and holes. [26] In a type-II system the radiative recombination lifetime is slow (compared with a type-I band alignment); therefore, while the sample is being pumped by a laser: the lifetime (therefore carrier concentration) of photogenerated carriers in the conduction band is larger than expected for a type-I quantum well with a direct transition. [27]

Figure 3.2 (b) shows the 2D electronic density of states (DOS) for each energy level in the InAs QW – overlaid with an emitted PL spectrum from the sample – at 300 K (shown by gray). In Figure 3.2 (b) the energy separation between the ground and first excited-states is relatively large (~ 655 meV) and the 2D electron density of state is on the order of $10^{13}\ eV^{-1}\ cm^{-2}$, which is four orders of magnitude larger than the excitation level induced optical pumping (for the laser excitation conditions used). Therefore, it is expected that significant occupation of excited states is negligible in any measurement performed. Furthermore, the PL spectrum in Figure 3.2 (b) does not display evidence of a significant shoulder due to state filling or occupation of higher order states on the high-energy tail of the PL.

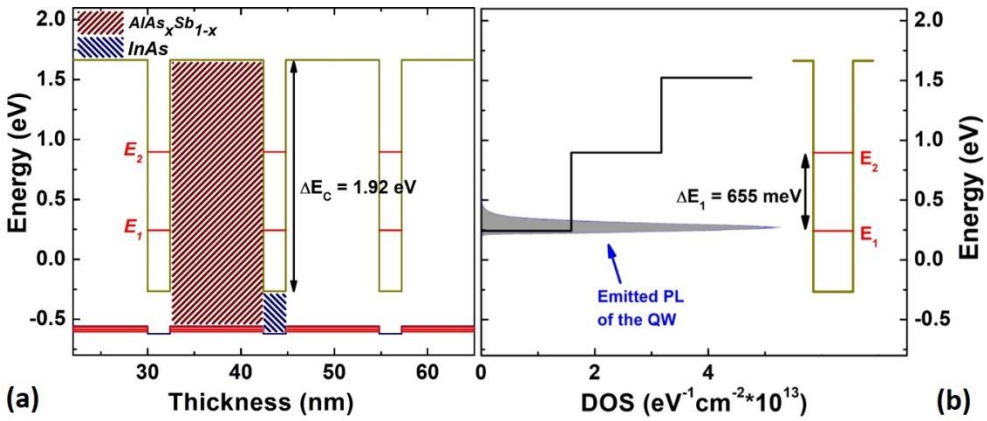

Figure 3. 2. (a) InAs QW structure with type-II band alignment for three quantum wells. (b) 2D electron density of states (DOS) for the InAs MQW structure as a function of energy and emitted PL spectrum from the sample at 300 K. [Reproduced from: *Esmaielpour, H., et al. "Suppression of phonon-mediated hot carrier relaxation in type-II InAs/AlAsSb quantum wells". Progress in Photovoltaics: Research and Applications, 24(5), (2016): 591-599.*] [27]

These characteristics imply the shape of the emitted PL and conditions of the measurements are not significantly affected by ambiguities associated with state filling and/or absorption in the barriers or higher-order states in the system under investigation. This further demonstrates the potential of InAs/AlAsSb QWs for practical hot carrier solar cells.

3.3. Photoluminescence spectroscopy of the InAs MQW structure

Continuous wave power and temperature dependent photoluminescence (PL) spectroscopy of the InAs QWs are studied using different lasers to pump below and above the band gap of the AlAsSb barrier material. As such, the sample under investigation was illuminated with a 442 nm He-Cd laser, a 633 nm He-Ne laser, or a 1064 nm diode-pumped solid state (DPSS) laser.

Figure 3.3 shows a temperature dependent PL of the sample from 4 K to 300 K using the 442 nm He-Cd laser. As the lattice temperature increases there is an initial shift in the peak energy towards higher values (blue-shift); then, the peak energy redshifts to lower energies. This is an example of a so-called "*s-shape*" behavior in the peak energy versus lattice temperature that typically arises due to the existence of localized states in the system. [21, 28]

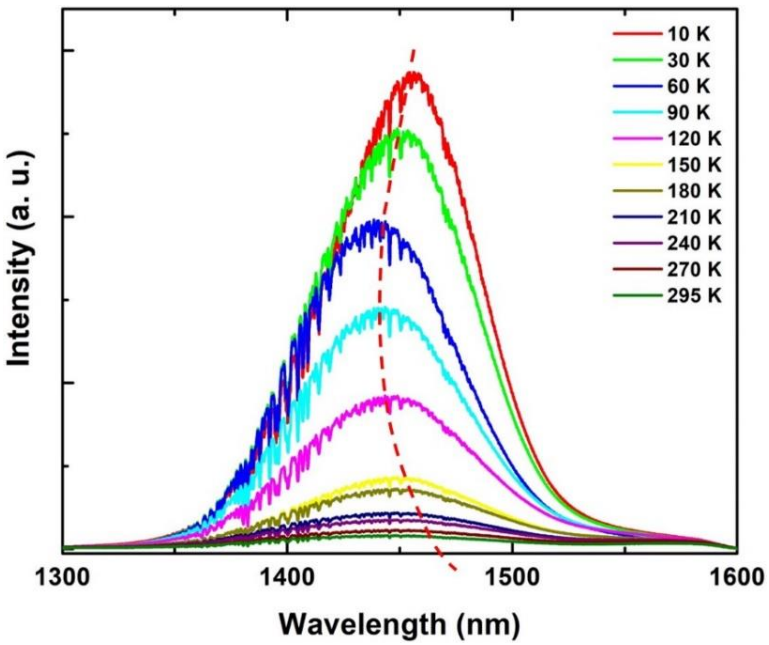

Figure 3. 3. Temperature dependent photoluminescence spectroscopy of InAs QW structure using the 442 nm laser. Dashed line shows the trend of peak position change against temperature, which is due to the existence of localized states at the interface between the QW and the barrier material. This figure is an example of "s-shape" behavior of peak energy due to existence of localized states at MQW interfaces.

Figure 3.4 shows the peak energy versus lattice temperature for the InAs QW pumped with He-Ne laser (632 nm) extracted from the PL spectra. It is observed that the peak energy first decreases (T < 75 K) and is then followed by an increase up to $T \sim 125$ K. Then, at $T > 125$ K the peak energy decreases (redshifts) following the typical thermal expansion behavior of the lattice. The behavior at T < 125 K ("*s-shape*" dependence) is attributed to trapping and de-trapping of photogenerated charges at localized states in the quantum well interface created by non-idealities or alloy fluctuations during sample growth. As a result, photogenerated charges (here especially holes due to large effective

mass and small band offset in the valence band, $\Delta E_V \rightarrow 0$) become trapped at localized centers, particularly at low temperatures. By increasing the lattice temperature, the holes gain enough thermal energy to delocalized and transfer to the lower potential within the barrier material (holes are at lower energy in the AlAsSb). At elevated lattice temperatures (T > 175 K) the peak PL energy follows a typical Varshni-like behavior given by: [29]

$$E(T) = E_0 - \frac{\alpha T^2}{\beta + T}, \tag{3.5}$$

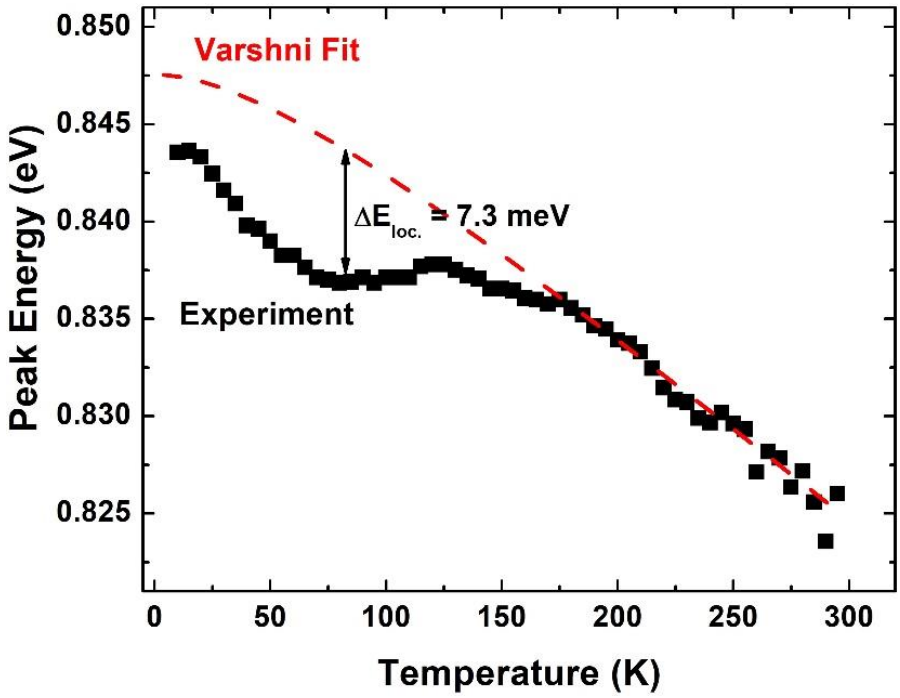

Figure 3. 4. Peak energy change for InAs MQW as a function of lattice temperature. Red dashed line shows the result of Varshni fitting on the experimental data. [Reproduced from: *Tang, J., Esmaielpour, H., et al. "Effects of localization on hot carriers in InAs/AlAsSb quantum wells" Applied Physics Letters, 106(6), (2015):061902.*] [21]

where α and β are material constants, E_0 is the band gap at $T = 0\ K$ and T is the lattice temperature. The red dashed line in Figure 3.4 shows the result of Varshni fitting to the experimental data. The extracted α and β values are $0.1\ meV/K$ and $93\ K$, respectively. These extracted values are slightly less than reported values in the literature, which is attributed to perturbations in the PL due to the existence of localized states in the system. [30, 31] $\Delta E_{loc.}$ indicated in Figure 3.4 shows the amount of energy that trapped carriers require to enable escape from the localization centers in this material.

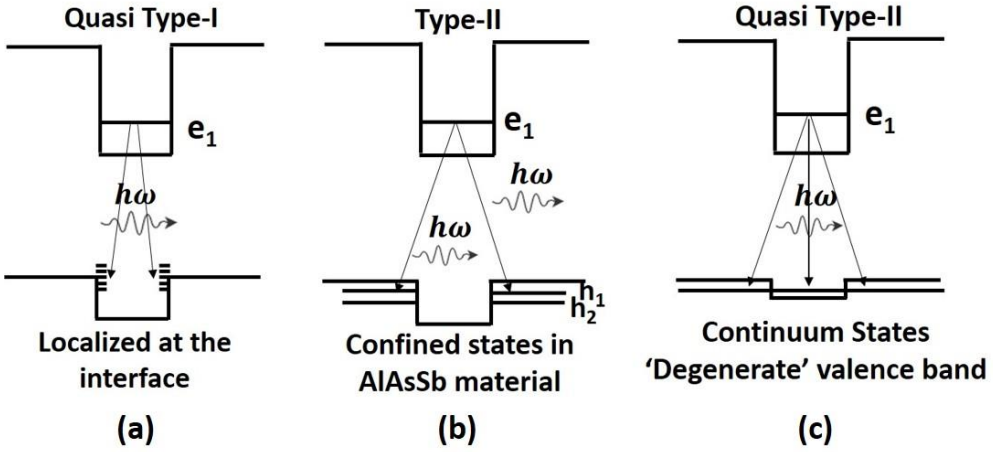

Figure 3. 5. Schematic of type-II InAs QW structure. Arrows show different transitions that happen in the structure at different lattice temperatures. (a) Quasi-type-I transition within the QW due to existence of localized states at interface. (b) Band to band transition (type-II transition) above 90 K. (c) Quasi-type-II transition at elevated temperatures when holes can escape from the shallow confinement in the valence band. [Reproduced from: *Esmaielpour, H., et al. "Enhanced hot electron lifetimes in quantum wells with inhibited phonon coupling." Scientific reports 8, no. 1 (2018): 12473.*] [32]

To provide a clearer picture when describing the recombination of photogenerated carriers in the system and the effective transitions at different temperatures a schematic of the InAs QW with type-II is shown in Figure(s) 3.5 under various conditions. At low temperatures (< 90 K – Figure 3.5 (a)), holes are trapped at the interface between the QW and the barrier in the valence band. As a result, they recombine with electrons in the conduction band following a *quasi-type-I* transition. In this condition, radiative recombination is efficient and the thermalization rate increases until 90 K (this is described more fully in Chapter 5, Section 5.2). [32]

As the lattice temperature is increased, the density of phonons also increases. Therefore, phonons will readily absorb the excess kinetic energy of the hot carriers facilitating thermalization of the carrier distribution. However, this expected behavior is not observed. This unusual behavior is attributed to the thermal redistribution of the photogenerated holes at T > 90 K that are delocalized from InAs/AlAsSb interface states and relax into the AlAsSb barrier. Consequently, the photogenerated electrons and holes carriers are spatially separated. Under these conditions, the radiative recombination efficiency is reduced, as expected in a type-II system (see Figure 3.5 (b)). The result of this spatial separation of the electron and hole wavefunctions is the increased lifetime – therefore, the density of electrons in the conduction band continues to grow as the sample is pumped under CW laser excitation. It is proposed that along with the increase in the electron density, there is a large hot LO phonons distribution, which inhibits the energy transfer to low energy acoustic phonons (heat) due to a large mismatch in the phonon density of states; i.e. a phonon bottleneck effect. [9, 11, 27] This hypothesis and its subtleties are further discussed in Chapter 5, Section 5.4.

Figure 3.5 (c) illustrates the situation at elevated lattice temperatures when the delocalized holes confined to the AlAsSb valence band gain further thermal energy such that they can escape from the shallow confinement (70 meV). [33] We describe this system as the *quasi-type-II* configuration whereby the fundamental band alignment is type-II but the holes are distributed throughout the valence band and the electron-hole interaction increases relative to the 'pure' type-II configuration at temperatures above 90 K and below 225 K. [32]

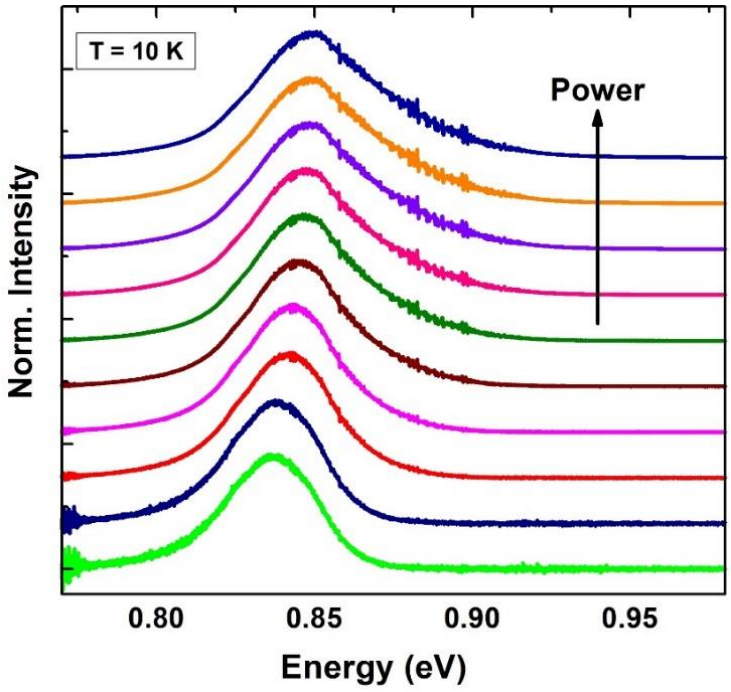

Figure 3. 6. Power dependent PL spectra at 10 K. At low excitation powers, peak position shows a blueshift behavior due to localized states and after state filling of these states (above intermediate excitation levels) it stabilizes. [Reproduced from: *Esmaielpour, H., et al. "Suppression of phonon-mediated hot carrier relaxation in type-II InAs/AlAsSb quantum wells". Progress in Photovoltaics: Research and Applications, 24(5), (2016):591-599.*] [27]

Figure 3.6 shows power dependent PL spectra for the InAs/AlAsSb MQW at 10 K. At low excitation powers there is a shift in the peak PL energy position. This is related to the influence of unintentional alloy fluctuations in the system that is prevalent at low temperature and excitation, which has been discussed in detail above. By increasing the excitation power to intermediate values, the localized states begin to fill and eventually saturate at higher powers, resulting in a blueshift in the peak PL energy as the localized states are occupied. Further increasing the excitation power causes the peak energy position to stabilize and a broadening on the high energy side of the spectra, which is indicative of the existence of hot carriers in the system.

The shift in peak energy that is also shown in Figure 3.7 indicates that the radiative recombination is not a conventional type-I transition since in such a configuration the energy would be independent of excitation power. However, since here the holes are spatially localized in a *fundamentally* type-II system, the excitation energy dependence follows two-dependencies, at low and higher powers, $P < \sim 2$ W/cm^2, and $P > 2$ W/cm^2, respectively. At lower power (and low temperature), the photogenerated carriers are localized at interface states, an increase in excitation power under these conditions causes a blueshift in the peak PL energy and a linear dependence of excitations as the photoexcited carriers start to occupying the localized states (see the inset to Fig. 3.7). [25, 34, 35] Once these states are occupied the system will convert to the 'pure' type-II configuration, and additional photogenerated carriers will be screened from the effects of the localized states and rapidly occupy the lowest energy bands in the system: electrons in the InAs QW and holes in the AlAsSb barrier. In this situation, the radiative recombination follows the expected power law of laser excitation intensity ($P^{1/3}$). [36]

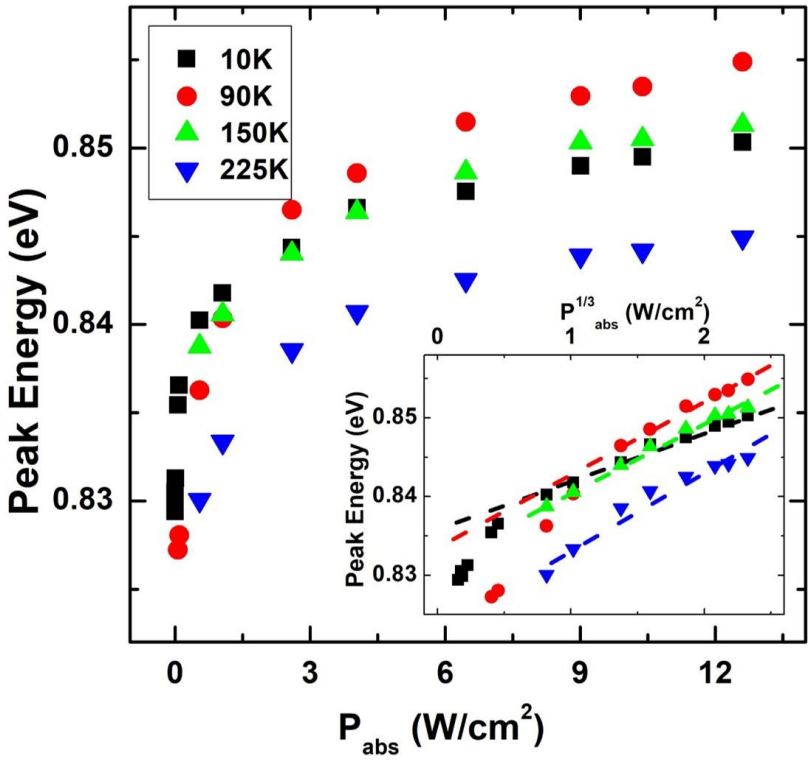

Figure 3. 7. Peak energy behavior as a function of excitation power for various lattice temperatures. Inset shows peak energy change versus $P^{1/3}$. Dashed lines show a linear dependence between peak energy and $P^{1/3}$. [Reproduced from: *Tang, J., Esmaielpour, H., et al. "Evidence of hot carriers at elevated temperatures in InAs/AlAsSb quantum wells." In Physics, Simulation, and Photonic Engineering of Photovoltaic Devices IV, vol. 9358, p. 93580Z. International Society for Optics and Photonics, 2015*] **[**35**]**

So far, the properties of the InAs QW structure has been described while under excitation of He-Cd (442 nm) and He-Ne (633 nm) lasers, which excite the QW above and close to the top of the AlAsSb, respectively. It is expected that higher energy photogenerated electrons will rapidly relax into the InAs QWs, on a shorter timescale than radiative recombination lifetime. This is confirmed by temperature dependent THz measurements (as described in Chapter 5, Section 5.4). However, under higher energy

excitation, issues related to the AlAsSb and possible interactions and contribution to impurities in this barrier cannot be excluded in contributions to the energy high PL spectrum. To further assess these possibilities, the QW was optically pumped below the barrier (between E_1 and E_2) using a 1064 nm IR diode laser to generate carriers resonantly within the InAs QW. Figure 3.8 shows the power dependent PL spectra of the InAs QW under 1064 nm excitation at two lattice temperatures (77 K (a) and 300 K (b)). The peak position of the PL spectrum at 300 K (Figure 3.8 (b)) is ~ 845 meV, which is close to the peak position at the same temperature when the sample was pumped with the He-Cd (442 nm) laser, confirming the high energy excitation predominately probes luminescence initiated in the QWs, with little contribution of the AlAsSb barriers.

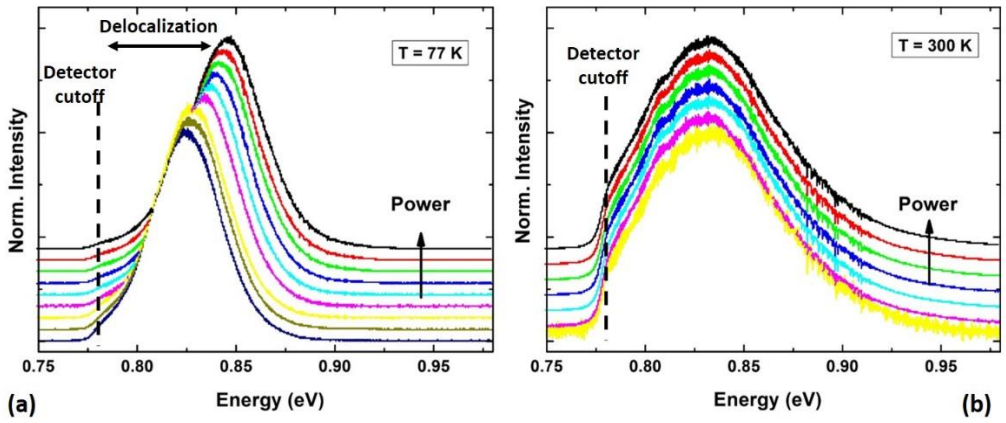

Figure 3. 8. Power dependent PL spectra at 77 K (a) and 300 K (b). Dashed Lines show where the InGaAs detector cutoff energy is.

Figure 3.8 (a) shows the power dependent PL at 77 K. With increasing fluence, the peak PL peak position increases. This blueshift is (again) attributed to the contribution

of localized centers at the InAs/AlAsSb interface. Figure 3.8 (b) shows the power dependence at 300 K. The change in PL energy at elevated temperatures is negligible, which is attributed the reduced confinement and spatial extension of the hole's wavefunction within the valence band; i.e., the *quasi-type-II* configuration of the system at higher temperatures. [32]

3.4. Extraction of carrier temperature using CW photoluminescence

3.4.1. Method 1: Generalized Planck's law – Simple linear fit of high energy PL spectra

The first technique is to determine the carrier temperature is applying a linear fit to the high energy side of natural logarithm of the PL spectra using Equation 3.3. A typical example of such a linear fit to the high energy tail of the PL spectrum is shown in Figure 3.9. [10, 11, 12, 27]

Recall that the first term in Equation 3.3:

$$\ln\big(I_{PL}(E)\big) = \ln\big(\varepsilon(E)\big) - \frac{E}{k_B T}, \tag{3.3}$$

is the *effective* emissivity (ε), which is related to the absorptivity of the system, and considered constant in Planck's radiation law, in this analysis. [27, 37] Figure 3.9 (a) shows the power dependent PL spectra at 10 K from a micro-PL system used to produce large power densities and generate robust hot carriers. [27] The blue squares show the natural logarithm of ε extracted by transposing Equation 3.3 for low power PL measurements at 10 K. Low excitation power rapidly generates carriers that are

predominately at equilibrium with the lattice. Therefore, it is possible to calibrate the system to determine the ε from the intercept $(\ln \varepsilon)$ of the graph.

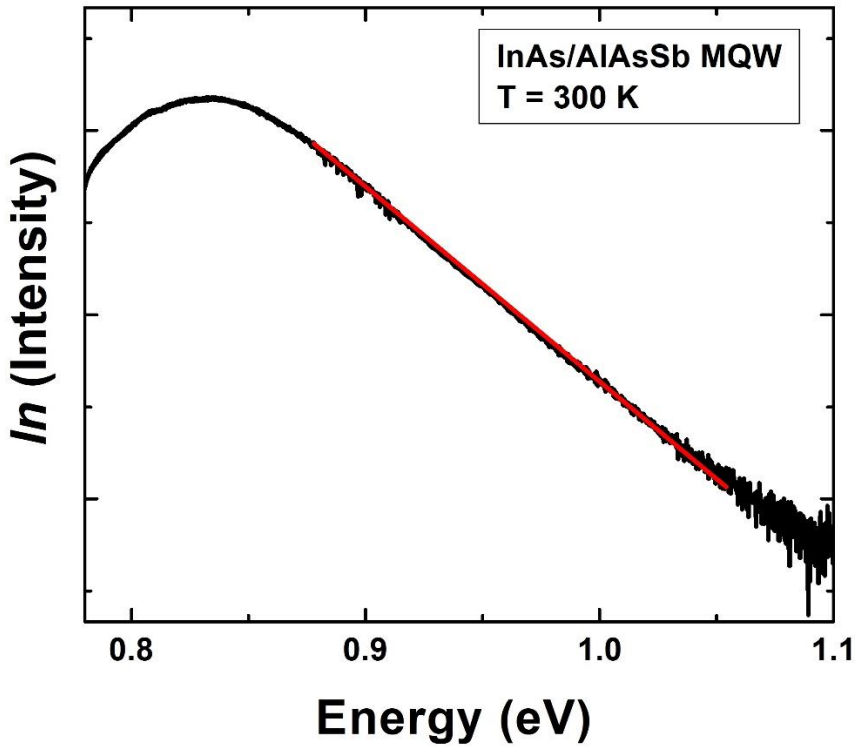

Figure 3. 9. Natural logarithm of PL spectrum at 300 K pumped with 1064 nm laser line. Red solid line shows the linear fit to the high energy side of the PL spectrum, which is inversely proportional to the carrier temperature.

In Figure 3.10 (a) is evident that an increase in the photon energy towards the band gap results in an increase of the natural logarithm of effective emissivity, up to the ground state (peak) energy of the InAs QW. Above this energy, the *effective* emissivity stabilizes *mimicking* (somewhat) the absorption profile of the InAs QW at higher energies.

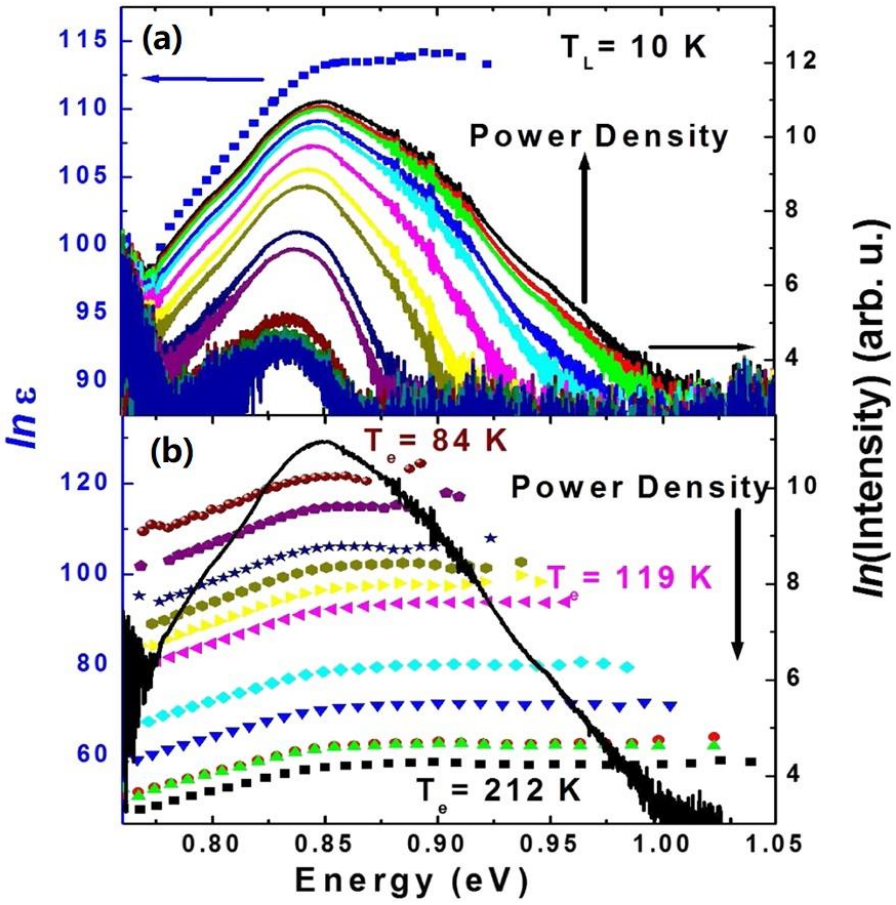

Figure 3. 10. (a) Power dependent PL spectra at 10 K. It is observed by increasing excitation power the slope at high energy side becomes shallower, which is indicative of increasing carrier temperature. Blue squares show the natural logarithm of effective emissivity when the excitation power is low and it is expected the carrier temperature in this condition to be close to the lattice temperature. (b) Solid black line shows the PL spectrum emitted from the excitation with highest excitation power. Dotted lines show natural logarithm of effective emissivity for power dependent PL spectra from panel (a). [Reproduced from: *Esmaielpour, H., et al. "Suppression of phonon-mediated hot carrier relaxation in type-II InAs/AlAsSb quantum wells". Progress in Photovoltaics: Research and Applications, 24(5), (2016):591-599.*] [27]

Figure 3.10 (b) shows the natural logarithm of the ε for the excitation power dependent PL spectra shown in panel (a), the solid black line shows the PL spectrum of the highest excitation power. It is evident that above the ground state energy (~ band gap) $\ln \varepsilon$ is constant, over a large energy range, which indicates that significant occupation of the excited states in the QW does not occur in this system – under the experimental conditions assessed. These measurements further support our hypothesis that the high energy spectra (and decreasing slope) with increasing excitation power in the PL is predominately the result of hot carriers, with little contribution from excited states in the QW. As a result, this simple technique is an appropriate method to extract carrier temperatures in the InAs/AlAsSb system. [27]

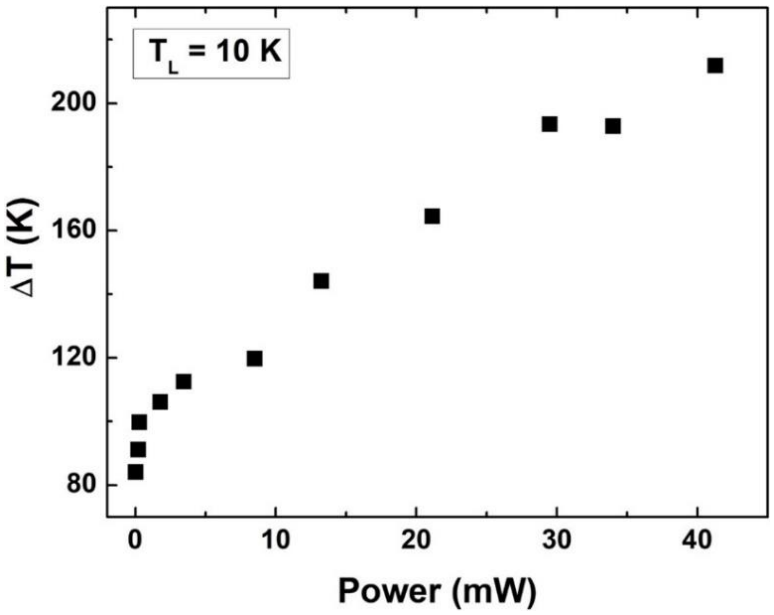

Figure 3. 11. Temperature difference (ΔT) versus excitation power at lattice temperature of 10 K. [Reproduced from: *Esmaielpour, H., et al. "Suppression of phonon-mediated hot carrier relaxation in type-II InAs/AlAsSb quantum wells". Progress in Photovoltaics: Research and Applications, 24(5), (2016):591-599.*] [27]

In general, it is expected that by increasing excitation power the number of photogenerated hot carriers increases and therefore the average carrier temperature increases. As shown in Figure 3.10 (a), when the excitation power increases the slope of the high energy side of the natural logarithm of the PL spectrum becomes shallower. This is indicative of a higher carrier temperature as the slope is inversely proportional with carrier temperature. [10, 11, 12, 21] Figure 3.11 shows the temperature difference (the difference between the extracted carrier and lattice temperatures, ΔT) as a function of excitation power for the power dependent PL spectra shown in Figure 3.10(a). Figure 3.11 indeed shows that ΔT increases as a function of excitation power.

3.4.2. Method 2: Equilibrium generalized Planck's law – Fitting the whole PL spectrum

Despite the simplicity of Equation 3.3 and its applicability to the InAs/AlAsSb QWs under investigation, full fitting of the whole PL spectrum can facilitate the extraction of additional parameters than the carrier temperature, including the quasi-Fermi level separation (chemical potential difference: $\Delta\mu = \mu_e - \mu_h$). This allows for assessment of the open circuit voltage using a contactless method – in simple optical structures. The whole PL spectrum can be simulated and fit using the so-called *equilibrium* generalized Planck's radiation law (Equation 3.1): [14, 15, 16, 17]

$$I_{PL}(E) = \frac{A(E)\,(E)^2}{4\pi^2 h^3 c^2}\left[exp\left(\frac{E-\Delta\mu}{k_B T}\right) - 1\right]^{-1}. \quad (3.1)$$

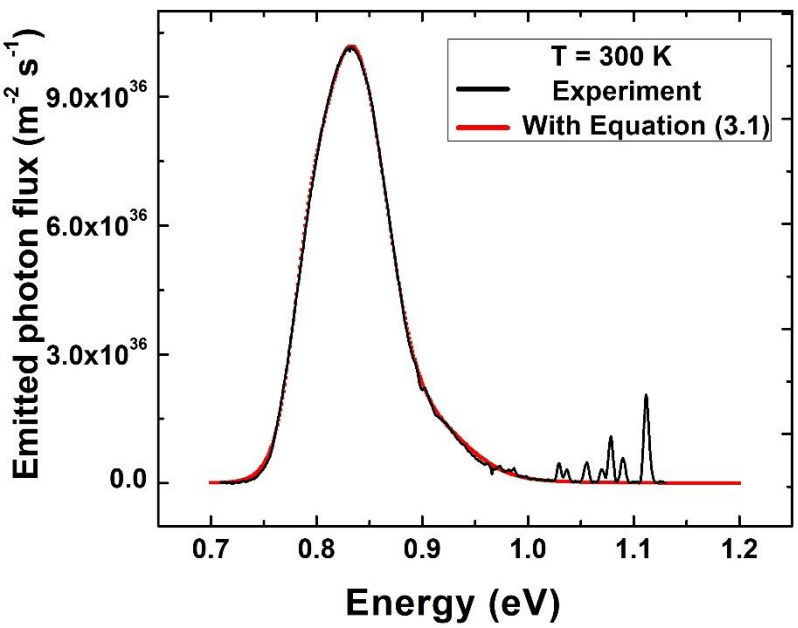

Figure 3. 12. Black line is the PL spectrum at 300 K. The red line shows the fit of the PL using the *equilibrium* generalized Planck's radiation (Equation 3.1).

Figure 3.12 shows the fit of the InAs MQW PL spectrum at 300 K applying Equation 3.1. There is a good agreement between PL spectrum and theory. This analysis is applied at 300 K and 150 K (above any affects due to carrier localization) to study the excitation power dependence behavior of the carrier temperature and chemical potential difference. Table 3.1 shows extracted parameters via fitting with Equation 3.1 at 300 K. Here (Table 3.1), "OD" in the first row represents optical density filter used to control the excitation power: a high value for optical density attenuates the signal more strongly and produces low excitation powers; in other words, OD00 and OD08 have the highest and the lowest excitation powers in Table 3.1, respectively. The extracted average carrier temperature (T) and quasi-Fermi level splitting ($\Delta\mu$) as a function of excitation power are provided in Table 3.1, and plotted in Figure 3.13.

Table 3. 1. Extracted parameters from fitting power dependent PL spectra at 300 K with Equation 3.1.

Excitation Power (mW)	OD00	OD01	OD02	OD03	OD05	OD08
	6.381	5.838	4.475	3.485	1.807	0.987
A_{hh}	9.8	9.8	9.8	9.6	9.6	9.6
A_{lh}	12.6	12.6	12.4	12.4	12.4	12.4
$A_{cont.}$	6.4	6.4	6.2	6.2	6.2	6.2
E_{hh} (eV)	0.838	0.838	0.838	0.839	0.839	0.839
E_{lh} (eV)	0.866	0.866	0.866	0.866	0.866	0.866
$E_{cont.}$ (eV)	0.89	0.89	0.89	0.89	0.89	0.89
Γ_{hh} (eV)	47/1000	47/1000	47/1000	47/1000	47/1000	47/1000
Γ_{lh} (eV)	83/2000	83/2000	83/2000	83/2000	83/2000	83/2000
$\Gamma_{cont.}$ (eV)	27/2000	27/2000	27/2000	27/2000	27/2000	27/2000
$\Delta\mu$ (eV)	0.5	0.494	0.486	0.475	0.443	0.405
T (K)	491	489	485	484	480	475

Applying this technique for a sample with a type-II band alignment can be challenging, especially if the sample suffers from non-idealities such as alloy fluctuations and non-idealities in its structure. As discussed previously, a system with a type-II band alignment experiences a peak energy shift to higher with increasing excitation power. A similar blueshift behavior occurs in the peak energy as a function of excitation power in the presence of localized states in the system. Therefore, it can be difficult to distinguish the contribution of the peak shift due these competing and independent mechanisms, which can affect the presumption of constant emissivity (absorptivity) from the PL spectrum. Under these conditions, the accuracy of extracted carrier temperature must be considered with care. However, these concerns are alleviated somewhat by the analysis described in section 3.4.1 and the extraction of the

carrier temperature using Equation 3.1 – linear fitting technique. Moreover, fitting whole the PL spectrum using Equation 3.1 still does not exclude (as per linear fitting) effects associated with the contribution of state filling or occupation of the excited states, which is highly probable for nanostructures with closely spaced energy levels. Again, the validity of this method is strong in the system presented here (InAs/AlAsSb QWs) since a larger ground to first excited state exist that limits the contribution of the higher order states to the measured PL spectrum (see Figure 3.2 (b)).

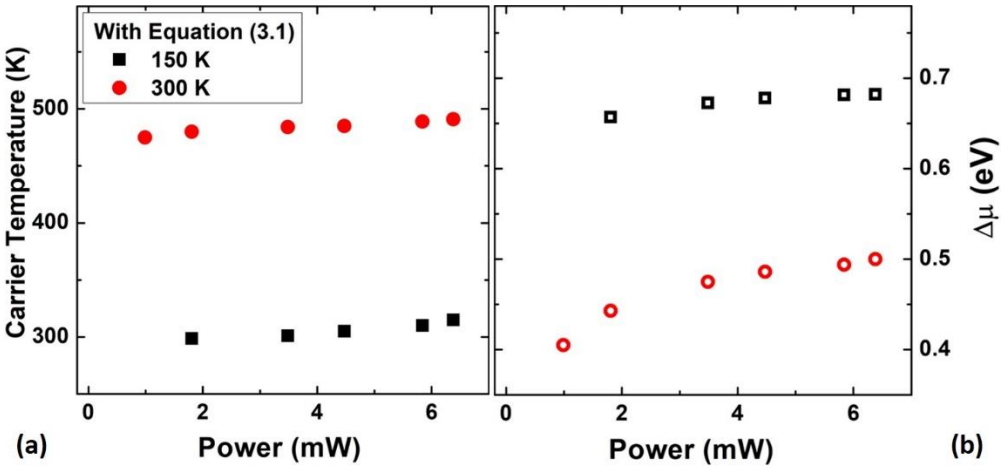

Figure 3. 13. Carrier temperature (a) and quasi-Fermi level splitting (b) at 150 K (black dots) and 300 K (red dots) extracted by Equation 3.1.

Figure 3.13 shows the extracted carrier temperatures (a) and quasi-Fermi level splitting (b), respectively, extracted from the fits using Equation 3.1 to the experimental results at 150 K and 300 K. It is evident that the extracted carrier temperatures at 150 K and 300 K show a power independent behavior, which was observed (and is consistent with the results found) from the linear fitting method (see Figure 3.17 (b)). [21, 27, 33]

In addition, it is seen that the quasi-Fermi level splitting (see Figure 3.13 (b)), which is proportional with operating voltage, slightly increases with excitation power. Similar behavior, as discussed in Chapter 6 Section 6.4, is observed for the open circuit voltage of the p-i-n device of the MQW structure as a function of excitation power.

The origin of this effect (as discussed in Section 3.5 and comprehensively in Chapter 5, Section 5.4) is attributed to the creation of a phonon bottleneck due to the slow radiative recombination lifetime of photogenerated hot electrons in the type-II InAs MQW, the inhibited anharmonic coupling between the LO and LA phonons in the system, along with the poor thermal dissipation of the phonons through the matrix. [32]

3.4.3. Method 3: Non-Equilibrium Generalized Planck's law – extension of full PL fit

To expand upon the equilibrium method (Section 3.4.2) a third technique has been recently developed by the hot carrier solar cell community. In this technique, the carrier temperature and separate chemical potentials for electrons and holes (instead of the chemical potential difference) are assessed in the system. [18] The *non-equilibrium* generalized Planck's radiation law is governed by Equation 3.4: [17]

$$I_{PL}(E) = \frac{A(E)\,(E)^2}{4\pi^2 h^3 c^2}\left[exp\left(\begin{array}{c}\frac{1}{k_B}\left(\frac{1}{T_H^e}-\frac{1}{T_H^h}\right)\times\left[\left(\frac{m^e}{m^e+m^h}\right)\left(\frac{E_G}{2}+E_c^i\right)-\left(\frac{m^h}{m^e+m^h}\right)\left(\frac{E_G}{2}+\left|E_v^j\right|\right)\right] \\ +\frac{E}{k_B\left(m^e+m^h\right)}\left(\frac{m^h}{T_H^e}+\frac{m^e}{T_H^h}\right)-\frac{\mu_H^e}{k_B T_H^e}-\frac{\mu_H^h}{k_B T_H^h}\end{array}\right)-1\right]^{-1}. \quad (3.4)$$

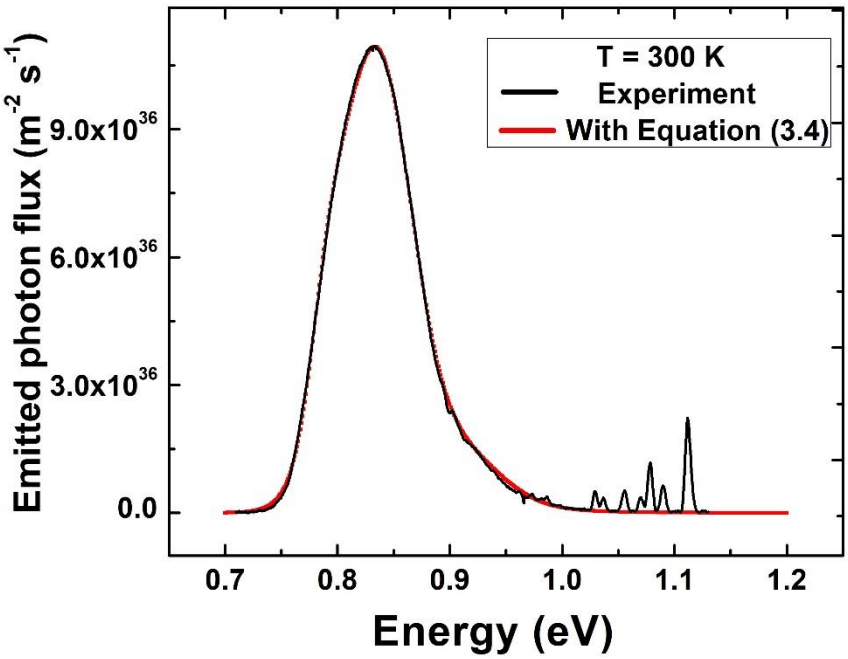

Figure 3. 14. Black line is PL spectrum at 300 K. Red line is the result of fitting of the whole PL spectrum using non-equilibrium generalized Planck's radiation (Equation 3.4).

Figure 3.14 shows the result of fitting Equation 3.4 to the PL spectrum for the InAs MQW at 300 K. As shown, there is a good agreement between experiment and theory. Here, to fit the experimental data with Equation 3.4 two assumptions are made: 1) there is no shift in peak position as a function of excitation power at 150 K and 300 K in the small range of powers studied; and 2) at elevated lattice temperatures, the photogenerated electrons and holes are spatially separated due to the type-II band alignment; i.e. electrons are in InAs QW and holes are in AlAsSb barrier. Therefore for the analysis, the bulk InAs effective mass and bulk AlSb (instead of AlAsSb due to low concentration (16%) of As) effective mass are considered for electrons (m_e^* = 0.027 m_e) and holes (m_h^* = 0.98 m_e), respectively. [38] Table 3.2 shows the extracted parameters considering these assumptions in Equation 3.4 at 300 K.

Table 3. 2. Extracted parameters from fitting power dependent PL spectra at 300 K with Equation 3.4.

Excitation Power (mW)	OD00	OD01	OD02	OD03	OD05	OD08
	6.381	5.838	4.475	3.485	1.807	0.987
A_{hh}	9.8	9.8	9.8	9.6	9.6	9.6
A_{lh}	12.6	12.6	12.4	12.4	12.4	12.4
$A_{cont.}$	6.4	6.4	6.2	6.2	6.2	6.2
E_{hh} (eV)	0.838	0.838	0.838	0.839	0.839	0.839
E_{lh} (eV)	0.866	0.866	0.866	0.866	0.866	0.866
$E_{cont.}$ (eV)	0.89	0.89	0.89	0.89	0.89	0.89
Γ_{hh} (eV)	47/1000	47/1000	47/1000	47/1000	47/1000	47/1000
Γ_{lh} (eV)	83/2000	83/2000	83/2000	83/2000	83/2000	83/2000
$\Gamma_{cont.}$ (eV)	27/2000	27/2000	27/2000	27/2000	27/2000	27/2000
μ_e (eV)	0.28	0.273	0.269	0.266	0.247	0.223
μ_h (eV)	0.19	0.19	0.188	0.184	0.177	0.168
T_e (K)	499.5	498	494	491	484	480
T_h (K)	308	306	306	305	303	303

Although extracting individual carrier temperatures and chemical potentials for both electrons and holes using this technique is advantageous, this technique has several limitations or uncertainties. As discussed, the presence of localized states in the type-II system can reduce the accuracy of the absorptivity considered – consequently, the extracted carrier temperatures as a function of excitation power must therefore be considered with care. Moreover, there are multiple several variables in Equation 3.4, which make the fitting process demanding and somewhat arbitrary without careful consideration of the constants and parameters inserted into the equation.

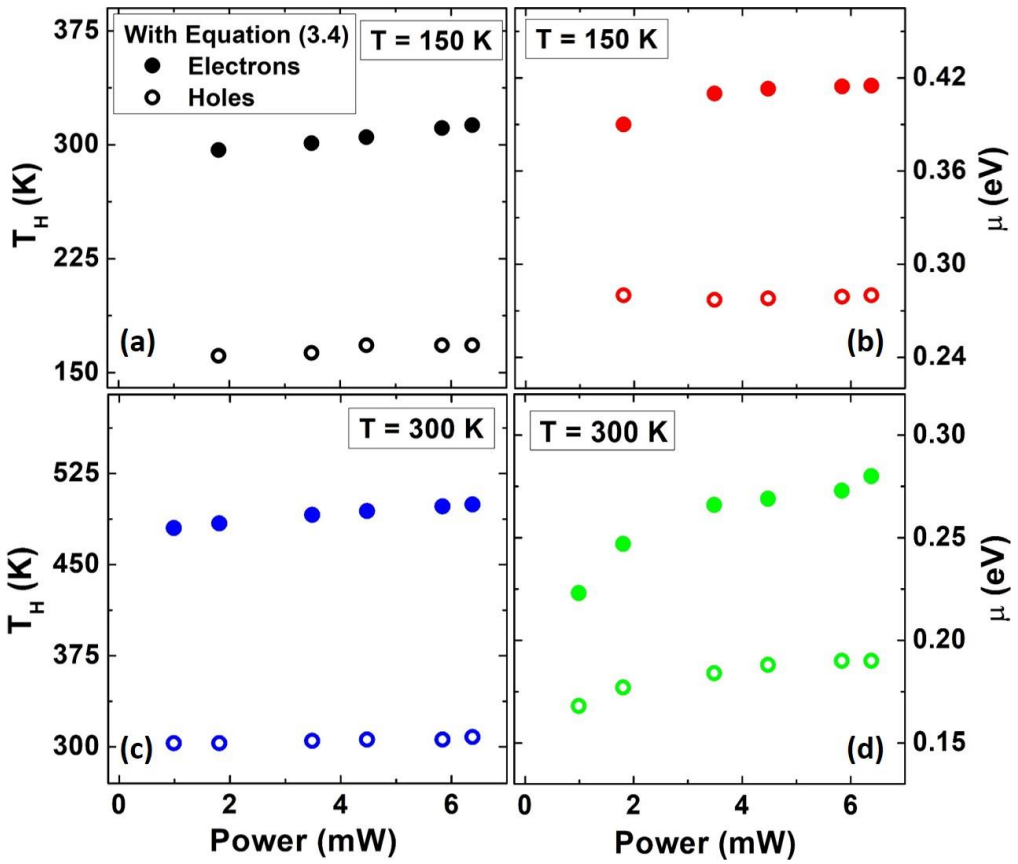

Figure 3. 15. (a) + (c) carrier temperature and (b) + (d) chemical potential at 150 K and 300 K, respectively, extracted from fitting with Equation 3.4.

Figure 3.15 (a) and (c) show carrier temperatures and Figure 3.15 (b) and (d) show chemical potentials at 150 K and 300 K, respectively, extracted from fitting the power dependent PL spectra with Equation 3.4. Comparison between results in Figure 3.15 (a, c) and Figure 3.13 (a) indicate a similar power independent behavior of the carrier temperatures at elevated temperature that were extracted using the non-equilibrium generalized (Equation 3.4) and generalized equilibrium (Equation 3.1) techniques, respectively. The similar extracted results further support the applicability of the simple

linear fit, which reduces some of the uncertainties introduced by the more advanced methodologies enacted to fit the full PL spectrum.

In Figure 3.15 (b), chemical potentials for electrons and holes at 150 K are shown as a function of excitation power. It is evident that the chemical potential of electrons is at higher values than holes, due to their smaller effective mass and their higher temperatures. [18] Similar behavior is observed for the extracted chemical potentials at 300 K for electrons and holes, which confirms more kinetic energy is transferred to electrons rather than holes. [24]

3.5. Temperature dependent behavior of phonon mediated hot carrier thermalization coefficient

In extracting the carrier temperature for the type-II InAs/AlAsSb QWs all techniques discussed above indicate an unusual behavior above T ~ 90 K, when the system is in the type-II regime. The effect of state filling and the role of hot carrier lifetime and phonon dissipation have been considered. [22, 23] Here, it is suggested that the hot carrier dynamics are quite different from these observed in the literature for type-I systems. [11, 12] This becomes apparent when considering Figure 3.16, which shows the carrier temperature extracted from power dependent PL at various lattice temperatures. In Figure 3.16, increasing the lattice temperature up to T = 90 K results in a reduction in the temperature difference (ΔT). Moreover, in this temperature regime (4.2 K < T < 90 K) there is a strong *conventional* power dependence for ΔT. These characteristics are indicative of efficient electron-phonon thermalization with a concomitant increase in phonon density as the lattice temperature increases.

However, by increasing the lattice temperature above 90 K, it is evident that the overall ΔT increases despite an increasing phonon density and the effect of power is reduced. This behavior suggests that at elevated temperatures there are other mechanisms dominating the thermalization in the system, rather than conventional phonon-mediated hot carrier thermalization processes. Indeed, remarkably, robust hot carriers are observed up to room temperature, which is significant for designing practical hot carrier solar cells at low concentrated solar power. [21, 27, 32]

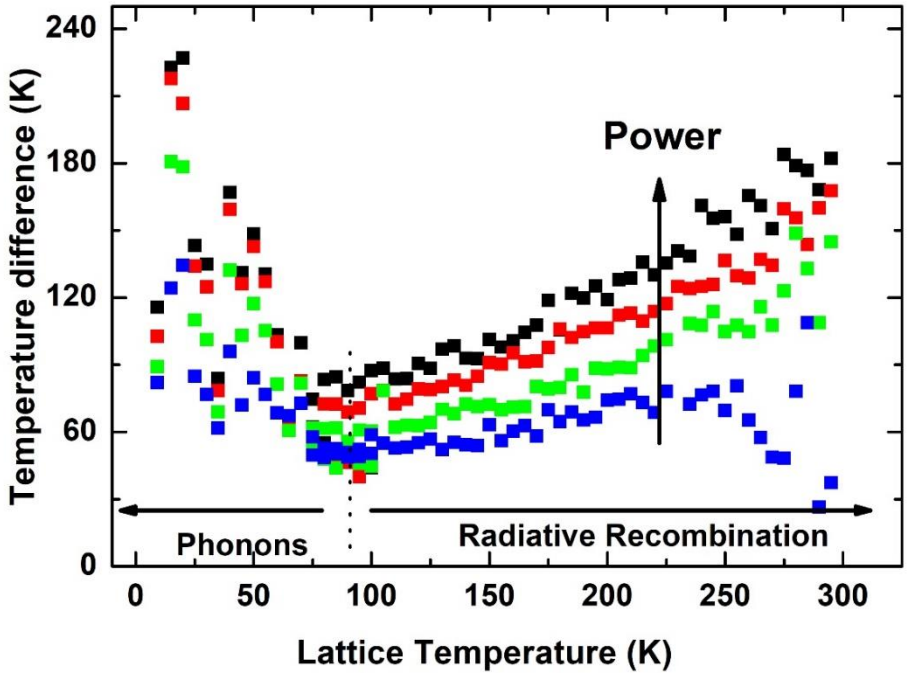

Figure 3. 16. Temperature difference (ΔT) versus lattice temperature for various excitation powers. [Reproduced from: *Tang, J., Esmaielpour, H., et al. "Effects of localization on hot carriers in InAs/AlAsSb quantum wells" Applied Physics Letters, 106(6), (2015):061902*.] [21]

The interaction of hot carriers with phonons in the system has been developod by Le Bris, *et al.* [9, 11] in hot carrier absorbers utilizing an analysis, which considers a

phonon-mediated thermalization coefficient (Q). The thermalization coefficient (Q) is an empirical parameter, which determines the amount of heat dissipation via interactions between electrons (holes) and phonons. In other words it represents how efficient phonon relaxation channels are in the system. A sample with a large phonon-mediated thermalization coefficient indicates the contribution of optical phonons in thermalization of hot carriers is large and phonon channels are efficient in thermalizing hot carriers.

The extracted power (P) in a solar cell is described by:

$$P = P_{abs} - P_{emit} - P_{th}, \tag{3.6}$$

where P_{abs} is the absorbed power, P_{th} the thermalized power and P_{emit} the emitted power. The emitted power is a much smaller quantity when compared with the other terms, if active light extraction methods are not used. The thermalized power is due to the transfer of heat to the system from the dissipation of energy from the hot carriers to the LO-phonon bath and is governed by: [11, 39]

$$P_{th} = \frac{t\, n_q\, E_{LO}}{\tau_{th}} \exp\left(-\frac{E_{LO}}{K_B T_H}\right), \tag{3.7}$$

where n_q, E_{LO}, and τ_{th} are the density of phonon modes, the LO-phonon energy, and the LO-phonon lifetime, respectively. Here for the InAs MQW structure, the LO-phonon energy (E_{LO}) is taken as 29 meV, which is the LO-phonon energy of bulk InAs. [40] Under open circuit conditions, such as during a photoluminescence measurement, the extracted power (P) is zero, therefore the absorbed power becomes equal to the thermalized power. Moreover, there is a linear relation between the temperature

difference and the ratio of phonon modes to LO-phonon lifetime $\left(\frac{n_q}{\tau_{th}}\right)$, as such, Equation 3.7 can be written: [9, 11]

$$P_{abs} = P_{th} = Q(T_H - T)\exp\left(-\frac{E_{LO}}{K_B T_H}\right). \quad (3.8)$$

The parameter (Q) in Equation 3.8 is the phonon-mediated thermalization coefficient, which is the related to the slope of the graph when the absorbed power divided by the exponential factor is plotted versus temperature difference. [11]

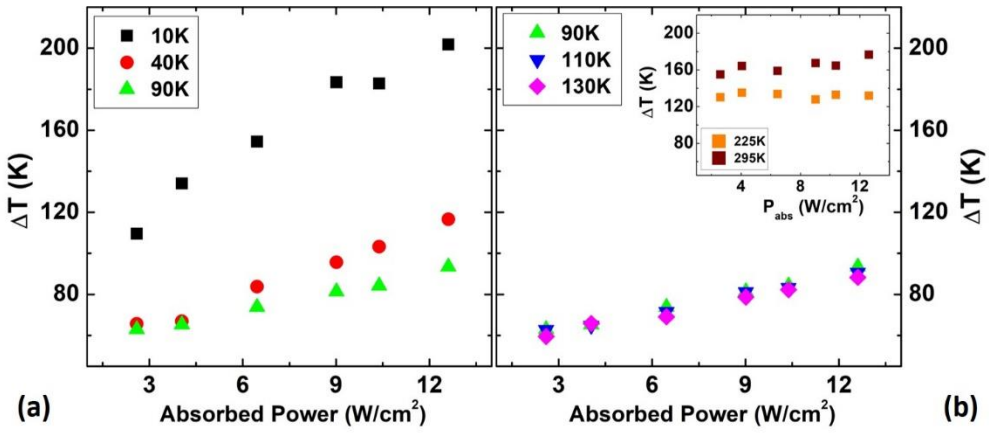

Figure 3. 17. (a) – (b) Temperature difference (ΔT) against absorbed power for various lattice temperatures and inset in panel (b) shows the results for 225 K and 295 K. [Reproduced from: *Esmaielpour, H., et al. "Suppression of phonon-mediated hot carrier relaxation in type-II InAs/AlAsSb quantum wells". Progress in Photovoltaics: Research and Applications, 24(5), (2016):591-599.*] [27]

The absorbed power is determined by calculating how much light is absorbed in the quantum well in units of W/cm^2, which is dependent on the spot size of the excitation laser. The spot size of the beam is measured utilizing a pinhole method and the amount

of light absorption in the active region is determined utilizing transfer matrix analysis. The details about the spot size measurement and light absorption are discussed in Appendix A and B, respectively.

To investigate the phonon-mediated thermalization coefficient of InAs MQW, power dependent photoluminescence measurements of the sample at various lattice temperatures were assessed. Figure 3.17 (a) and (b) show power dependent behavior of the temperature difference (ΔT) at several lattice temperatures. As has been discussed, at elevated temperature ΔT increases but, its dependence upon excitation power reduces – becoming effectively independent of power under the measurement conditions investigated. This is illustrated in the inset to Figure 3.17 (b), which shows that although ΔT increases at elevated lattice temperatures (225 K and 295 K), it does not depend on excitation power at these temperatures. Similar power independent behavior has been observed when the whole PL spectrum was fit using both equilibrium (Figure 3.13 (a)) and non-equilibrium (Figure 3.15 (a) and (c)) generalized Planck's radiation laws. [21, 25, 27] The power independent behavior has been attributed to the creation of a phonon bottleneck in type-II QWs, where the photogenerated carriers are spatially separated. Under these this conditions, radiative recombination is less efficient (than a type-I band system), and as a result the density of photogenerated carriers within the QW is high and longer lived than more conventional type-I QWs. In it suggested that these properties facilitate the creation of a strong phonon bottleneck in the InAs/AlAsSb QWs. Similar behavior has been observed in spatially separated carriers in GaAs/AlGaAs quantum dots (QDs) [41] and indirect band gap Si colloidal QDs [42]

with slow radiative recombination rates, each feature critical for the creation of a phonon bottleneck effect in their respective systems.

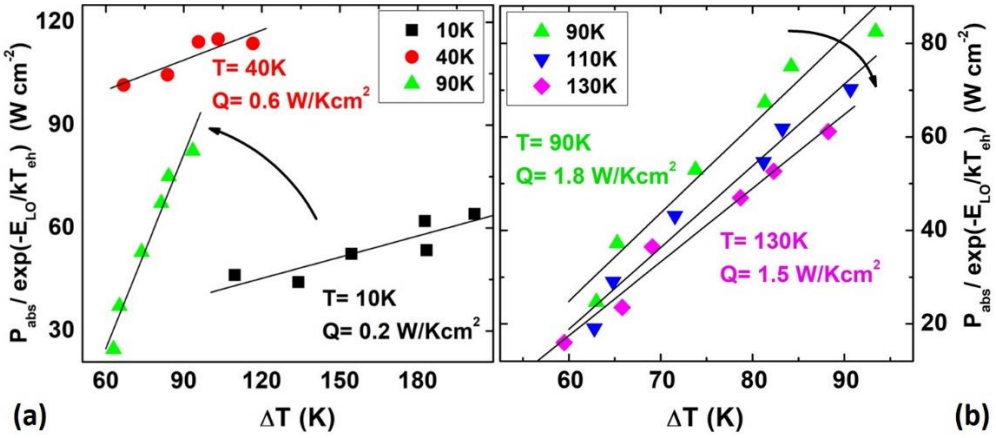

Figure 3. 18. (a) – (b) Phonon-mediated thermalization coefficient (Q-factor) analysis is applied to the same data as Figure 3.17 (a) and (b). The extracted slope from each set of data is equal to thermalization coefficient at that lattice temperature. [Reproduced from: *Esmaielpour, H., et al. "Suppression of phonon-mediated hot carrier relaxation in type-II InAs/AlAsSb quantum wells". Progress in Photovoltaics: Research and Applications, 24(5), (2016):591-599.*] [27]

In the InAs MQWs, a stabilized hot carrier distribution is observed at elevated temperatures when the MQW sample reveals its dominant type-II behavior. At this condition, although there is a considerable density of phonons in the system, the thermalization effect does not appear to be the dominant carrier relaxation mechanism. This conclusion is supported when applying Equation 3.8 to the results in Figure(s) 3.17 (a) and (b), and assessing the thermalization coefficient for the sample at various lattice temperatures, as shown in Figure 3.18 (a) and (b). It is observed by increasing the lattice temperature, the thermalization coefficient increases up to 90 K, and then above that

temperature, it stabilizes. The increase of thermalization coefficient up to 90 K is expected because as the lattice temperature increases, the density of phonons in the system increases. Therefore, electron-phonon interactions will increase in efficiency serving to thermalize the hot carrier distribution. [11, 12, 27]

However, despite the further increase in phonons above 90 K, the thermalization coefficient stabilizes actually starts to decrease, then becomes unphysical above 150 K (see the inset to Figure 3.19). This indicates that in the temperature regime above 90 K, electron-phonon interactions *are not the dominant thermalization mechanism*. These results are consistent with those described in Figure 3.15 where above 90 K, there is an increase in carrier temperature due to ineffective phonon relaxation channels in the system (see also Figure 3.19).

This hypothesis is summarized in Figure 3.19, which shows a comparison of the thermalization coefficient (blue open triangles) and the ΔT (closed black stars), versus lattice temperature. The thermalization coefficient increases – as expected – up to 90K, but then starts to decrease – at 150 K and above no Q-value can be extracted. The ability to extract a reasonable Q-value up to 90 K occurs in the low temperature regime where a quasi-type-I regime dominates the PL. However, when the type-II transition occurs (at T > 90 K) the thermalization analysis is no longer valid supporting the hypothesis that it is the radiative lifetime of the photogenerated carrier, rather than electron-phonon interactions that define the thermalization rate of the hot carriers in the type-II QWs. The inset of Figure 3.19 shows the results of Equation 3.8 applied to the power dependent PL at 225 K and 295 K, where the carrier temperature is independent of excitation power. These data show no clear trend since ΔT (x-axis) is independent of

excitation power, as such, no physical thermalization coefficient can be determined. [27]

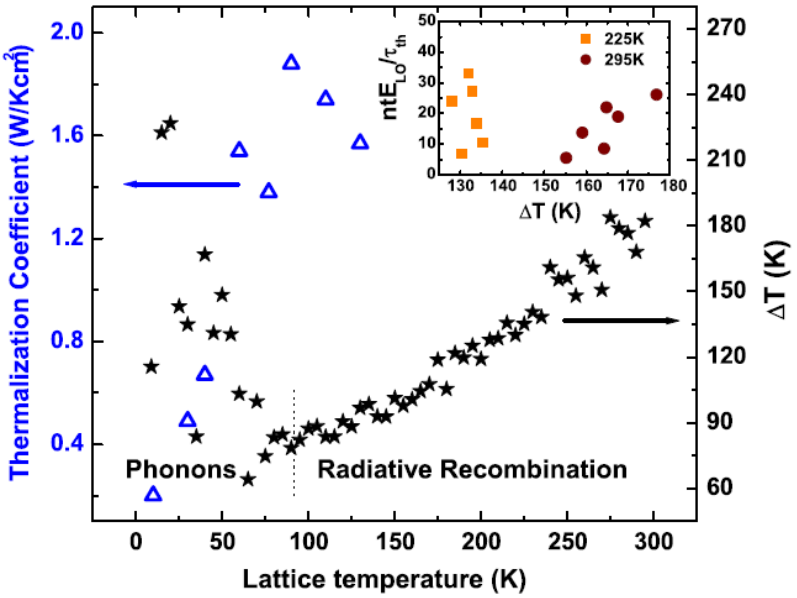

Figure 3. 19. Thermalization coefficient (blue triangles) and temperature difference (black stars) are plotted as a function of lattice temperature. Inset of this graph shows thermalization analysis at elevated temperatures (225 K and 295 K), which shows there is no clear slope for the data when the dominant mechanism in the system is type-II radiative recombination thus, providing a condition for phonon-bottleneck effect. [Reproduced from: *Esmaielpour, H., et al. "Suppression of phonon-mediated hot carrier relaxation in type-II InAs/AlAsSb quantum wells". Progress in Photovoltaics: Research and Applications, 24(5), (2016):591-599.*] [27]

Conclusion

InAs/AlAsSb QW heterostructures have been proposed as candidate systems for hot carrier absorbers. Continuous wave power and temperature dependent photoluminescence show evidence of robust hot carrier effects at elevated lattice

temperatures in these structures. At low lattice temperatures (up to 90 K), holes are trapped at the interface between the QW and the barrier material. Therefore, recombination occurs within the InAs QW following a *quasi-type-I* transition, whereby localized hole recombine with electrons confined in the deep InAs QWs. As lattice temperature increases beyond 90 K, the holes receive enough thermal energy to escape from theses interface states and relax into the barrier material and the electrons and holes become spatially separated. As such, at $T > 90$ K, the radiative recombination follows a type-II band alignment, which is a relatively inefficient and slow process. Therefore, the lifetime and density of electrons in the QW increases and provides the conditions for the creation of a strong phonon bottleneck. Excitation power dependent PL at room temperature has shown evidence of hot carriers even at low excitation powers (a few hundred suns).

The hot carrier temperature has been evaluated and analyzed using three alternative methods: linear fitting to the high energy side of PL spectrum; fitting the whole PL spectrum with equilibrium generalized Planck's radiation law; and fitting the full spectrum with the non-equilibrium generalized Planck's radiation law. There is a consistency among the results from these three methods, which all support the presence of a robust hot carrier distribution at elevated temperatures.

Finally, temperature and power dependent PL measurements supported the hypothesis that the hot carrier thermalization in these systems are dominated by the hot electron lifetime in the InAs QWs, rather than electron-phonon interactions, especially at elevated temperatures. This conclusion was further supported by analysis of the phonon-mediated thermalization coefficient, which although valid in type-I systems (where the

non-equilibrium carrier distribution is thermalized by phonons) is shown to be unphysical in type-II systems – due to the difference in dominate thermalization mechanisms in these novel structures.

References

[1] Conibeer, Gavin, Nicholas Ekins-Daukes, Jean-François Guillemoles, Dirk Kőnig, Eun-Chel Cho, Chu-Wei Jiang, Santosh Shrestha, and Martin Green. "Progress on hot carrier cells." Solar Energy Materials and Solar Cells 93, no. 6-7 (2009): 713-719.

[2] Conibeer, Gavin, Santosh Shrestha, Shujuan Huang, Robert Patterson, Hongze Xia, Yu Feng, Pengfei Zhang *et al.* "Hot carrier solar cell absorber prerequisites and candidate material systems." Solar Energy Materials and Solar Cells 135 (2015): 124-129.

[3] Nozik, Arthur J. "Spectroscopy and hot electron relaxation dynamics in semiconductor quantum wells and quantum dots." Annual review of physical chemistry 52, no. 1 (2001): 193-231.

[4] Conibeer, G. J., D. König, M. A. Green, and J. F. Guillemoles. "Slowing of carrier cooling in hot carrier solar cells." Thin solid films 516, no. 20 (2008): 6948-6953.

[5] Rosenwaks, Y., M. C. Hanna, D. H. Levi, D. M. Szmyd, R. K. Ahrenkiel, and A. J. Nozik. "Hot-carrier cooling in GaAs: Quantum wells versus bulk." Physical Review B 48, no. 19 (1993): 14675.

[6] Pelouch, W. S., R. J. Ellingson, P. E. Powers, C. L. Tang, D. M. Szmyd, and A. J. Nozik. "Comparison of hot-carrier relaxation in quantum wells and bulk GaAs at high carrier densities." Physical Review B 45, no. 3 (1992): 1450.

[7] Conibeer, Gavin, Martin Green, Richard Corkish, Young Cho, Eun-Chel Cho, Chu-Wei Jiang, Thipwan Fangsuwannarak *et al.* "Silicon nanostructures for third generation photovoltaic solar cells." Thin solid films 511 (2006): 654-662.

[8] Rota, L., F. Rossi, S. M. Goodnick, P. Lugli, Elisa Molinari, and W. Porod. "Reduced carrier cooling and thermalization in semiconductor quantum wires." Physical Review B 47, no. 3 (1993): 1632.

[9] Le Bris, Arthur. "Feasibility study of a hot carrier photovoltaic device." PhD diss., Ecole Centrale Paris, 2011.

[10] Shah, Jagdeep. "Hot carriers in quasi-2-D polar semiconductors." IEEE Journal of Quantum electronics 22, no. 9 (1986): 1728-1743.

[11] Le Bris, A., L. Lombez, S. Laribi, G. Boissier, P. Christol, and J-F. Guillemoles. "Thermalisation rate study of GaSb-based heterostructures by continuous wave photoluminescence and their potential as hot carrier solar cell absorbers." Energy & Environmental Science 5, no. 3 (2012): 6225-6232.

[12] Hirst, Louise C., Hiromasa Fujii, Yunpeng Wang, Masakazu Sugiyama, and Nicholas J. Ekins-Daukes. "Hot carriers in quantum wells for photovoltaic efficiency enhancement." IEEE Journal of Photovoltaics 4, no. 1 (2014): 244-252.

[13] Leo, K., W. W. Rühle, H. J. Queisser, and K. Ploog. "Hot carrier cooling in GaAs quantum wells." Applied Physics A 45, no. 1 (1988): 35-39.

[14] Lasher, Gordon, and Frank Stern. "Spontaneous and stimulated recombination radiation in semiconductors." Physical Review 133, no. 2A (1964): A553.

[15] De Vos, A., and H. Pauwels. "On the thermodynamic limit of photovoltaic energy conversion." Applied physics 25, no. 2 (1981): 119-125.

[16] Wurfel, Peter. "The chemical potential of radiation." Journal of Physics C: Solid State Physics 15, no. 18 (1982): 3967.

[17] Gibelli, François, Laurent Lombez, and Jean-François Guillemoles. "Accurate radiation temperature and chemical potential from quantitative photoluminescence analysis of hot carrier populations." Journal of Physics: Condensed Matter 29, no. 6 (2016): 06LT02.

[18] Gibelli, François, Laurent Lombez, and Jean-François Guillemoles. "Two carrier temperatures non-equilibrium generalized Planck law for semiconductors." Physica B: Condensed Matter 498 (2016): 7-14.

[19] Chen, Y., R. Cingolani, L. C. Andreani, F. Bassani, and J. Massies. "Photoluminescence in quantum well and bulk GaAs: a direct comparative study." Il Nuovo Cimento D 10, no. 7 (1988): 847-859.

[20] Chemla, D. S., D. Miller, P. Smith, A. Gossard, and William Wiegmann. "Room temperature excitonic nonlinear absorption and refraction in GaAs/AlGaAs multiple quantum well structures." IEEE Journal of Quantum Electronics 20, no. 3 (1984): 265-275.

[21]Tang, J., V. R. Whiteside, H. Esmaielpour, S. Vijeyaragunathan, T. D. Mishima, M. B. Santos, and I. R. Sellers. "Effects of localization on hot carriers in InAs/$AlAs_xSb_{1-x}$ quantum wells." Applied Physics Letters 106, no. 6 (2015): 061902.

[22] Esmaielpour, Hamidreza, Vincent R. Whiteside, Louise C. Hirst, Joseph G. Tischler, Chase T. Ellis, Matthew P. Lumb, David V. Forbes, Robert J. Walters, and Ian R. Sellers. "Effect of occupation of the excited states and phonon broadening on the determination of the hot carrier temperature from continuous wave photoluminescence in InGaAsP quantum well absorbers." Progress in Photovoltaics: Research and Applications 25, no. 9 (2017): 782-790.

[23] Esmaielpour, Hamidreza, Vincent R. Whiteside, Louise C. Hirst, Joseph G. Tischler, Robert J. Walters, and Ian R. Sellers. "The effect of excited state occupation and phonon broadening in the determination of the non-equilibrium hot-carrier temperature in InGaAsP quantum-well absorbers (Conference Presentation)." In Physics, Simulation, and Photonic Engineering of Photovoltaic Devices VII, vol. 10527, p. 1052706. International Society for Optics and Photonics, 2018.

[24] König, D., Y. Takeda, and B. Puthen-Veettil. "Technology-compatible hot carrier solar cell with energy selective hot carrier absorber and carrier-selective contacts." Applied Physics Letters 101, no. 15 (2012): 153901.

[25] Tang, Jinfeng. "Hot Carriers in InAs Quantum Wells for Applications in 3rd Generation Photovoltaics." Master Thesis., University of Oklahoma, 2015.

[26] Kroemer, Herbert. "The 6.1 A family (InAs, GaSb, AlSb) and its heterostructures: a selective review." Physica E: Low-dimensional Systems and Nanostructures 20, no. 3-4 (2004): 196-203.

[27] Esmaielpour, Hamidreza, Vincent R. Whiteside, Jinfeng Tang, Sangeetha Vijeyaragunathan, Tetsuya D. Mishima, Shayne Cairns, Michael B. Santos, Bin Wang, and Ian R. Sellers. "Suppression of phonon-mediated hot carrier relaxation in type-II InAs/AlAsxSb1− x quantum wells: a practical route to hot carrier solar cells." Progress in Photovoltaics: Research and Applications 24, no. 5 (2016): 591-599.

[28] Nuytten, Thomas, Manus Hayne, Bhavtosh Bansal, H. Y. Liu, Mark Hopkinson, and Victor V. Moshchalkov. "Charge separation and temperature-induced carrier migration in $Ga_{1-x}In_xN_yAs_{1-y}$ multiple quantum wells." Physical Review B 84, no. 4 (2011): 045302.

[29] Varshni, Yatendra Pal. "Temperature dependence of the energy gap in semiconductors." physica 34, no. 1 (1967): 149-154.

[30] Heitz, R., I. Mukhametzhanov, A. Madhukar, A. Hoffmann, and D. Bimberg. "Temperature dependent optical properties of self-organized InAs/GaAs quantum dots." Journal of electronic materials 28, no. 5 (1999): 520-527.

[31] Klein, B., E. Plis, M. N. Kutty, N. Gautam, A. Albrecht, S. Myers, and S. Krishna. "Varshni parameters for InAs/GaSb strained layer superlattice infrared photodetectors." Journal of Physics D: Applied Physics 44, no. 7 (2011): 075102.

[32] Esmaielpour, Hamidreza, Vincent R. Whiteside, Herath P. Piyathilaka, Sangeetha Vijeyaragunathan, Bin Wang, Echo Adcock-Smith, Kenneth P. Roberts *et al.* "Enhanced hot electron lifetimes in quantum wells with inhibited phonon coupling." Scientific reports 8, no. 1 (2018): 12473.

[33] Whiteside, V. R., Magilly, B. A., Lumb, M. P., Esmaielpour, H., Meeker, M. A., Mudiyanselage, R. R. H. H., Messager, A., Santos, M. B., Vurgaftman, I., Khodaparast, G. A., and Sellers, I. R., Valence Band states in a InAs/AlAsSb multi-quantum well hot carrier absorber, Semiconductor Science and Technology (2018).

[34] Esmaielpour, Hamidreza, Vincent R. Whiteside, Louise C. Hirst, Joseph G. Tischler, Robert J. Walters, and Ian R. Sellers. "The effect of an InP cap layer on the photoluminescence of an $In_xGa_{1-x}As_{1-y}P_y/In_zAl_{1-z}As$ quantum well heterostructure." Journal of Applied Physics 121, no. 23 (2017): 235301.

[35] Tang, J., Vincent R. Whiteside, H. Esmaielpour, S. Vijeyaragunathan, T. D. Mishima, M. B. Santos, and I. R. Sellers. "Evidence of hot carriers at elevated temperatures in $InAs/AlAs_{0.84}Sb_{0.16}$ quantum wells." In Physics, Simulation, and Photonic Engineering of Photovoltaic Devices IV, vol. 9358, p. 93580Z. International Society for Optics and Photonics, 2015.

[36] Weisbuch, Claude, and Borge Vinter. Quantum semiconductor structures: fundamentals and applications. Elsevier, 2014.

[37] Hirst LC. How to build a hot-carrier solar cell: material development and device design, CMP Seminar Series, Department of Physics & Astronomy, University of Oklahoma, October 2014.

[38] http://www.eecs.umich.edu/courses/eecs320/f00/bk7ch03.pdf

[39] Klimov, V., P. Haring Bolivar, and H. Kurz. "Hot-phonon effects in femtosecond luminescence spectra of electron-hole plasmas in CdS." Physical Review B 52, no. 7 (1995): 4728.

[40] http://www.ioffe.ru/SVA/NSM/Semicond/InAs/optic.html

[41] Chang, Yu-Chen, A. J. Robson, Samuel Harrison, Q. D. Zhuang, and Manus Hayne. "Phonon bottleneck in GaAs/$Al_xGa_{1-x}As$ quantum dots." AIP Advances 5, no. 6 (2015): 067141.

[42] Zhang, Pengfei, Yu Feng, Xiaoming Wen, Wenkai Cao, Rebecca Anthony, Uwe Kortshagen, Gavin Conibeer, and Shujuan Huang. "Generation of hot carrier population in colloidal silicon quantum dots for high-efficiency photovoltaics." Solar Energy Materials and Solar Cells 145 (2016): 391-396.

Chapter **4**

Effects of state filling, band structure, and phonon broadening on carrier temperature determination

4.1. Introduction: Hot carrier temperature

The light emitted from semiconductor structures provides valuable information about their physical properties such as material composition, energy, and carrier temperature. [1, 2] At thermal equilibrium, the emission is governed by Planck's radiation law. This model has been developed to describe a more *generalized* law for the luminescence from a hot carrier absorber and facilitate the determination of the carrier temperature and the quasi-Fermi level splitting of the electron-hole populations, when the system is in quasi-equilibrium. [3, 4, 5] The carrier temperature becomes the topic of interest due to the importance of hot carrier relaxation in optoelectronic devices and third generation solar cells, especially hot carrier solar cells. [6, 7, 8, 9, 10, 11, 12]

High-energy photogenerated carriers (with excess kinetic energy or higher temperature than the lattice) are referred to as hot carriers. These "hot carriers" lose their excess energy via electron-phonon interactions; typically in III-V semiconductors this occurs via the Fröhlich interaction and the emission of LO phonons. [13, 14] These LO-phonons then decay into lower energy acoustic phonons (or heat) via the Klemens [30] and/or Ridley [31] mechanisms thermalizing on a picosecond time scale. [15]

The behavior of hot carriers in system can be determined using CW and ultrafast photoluminescence spectroscopy. The various methods to extract the carrier

temperature using CW PL have been explained in Chapter 3 by implementing various forms of Planck's radiation law. As has been discussed, the simplest technique to extract the carrier temperature is by performing a linear fit on the high-energy tail of the CW PL spectrum. [7, 8, 9] However as was also discussed previously, the presence of energy levels in quantum wells complicates this analysis, especially when the separation of the confined energy levels is on the order of ($\sim k_B T$). [16, 17] Therefore, studying the effects of excitation power and lattice temperature on the absorption spectrum is important. Occupation of excited states (state filling) is probable for QWs with small energy separations ($\sim k_B T$) between the quantum states within the conduction band and/or the valence band since carriers will redistribute and occupy these higher order excited states at elevated lattice temperatures and/or high excitation powers. Under such conditions, recombination of carriers in these high-energy states will increase the luminescence and therefore broaden the high-energy tail of the PL spectrum making extraction of the carrier temperature via linear fitting problematic. This effect becomes considerable when the separation of the confined states is less than three times the full width at half maximum (FWHM) of the PL spectrum. In this scenario, the transitions from the excited states will serve to screen the physical hot carrier temperature. [16, 18]

In addition to the effects of the occupation of higher order states when extracting the carrier temperature from experimental PL, the influence of phonon-mediated processes on the shape of PL spectrum must also be considered. Phonon mediated line-width broadening has been studied both theoretically and experimentally in various materials and structures for a number of years, including in III-V quantum wells. [16, 19, 20]

The net result of occupation of excited states and/or phonon-mediated processes broadening (an increase in lattice temperature) is a decrease in the slope on the high-energy side of the PL spectrum. As a result, the carrier temperature extracted from this region – and where these mechanisms are effective – is screened and the actual temperature derived false. To investigate and demonstrate the effects of state filling and phononic broadening on carrier temperature, we have studied a high-quality InGaAsP QW structure with multiple energy levels within the conduction band with small energy separations ($\sim k_B T$). Here, the linear fitting method is applied to determine the carrier temperature and the conditions for the validity of the extracted results are studied comprehensively. Moreover, a method is discussed to improve the accuracy of the extracted carrier temperature in such systems.

4.2. Description of InGaAsP/AlInAs quantum well structure

An InGaAsP QW with a *quasi*-type-II band alignment (where the valence band is approximately degenerate) is used to study the effects of occupation of excited states and hot carrier extraction. Both a schematic and band energy diagram of the structure are shown in the Figure 4.1. The quantum well structure consists of a single $In_xGa_{1-x}As_yP_{1-y}$ QW (20 nm) (x = 0.812, y = 0.4) encapsulated with an $Al_zIn_{1-z}As$ barrier material (200 nm) (z = 0.48) grown on an n-type InP substrate ($\sim 3 \times 10^{15}\ cm^{-3}$) by metal-organic chemical vapor deposition (MOCVD). A 10 nm InP cap layer was grown on top of the structure to isolate the Al-containing compound from oxidization. However in this study, the cap layer was chemically wet etched after growth to eliminate any

effects associated with interface transitions and localized states at the interface that are known to occur between the cap layer and the barrier material. [16]

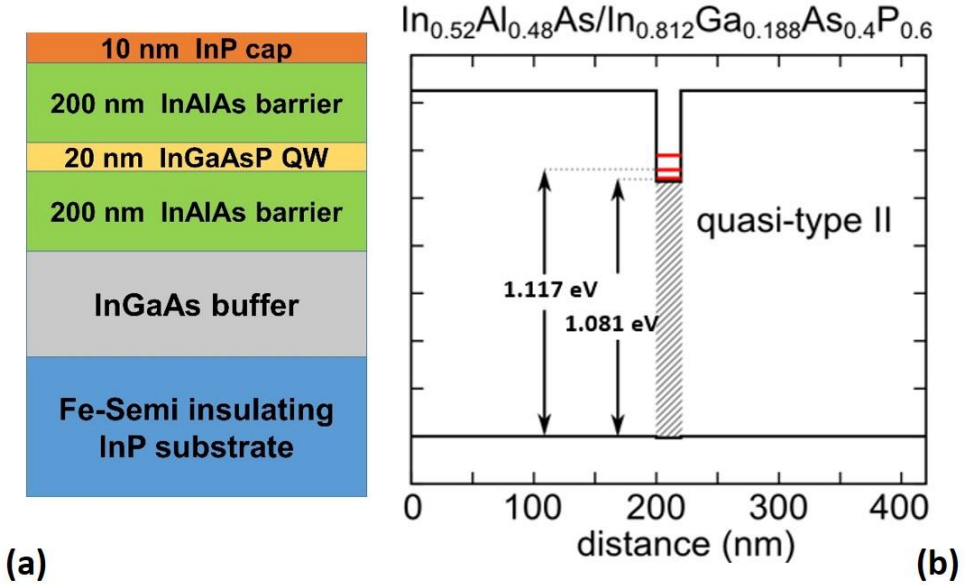

Figure 4. 1. Schematic (a) and band energy diagram (b) of the InGaAsP QW sample. [Reproduced from: Esmaielpour, H., *et al.* "Effect of occupation of the excited states and phonon broadening on the determination of the hot carrier temperature", Progress in Photovoltaics: Research and Applications 25.9 (2017): 782-790.] [16]

The energies of the confined levels within the QW were calculated using NRL Multibands® [21] and shown in Figure 4.1 (b). The ground state and first excited state energy levels are calculated at 1.081 eV and 1.117 eV, respectively. As such, the separation energy between the ground and first excited state is $\sim$ 36 meV ($\sim k_B T$). [22] Therefore, it is expected by increasing both excitation power and lattice temperature significant occupation of the higher-order states will result. The valence band offset is approximately degenerate, which is attractive for solar cell applications. The advantages

of utilizing a system that has a type-II band alignment with shallow confinement in the valence band for hot carrier solar cell applications are: the reduction in hot carrier cooling rate (thermalization rate) due to spatially separated charges and (especially for a degenerate valence band) facilitated hole transport in the system. [11, 12, 22, 23]

4.3. Experimental results and discussion for InGaAsP/AlInAs quantum well structure

4.3.1. Effects of occupation of excited states on carrier temperature determination

Continuous wave power and temperature dependent photoluminescence of the sample are measured using a He-Cd (442 nm) laser. Figure 4.2 (a) shows PL spectra of the InGaAsP QW structure at three different lattice temperatures. At 4 K, the PL spectrum is narrow. However as the lattice temperature increases, it broadens significantly. The reason for this broadening is attributed to two main effects: (1) the occupation of excited states; and (2) phonon-mediated PL line-width broadening at elevated lattice temperatures. As has been discussed, the small separation between the energy levels in the QW results in carriers redistributing amongst the excited states with increasing lattice temperature. In Figure 4.2, (above 150 K) this behavior manifests itself in a shoulder on the high-energy side of the PL spectrum. [16] As the temperature is increased to 300 K the excited state contribution increases further, as expected.

Figure 4.2 (b) shows the power dependent PL of the InGaAsP QW at 4 K. At highest excitation power (black line), the PL spectrum is symmetric. However as power

decreases, the shape of the PL spectrum changes becoming asymmetric with features on the low energy side of the PL. This additional low energy contribution to the PL is attributed to unavoidable transitions associated with localized states at the interface between InP cap and AlInAs barrier material. [24]

The power dependent PL at 4 K displays a marked blueshift in peak energy with increasing power (see Figure 4.2 (b)). Once more (in these type-II systems) the shift follows a $P^{1/3}$ power dependence, which is typical in type-II QWs. [16, 24, 25] More specifically, by solving the Hamiltonian of an infinite triangular quantum well, the ground state energy level is determined as:

$$E = (\hbar^2/2m^*)^{1/3}\left(\frac{9}{8}\pi e^2 n/\epsilon_0\epsilon_R\right)^{2/3}, \tag{4.1}$$

where $\hbar$, m^*, e, ϵ_0, ϵ_R, and n are the reduced Planck constant, effective mass, Coulomb charge, vacuum permittivity, dielectric constant, and density of electrons, respectively. Therefore, the peak energy (ground state transition) is proportional to $n^{2/3}$. Therefore, since the relationship between carrier density and excitation power is: $n \propto P^{1/2}$ the subsequent change in peak energy follows $P^{1/3}$. However, as is shown inset (i) to Figure 4.2 (b), at very low excitation powers the linear dependence between peak energy and $P^{1/3}$ is not valid. This effect is related to the distortion of the PL peak position due to the contribution of localized states. The inset (ii) in Figure 4.2 (b) shows further of the evidence of the contribution of the 1st excited state at 4 K, when the excitation power is large. [16]

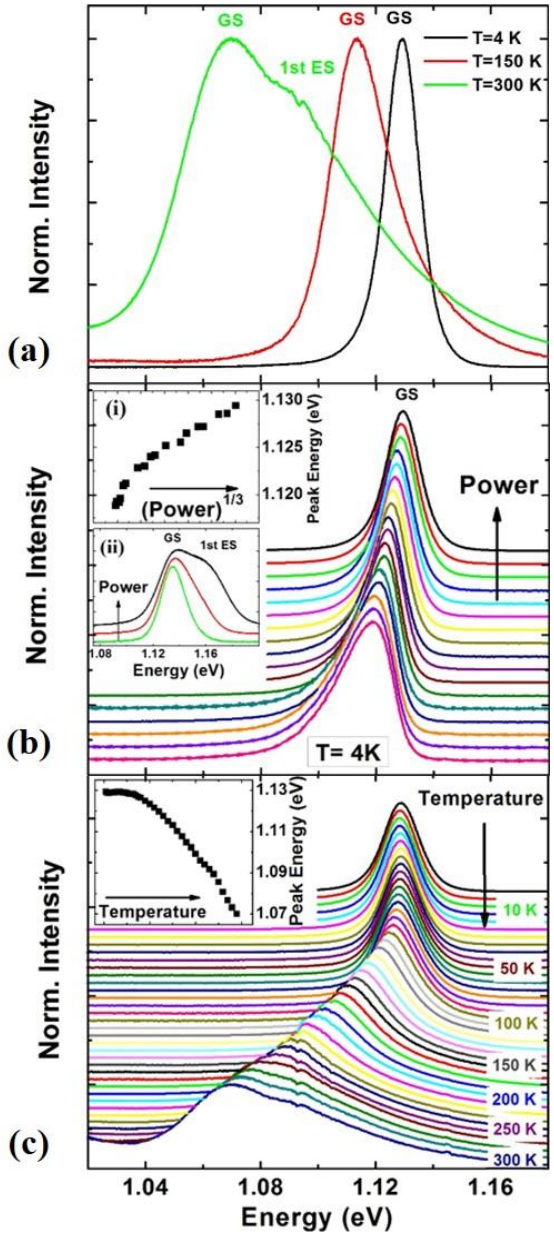

Figure 4. 2. (a) Normalized PL spectra at 4 K, 150 K and 300 K. (b) Excitation power dependent normalized PL spectra at 4 K. Insets (i) and (ii) show peak energy at 4 K versus $P^{1/3}$ and normalized PL spectra at 4 K for three excitation powers, respectively. (c) Temperature dependent normalized PL spectra. Inset shows peak energy versus lattice temperature. [Reproduced from: *Esmaielpour, H., et al. "Effect of occupation of the excited states and phonon broadening on the determination of the hot carrier temperature", Progress in Photovoltaics: Research and Applications 25.9 (2017): 782-790.*] [16]

The temperature dependent PL of the sample is shown in Figure 4.2 (c). The redshift behavior in peak energy is associated with the lattice expansion with increasing lattice temperature. Figure 4.2 (c) shows that the low temperatures PL spectrum is symmetric and with increasing lattice temperature a high-energy shoulder becomes apparent. The existence of the structure at high energy is (again) related to contribution of the excited state transitions. The inset of the Figure 4.2 (c) shows peak energy versus lattice temperature. The behavior of peak energy in this sample follows the typical Varshni-model, which is discussed in detail in Chapter 3, Section 3.3. At low temperatures ($T <$ 25 K), however, some evidence of an "s-shape" behavior is observed. As discussed in Chapter 3, Section 3.3, the origin of the "s-shape" behavior is associated with the existence of localized states, which are usually observed at low temperatures and low excitation powers, particularly in ternary and quaternary systems. [11, 26]

As has been discussed extensively in Chapter 3, Section 3.4.1, the carrier temperature can be extracted from the PL by a simple linear fit to the high energy side of the natural logarithm of PL spectrum. The experimental results can be modeled by Planck's radiation equation, [5, 7, 8, 9, 10, 11, 12]

$$I_{PL}(E) = \varepsilon(E)\ exp\left(-\frac{E}{k_B T_H}\right), \tag{4.2}$$

where $I_{PL}(E)$ is PL intensity as a function of photon energy, k_B Boltzmann constant, T_H carrier temperature and $\varepsilon(E)$ energy-dependent effective emissivity, which includes absorptivity of the sample.

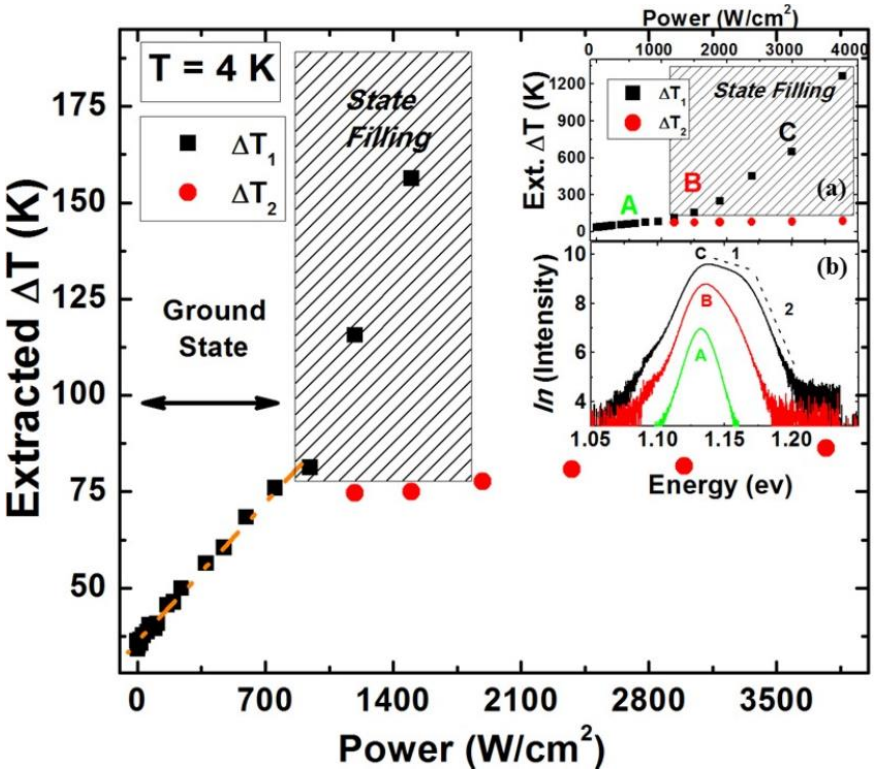

Figure 4. 3. Extracted ΔT at 4 K (through doing a linear fit) as a function of excitation power. (a) Full range of extracted ΔT versus excitation power, as shown in the main panel. (b) PL spectra at three different powers before state filling "A", transition to contribution from state filling "B" and dominant state filling effect "C". [Reproduced from: *Esmaielpour, H., et al. "Effect of occupation of the excited states and phonon broadening on the determination of the hot carrier temperature", Progress in Photovoltaics: Research and Applications 25.9 (2017): 782-790.*] [16]

Figure 4.3 shows the extracted ΔT (temperature difference between extracted temperature and lattice temperature) as a function of power at 4.2 K. With increasing power there is a linear behavior up to a ~ 1000 W/cm^2 (threshold power), then above that power two extracted temperatures are determined/required. Three PL spectra are shown in Figure 4.3 (b), the occupation of both the ground and first excited states

becomes evident with increasing excitation power (from (A) to (B) to (C)). In spectra (B) and (C) two well define slopes/regimes exist; therefore, two associated temperatures may be determined. However, it is seen that the temperature labeled T_1, (extracted from slope 1) is related to the overlap between two PL spectra (the ground state and first excited state), which increases rapidly with increasing excitation power (see Figure 4.3 (a)).

The second extracted temperature (T_2) likely represents the actual carrier temperature in the system, which is not perturbed by the occupation of higher order states as the power increases – only T_1 is. Spectrum (A) in Figure 4.3 (b) shows the PL spectrum at low excitation power, which does not display any significant effect related to a shoulder on the high-energy side of the PL spectrum.

The main panel in Figure 4.3 (a) shows the full range of extracted ΔT versus excitation power and it is observed that above the threshold power ($\sim$1000 W/cm^2) that the slope T_1 increases significantly as the excitation power increases. This increase is attributed to the conditions in which the extraction of the hot carrier temperature via the simple fitting of the high-energy slope cannot be used to determine the physical behavior of hot carriers in the ground state of the system, since the broadening reflects the contribution of the excited state luminescence. So with respect to the GS in the QW, the broadening screens the hot carrier dynamics.

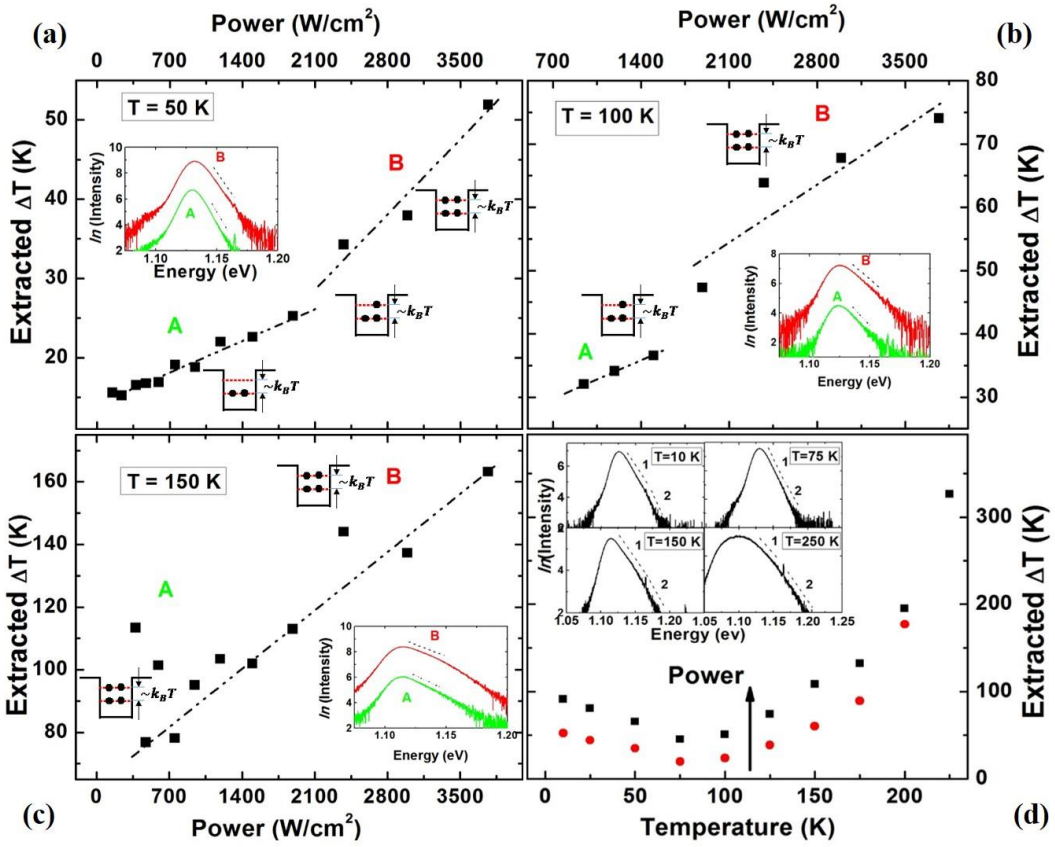

Figure 4. 4. Extracted ΔT as a function of excitation power at 50 K (a), 100 K (b) and 150 K (c). Schematic of QW in the figures represents electron populations in the ground state and first excited state at various excitation powers. (d) Extracted ΔT versus lattice temperature for two excitation power shown by black (high power) and red (low power). Insets show the PL spectra at different lattice temperatures and it is observed that there are two slopes at high energy side of PL spectrum, which result two extracted temperatures. [Reproduced from: *Esmaielpour, H., et al. "Effect of occupation of the excited states and phonon broadening on the determination of the hot carrier temperature", Progress in Photovoltaics: Research and Applications 25.9 (2017): 782-790.*] [16]

The *extracted* ΔT versus excitation power at 50 K, 100 K and 150 K are shown in Figure(s) 4.4 (a), (b) and (c), respectively. A qualitative behavior of electron populations in the ground state and first excited state is shown in Figure(s) 4.4 (a) and (b). At 50 K, when the excitation power is low, the photogenerated electrons mainly occupy the ground state in the QW. However, as the excitation power increases carriers begin to occupy the excited states. Moreover, it is observed by increasing the laser excitation power, the extracted ΔT becomes larger. It is clear that the rate of the increase in extracted ΔT can be fit with two distinct linear regimes, whose threshold power (or the inflection point) shifts to lower excitation powers as the lattice temperature increases (see Figure 4.4 (a) and (b)). This behavior is attributed to the fact that at higher lattice temperatures carriers with higher thermal energy redistribute into the excited states at lower excitation powers. This consequently lowers the threshold at which hot carrier effects are screened by the excited state luminescence in these systems. As shown in Figure 4.4 (c), there is only one slope observed at 150 K. Here, the increase of extracted ΔT has no physical meaning – the broadening due to excited state emission at this temperature occurs for all excitation powers and no longer represents the true T_{eh}. [16, 27]

Figure 4.4 (d) shows the extracted ΔT versus lattice temperature for two excitation powers: closed black squares (higher power) and closed red circles (lower power), respectively. It is observed that increasing the lattice temperature decreases ΔT up to $\sim$ 75 K, followed by an increase in ΔT thereafter. The initial reduction in ΔT is expected and is associated with phonon-mediated thermalization processes, which become more effective as the lattice temperature increases. [9] However, above 75 K the behavior is

unusual – increasing the lattice temperature increases ΔT. This behavior is related to the influence of the occupation of excited states and indicates further that: at low temperatures (and low power) the *extracted* ΔT reflects the carrier temperature in the system. However, as the lattice temperature increases it does not!

4.3.2. Effects of phonon mediated processes on carrier temperature determination

Another important mechanism, which affects accurate determination of the carrier temperature is: homogeneous photoluminescence line-width broadening. The origin of thermal broadening of the PL, $\Gamma_{tot}(T)$, has been studied theoretically by Lee *et al*. [19] and described by the following equation:

$$\Gamma_{tot}(T) = \Gamma_0 + \Gamma_{LA}T + \frac{\Gamma_{LO}}{[exp(h\omega_{LO}/k_BT)-1]} + \Gamma_{imp}exp\left[-\frac{E_B}{k_BT}\right]. \quad (4.3)$$

where Γ_0, Γ_{LA}, Γ_{LO} and Γ_{imp} are PL broadening due to: inhomogeneous broadening at 0 K, interactions with acoustic (LA) phonons, interactions with longitudinal optical (LO) phonons, and the contribution of ionized impurities scattering mechanisms, respectively. $h\omega_{LO}$ is the optical phonon energy and E_B the binding energy of the ionized impurities. [19, 20] The LO-phonon energy used for the sample is 37 meV, which is calculated by extrapolating the LO-phonon energies of InP and GaAs compounds consistent with the composition of the quaternary. [28] The binding energy of ionized impurities E_B for the InGaAsP QW structure is 16 meV, which was determined from the activation energy extracted from temperature dependent PL measurements.

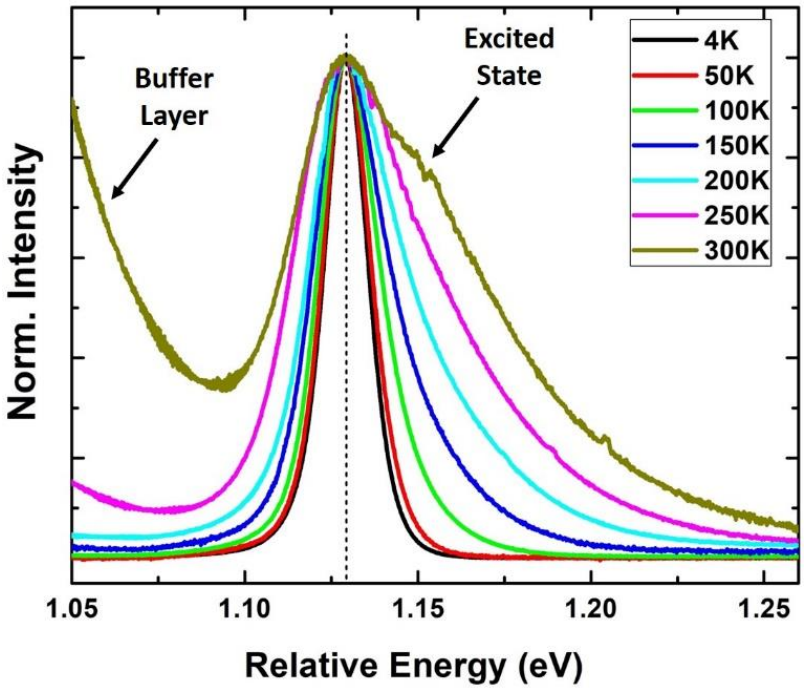

Figure 4. 5. PL spectra at a range of lattice temperatures between 4 K and 300 K. It is seen by increasing lattice temperature, the PL spectrum becomes broader, especially on the high energy side. [Reproduced from: *Esmaielpour, H., et al. "Effect of occupation of the excited states and phonon broadening on the determination of the hot carrier temperature", Progress in Photovoltaics: Research and Applications 25.9 (2017): 782-790.*] [16]

Figure 4.5 shows PL spectra at different lattice temperatures. In order to compare the PL broadening for several lattice temperatures between 4 K and 300 K, the PL spectra (T > 4.2 K) are shifted to the peak position of the 4.2 K PL spectrum (thus, the x-axis of Figure 4.5 is labeled "Relative Energy"). PL broadening due to scattering mechanisms should be symmetric on both energy sides of the PL spectrum. [19, 16, 27] However, as is shown in Figure 4.5, it is evident that the high-energy broadening of the PL spectra is larger than that of the low energy as the temperature is increased. At high energy, the PL broadening is associated with the contribution of phonons, state filling, and/or the

possible existence of hot carriers. However, the PL broadening on the low energy tail of the PL is mainly due to the presence of phonons, especially at elevated lattice temperatures. Hence, to study the PL broadening due to the intrinsic properties of the sample, the low energy side of PL spectrum is assessed.

The PL spectrum at room temperature is shown in Figure 4.5. An obvious shoulder is evident at high energy, which is (once more) related to the occupation of excited states. Also, the feature evident at low energy (particularly at higher T) is a transition associated with the InGaAs buffer layer, which is used to compensate strain from the InP substrate.

The behavior of the PL linewidth broadening as a function of lattice temperature can be determined by taking the *half width at half maximum* (HWHM) from the low energy side of the PL spectrum and plotting it versus lattice temperature. [19, 20] Figure 4.6 shows the HWHM of the PL spectra as a function of lattice temperature. The solid red line is the result of applying the theoretical model (Equation 4.3) to the extracted HWHM, and the dashed lines show the individual contribution of each scattering mechanism contributing to this model. It is seen that the temperature independent inhomogeneous broadening at T = 0 K is 7.47 meV. This set the linewidth associated with impurities and inhomogeneities in the sample. In addition, the linewidth broadening due to acoustic phonons is also small ($\sim 6\ \mu eV/K$), only contributing 1.8 meV at room temperature. This is very small when compared to the contribution of the LO-phonon Fröhlich scattering terms, which contributes $\sim$ 10 meV and is known to dominate in III-V semiconductors. [29]

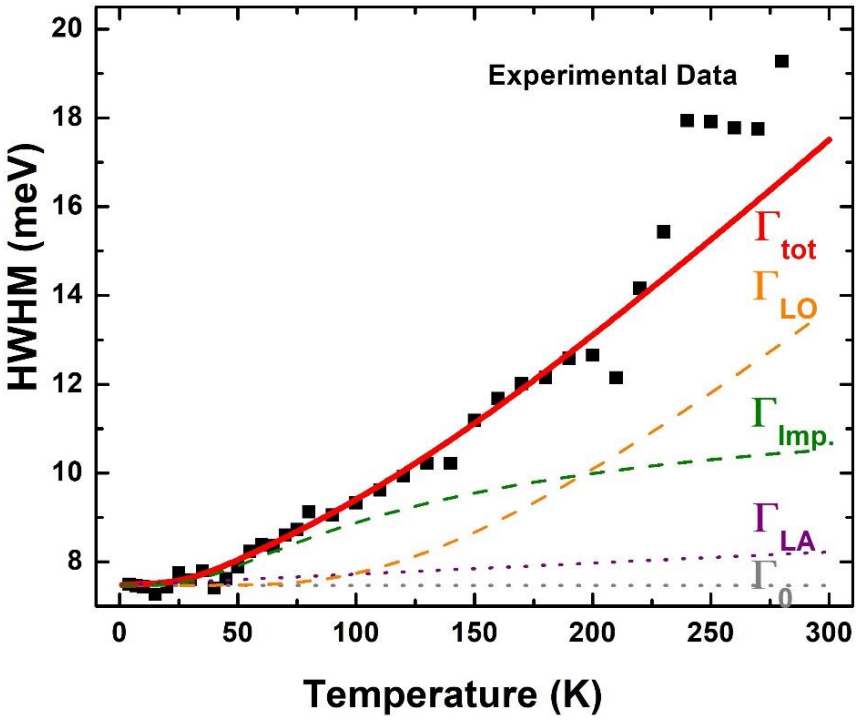

Figure 4. 6. Half width at half maximum (HWHM) of PL spectrum (black squares) at a range of temperatures between 4 K and 300 K. Solid red shows the result of fitting with theoretical model shown in Equation 4.3 and dashed lines show the individual contribution of each broadening mechanism. [Reproduced from: *Esmaielpour, H., et al. "Effect of occupation of the excited states and phonon broadening on the determination of the hot carrier temperature", Progress in Photovoltaics: Research and Applications 25.9 (2017): 782-790.*] [16]

In Figure 4.6 there is a reasonable fit between theory and experiment up to ~ 200 K. Above 200 K, it is clear that the increase of the experimental result is larger than that predicted by theory. This is attributed to the influence of the contribution of the excited states in the QW on the broadening of the PL spectrum. However, the fit can be used to qualitatively follow the effect of the linewidth broadening up to 300 K, in the absence of state filling.

At low temperatures (T < 50 K) the contribution of ionized impurities dominates the broadening, which is predominantly related to transitions at the interface between the InP cap layer and the InAlAs barrier material, and reflects the TD PL in this temperature range (see Figure 4.2 (c)). Above T ~ 50 K the increased contribution of LO dominates the broadening of PL spectrum, reflecting their role as a major source of hot carrier thermalization in III-V semiconductors. [30, 31] Table 4.1 shows the parameters extracted by fitting the experimental spectra with Equation 4.3:

Table 4. 1. Extracted values for the fitting of HWHM from experiment with theory (Equation 4.3). [Reproduced from: *Esmaielpour, H., et al. "Effect of occupation of the excited states and phonon broadening on the determination of the hot carrier temperature", Progress in Photovoltaics: Research and Applications 25.9 (2017): 782-790.*] [16]

$\boldsymbol{\Gamma_0\ (meV)}$	$\boldsymbol{\Gamma_{LA}(meV/K)}$	$\boldsymbol{\Gamma_{LO}(meV)}$	$\boldsymbol{\Gamma_{imp}(meV)}$
$\mathbf{7.47}$	6×10^{-3}	10	7.6

By fitting both the high and the low energy sides of the PL it also is possible to extract slopes, which are proportional to the extracted ΔT. Figure 4.7 shows ΔT from both the low (solid red circles) and high (solid black squares) energy sides of the temperature dependent PL spectra. As shown in Figure 4.7, there are three distinct regions: "impurity" (< 50 K); "phononic effect" (50 K < T < 200 K); and "state filling" (> 200 K). The reason for this designation is related to the dominant PL broadening mechanisms within different temperature ranges assessed.

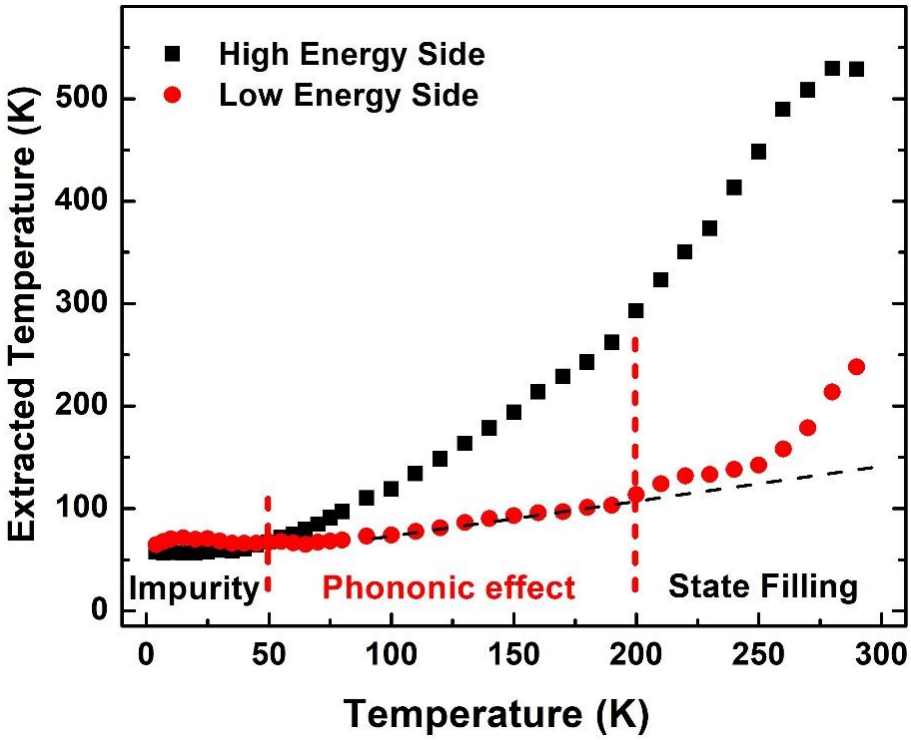

Figure 4. 7. Extracted ΔT from both high and low energy sides of PL spectrum as a function of lattice temperature. [Reproduced from: *Esmaielpour, H., et al. "Effect of occupation of the excited states and phonon broadening on the determination of the hot carrier temperature", Progress in Photovoltaics: Research and Applications 25.9 (2017): 782-790.*] [16]

At lattice temperatures above 50 K, the rate of increase in extracted ΔT on the high energy side is larger than that on the low energy side (see Figure 4.7). The reason for this behavior is attributed to the influence of several mechanisms such as: phonon mediated broadening, the existence of hot carriers, and/or the occupation of excited states (especially > 200 K). However, the increase in extracted temperature from the low energy side (in addition to the contribution of the temperature independent inhomogeneous broadening) is due only to the contribution of phonons below 200 K

(when there is no influence from the buffer transition). Therefore, the contribution of phonon mediated broadening on the low energy side can be subtracted from ΔT on the high energy side of the spectra to adjustment the extracted value and produce a more accurate determination of the hot carrier temperature. In order to do this analysis, it is required to define a reference value. It is known that at low temperature (4.2 K) the PL broadening due to phonon processes is negligible. [19] Therefore, it is possible to determine the relative linewidth broadening at higher lattice temperatures by comparing it with the reference (inhomogeneous term) at the lowest temperature. [16, 27]

Figure 4.7 shows that above 200 K the extracted temperature (from the low energy side of PL spectrum) does not follow a linear dependence, except between 50 K and 200 K. The reason for this discrepancy is once more the influence of the occupation of the excited states at elevated lattice temperatures. However, this linear fit is extended up to room temperature to show how the extracted temperature is expected to change in the absence of screening due to the thermal redistribution of carriers into to higher order states in the QW. In addition, it is evident in Figure 4.7 that the temperature extracted follows a non-linear dependence below 50 K, which is again associated with the effects of localization at lower temperatures. A linear dependence in the carrier temperature as extracted from the low energy side of the PL is evident when phonon-mediated processes are substantial and dominate in PL linewidth, i.e. $T > 100$ K (see Figure 4.6).

Figure 4.8 shows the extracted ΔT as a function of lattice temperature with and without adjusting the effects of linewidth broadening. The inset of this figure shows a magnified region between 50 K and 200 K where the effect of linewidth broadening due to phonons dominates. A comparison between the solid and empty squares indicates that the shape

of the extracted ΔT versus lattice temperature is conserved. However, the minima of the adjusted data (empty squares) has shifted towards higher lattice temperatures (100 K). Moreover, excluding the phononic temperature causes the extracted ΔT to become shallower, which is observed clearly in the magnified response shown in the inset in Figure 4.8. [16, 27]

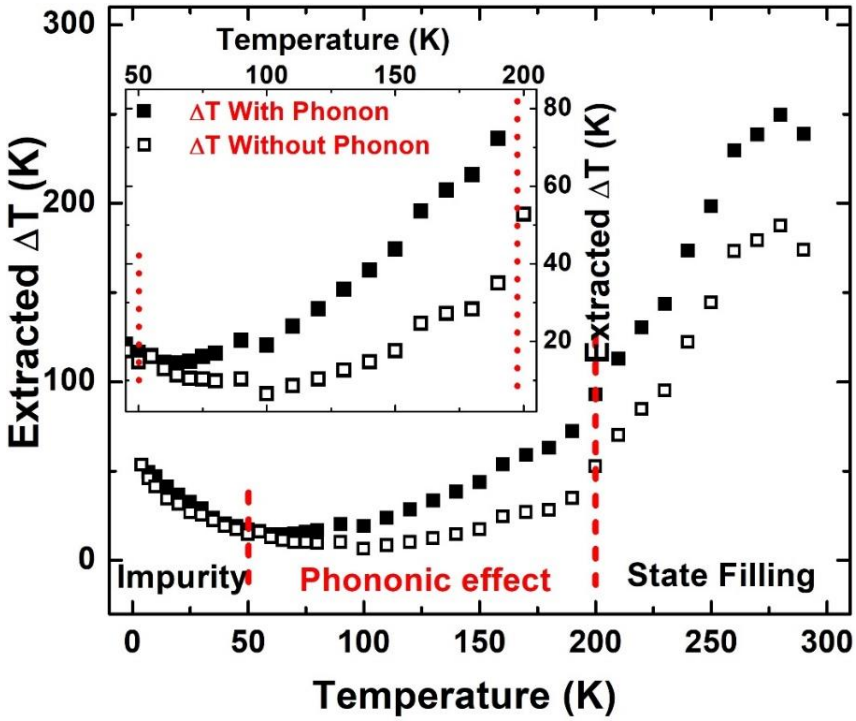

Figure 4. 8. Extracted ΔT versus lattice temperature from 4 K to room temperature. Inset shows the zoom in region between 50 K and 200 K of the data in the main panel. Solid and hollow squares show extracted ΔT before and after adjusting with phononic broadening. [Reproduced from: *Esmaielpour, H., et al. "Effect of occupation of the excited states and phonon broadening on the determination of the hot carrier temperature", Progress in Photovoltaics: Research and Applications 25.9 (2017): 782-790.*] [16]

To summarize, in this section, the effects of occupation of excited states and linewidth broadening in the determination of carrier temperature have been assessed. It is observed when a shoulder due to state filling effects are evident on the high-energy tail of the PL spectrum, the temperature extracted by a simple linear fit is larger than the actual "hot" carrier temperature. The TD PL linewidth broadening is split into three distinct regimes: impurities related below 50 K, phonon-mediated in the window 50 K to 200 K, and one dominated by higher order state filling above 200 K. These contributions demonstrate the care that must be taken when using a simple linear fit (based on the generalized Planck equation) of the high-energy tail of the PL; particularly, in low dimensional systems where occupation of the excited states and phonon broadening must be considered.

4.4. Effects of degeneracy of the valence band in *deep* type-II InAs/AlAsSb quantum wells

So far, the discussion has revolved around: how occupation of excited states and line-width broadening can affect the determination of carrier temperature for structures with closely spaced energy levels. Figure 4.9 (a) shows power dependent PL spectra of a type-II InAs/AlAsSb MQW at 300 K. The InAs MQW structure investigated in this thesis has a large separation of energy levels within the QW conduction band ($\sim 655\, meV$). [11, 12] Therefore, transitions due to first excited state in the QW structure are not thought to significantly contribute to the PL spectrum (see Figure 4.9 (a)). However, in addition to confined states in the QW, the valence band degeneracy

must be considered; particularly, in this system where mobile holes redistribute throughout the valence band, especially at higher temperatures.

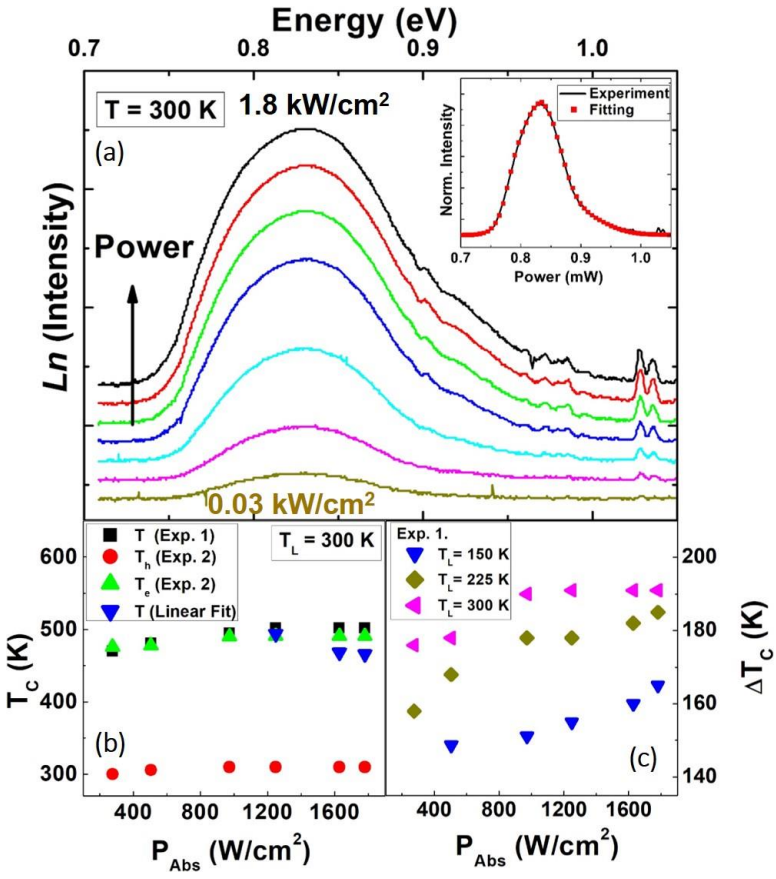

Figure 4. 9. (a) Excitation power dependent natural logarithm of PL spectrum at 300 K for InAs MQW. Inset shows an example of fitting the whole PL spectrum applying equilibrium generalized Planck's radiation law. (b) Comparison of extracted carrier temperature versus excitation power using equilibrium generalized Planck's law (black squares), non-equilibrium generalized Planck's law (red circles for holes and green triangles for electrons) and the high energy side linear fitting (blue triangles). (c) Extracted ΔT applying linear fitting for various lattice temperatures (150 K, 225 K and 300 K). [Reproduced from: *Whiteside, Vincent R., et al. "Valence band states in an InAs/AlAsSb multi-quantum well hot carrier absorber." Semiconductor Science and Technology (2018).*] [18]

Previously three methods for extracting the carrier temperature were described, comparing the three methods demonstrates that ΔE for e1-e2 is large and the contribution for state filling is expected to be negligible within the linewidth of the PL spectrum. However, structure in the PL spectrum around the peak energy indicates other effects may contribute to the linewidth of the PL in this system. The carrier temperature versus excitation power is plotted in Figure 4.9 (b). To determine the carrier temperature, the three methods proposed in Equations 3.1, 3.3, and 3.4 have been applied. As shown in Figure 4.9 (b), electrons (closed green triangles) are at an elevated temperature with respect to the lattice, while the holes (closed red circles) thermalize rapidly due to their large(r) effective mass as compared to electrons ($\frac{m_h}{m_e} \approx 50$). [32] Figure 4.9 (c) shows carrier temperature extracted through doing the linear fit method for three lattice temperatures 150 K (blue), 225 K (olive) and 300 K (magenta). Notably, it is observed there is an increase in hot carrier temperature at higher lattice temperatures, which is again attributed to the spatial separation of photogenerated charges and delocalization of holes from the shallow confinement within the valence band. [11, 12, 18, 23]

Despite the apparent absence of excited state occupation in InAs QWs, it has been shown (when the QW structure was pumped with high excitation power) subtle features are evident in the PL spectra resulting in a "flattening" around the PL peak. To better understand the origin of this behavior, simulations for the QW structure were performed using NRL MultiBands®.

In this program, the band structure of a periodic multilayer design is calculated via $k \cdot p$ theory. Through this analysis, the information for creating an effective medium for

the superlattice structure is provided/defined. The simulated effective medium provides useful information about the superlattice structure utilizing optical matrix elements. In the simulation, the largest probability of s-like and p_z-like characteristics of hole energy levels is for light holes due to their sp3 hybridization, while heavy holes in the valence band behave more p_x-like and p_y-like. Through this simulation, it is possible to determine the probability of transitions from individual valence band energy levels (lh_1, hh_1, hh_2, and hh_3) to conduction band states. [21]

Figure 4.10 (a) shows a single InAs quantum well with associated energy levels at 4 K and 300 K for both the conduction and valence bands, respectively. In the simulation, the AlAsSb band gap is calculated based on the *direct* gamma conduction band minima (2.2 eV at 300 K). The indirect band gap of $AlAs_{0.16}Sb_{0.84}$ material (~ 1.6 eV at 300 K) is not considered for calculations due to its small absorption coefficient, especially for the relatively thin layers used here (10 nm). The conduction band offset (CBO) determined for the QW structure is ~ 1.95 eV at 4 K, which shrinks by ~ 25 meV at 300 K. The valence band offset (VBO) at 4 K is ~ 63 meV and there is a negligible contraction ($\sim 1\, meV$) up to 300 K, due to the large effective mass of holes in the valence band. In addition, the energy separation between the ground state in the InAs QW (e1) and the valence band ground state (hh1) is ~ 857 meV at 4 K.

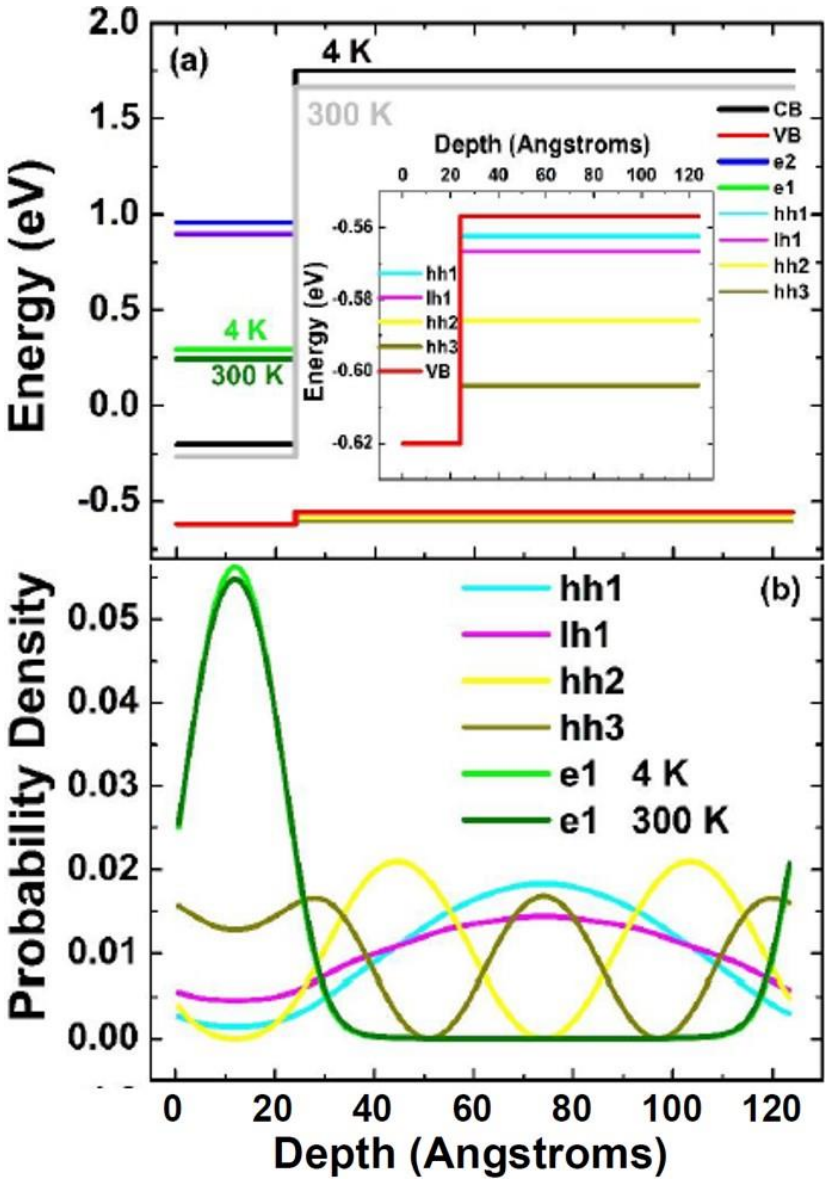

Figure 4. 10. (a) Band energy diagram of InAs QW structure at 4 K and 300 K. Inset shows a zoom in of the valence band diagram. (b) Probability density of the wavefunctions of electrons and holes associated with energy levels (a) in the conduction and valence bands in the QW structure are shown by different colors. [Reproduced from: *Whiteside, Vincent R., et al. "Valence band states in an InAs/AlAsSb multi-quantum well hot carrier absorber." Semiconductor Science and Technology (2018).*] [18]

Figure 4.10 (a) shows the simulated band diagram in the QW and includes two energy levels (e1 and e2) within the InAs conduction band with an energy separation of 685 meV at 4 K. In the valence band, four energy levels are observed (hh1, lh1, hh2 and hh3), as shown in the inset of Figure 4.10 (a), where the energy separation between the lowest and highest energy levels ~ 31 meV. Figure 4.10 (b) shows the associated probability density of the wavefunctions of the electrons and holes for these individual energy levels (shown in 4.10 (a)). It is observed that the wavefunctions of the electrons in the ground and first excited states penetrate significantly into the AlAsSb barriers, and have non-negligible overlap with the wavefunctions of the holes. This overlap in the narrow quantum wells investigated (2.4 nm InAs QW) serves to relax some of the optical selection rules, making transitions from e1 to hh2, which are typically forbidden, possible. [18]

Figure 4.10 (b) indicates that the largest penetration of hole wavefunctions (largest probability) in the InAs QW is for hh3 and the lowest for the hh2 level. Although light and heavy holes have different characteristics, the results show a transition between e1 to both light and heavy holes states is probable in this structure. The least probable transition is associated with e1-hh2 since the hh2 wavefunction has a zero minima at the QW region – see Figure 4.10 (b).

Figure 4.11 shows the dispersion relation for all energy levels in the QW structure in momentum space. The left hand side of the graph is plotted against k_z (growth direction) and the right hand side is the in-plane axis, $k_{x,y}$. The inset of Figure 4.11 is the expanded dispersion in the valence band. As shown in the inset, there is structure in the valence band dispersion at "k" values larger than zero and as discussed later, these create optical

transitions that are responsible for high energy features evident in the absorption profiles, shown in Figure 4.12. [18]

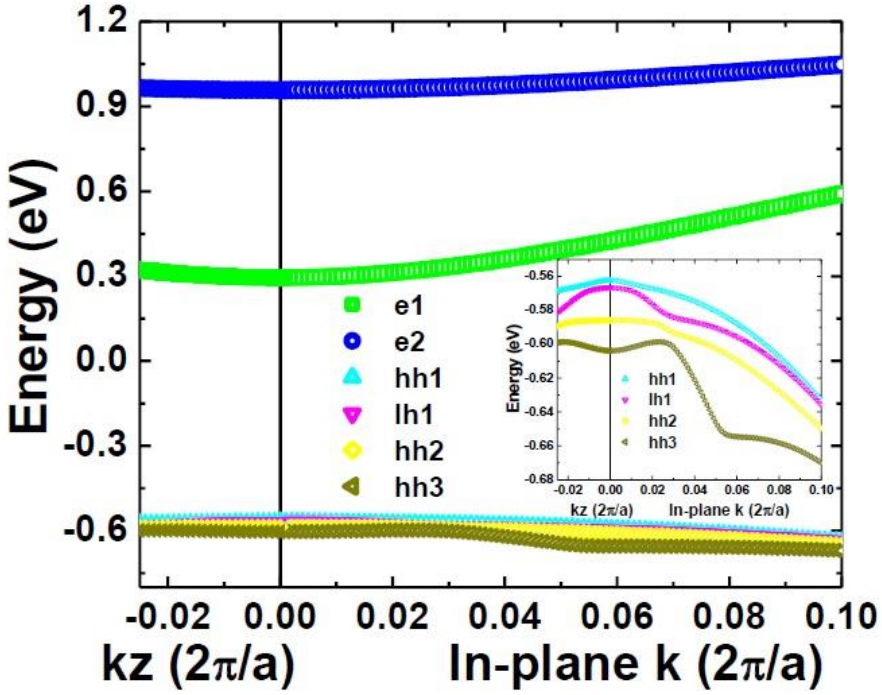

Figure 4. 11. Dispersion relation of InAs QW structure for multiple energy levels as a function of in-plane and out of plane wavenumbers. Inset shows a zoomed in region for the valence band dispersion relation. [Reproduced from: *Whiteside, Vincent R., et al. "Valence band states in an InAs/AlAsSb multi-quantum well hot carrier absorber." Semiconductor Science and Technology (2018).*] [18]

Figure 4.12 (a) and (b) show the simulated photogenerated carrier recombination or PL spectra (dotted squares) and absorption (solid lines) profiles of the QW structure at several lattice temperatures for two excitation powers. It is observed that by the increasing lattice temperature, a redshift in peak position is evident as expected due to thermal expansion of the lattice. In addition, there are four distinct peaks in the absorption profiles (p_1, p_2, p_3 and p_4). The first peak, p_1, has energy value of 0.805 eV

at room temperature, which is attributed to the transition between e1 to hh1. The simulated value is similar to the experiment value of 0.8 eV at room temperature. The energy separation between p_2-p_1, p_3-p_2 and p_4-p_3 in the absorption profiles are 31 meV, 77 meV and 91 meV, respectively. Based on the above values, the second peak (p_2) in the absorption profile is attributed to the e1-hh3 transition, and the higher energy peaks are related to absorption due to the non-zero momentum values, as evident in the inset to Figure 4.11. [18]

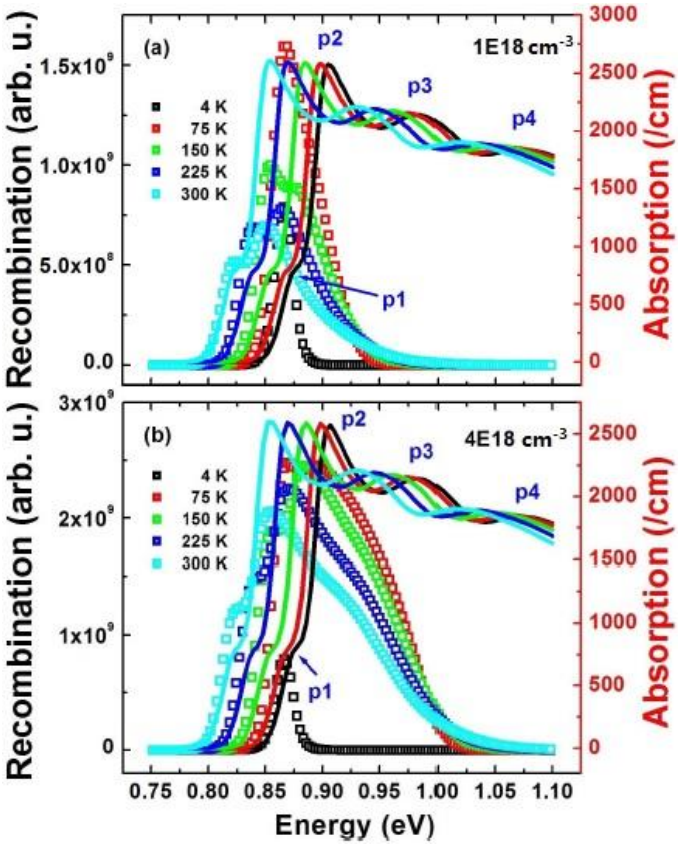

Figure 4. 12. Recombination (hollow squares) and absorption (solid lines) profiles for InAs MQW structure at various lattice temperatures for two carrier densities simulated: (a) $1 \times 10^{18} cm^{-3}$ and (b) $4 \times 10^{18} cm^{-3}$. [Reproduced from: *Whiteside, Vincent R., et al. "Valence band states in an InAs/AlAsSb multi-quantum well hot carrier absorber." Semiconductor Science and Technology (2018).*] [18]

In Figure 4.12 (a), two distinct peaks are observed in the simulated charge recombination spectra at temperatures above 75 K. These two peaks are related to the p_1 (e1-hh1) and p_2 (e1-hh3) transitions, respectively. By increasing the lattice temperature $\geq$150 K, a further feature is evident on the high-energy side of the recombination spectra, which is related to the higher energy transition, p_3. However at 4 K, the simulated recombination spectrum only displays one peak, which indicates that at low temperatures transitions from excited states in the valence band are negligible. Figure 4.12 (b) shows the simulated results for recombination mechanisms at higher excitation powers than in panel (a). At high excitation power, as shown in Figure 4.12 (b), occupation of the excited states becomes more significant as compared with that at lower excitation power (see panel (a)), especially at elevated lattice temperatures.

Figure 4.13 (a) shows simulated power dependent recombination (PL) at 150 K. It is observed that by increasing the excitation power, transitions due to the excited states become more apparent. The solid red line in Figure 4.13 (a) shows the absorption profile of the sample where optical transitions due to the excited states occur. It is evident that at higher excitation powers the peak intensity of p_2 is larger than the first peak p_1. Moreover, at higher lattice temperatures occupation of the excited states (peak P_2 associated with e1-hh3 transition) occurs at lower powers, which indicates carriers require less energy to start this process.

Figure 4.13 (b) shows the peak energy as a function of lattice temperature for both the absorption and recombination spectra, which both decrease following the thermal expansion of the lattice. [33] In this Figure, the solid and hollow symbols are the peak energy positions for the absorption and recombination spectra, respectively. The

simulated absorption spectra show transitions associated with multiple states at all lattice temperatures. However, only at higher lattice temperatures and excitation powers (which are at least two orders of magnitude larger than the highest power measured PL) do the features due to these transitions arise in the recombination spectra.

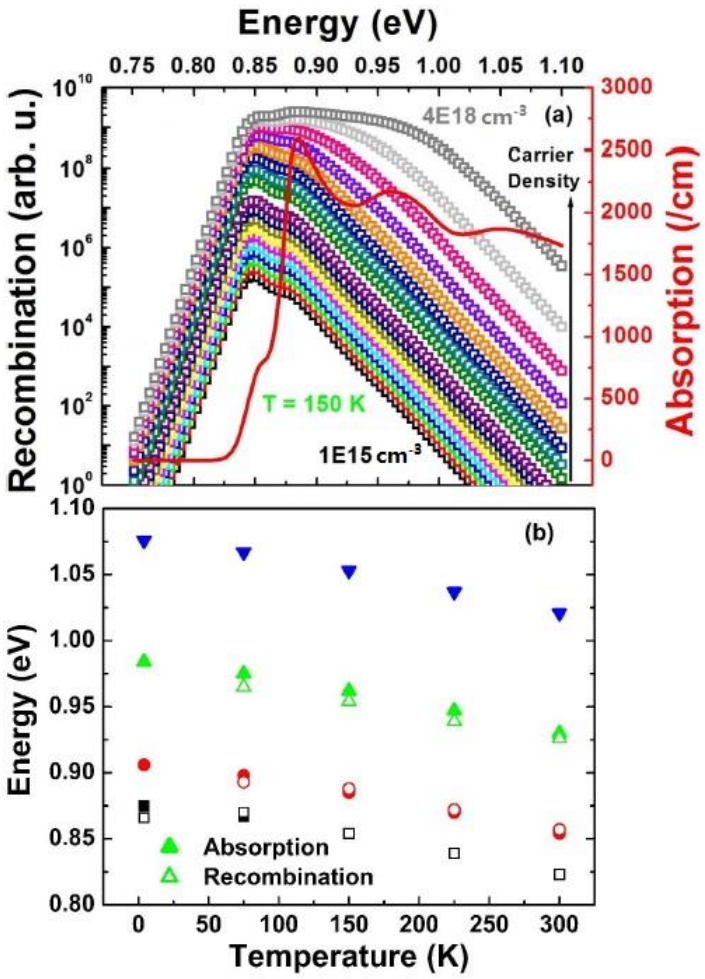

Figure 4. 13. (a) Simulated photogenerated carrier recombination (hollow squares) and simulated absorption (solid red line) profile of InAs MQW structure at 150 K as a function of carrier density. (b) Peak energy versus lattice temperature for absorption (solid dots) and recombination (hollow dots) extracted from simulation results of temperature dependent study. [Reproduced from: *Whiteside, Vincent R., et al. "Valence band states in an InAs/AlAsSb multi-quantum well hot carrier absorber." Semiconductor Science and Technology (2018).*] [18]

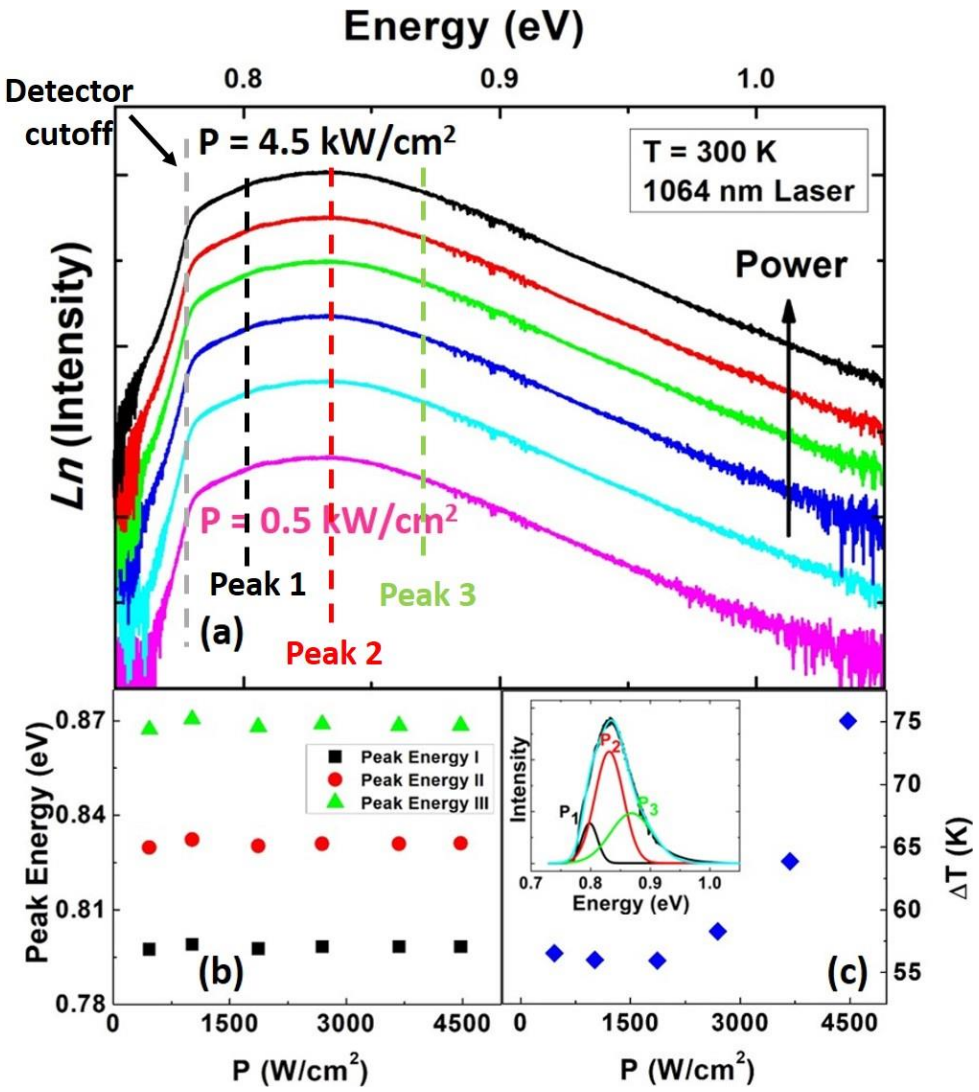

Figure 4. 14. (a) Excitation power dependent natural logarithm PL spectra at 300. Black, Red, and green dashed lines show peak positions of three Gaussian fitting. The gray dashed line shows the position of the detector's cutoff energy. (b) Peak energy extracted from Gaussian fitting versus absorbed power density. (c) Extracted ΔT applying linear fit versus absorbed power. Inset shows an example of Gaussian fitting on the PL spectrum. [Reproduced from: *Whiteside, Vincent R., et al. "Valence band states in an InAs/AlAsSb multi-quantum well hot carrier absorber." Semiconductor Science and Technology (2018).*] [18]

Figure 4.14 (a) shows natural logarithm of *measured* PL intensity at 300 K for various excitation powers. It is observed the slope at low energy side (below 0.78 eV) drops abruptly, which is related to the cut-off of the utilized InGaAs array detector in the system used. On the high energy side, the slope has a strong linear dependence (which improves the accuracy of the fit for carrier temperature) and it becomes shallower at higher excitation powers. As shown in Figure 4.14 (c), the extracted ΔT is essentially independent of power, even though the carriers are "hot" – i.e., show temperature in excess of the lattice temperature. Through Gaussian fitting (as shown in inset of Figure 4.14 (c)) it is possible to extract multiple peaks associated with the transitions in the system. Figure 4.14 (b) shows the peak energy versus excitation power. It is evident that there are three main transitions in the PL spectra where the main peak is at 798 meV and the separations of the main peak with second and third peaks are 33 meV and 37 meV, respectively. [18]

The simulated carrier recombination at 300 K (see Figure(s) 4.12 (a) and (b)) shows the dominant peak is 805 meV (the e1-hh1 transition) and the separation of two other peaks from the main peak are 31 meV, 110 meV, respectively. By comparing the experimental and simulation results, it is evident that the first peak P_1 (dominant peak) is associated with the transition from e1 to hh1, however there is a small difference between experiment and simulation ($\sim 7\ meV$; 798 meV from the experiment compared with 805 meV form the simulation). Based on simulations, the second peak P_2 on the high-energy side of the PL spectrum is associated with the transition from e1 to hh3, which is consistent with an energy separation between ($P_2 - P_1$) of 33 meV, which is very close to the simulation result (31 meV). [18]

The third peak P_3 in simulation has an energy separation of 77 meV from P_2 (or 110 meV from the ground state), which is larger than the valence offset in the QW structure (63 meV). As mentioned previously, this transition as predicted by simulation may be due to structure with higher k-values (see the inset of Figure 4.11). However, since a limited number of energy levels are included in the model for the valence band, the simulated for P_3 and P_4 features should be considered carefully. The separation energy between the third and second peaks ($P_3 - P_2$) extracted from the Gaussian fit of the experimental results is ~ 37 meV, which is less than the simulated energy separation between the second and third peaks. The third peak P_3 in experimental results is related to the direct transition from e1 to the valence band of the InAs QW, which is also not considered in NRL MultiBands®. The difference in energy between P_2 and the InAs valence band is ~ 26 meV, as shown in the inset of Figure 4.10 (a). Although this value is less than the energy separation between the third and second peaks in the experiment, adjusting the valence band offset by 7 meV (the difference between experiment and simulated results for the dominant peak P_1) results in an energy difference of ~ 33 meV – which is closer to the experimental results. [18] Here the comparison between experiment and theory indicate the contribution of multiple transitions related to the valence band states contribute significantly to the structure of the PL spectrum. However, despite the contribution of these closely separated valence band states, their effect on T_{eh} extraction is negligible – as the structure is outside of the linear portion on the high energy side with respect to the natural logarithm of the PL intensity.

Conclusion

In this chapter, the effects of the occupation of the excited states in QW structures and phonon-mediated PL linewidth broadening on the determination of the carrier temperature from CW PL are presented. Specifically, an $In_{0.812}Ga_{0.188}As_{0.4}P_{0.6}$ / $Al_{0.48}In_{0.52}As$ QW structure with small energy level separation between in the confined states was investigated to study the effects of state filling, in addition to phonon broadening, on determination of carrier temperature. Increasing the laser excitation power produced a shoulder on the high-energy side of the emitted PL, which was attributed to the occupation of the first excited state. This allowed analysis of the system when the PL was broadened due to the redistribution of carriers into the high order states; as well as, to determine the issues that arise when extracting the carrier temperature from linear fitting in this regime.

In addition, temperature dependent PL linewidth broadening of the InGaAsP QW structure was assessed and the results correlated with a theoretical model to evaluate the contribution of the potential various linewidth broadening mechanisms. It was observed that at low temperature localized states at the interface between the preexisting InP cap and AlAsSb barrier material dominant the PL linewidth. However, as the lattice temperature increases, broadening due to LO-phonon processes increases, especially above 150 K. Above 200 K, the influence of excited state occupation in the QW becomes significant distorting the correlation between the theoretical model and experimental data. Between 50 K and 200 K, where the contribution of broadening due to phonons is dominant, it is possible to accurately determine the thermal broadening due to phonons (without screening of these effects due to the contribution of localized

or confined states). By subtracting these phononic effects from the extracted carrier temperature a better estimation of the hot carrier temperature can therefore be determined.

Finally, the effect of occupation of the degeneracy in the valence band states in deep type-II InAs/AlAsSb QWs in PL emission on the determination of carrier temperature was also studied. It was evident that at elevated lattice temperatures – when excitation power increases – the contribution of mixed valence band states become more prevalent. Both the experimental and simulation results confirm that at elevated lattice temperatures, transitions due to higher order valence band states occur and affect the PL line shape, particularly around the peak PL energy. However, despite these effects, their effect on the carrier temperature extraction is negligible. This hypothesis is supported through comparing the extracted carrier temperatures using three different methods for the InAs MQW structure and by simulations using NRL MultiBands®.

References

[1] Gfroerer, Timothy H. "Photoluminescence in analysis of surfaces and interfaces." Encyclopedia of analytical chemistry: applications, theory and instrumentation (2006).

[2] Pankove, Jacques I. Optical processes in semiconductors. Courier Corporation, 1975.

[3] Lasher, Gordon, and Frank Stern. "Spontaneous and stimulated recombination radiation in semiconductors." Physical Review 133, no. 2A (1964): A553.

[4] De Vos, A., and H. Pauwels. "On the thermodynamic limit of photovoltaic energy conversion." Applied physics 25, no. 2 (1981): 119-125.

[5] Wurfel, Peter. "The chemical potential of radiation." Journal of Physics C: Solid State Physics 15, no. 18 (1982): 3967.

[6] Ross, Robert T., and Arthur J. Nozik. "Efficiency of hot-carrier solar energy converters." Journal of Applied Physics 53, no. 5 (1982): 3813-3818.

[7] Shah, Jagdeep. "Hot carriers in quasi-2-D polar semiconductors." IEEE Journal of Quantum electronics 22, no. 9 (1986): 1728-1743.

[8] Conibeer, Gavin, Nicholas Ekins-Daukes, Jean-François Guillemoles, Dirk Kőnig, Eun-Chel Cho, Chu-Wei Jiang, Santosh Shrestha, and Martin Green. "Progress on hot carrier cells." Solar Energy Materials and Solar Cells 93, no. 6-7 (2009): 713-719.

[9] Le Bris, A., L. Lombez, S. Laribi, G. Boissier, P. Christol, and J-F. Guillemoles. "Thermalisation rate study of GaSb-based heterostructures by continuous wave photoluminescence and their potential as hot carrier solar cell absorbers." Energy & Environmental Science 5, no. 3 (2012): 6225-6232.

[10] Hirst, Louise C., Hiromasa Fujii, Yunpeng Wang, Masakazu Sugiyama, and Nicholas J. Ekins-Daukes. "Hot carriers in quantum wells for photovoltaic efficiency enhancement." IEEE Journal of Photovoltaics 4, no. 1 (2014): 244-252.

[11] Tang, J., V. R. Whiteside, H. Esmaielpour, S. Vijeyaragunathan, T. D. Mishima, M. B. Santos, and I. R. Sellers. "Effects of localization on hot carriers in InAs/$AlAs_xSb_{1-x}$ quantum wells." Applied Physics Letters 106, no. 6 (2015): 061902.

[12] Esmaielpour, Hamidreza, Vincent R. Whiteside, Jinfeng Tang, Sangeetha Vijeyaragunathan, Tetsuya D. Mishima, Shayne Cairns, Michael B. Santos, Bin Wang, and Ian R. Sellers. "Suppression of phonon-mediated hot carrier relaxation in type-II InAs/ $AlAs_xSb_{1-x}$ quantum wells: a practical route to hot carrier solar cells." Progress in Photovoltaics: Research and Applications 24, no. 5 (2016): 591-599.

[13] Fröhlich, Herbert, Hans Pelzer, and Sigurd Zienau. "XX. Properties of slow electrons in polar materials." The London, Edinburgh, and Dublin Philosophical Magazine and Journal of Science 41, no. 314 (1950): 221-242.

[14] Zhang, X. B., Thierry Taliercio, S. Kolliakos, and Pierre Lefebvre. "Influence of electron-phonon interaction on the optical properties of III nitride semiconductors." Journal of Physics: Condensed Matter 13, no. 32 (2001): 7053.

[15] Shah, Jagdeep. Hot carriers in semiconductor nanostructures: Physics and applications. Elsevier, 2012.

[16] Esmaielpour, Hamidreza, Vincent R. Whiteside, Louise C. Hirst, Joseph G. Tischler, Chase T. Ellis, Matthew P. Lumb, David V. Forbes, Robert J. Walters, and Ian R. Sellers. "Effect of occupation of the excited states and phonon broadening on the determination of the hot carrier temperature from continuous wave photoluminescence in InGaAsP quantum well absorbers." Progress in Photovoltaics: Research and Applications 25, no. 9 (2017): 782-790.

[17] Heitz, R., A. Kalburge, Q. Xie, M. Grundmann, P. Chen, A. Hoffmann, A. Madhukar, and D. Bimberg. "Excited states and energy relaxation in stacked InAs/GaAs quantum dots." Physical Review B 57, no. 15 (1998): 9050.

[18] Whiteside, Vincent R., Brenden A. Magill, Matthew P. Lumb, Hamidreza Esmaielpour, Michael A. Meeker, Rathsara RHH Mudiyanselage, Adrien Messager *et al.* "Valence band states in an InAs/AlAsSb multi-quantum well hot carrier absorber." Semiconductor Science and Technology (2018).

[19] Lee, Johnson, Emil S. Koteles, and M. O. Vassell. "Luminescence linewidths of excitons in GaAs quantum wells below 150 K." Physical Review B 33, no. 8 (1986): 5512.

[20] Veliadis, J. V. D., J. B. Khurgin, Y. J. Ding, A. G. Cui, and D. S. Katzer. "Investigation of the photoluminescence-linewidth broadening in periodic multiple narrow asymmetric coupled quantum wells." Physical Review B 50, no. 7 (1994): 4463.

[21] Lumb, Matthew P., Igor Vurgaftman, Chaffra A. Affouda, Jerry R. Meyer, Edward H. Aifer, and Robert J. Walters. "Quantum wells and superlattices for III-V photovoltaics and photodetectors." In Next Generation (Nano) Photonic and Cell Technologies for Solar Energy Conversion III, vol. 8471, p. 84710A. International Society for Optics and Photonics, 2012.

[22] Hirst, Louise C., Michael K. Yakes, Chaffra A. Affouda, Christopher G. Bailey, Joseph G. Tischler, Hamidreza Esmaielpour, Vincent R. Whiteside *et al.* "Hot-carrier effects in type II heterostructures." In 2015 IEEE 42nd Photovoltaic Specialist Conference (PVSC), pp. 1-3. IEEE, 2015.

[23] Esmaielpour, Hamidreza, Vincent R. Whiteside, Herath P. Piyathilaka, Sangeetha Vijeyaragunathan, Bin Wang, Echo Adcock-Smith, Kenneth P. Roberts *et al.* "Enhanced hot electron lifetimes in quantum wells with inhibited phonon coupling." Scientific reports 8, no. 1 (2018): 12473.

[24] Esmaielpour, Hamidreza, Vincent R. Whiteside, Louise C. Hirst, Joseph G. Tischler, Robert J. Walters, and Ian R. Sellers. "The effect of an InP cap layer on the photoluminescence of an $In_xGa_{1-x}As_{1-y}P_y/In_zAl_{1-z}As$ quantum well heterostructure." Journal of Applied Physics 121, no. 23 (2017): 235301.

[25] Weisbuch, Claude, and Borge Vinter. Quantum semiconductor structures: fundamentals and applications. Elsevier, 2014.

[26] Nuytten, Thomas, Manus Hayne, Bhavtosh Bansal, H. Y. Liu, Mark Hopkinson, and Victor V. Moshchalkov. "Charge separation and temperature-induced carrier migration in $Ga_{1-x}In_xN_yAs_{1-y}$ multiple quantum wells." Physical Review B 84, no. 4 (2011): 045302.

[27] Esmaielpour, Hamidreza, Vincent R. Whiteside, Louise C. Hirst, Joseph G. Tischler, Robert J. Walters, and Ian R. Sellers. "The effect of excited state occupation and phonon broadening in the determination of the non-equilibrium hot-carrier temperature in InGaAsP quantum-well absorbers (Conference Presentation)." In Physics, Simulation, and Photonic Engineering of Photovoltaic Devices VII, vol. 10527, p. 1052706. International Society for Optics and Photonics, 2018.

[28] http://www.ioffe.ru/SVA/NSM/Semicond/

[29] Fröhlich, Herbert, Hans Pelzer, and Sigurd Zienau. "XX. Properties of slow electrons in polar materials." The London, Edinburgh, and Dublin Philosophical Magazine and Journal of Science 41, no. 314 (1950): 221-242.

[30] Klemens, P. G. "Anharmonic decay of optical phonons." Physical Review 148, no. 2 (1966): 845.

[31] Ridley, B. K. "The LO phonon lifetime in GaN." Journal of Physics: Condensed Matter 8, no. 37 (1996): L511.

[32] König, D., Y. Takeda, and B. Puthen-Veettil. "Technology-compatible hot carrier solar cell with energy selective hot carrier absorber and carrier-selective contacts." Applied Physics Letters 101, no. 15 (2012): 153901.

[33] Varshni, Yatendra Pal. "Temperature dependence of the energy gap in semiconductors." physica 34, no. 1 (1967): 149-154.

Chapter **5**

Hot carriers in type-II InAs/AlAsSb MQWs

5.1. Introduction

Recently, there has been a lot of interest to study interactions between hot carriers and phonons in semiconductors because these interactions are a major source of heat generation in semiconductor structures. [1, 2, 3] Manipulation and control of heat loss in electronic devices has many potential applications: including hot carrier solar cells, [4, 5] near infrared (NIR) photodetectors, [6] and plasmonic devices [7] (amongst others). As such, several candidate systems (alternatives to current commercial materials) have been investigated to aid inhibited hot carrier relaxation in systems, which include: InN, BSb, and AlSb. [8, 9, 10, 11] Moreover, nanostructures have also been shown to have the potential to inhibit (or reduce) hot carrier-phonon interactions via manipulating the phonon dynamics in the system. [12, 13, 14]

The dominant hot carrier relaxation mechanism in III-V semiconductors is the coupling of electrons with longitudinal optical (LO) phonons through the Fröhlich interaction. In polar semiconductors, the generated LO phonons decay into two low energy (identical energy but opposite directions) acoustic (LA) phonons via the Klemens mechanism [15] or via a low energy transverse optical (TO) phonon and an acoustic (LA) phonon via the Ridley mechanism. [13, 16, 17] If such processes can be perturbed, a phonon bottleneck can develop and hot LO-phonons will be reabsorbed via carriers, which are therefore sustains an elevated carrier temperature. [18, 19, 20]

In this thesis, InAs/AlAsSb MQW structures have been proposed as a candidate system to inhibit hot carrier thermalization. As has been discussed in Chapter 3, Section 3.5, in these type-II QWs the spatial separation of photogenerated carriers results in a longer radiative recombination lifetime than that of a type-I system. Therefore, it is expected the density of photogenerated hot carriers within the QW region are longer-lived (due to less efficient radiative recombination process in type-II systems) than for a type-I structure [21, 22], which promotes the creation of a phonon bottleneck at lower carrier densities in QWs with type-II band alignment.

5.2. InAs/AlAs$_x$Sb$_{1-x}$ multi-quantum well (MQW) structures: Details and Fabrication

The InAs/AlAs$_{0.16}$Sb$_{0.84}$ MQW structure investigated was grown on a semi-insulating (SI) GaAs substrate by molecular beam epitaxy (MBE). A schematic and band energy diagram for the MQW structure are shown in Figures 5.1 (a) and (b), respectively. As discussed in Chapter 3, this design has interesting features for hot carrier absorber applications. First, there is a large band offset in the conduction band ($\Delta E_C = 1.93\ eV$, see Figure 5.1 (b)), which results in strong confinement for electrons within the InAs QW. On the other hand, there is a relatively shallow confinement for holes in the valence band ($\Delta E_V = 63\ meV$), which provides a condition for their thermally mediated escape at elevated temperatures. [23] In addition, the MQW structure has a type-II band alignment, which rapidly ($\sim ps$) spatially separates photogenerated carriers. The advantage of the design is strong absorption within the InAs QW followed by radiative

losses to the type-II band alignment. This condition again facilitates the creation of a phonon bottleneck effect due to low recombination rate in the type-II QWs.

The sample configuration is shown in Figure 5.1 (a). Initially, a 2000 nm InAs buffer layer is deposited on the GaAs substrate prior to the growth of the active layers to compensate the lattice mismatch between the GaAs substrate and the MQW structure. Thereafter, a 30 period MQW structure was grown with 10 nm $AlAs_{0.16}Sb_{0.84}$ barriers and 2.4 nm InAs QWs, respectively. Finally, a 10 nm $AlAs_{0.16}Sb_{0.84}$ barrier material was grown upon the active region followed by a 50 nm InAs cap layer to prevent the Al-containing barrier material from being oxidized.

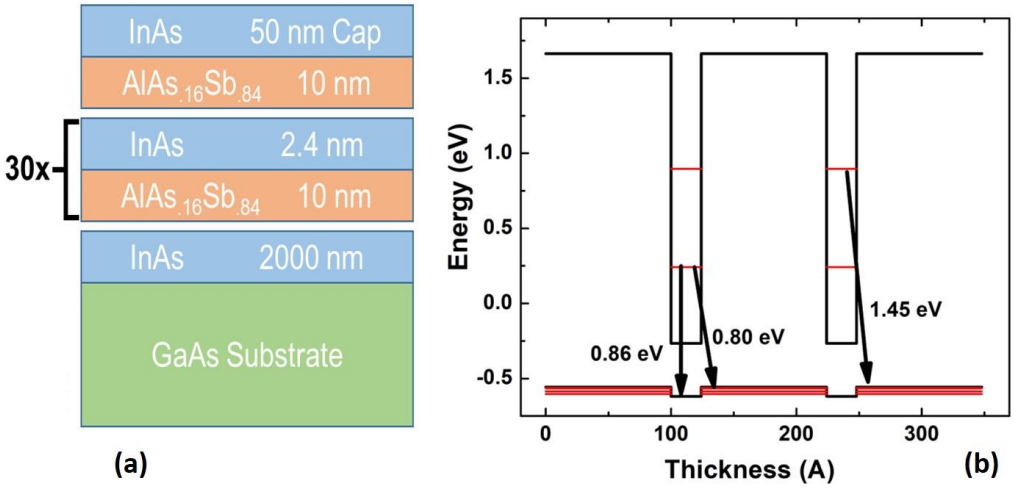

Figure 5. 1. (a) Schematic and (b) band structure (only two potential wells) of the InAs MQW structure.

Figure 5.1 (b) shows the simulated band energy diagram of two quantum wells of the InAs MQW structure at 300 K using NRL MultiBands®. [24] The separation between the confined energy levels in the conduction band is ~ 655 meV. The confinement in

the valence band is significantly less (~ 63 meV). Several transitions are indicated in Figure 5.1 (b): the lowest confined energy in the conduction band to valence band (the type-II transition at ~ 0.8 eV); the lowest energy transition *within* InAs itself (type-I at ~ 0.86 eV); and the transition from the first electron excited state to the valence band (~ 1.45 eV).

In order to investigate the dynamics of photogenerated hot carriers in the MQW structure, TD THz absorption spectroscopy was performed. In this type of ultrafast time-resolved spectroscopy, it is possible to probe electronic transitions that happen on the order of sub-picosecond timescales. In TD THz spectroscopy, electrons are pumped to excited states using a pulsed (femtosecond) laser with photon energy larger than the semiconductor band gap. Then, a weak (or low intensity) THz probe signal with a delay time of τ (with respect to the pump pulse) is *transmitted* through the sample. By measuring the amount of difference in light absorption (ΔA) versus delay time information about the dynamics of photogenerated *free* carriers in the systems can be deduced. [25, 26] To facilitate the experiment and to avoid light absorption in the low energy InAs buffer and capping layers, a combination of mechanical polishing and wet chemical etching is applied on the MQW structure to remove the GaAs substrate, InAs buffer layer, and InAs cap layer. Thus, enabling absorption directly within the MQW active region of the sample.

A full description of sample processing is as follows: firstly, the InAs MQW structure is immersed into the selective etchant: concentrated citric acid ($C_6H_8O_7$) (1gr: 1mL DI water): Hydrogen peroxide (H_2O_2) (5 ml: 1 ml), for 1 minute to remove only the InAs cap layer without etching the upper most AlAsSb barrier material. The *cap-less* sample

is then attached to a thin (1 mm) piece of sapphire (1x1 cm^2) using a transparent Norland Optical Adhesive (NOA88). A UV-light source (325 nm) is utilized to cure the adhesive and to bond the sample to the sapphire window. An Allied High-Tech Metprep system is then employed to remove > 550 μm of the 600 μm GaAs substrate by mechanical polishing. The final wet etching process removes the remaining GaAs substrate using: ammonium hydroxide (NH_4OH): hydrogen peroxide (H_2O_2): and DI Water (H_2O) (1 ml: 3 ml: 16 ml). The sample is then immersed in a second selective etchant for 50 minutes to remove the InAs buffer layer (2000 nm), without etching the AlAsSb barrier material using a concentrated citric acid ($C_6H_8O_7$): Hydrogen peroxide (H_2O_2) (5 ml: 1 ml) solution.

The sample processing steps are summarized in Table 5.1.

Table 5. 1. Sample Processing steps using chemicals for removing different layers of InAs MQW structure.

Step	Chemical Solution	Immersing Time (min)	Etching Layer	Removed Thickness (nm)
1	$C_6H_8O_7$ (1gr:1mL H_2O): H_2O_2 (5 ml: 1 ml)	1	InAs Capping Layer	50
2	NH_4OH: H_2O_2: H_2O (1 ml: 3 ml : 16 ml)	90	GaAs Substrate	> 50000
3	$C_6H_8O_7$ (1gr:1mL H_2O): H_2O_2 (5 ml: 1 ml)	50	InAs Buffer	2000

After removing the InAs buffer layer only, the InAs/$AlAs_{0.16}Sb_{0.84}$ MQWs remain on the sapphire window (~ 350 nm thick) and displays a brownish color. The inset of Figure 5.2 shows the schematic of the InAs MQW structure after sample processing. The main panel of Figure 5.2 shows a comparison of the PL spectra before and after substrate removal at 4 K. The PL spectra of the InAs MQW structure before and after sample processing are similar – demonstrating the integrity of the active region upon substrate removal. There is, however, a small blueshift evident for the processed sample, which is attributed to the effect of strain relaxation upon substrate removal. [27]

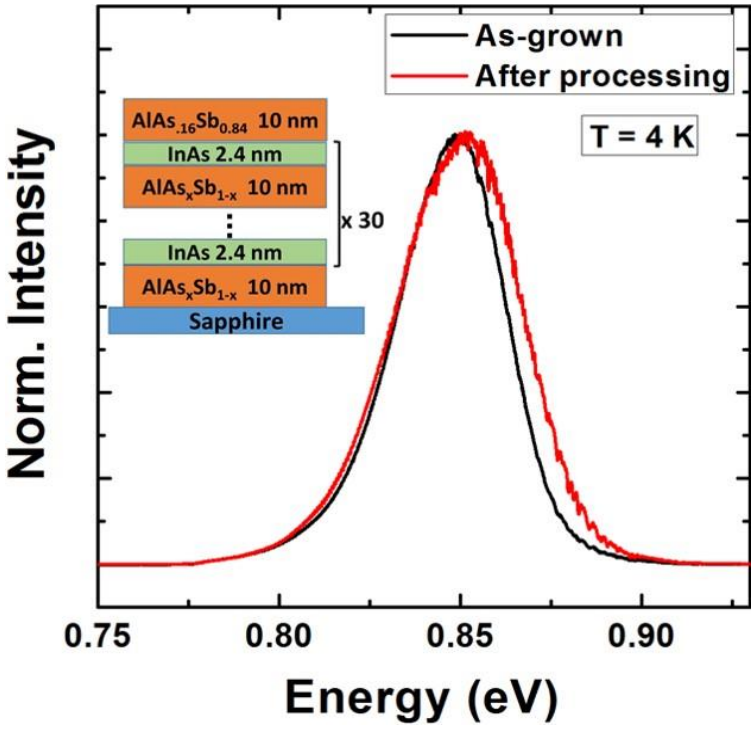

Figure 5. 2. PL spectra of the InAs MQW structure before and after sample processing at 4 K. The inset shown in this graph shows the schematic of the processed sample attached to a sapphire plate. [Reproduced from: *Esmaielpour, H., et al. "Enhanced hot electron lifetimes in quantum wells with inhibited phonon coupling." Scientific reports 8, no. 1 (2018): 12473.*] [27]

Figure 5.3 (a) shows the schematic of the type-II band energy diagram of InAs/$AlAs_{0.16}Sb_{0.84}$ MQW structure. After removing the InAs cap and buffer layers, it is possible to perform TD THz in the absorption geometry and study the dynamics of photogenerated carriers in the QWs. The blue and red wavy arrows (in Figure 5.3 (a)) represent the photons, which pump and probe the photogenerated carriers, respectively; while, the black arrow shows the emitted PL signal from the structure. Figures 5.3 (b) to (d) show the different effective band geometries at different temperatures for the InAs MQW structure, where the *effective confinement* of the carriers within the valence band potential well changes. As discussed in Chapter 3, Section 3.3, photogenerated carriers show different effective confinements at different lattice temperatures. This is summarized once more for clarity: at low temperatures (T < 100 K) photogenerated carriers (especially holes) are trapped at the localized states at the QW interfaces created by alloy fluctuations. As a result, radiative recombination occurs 'within' (between e_1 and interface states) the InAs QW predominantly in what we call the quasi-type-I band configuration (see Figure 5.3 (b)). By increasing the lattice temperature, holes localized at the interface are thermally excited and relax into the AlAsSb barrier material revealing the '*pure*' type-II band alignment of the system. As a result, photogenerated charges become spatially separated, as shown in Figure 5.3 (c).

At (even more) elevated lattice temperatures, the holes redistribute throughout the valence band due to the relatively shallow confinement potential in the AlAsSb barrier, see Figure 5.3 (d). Therefore, a continuum (or degenerate) state is created in the valence band whereby holes can move freely around in the system. This regime (termed here the *quasi-type-II* configuration) is significant because it can further reduce the radiative

recombination rate, a major loss mechanism (due to reducing the number of photogenerated carriers) of confined systems when used for solar cells.

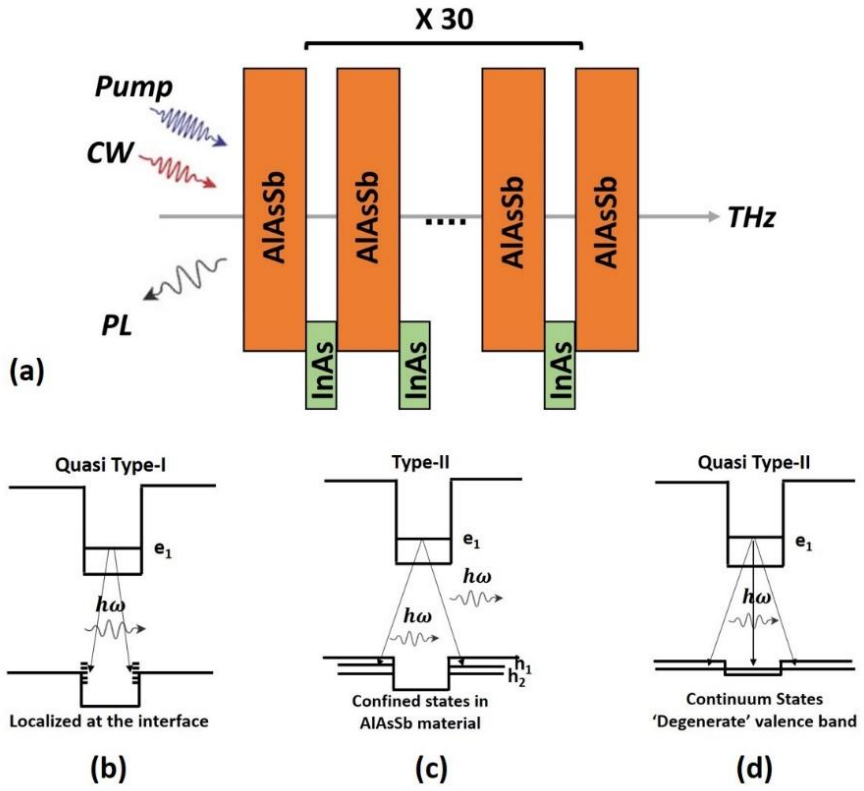

Figure 5. 3. (a) Schematic of type-II band energy diagram of the InAs MQW structure. Wavy arrows are representative of pump, probe, and PL signals associated with the InAs MQW structure. The schematics of the band energy diagrams from (b) to (d) show the effective carrier confinement at different lattice temperatures. At low temperature (T < 100 K), the holes are trapped at the interface due to non-idealities in the structure, see panel (b). By increasing the lattice temperature, as shown in panel (c), holes move to the barrier material and recombination follows a pure-type-II band alignment. At elevated lattice temperatures, holes can escape from the shallow confinement in the valence band and create a degenerate energy level, see panel (d). [Reproduced from: *Esmaielpour, H., et al. "Enhanced hot electron lifetimes in quantum wells with inhibited phonon coupling." Scientific reports 8, no. 1 (2018): 12473.*] [27]

5.3. Optical spectroscopy of the InAs MQW

Figure 5.4 shows temperature dependent PL spectroscopy of the processed InAs MQW structure excited by a He-Ne laser (633 nm). Previously, it was discussed that at low temperatures (T < 100 K) evidence of the existence of localized states is observed. As shown in Figure 5.4 (b), this manifests itself in the appearance of an "s-shape" behavior in peak energy as a function of lattice temperature. The blueshift for the peak energy with increasing lattice temperature (T < 100 K) is associated with the de-trapping of photogenerated holes at the interface and their transfer into the AlAsSb. With a further increase in lattice temperature, the change in peak energy follows the typical Varshni dependence of the band gap. In addition to a change in the band gap, increasing the lattice temperature also results in a significant reduction in the PL peak intensity, especially above 100 K. This PL intensity reduction (at T > 100 K) along with the "s-shape" behavior of peak energy in the temperature dependent PL spectra is symptomatic of a transition from the quasi-type-I condition (see Figure 5.3 (b)) to a dominant type-II geometry (see Figure 5.3 (c)). [21, 22, 27]

Figure 5.4 (a) shows PL spectra for three lattice temperatures, 150 K (black), 225 K (red), and 300 K (green). To study quantitatively the carrier temperature and chemical potential difference, the PL spectra shown in Figure 5.4 (a) are fit with the generalized Planck's radiation law described by Equation 3.1: [28, 29]

$$I_{PL}(E) = \frac{A(E)\,(E)^2}{4\pi^2 h^3 c^2}\left[exp\left(\frac{E-\Delta\mu}{k_B T}\right) - 1\right]^{-1}.$$

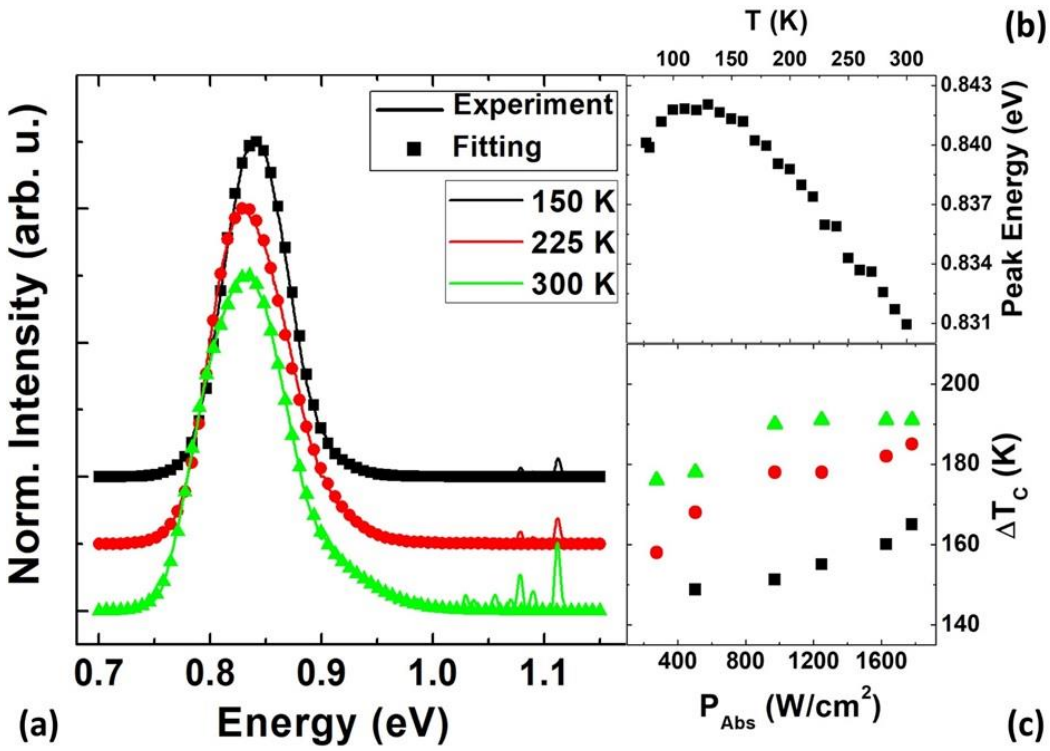

Figure 5. 4. (a) PL spectra of the InAs MQW structure (solid lines) with the fitting (symbols) using generalized Planck's radiation law at 150 K (black), 225 K (red), and 300 K (green). (b) Peak energy versus lattice temperature. (c) Extracted ΔT_C from fitting with generalized Planck's law as a function of absorbed power at 150 K, 225 K, and 300 K. [Reproduced from: *Esmaielpour, H., et al. "Enhanced hot electron lifetimes in quantum wells with inhibited phonon coupling." Scientific reports 8, no. 1 (2018): 12473.*] [27]

Here, the fitting has been performed for PL spectra at elevated temperatures (T > 150 K) where the type-II band configuration is dominant. Figure 5.4 (c) shows the temperature difference (ΔT_C, temperature difference between the carrier and lattice temperatures) extracted by fitting the PL with Equation 3.1. It is evident that ΔT_C increases as a function of excitation power. In addition, ΔT_C has higher values at higher

lattice temperatures, which indicates that by increasing the lattice temperature the hot carrier effect becomes stronger.

At elevated lattice temperatures, the type-II band alignment of the system dominates the carrier recombination dynamics. Increasing the excitation power causes the temperature difference (ΔT_c) to increase – indicating significant hot carriers exist in the system. It has been suggested that the presence and temperature of hot carriers rises at higher lattice temperatures, despite the simultaneous increase in phonons at elevated temperatures. Although significant for potential hot carrier absorber applications because it is the regime where hot carrier solar cell would be expected to operate, this behavior is unusual and as such requires further assessment.

To further investigate the carrier lifetime and study the hot carrier dynamics in the MQW, time resolved terahertz (TR-THz) pump-probe measurements were performed. For the ultrafast spectroscopy, a $\sim$ 100 fs pulsed laser generated by a 1 kHz laser amplifier (with excitation wavelength of 800 nm) was utilized. The laser pulses were tuned using an optical parametric amplifier (OPA). THz pulses are created by transmitting an 800 nm pulse laser beam through a (110) $CdSiP_2$ crystal (with a thickness of 1 mm). Then, the sample is exposed by the THz pulsed between 4.2 K and 300 K, and the transmitted light detected using an electro-optic ZeTe crystal. In order to measure the dynamics of the photogenerated carriers, the delay time ($\Delta\tau$) between the THz and the transmitted pulses through the sample were measured. The delay time had a time resolution of < 1 ps and it is measured over a temporal range of 2000 ps.

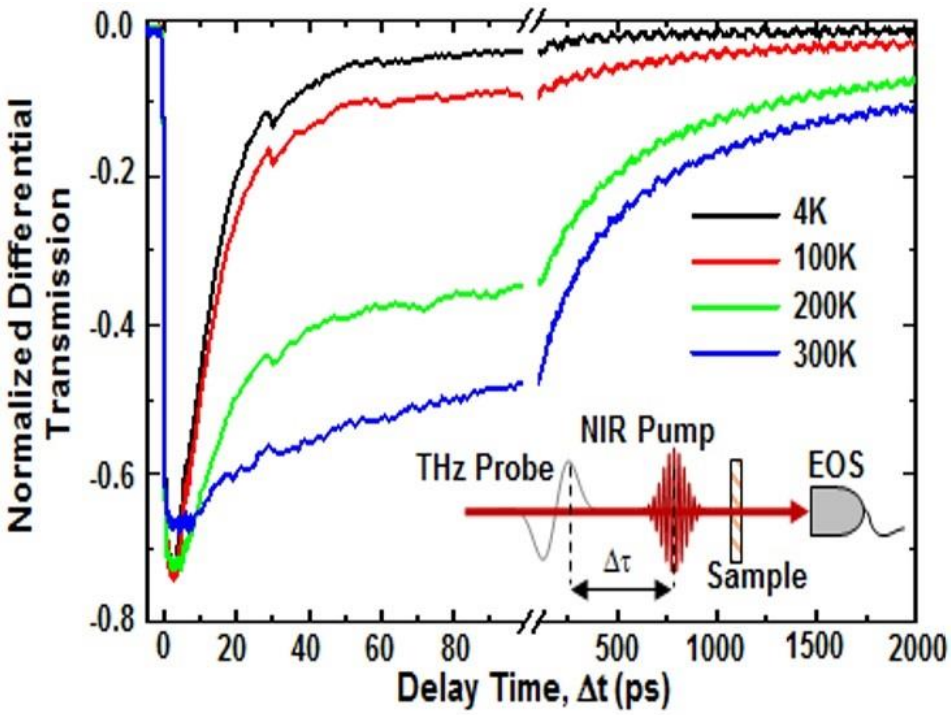

Figure 5. 5. Normalized differential transmission of pump-probe time resolved terahertz (TR-THz) measurement at various lattice temperatures. The inset shows the schematic of pump-probe signals that have been shone on the sample. [Reproduced from: *Esmaielpour, H., et al. "Enhanced hot electron lifetimes in quantum wells with inhibited phonon coupling." Scientific reports 8, no. 1 (2018): 12473.*] [27] (Acknowledged: Mr. Herath P. Piyathilaka and Dr. Alan D. Bristow)

Figure 5.5 shows a TR-THz pump probe measurement at various lattice temperatures. In this experiment, the change in the THz signal due to the absorption of free carriers pumped above the effective band gap of the InAs QW is plotted versus delay time. The change in peak electric field ($^{\Delta E}/_{E}$) due to absorption by free carriers (as a function of delay time) provides information about the carrier dynamics and lifetime. As shown in the main panel of Figure 5.5, there are two distinct temporal regimes observed in the

measured response. The smaller range (0-100 ps) shows the change in peak electric field and an extended range (100 ps – 2000 ps) is used to observe the electric field decay.

In Figure 5.5 it is evident that there are two dominant decay mechanisms in the system, an initial fast component, followed by a much slower temporal effect. At low temperatures, the fast decay process dominates. However, as the lattice temperature increases, the contribution of the fast decay process becomes less significant and the slow mechanism prevails.

5.4. Phenomenological description of hot carrier dynamics in the MQW

The ultrafast transient absorption are fit by a three-component decay model to extract the amplitude(s) and recombination lifetime(s) of the system:

$$\Delta \mathrm{E(t)/E} = \sum_{i=1}^{3} A_i \, exp[-(t - t_0)/\tau_i], \tag{5.1}$$

where A_i and $1/\tau_i$ are the amplitude and lifetime of each recombination mechanism. The extracted values from fitting the experiment with Equation 5.1 are shown in Figure 5.6. The relative amplitudes of recombination mechanisms are shown in Figure 5.6 (a), (c), and (e), respectively. Moreover, the recombination lifetime values are provided in Figure 5.6 (b), (d), and (f). The amplitude of the fast decay mechanism (see panel (a)) is large at low temperatures and decreases with increasing lattice temperature. In addition, it is also observed that the recombination lifetime associated with the fast decay does not change considerably between 4 K and 200 K, but more appreciably for lattice temperatures greater than 200 K (see Figure 5.6 (b)). The fast decay mechanism

is attributed to transitions that arise at localized states, which are dominant at low temperatures and whose contribution becomes less significant at higher temperatures, as these states depopulate.

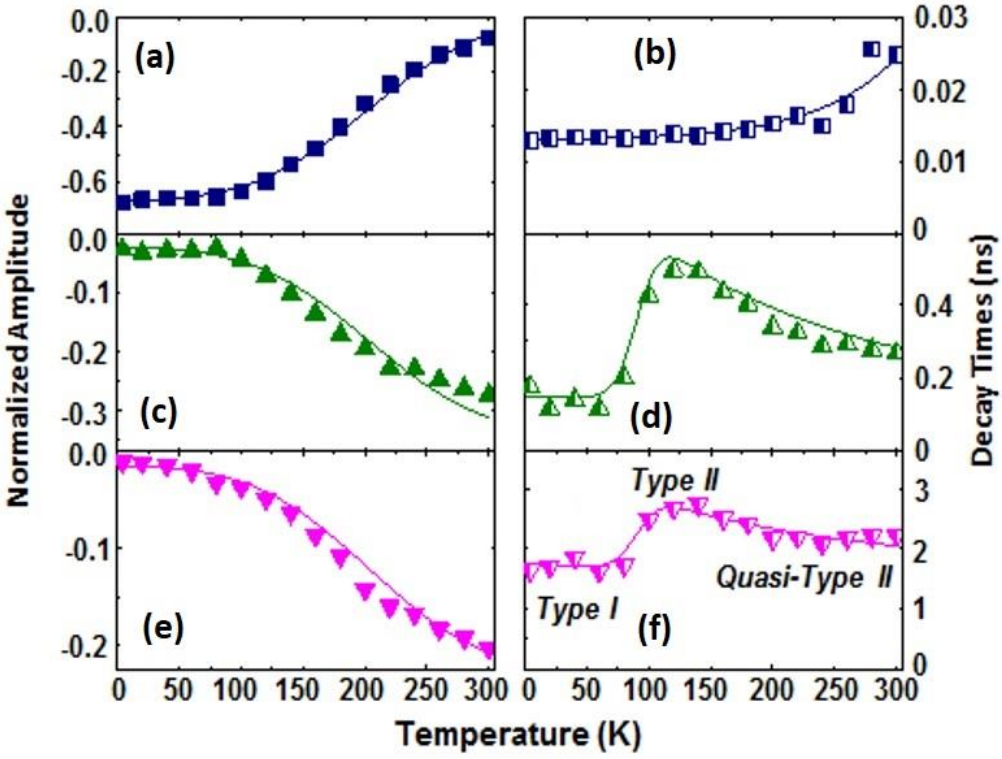

Figure 5. 6. Amplitude ((a), (c), and (e)) and decay time ((b), (d), and (f)) as a function and lattice temperature for different recombination mechanisms in the InAs MQW structure. [Reproduced from: *Esmaielpour, H., et al. "Enhanced hot electron lifetimes in quantum wells with inhibited phonon coupling." Scientific reports 8, no. 1 (2018): 12473.*] [27] (Acknowledged: Mr. Herath P. Piyathilaka and Dr. Alan D. Bristow)

In contrast, it is observed the amplitudes of the slow recombination mechanism (see Figure 5.6 (c) and (e)) increases at elevated lattice temperatures. In addition, the recombination lifetime for both transitions increase non-monotonically (Figure 5.6 (d)

and (f)). The non-monotonic behavior of recombination lifetime is attributed to transitions from the so-called quasi-type-I condition at low temperatures (T < 100 K) to the pure type-II geometry at higher lattice temperatures (due to de-trapping of holes from localized states at QW interfaces), and finally from a type-II to a quasi-type-II behavior at elevated lattice temperatures. The reduction of the recombination lifetime at even higher temperatures is associated with occupation of continuum states due to the shallow confinement of the barrier material – resulting in a 'degenerate' valence band. The origin of *two* band-to-band transitions (intermediate and slow) is associated with the multiple transitions from the nearby states within the valence band (mixing of the valence band states) into the QW ground state (e1). The effects of multiple valence band transitions in the MQW are also observed in the steady state PL spectroscopy.

With increasing excitation power, it is expected the probability of non-radiative Auger recombination increases. [30, 31] To study Auger recombination lifetime it is required to pump with a high power laser, however, the excitation power of the utilized laser is rather limited. In addition, it was previously discussed by Tang *et al.* [21] that the contribution of Auger recombination for the range of studied powers in steady state photoluminescence spectroscopy is low (< 10%). Therefore, it is expected Auger recombination does not have a significant contribution in the InAs MQW structure.

It has been discussed previously, in a semiconductor when a photon with energy above the band gap is absorbed it creates carriers with excess kinetic energy called (hot carriers). The photogenerated hot carriers distribute thermal energy among themselves in a femtosecond time scale through carrier-carrier interactions. This process is much faster than interactions between photogenerated carriers and phonons, which occur in a

few picoseconds. Then, hot carriers lose their excess kinetic energy through emitting optical (LO) phonons via the Fröhlich mechanisms. Thereafter, the LO-phonons decay in to low energy acoustic (LA) phonons via Klemens interactions [15] or a transverse optical (TO) phonon and an LA-phonon via Ridley interactions. [16] As a result of phonon-mediated thermalization process, the excess kinetic energy of hot carriers will be lost via heat dissipation.

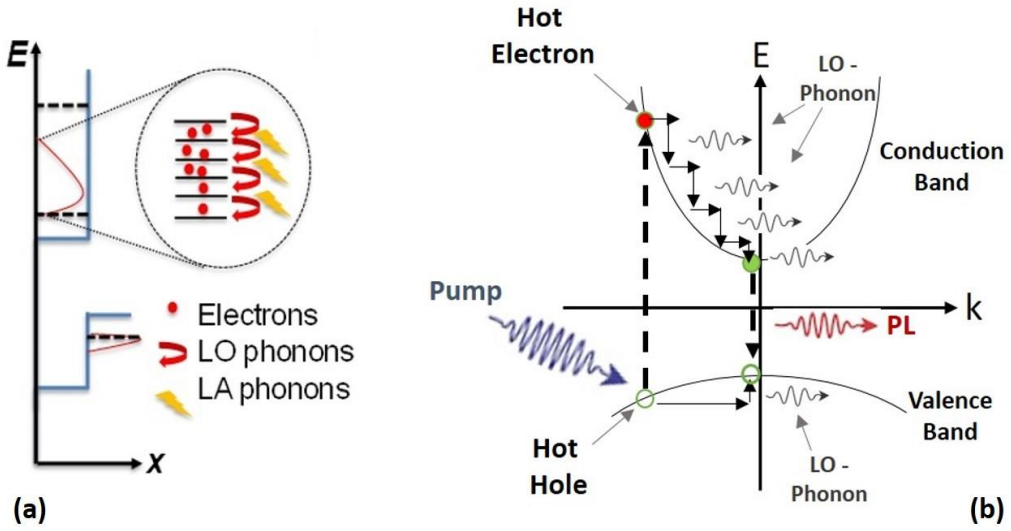

Figure 5. 7. (a) Schematic of the type-II band alignment InAs QW band structure with optical (LO) and acoustic (LA) phonon emissions shown by red and yellow arrows, respectively. (b) Schematic of a semiconductor band gap. Blue, red, and black arrows represent excitation photon, emitted PL photon, and LO-phonon, respectively. Different steps from photoabsorption to thermalization and finally recombination are shown. [Reproduced from: *Esmaielpour, H., et al. "Enhanced hot electron lifetimes in quantum wells with inhibited phonon coupling." Scientific reports 8, no. 1 (2018): 12473.*] [27]

Figure 5.7 (a) shows a schematic of the proposed relaxation phonon dissipation processes in the system. Hot carriers are absorbed and begin to thermalize by emitting LO-phonons (red arrows), which subsequently couple anharmonically with LA-phonons (yellow arrows). As shown in this schematic, the energy distribution of electrons within the conduction band is larger than the one for holes in the valence band. This effect is associated with the low effective mass of electrons in the InAs QW and large effective mass of holes in the AlAsSb barrier material. As a result, it is expected that the electrons will be hotter (with a larger thermal distribution) than the holes in this system. [27, 32]

When the excitation power increases, more LO-phonons are created due to the increase in the hot carrier generation rate, which creates an imbalance between the LO-phonon and LA– or TO-phonon populations. As a result, the generation of non-equilibrium LO-phonons creates favorable conditions for a phonon-bottleneck effect in the system. [27, 33] Figure 5.7 (b) depicts the absorption recombination process with respect to momentum space to further clarify how hot carriers lose excess kinetic energy through the sequential emission of LO-phonons.

To further consider the effect of electron-phonon and phonon-phonon interactions in the InAs/AlAsSb system, Raman spectroscopy was performed along with DFT calculations (by Professor Bin Wang – CBME OU). Figure 5.8 shows the results of density functional theory (DFT) calculations for (a) AlSb and (b) InAs compounds, respectively. AlSb is considered for simplicity (instead of AlAsSb) since the differences in performance is considered negligible when considering the low concentration of As

(16%) in the ternary compound. It is assumed, therefore, that bulk AlSb provides a first order description of the phonon dispersion relation in the system under investigation.

In Figure 5.8, there is a large offset in the phonon energy between AlSb barrier and InAs QW materials at the Γ point (k = 0), where radiative recombination and LO-phonon emission (or absorption) predominantly occur. The LO-phonon energy of InAs is 29 meV and the green shaded region shows the phononic band gap between optical and acoustic phonons in the system (See Figure 5.8 (b)).

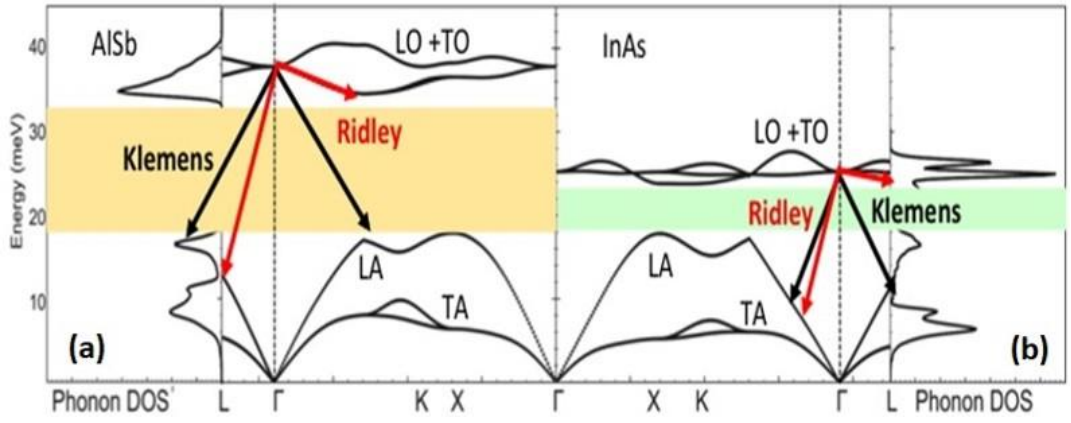

Figure 5. 8. DFT calculations for AlSb (a) and InAs (b) bulk materials. Density of states and phonon dispersion for both systems are shown. The shaded regions show the phononic band gap between LO and LA phonons. [Reproduced from: *Esmaielpour, H., et al. "Enhanced hot electron lifetimes in quantum wells with inhibited phonon coupling." Scientific reports 8, no. 1 (2018): 12473.*] [27] (Acknowledged: Dr. Bin Wang)

As has been described, in polar semiconductors anharmonic coupling between the optical and acoustic modes is driven by either Klemens or Ridley processes. In InAs, the Ridley mechanism is negligible due to a strong mixing between LO– and TO–

phonons. [16] In contrast, the Klemens interaction in InAs is significant due to the coupling between optical and acoustical phonons that is specifically associated with the small difference in atomic mass between the anion and cation in polar materials; thus, the small phononic band gap in InAs. In general, the Klemens channel is inhibited if the energy of LO-phonons in the system is larger than twice the LA-phonon energy ($\hbar\omega_{LO}/\hbar\omega_{LA} > 2$). The ratio between optical and acoustic phonon energies in InAs is close to 1 ($\hbar\omega_{LO}/\hbar\omega_{LA} \sim 1$) resulting in a strong Klemens process in bulk InAs.

However, for AlSb there is a large phononic band gap (see Figure 5.8 (a)), due to the large difference between anion and cation mass in this system. Indeed, the ratio of LO-phonon energy to LA-phonon energy ($\hbar\omega_{LO}/\hbar\omega_{LA} \sim 1.9$) is approximately 2 in AlSb. This indicates that Klemens thermalization for AlSb is inhibited or weak. A further consequence of this is property is that AlSb is also a poor thermal conductor. [34] As shown in Figure 5.8 (a) and (b), there is a large mismatch between the LO-phonon energies of InAs and AlSb at the interface. This discontinuity contributes to an impedance mismatch at the interface and the inhibition of heat propagation from the InAs QW into the AlSb barrier material. [32]

To further consider the role of the phonon mismatch in the InAs and AlAsSb layers and the origin of the stable hot carriers in this system, Raman spectroscopy was performed to investigate the nature of the LO-phonon energies of the MQW. Raman spectroscopy was performed using a Witec (Ulm) system at the University of Tulsa. Figure 5.9 shows Raman spectra for a GaAs substrate (black line), a bulk reference InAs layer (red line), an $AlAs_xSb_{1-x}$ epilayer (green line) – all materials that comprise the full MQW sample, which is also shown by blue in Figure 5.9 in blue.

It is evident that the LO-phonon energies of Al(As)Sb epilayer and InAs buffer materials are well separated, which confirms the large difference determined with DFT calculations (Figure 5.8 (a) and (b), respectively). Also, the shoulder of the low energy AlAsSb epilayer (green spectra) confirms the assumptions made in using AlSb for those calculations – there is only a small change in the peak position of AlSb as compared to AlAsSb.

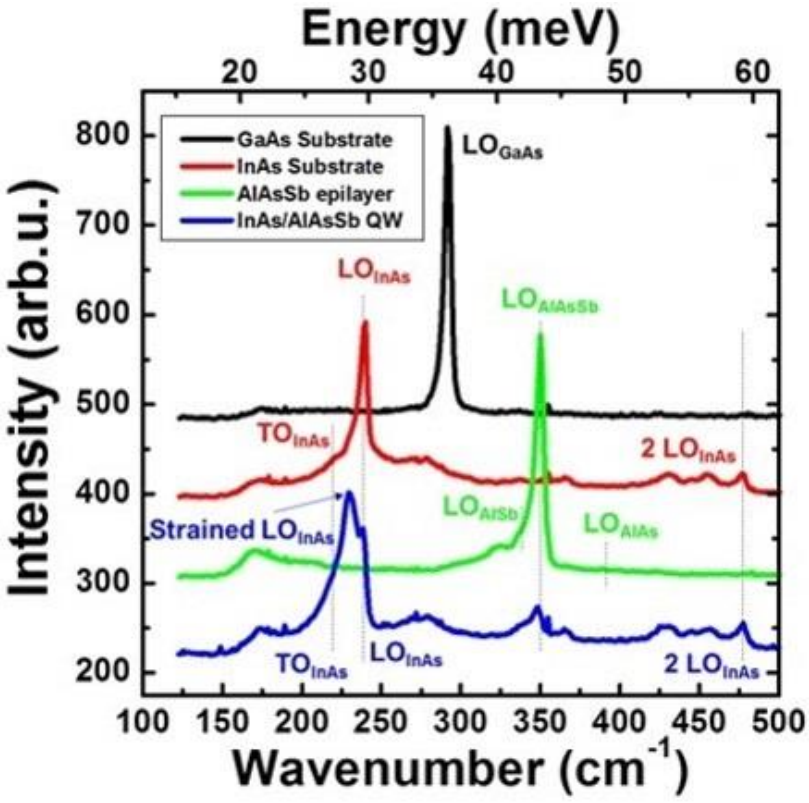

Figure 5. 9. Raman spectra for GaAs substrate (black), InAs buffer layer (red), $AlAs_xSb_{1-x}$ epilayer (green), and the InAs/ $AlAs_xSb_{1-x}$ MQW structure (blue) at 300 K. [Reproduced from: *Esmaielpour, H., et al. "Enhanced hot electron lifetimes in quantum wells with inhibited phonon coupling." Scientific reports 8, no. 1 (2018): 12473.*] [22] (Acknowledged: Dr. Echo Adcock-Smith, Dr. Kenneth P. Roberts)

The Raman spectrum of the InAs/AlAsSb MQW structure (blue line) in Figure 5.9 is dominated by the peak associated with the LO-phonon energy of the MQW structure. It is evident that the MQW peak is near resonant with that of the InAs buffer (close to the one for the strained InAs) LO-phonon energy. In addition, there is a small peak associated with AlAsSb barrier material, which supports the hypothesis that the dominant phonon processes (or thermalization) occurs within the InAs QW rather than in AlAsSb. [12, 27]

Both theory and experiment show that the InAs/AlAsSb system has unusual properties that support the presence of stable hot electrons in the system. This appears related to a combination of longer-lived hot electrons within the InAs MQW (due to the spatially separated photogenerated charges in the type-II heterostructure) as well as, inhibited phonon dissipation and heat transport away from the active region due to a thermal mismatch at the QW/barrier interface. Here it is suggested that the reabsorption of low energy LA-phonons (heat) within the InAs QW may further support the formation of a stable LO phonon bottleneck (therefore hot electrons in the system) [27] a mechanism, which has also been observed recently in the related GaAs and CdSe systems. [35]

To infer further physical information regarding the carrier cooling processes particularly with respect to LO-phonon emission and lifetime a simple relationship between thermalized power and LO-phonon scattering mechanisms can be considered. [36] For a system where the dominant cooling process is associated with LO-phonon emission, it is possible to model hot carrier cooling process via LO-phonon Fröhlich interactions using Equation 5.2 and to determine the scattering lifetime of LO-phonons.

Here, a stable non-equilibrium hot LO-phonon distribution created by long-lived hot carriers is model by: [36]

$$P_{th} = \frac{E_{LO}}{\tau_m}\left(exp\left(-\frac{E_{LO}}{k_B T_C}\right) - exp\left(-\frac{E_{LO}}{k_B T_L}\right)\right), \tag{5.2}$$

where P_{th} is the thermalized power associated with LO-phonon scattering, E_{LO} the LO-phonon energy for the InAs QW (29 meV), τ_m the effective LO-phonon scattering in the system, k_B the Boltzmann constant, T_C the carrier temperature, and T_L the lattice temperature. Equation 5.2 represents the amount of LO-phonon scattering during thermalization in the InAs/AlAsSb QW investigated. Since in PL spectroscopy no electric power is extracted, the absorbed power is equal to thermalized power.

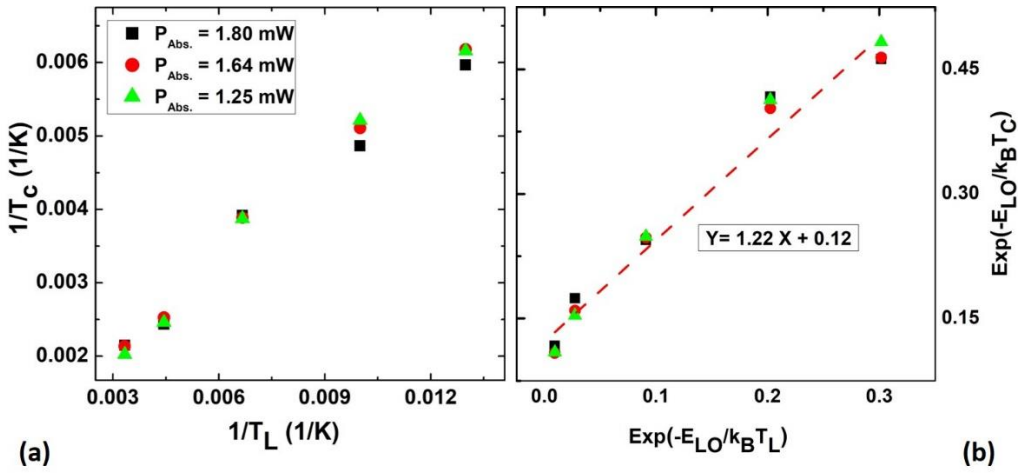

Figure 5. 10. (a) Inverse of carrier temperature versus inverse of lattice temperature for the InAs MQW structure. (b) The exponential of the inverse of carrier temperature versus exponential of lattice temperature following the relationship in the Equation 5.2. [Reproduced from: *Esmaielpour, H., et al. "Enhanced hot electron lifetimes in quantum wells with inhibited phonon coupling." Scientific reports 8, no. 1 (2018): 12473.*] [27]

Figure 5.10 (a) shows the inverse of the carrier temperature extracted from continuous wave PL versus the inverse of the lattice temperature. In this experiment, the sample was excited by a He-Ne laser (633 nm) at three different excitation powers, as indicated in the graph. According to the amount of power absorbed in the system, the number of photogenerated carriers are calculated based on two assumptions: 1) there is one electron-hole pair created per photon, and 2) the radiative recombination lifetime for the photogenerated carriers at all temperatures is ~ 1 ns, which is consistent with the carrier lifetime extracted from the ultrafast TR-THz spectroscopy. As a result, the photogenerated carrier density in the system for low, medium, and high excitation powers were calculated and determined to be: 4.0×10^{12} cm^{-2}, 5.2×10^{12} cm^{-2}; and 5.7×10^{12} cm^{-2}, respectively. Figure 5.10 (b) shows an alternative representation of the relationship between T_C and T_L; the exponential component of T_C as a function of the exponential component of T_L. According to Equation 5.2, the extracted y-intercept from the graph is proportional to LO-phonon scattering lifetime (τ_{eff}) in the system. The extracted τ_{eff} for the experimental results is 1.9 ps, which is an order of magnitude higher than that typically observed in bulk III-V semiconductors. [27] This is a further support for the existence of long-lived non-equilibrium hot LO-phonons in the InAs MQW structure presented.

Conclusion

In conclusion, strong hot carrier effects have been measured in a type-II $InAs/AlAs_xSb_{1-x}$ MQW structure at temperatures above 100 K. The origin of this behavior is attributed to a combination of the type-II band alignment (longer hot carrier

lifetime) and the disparate phononic properties at the InAs QW and AlAsSb barrier inhibit the dissipation of heat (thermalization process) from the system. Specifically, it is suggested that the poor thermal conductivity in the AlAsSb barrier inhibits the transfer of heat from the QW. Although more direct evidence for this effect is required, the data and theory are consistent with this hypothesis. Time resolved photoluminescence (TRPL) and ultrafast transient absorption spectroscopy are now underway to further investigate the origin of robust hot carriers in this system. Recent DFT calculations and Monte Carlo simulations also indicate that transitions to higher order "X" and "L" valleys may also be important.

References

[1] Hung, Chen-I. "Heat generation in electron-phonon scattering processes of quantum well structures." Journal of Physics D: Applied Physics 30, no. 22 (1997): 3142.

[2] Takagahara, Toshihide. "Electron-phonon interactions in semiconductor quantum dots." In Semiconductor Quantum Dots, pp. 115-147. Springer, Berlin, Heidelberg, 2002.

[3] Park, Cheol-Hwan, Nicola Bonini, Thibault Sohier, Georgy Samsonidze, Boris Kozinsky, Matteo Calandra, Francesco Mauri, and Nicola Marzari. "Electron–phonon interactions and the intrinsic electrical resistivity of graphene." Nano letters 14, no. 3 (2014): 1113-1119.

[4] Conibeer, Gavin, Robert Patterson, Lunmei Huang, Jean-Francois Guillemoles, Dirk Kőnig, Santosh Shrestha, and Martin A. Green. "Modelling of hot carrier solar cell absorbers." Solar energy materials and solar cells 94, no. 9 (2010): 1516-1521.

[5] Conibeer, Gavin, Nicholas Ekins-Daukes, Jean-François Guillemoles, Dirk Kőnig, Eun-Chel Cho, Chu-Wei Jiang, Santosh Shrestha, and Martin Green. "Progress on hot carrier cells." Solar Energy Materials and Solar Cells 93, no. 6-7 (2009): 713-719.

[6] Lao, Yan-Feng, AG Unil Perera, L. H. Li, S. P. Khanna, E. H. Linfield, and H. C. Liu. "Tunable hot-carrier photodetection beyond the bandgap spectral limit." Nature Photonics 8, no. 5 (2014): 412.

[7] Khosravi Khorashad, Larousse, Lucas V. Besteiro, Zhiming Wang, Jason Valentine, and Alexander O. Govorov. "Localization of excess temperature using plasmonic hot spots in metal nanostructures: combining nano-optical antennas with the Fano effect." The Journal of Physical Chemistry C 120, no. 24 (2016): 13215-13226.

[8] Aliberti, P., Y. Feng, Y. Takeda, S. K. Shrestha, M. A. Green, and G. Conibeer. "Investigation of theoretical efficiency limit of hot carriers solar cells with a bulk indium nitride absorber." Journal of Applied Physics 108, no. 9 (2010): 094507.

[9] Yao, Yao, Dirk König, and Martin Green. "Investigation of boron antimonide as hot carrier absorber material." Solar Energy Materials and Solar Cells 111 (2013): 123-126.

[10] Barman, Saswati, and G. P. Srivastava. "Long-wavelength nonequilibrium optical phonon dynamics in cubic and hexagonal semiconductors." Physical Review B 69, no. 23 (2004): 235208.

[11] Yao, Yao, and Dirk König. "Comparison of bulk material candidates for hot carrier absorber." Solar Energy Materials and Solar Cells 140 (2015): 422-427.

[12] Conibeer, Gavin, Santosh Shrestha, Shujuan Huang, Robert Patterson, Hongze Xia, Yu Feng, Pengfei Zhang *et al.* "Hot carrier solar cell absorber prerequisites and candidate material systems." Solar Energy Materials and Solar Cells 135 (2015): 124-129.

[13] Rosenwaks, Y., M. C. Hanna, D. H. Levi, D. M. Szmyd, R. K. Ahrenkiel, and A. J. Nozik. "Hot-carrier cooling in GaAs: Quantum wells versus bulk." Physical Review B 48, no. 19 (1993): 14675.

[14] Kash, Kathleen, Jagdeep Shah, Dominique Block, A. C. Gossard, and W. Wiegmann. "Picosecond luminescence measurements of hot carrier relaxation in III–V semiconductors using sum frequency generation." Physica B+ C 134, no. 1-3 (1985): 189-198.

[15] Klemens, P. G. "Anharmonic decay of optical phonons." Physical Review 148, no. 2 (1966): 845.

[16] Ridley, B. K. "The LO phonon lifetime in GaN." Journal of Physics: Condensed Matter 8, no. 37 (1996): L511.

[17] Lindsay, L., D. A. Broido, and T. L. Reinecke. "Ab initio thermal transport in compound semiconductors." Physical Review B 87, no. 16 (2013): 165201.

[18] Murdin, B. N., W. Heiss, C. J. G. M. Langerak, S-C. Lee, I. Galbraith, G. Strasser, E. Gornik, M. Helm, and C. R. Pidgeon. "Direct observation of the LO phonon bottleneck in wide GaAs/$Al_xGa_{1-x}As$ quantum wells." Physical Review B 55, no. 8 (1997): 5171.

[19] Zibik, E. A., Thomas Grange, B. A. Carpenter, N. E. Porter, R. Ferreira, G. Bastard, D. Stehr *et al.* "Long lifetimes of quantum-dot intersublevel transitions in the terahertz range." Nature materials 8, no. 10 (2009): 803.

[20] Fröhlich, Herbert, Hans Pelzer, and Sigurd Zienau. "XX. Properties of slow electrons in polar materials." The London, Edinburgh, and Dublin Philosophical Magazine and Journal of Science 41, no. 314 (1950): 221-242.

[21] Tang, J., V. R. Whiteside, H. Esmaielpour, S. Vijeyaragunathan, T. D. Mishima, M. B. Santos, and I. R. Sellers. "Effects of localization on hot carriers in

InAs/$AlAs_xSb_{1-x}$ quantum wells." Applied Physics Letters 106, no. 6 (2015): 061902.

[22] Esmaielpour, Hamidreza, Vincent R. Whiteside, Jinfeng Tang, Sangeetha Vijeyaragunathan, Tetsuya D. Mishima, Shayne Cairns, Michael B. Santos, Bin Wang, and Ian R. Sellers. "Suppression of phonon-mediated hot carrier relaxation in type-II InAs/$AlAs_xSb_{1-x}$ quantum wells: a practical route to hot carrier solar cells." Progress in Photovoltaics: Research and Applications 24, no. 5 (2016): 591-599.

[23] Whiteside, Vincent R., Brenden A. Magill, Matthew P. Lumb, Hamidreza Esmaielpour, Michael A. Meeker, Rathsara RHH Mudiyanselage, Adrien Messager *et al.* "Valence band states in an InAs/AlAsSb multi-quantum well hot carrier absorber." Semiconductor Science and Technology (2018).

[24] Lumb, Matthew P., Igor Vurgaftman, Chaffra A. Affouda, Jerry R. Meyer, Edward H. Aifer, and Robert J. Walters. "Quantum wells and superlattices for III-V photovoltaics and photodetectors." In Next Generation (Nano) Photonic and Cell Technologies for Solar Energy Conversion III, vol. 8471, p. 84710A. International Society for Optics and Photonics, 2012.

[25] Berera, Rudi, Rienk van Grondelle, and John TM Kennis. "Ultrafast transient absorption spectroscopy: principles and application to photosynthetic systems." Photosynthesis research 101, no. 2-3 (2009): 105-118.

[26] Ulbricht, Ronald, Euan Hendry, Jie Shan, Tony F. Heinz, and Mischa Bonn. "Carrier dynamics in semiconductors studied with time-resolved terahertz spectroscopy." Reviews of Modern Physics 83, no. 2 (2011): 543.

[27] Esmaielpour, Hamidreza, Vincent R. Whiteside, Herath P. Piyathilaka, Sangeetha Vijeyaragunathan, Bin Wang, Echo Adcock-Smith, Kenneth P. Roberts *et al.* "Enhanced hot electron lifetimes in quantum wells with inhibited phonon coupling." Scientific reports 8, no. 1 (2018): 12473.

[28] Wurfel, Peter. "The chemical potential of radiation." Journal of Physics C: Solid State Physics 15, no. 18 (1982): 3967.

[29] Gibelli, François, Laurent Lombez, and Jean-François Guillemoles. "Accurate radiation temperature and chemical potential from quantitative photoluminescence analysis of hot carrier populations." Journal of Physics: Condensed Matter 29, no. 6 (2016): 06LT02.

[30] Huang, Jian-Jang, Hao-Chung Kuo, and Shyh-Chiang Shen. Nitride Semiconductor Light-Emitting Diodes (LEDs): Materials, Technologies, and Applications. Woodhead Publishing, 2017.

[31] Gribkovskii, V. P., and G. N. Yaskevich. "Auger recombination in semiconductors with intense excitation." Journal of Applied Spectroscopy 20, no. 3 (1974): 307-310.

[32] König, D., Y. Takeda, and B. Puthen-Veettil. "Technology-compatible hot carrier solar cell with energy selective hot carrier absorber and carrier-selective contacts." Applied Physics Letters 101, no. 15 (2012): 153901.

[33] Yang, Ye, David P. Ostrowski, Ryan M. France, Kai Zhu, Jao Van De Lagemaat, Joseph M. Luther, and Matthew C. Beard. "Observation of a hot-phonon bottleneck in lead-iodide perovskites." Nature Photonics 10, no. 1 (2016): 53-59.

[34] Lindsay, L., D. A. Broido, and T. L. Reinecke. "Ab initio thermal transport in compound semiconductors." Physical Review B 87, no. 16 (2013): 165201.

[35] Hejda, B., and K. Kra. "Hot-electron cooling and second-generation phonons in polar semiconductors." Physical Review B 47, no. 23 (1993): 15554.

[36] Zanato, D., N. Balkan, B. K. Ridley, G. Hill, and W. J. Schaff. "Hot electron cooling rates via the emission of LO-phonons in InN." Semiconductor science and technology 19, no. 8 (2004): 1024.

Chapter **6**

Optoelectronic properties of type-II InAs/AlAsSb quantum well p-i-n diodes

6.1. Introduction

Hot carrier solar cells are one type of third generation photovoltaic device, which have been proposed to increase the power conversion efficiency of single band gap solar cells beyond the Shockley-Queisser limit (33%). [1, 2, 3] As has been discussed, a major loss mechanism in photovoltaic devices is through heat generation, which occurs when photogenerated hot carriers lose their excess kinetic energy via interactions with the crystal lattice (phonons). Since the first proposal of the hot carrier solar cell by Ross and Nozik in 1982, [2] there has been considerable interest in this type of solar cell. [4, 5, 6, 7, 8, 9, 10] However, there remain two main challenges for the realization of practical hot carrier solar cells: (1) to design a hot carrier absorber, which inhibits heat loss (thermalization); and (2) to extract photogenerated hot carriers rapidly i.e., before thermalization occurs. [4, 5, 8]

To approach the first challenge various designs have been proposed. [11, 12, 13] It has been shown that nanostructures, such as quantum wells and/or quantum dots [14] are potential candidates for hot carrier absorber applications due to the reduced thermalization losses in these structures. [15, 16] In Chapter 3 and Chapter 4, the optical properties and phononic properties of InAs/$AlAs_xSb_{1-x}$ MQWs were presented. Here, p-

i-n diodes based on these InAs MQWs are presented to study and develop hot carrier effects in device architectures.

6.2. Description of InAs/AlAs$_x$Sb$_{1-x}$ multi-quantum well diodes

A schematic of the InAs/AlAs$_{0.16}$Sb$_{0.84}$ multi-quantum well (MQW) structure investigated is shown in Figure 6.1 (a). Two MQW structures with different AlAs$_{0.16}$Sb$_{0.84}$ barrier thicknesses (2 nm and 5 nm) were grown by molecular beam epitaxy (MBE) onto semi-insulating (SI) GaAs (001) substrates. A p^+-AlAsSb buffer layer (1000 nm) was grown on top of SI GaAs substrates to compensate the lattice mismatch between the substrate and InAs QWs. Then, on top of the p^+-AlAsSb buffer layer a thin intrinsic layer (50 nm) of the AlAsSb barrier material was grown followed by 10 InAs/AlAs$_{0.16}$Sb$_{0.84}$ QWs, which comprise the active region. The width of the InAs QWs for both structures was 2.4 nm. Finally to complete the p-i-n structure, a 25 nm n^+-In$_{0.65}$Al$_{0.35}$As layer followed by a 5 nm n^+-GaSb cap were grown on top of the MQW active region. The band energy diagram (at equilibrium) of an InAs/AlAs$_{0.16}$Sb$_{0.84}$ MQW device with 2 nm thick barriers is shown in Figure 6.1 (b).

6.3. Optical Characterization of the InAs/AlAs$_x$Sb$_{1-x}$ MQW Diodes

Continuous wave photoluminescence (PL) of the MQW structures was assessed using an IR diode laser (1064 nm). The lattice temperature was controlled using a Janis close-cycle system, which can operate between 4.2 K and 300 K. The temperature of the sample was monitored using an Allen-Bradley thermistor. The excitation power of the laser was controlled using reflective neutral density filters. The emitted PL signal from

the sample was dispersed using a SPEX 270M spectrometer and detected by a liquid nitrogen cooled Ge-photodetector.

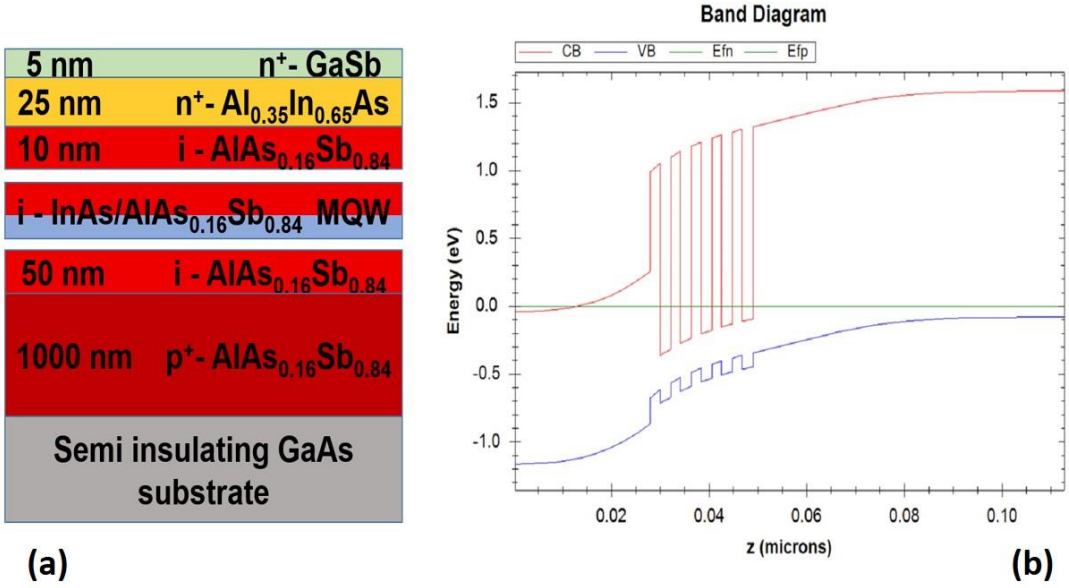

Figure 6. 1. (a) Schematic and (b) band energy diagram of (p-i-n) doped InAs/$AlAs_xSb_{1-x}$ MQW structure. The MQW region consists of 10 repetitions of InAs quantum-wells (2.2 nm) and $AlAs_{0.16}Sb_{0.84}$ barrier materials. The thicknesses of $AlAs_{0.16}Sb_{0.84}$ barrier for the two structures are 2 nm and 5 nm.

Figure 6.2 (a) shows the power dependent photoluminescence for an InAs/$AlAs_{0.16}Sb_{0.84}$ MQW structure with a 5 nm barrier at 77 K. The normalized intensity of the PL spectra plotted on a logarithm scale is shown in Figure 6.2 (a). A clear power dependence of the high energy tail of the PL spectrum is observed, which is indicative of an increase in carrier temperature of the system. Figure 6.2 (b) shows the temperature dependence of the peak energy as a function of $P^{1/3}$ for the same sample. A linear dependence with $P^{1/3}$ is observed, which is indicative of type-II band alignment

at all temperatures. Figure 6.2 (c) shows the temperature difference (ΔT: difference between carrier and lattice temperatures) versus excitation power at temperatures between 77 K and 300 K. It is evident that by increasing excitation power ΔT becomes larger as more hot carriers are created and at 300 K the temperature difference is greatest for all powers. [5, 9, 17] These properties demonstrate the presence of hot carriers in the active region of the device architectures and enable the investigation of their effects in the optoelectronic characteristics of the diodes.

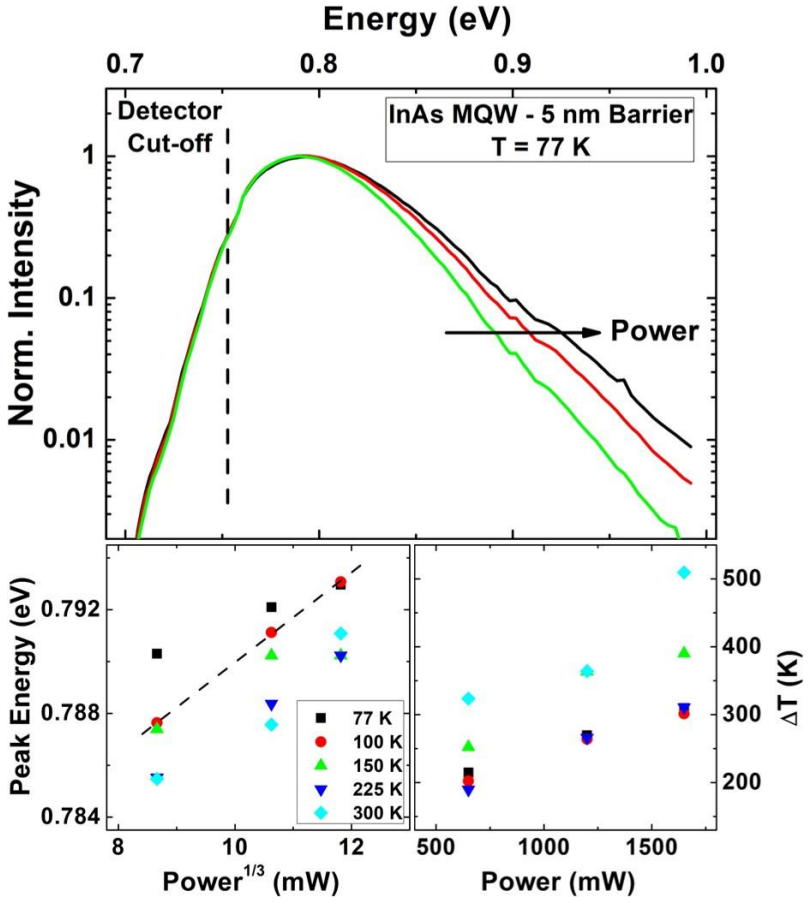

Figure 6. 2. (a) Excitation power dependent PL of 5 nm barrier thick MQW structure at 77 K. (b) Peak energy versus $P^{1/3}$ for various lattice temperatures. (c) Temperature difference (ΔT) against excitation power.

In addition to QW devices with 2 nm and 5 nm barriers, two similar MQW structures (one doped and the other one undoped) were grown on a (001) p^+-InAs substrate. The thickness of $AlAs_{0.16}Sb_{0.84}$ barrier material for both MQW structures was 10 nm. The band energy diagram of the MQW structures for these newer structures is shown in Figure 6.3 (a). The band gap energy value for AlAsSb barrier material is 2.21 eV at room temperature, as determined by NRL MultiBands®, [18] is associated with the direct band gap value for this compound. Since this system is lattice matched, it is possible to grow a thinner buffer layer prior to the MQW region and the quality of the grown MQW is expected to be better.

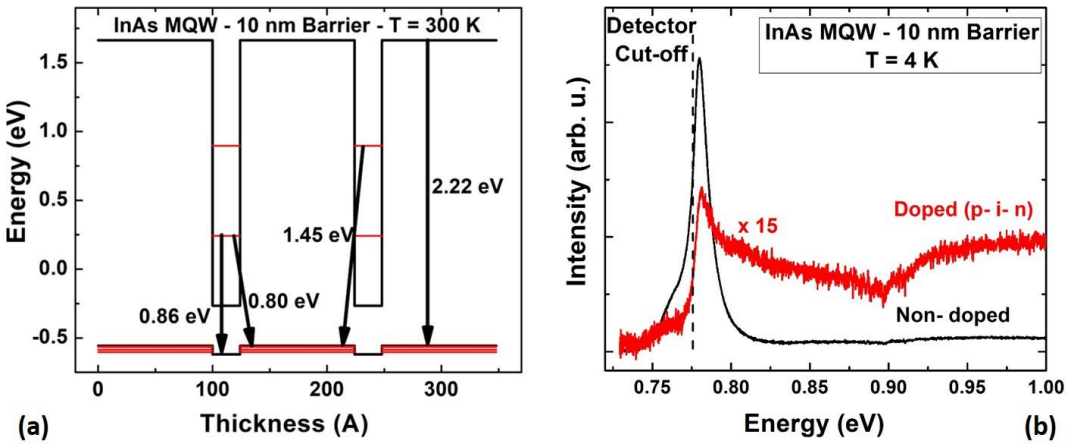

Figure 6. 3. (a) Band energy diagram of 10 nm barrier thick single InAs/$AlAs_{0.16}Sb_{0.84}$ QW structure at 300 K. (b) PL spectra of doped (red) and non-doped (black) InAs MQW at 4 K. Dash line shows where the cut-off energy is for the InGaAs-photodetector.

Figure 6.3 (b) shows a comparison between the PL spectra of the doped and non-doped samples. As is shown in Figure 6.3 (b), the main peak (or the maximum) is very close to the cut-off frequency (energy) of the InGaAs photodetector. In addition, it is

also evident that the emitted PL spectrum from the doped sample is much weaker than that of the undoped sample. This behavior is attributed to the separation of photogenerated charges due to the internal electric field in the intrinsic region of the electrical device. Although the undoped sample has a stronger signal than the doped device, its PL intensity is still relatively weak, even at 4.2 K. This is attributed to the high quality (therefore reduced localization effects) of the type-II QWs, which enables rapid spatial separation of the photogenerated carriers in these devices. The low intensity of the emitted PL signal and the limitation of the InGaAs photodetector inhibit significant further investigation of optical properties of photogenerated hot carriers in the systems. As such, the analysis focuses primarily on the optoelectronic properties of the devices.

6.4. Current density-voltage (J-V) characterizations of $InAs/AlAs_xSb_{1-x}$ MQW diodes

To study the electrical properties of the MQW diodes, metal (ohmic) contacts were deposited on the n- and p-regions. To determine an optimum system (metal) of these layers a comprehensive analysis of various metals and rapid thermal annealing (RTA) conditions were assessed. For a comparative study of the n-region ohmic contacts, four different metal contacts with low work functions were deposited upon the upper n^+-GaSb cap layer on four different samples from the device with 10 nm AlAsSb barriers. [19, 20, 21] It is observed that the deposited metals did not "stick" well on the samples, especially prior to rapid thermal annealing (RTA). However, upon removing the GaSb cap, a better quality of deposition was observed. The GaSb cap layer was therefore

removed by wet chemical etching before full processing. As such, the four low work functions metals were deposited (once more) on the exposed n^+-InAlAs layer. [20, 21] The thickness of deposited metals was ~ 120 nm, followed by a 30 nm gold (Au) layer to improve the quality for subsequent wire bonding. For the back contact on the p^+-InAs substrate, a 120 nm gold layer is deposited for all samples. The deposited metal at the p-layer was kept constant so as to compare the behavior of different contacts for the n-region and to determine the optimum n-contact for these structures.

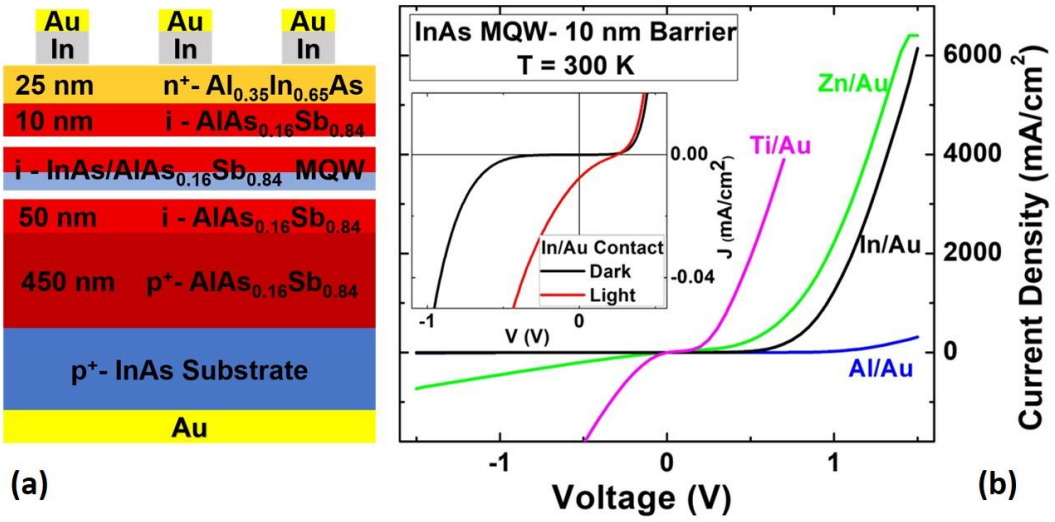

Figure 6. 4. (a) Schematic of 10 nm barrier thick InAs MQW structure with metal contacts. (b) Comparison of dark current density-voltage (J-V) characteristics of 10 nm barrier thick samples with different metal contacts deposited onto the n-region. Inset shows dark (black) and light (red) *J-V* curves for processed sample with In/Au metal contact at the n-region.

Figure 6.4 (a) shows a schematic of the fully processed InAs MQW structure with the 10 nm thick AlAsSb barrier. Figure 6.4 (b) shows the dark current density-voltage (*J-V*) characteristics (when no light is illuminated on the sample) of the structures

comparing the four different metals deposited on the n^+-InAlAs layer at 300 K. By comparing the *J-V* curves of the MQW samples with the different contacts, it is clear that the *J-V* characteristic associated with In/Au contact has the largest turn on voltage (the extrapolated voltage value when a straight line parallel to *J-V* curve at forward bias crosses the horizontal axis) as compared with the other metal contacts. In addition, the amount of extracted current from this In/Au contacted sample is considerable, indicating a lower contact resistance. As a result, the In/Au contact was selected for the n-layer of the device. Although the extracted current in the dark from the MQW structure is large, the amount of short circuit current density (J_{SC}) under illumination for this sample was quite small, even at low temperatures. This is shown as an inset to Figure 6.4, which shows the low temperature (77 K) dark (black) and light current (red) for the MQW structure when a In/Au contact is used. This behavior suggests that it is necessary to find a better contact for the back p-region and further optimize the RTA temperature to improve the device performance.

Figure 6.5 (a) shows *J-V* curves for several different metal contacts on a p^+-AlAsSb epilayer. [20, 21] A schematic of the p^+-AlAsSb epilayer with a metal contact is shown in the inset of Figure 6.5 (a). For further solar cell processing, we have focused on optimizing the ohmic contact of the p^+-AlAsSb layer in order to have a direct comparison among three samples with different barrier thicknesses (2 nm, 5 nm and 10 nm).

Upon optimization, it was determined that a thin layer of Ni (10 nm) deposited on the p^+-AlAsSb layer followed by 120 nm of AuGe alloy (88:12 concentration) produced a high quality metal contact. When comparing other potential candidates for this contact,

it was also observed that poor adhesion occurred for the alloys: Au/Zn/Au and Ni/Au, which "peeled-off" at RTA temperatures above 350 ^{o}C. Moreover, it was observed that the contact resistance measured for AuGe improved by three orders of magnitude when annealed at 275 ^{o}C for 60 seconds. The improvement of the Ni/AuGe contact with respect to the other potential contacts investigated is shown in Figure 6.5 (a). The resistance observed for Ni/AuGe metal contact on the p^{+}-AlAsSb epilayer is clearly less than those of Au/Zn/Au and Ni/Au contacts. As a result, Ni/AuGe was selected as a suitable contact for the p^{+}-AlAsSb layer.

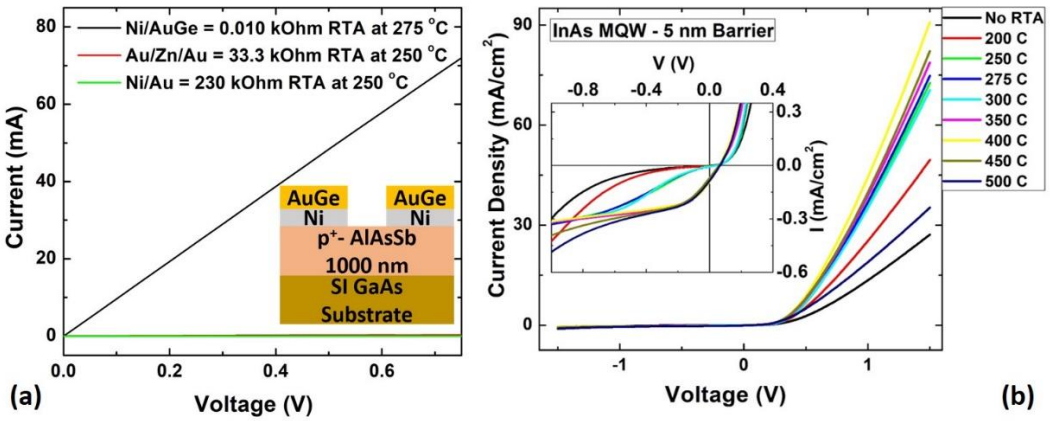

Figure 6. 5. (a) Comparison of current density-voltage (J-V) curves for a p^{+}-AlAsSb epilayer with different metal contacts. Inset shows the schematic of a processed sample with Ni/AuGe metal contacts. (b) *J-V* characteristics of 5 nm barrier thick InAs MQW structure with In/Au (n-region) and Ni/AuGe (p-region) metal contacts at various RTA temperatures.

Figure 6.5 (b) shows the *J-V* characteristics for the MQW structure at various RTA temperatures when In/Au (120 nm / 30 nm) and Ni/AuGe (10 nm / 120 nm) metal contacts are deposited on n-region and p-region, respectively. It is observed that by

increasing the RTA temperature up to 400 ^{o}C, the extracted J_{SC} increases and less leakage (dark) current is observed. However, above 400 ^{o}C an increase in leakage current becomes apparent.

The temperature dependent *J-V* for the p-i-n MQW structure with 10 nm barriers is shown in Figure 6.6. A schematic of the processed solar cell is also shown as an inset to Figure 6.6 (b). In this structure, a lateral contact is created by wet chemically etching the sample down into the p^{+}-AlAsSb layer using Hydrogen Fluoride (HF): Hydrogen Peroxide (H_2O_2): DI Water (H_2O) (1 ml: 2 ml: 40 ml). This solution is not a selective etchant for a particular layer and therefore all the layers in the structure are etched. To create a mesa and enable a lateral contact in the AlAsSb region, the device was etched for 13 seconds exposing a depth of $\sim 700\ nm$.

The temperature dependent dark *J-V* curves for the 10 nm barrier InAs MQW structure are shown in Figure 6.6 (a). It is evident that as the lattice temperature increases the turn on voltages for the *J-V* curves shift to lower values. This effect is consistent with the reduction in the solar cell's band gap energy. However, it is also evident that at elevated lattice temperatures, the reverse leakage current increases. This behavior is indicative of an increase in tunneling of the dark current. The origin of this behavior may be due to: tunneling of the confined electrons within the QW into the n-doped material; or tunneling of electrons (either from the n-doped material or from the potential well) into the valence band of the p-doped material, which is similar to avalanche breakdown or Zener tunneling. [22] Simulations using NRL MultiBands® show that by increasing the width of the last barrier (next to the n-region), the amount of leakage current drops

significantly; further supporting the hypothesis: that unintentional tunneling processes are currently limiting the performance of these devices.

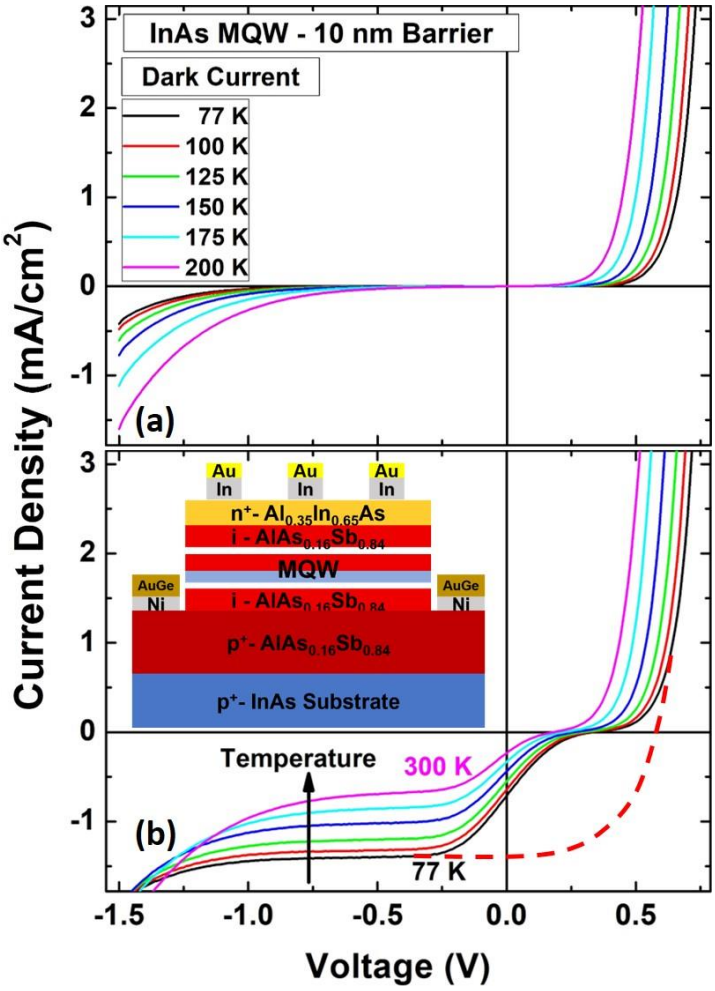

Figure 6. 6. Temperature dependent (a) dark and (b) light J-V characteristics of 10 nm barrier thick InAs MQW structure. Red dashed line in panel (b) shows the shape of J-V curve in the absence of barrier effects. Inset in panel (b) shows a schematic of a processed InAs MQW structure with In/Au contacts on top (n-region) and Ni/AuGe contacts on the sides (lateral contact: p-region).

Figure 6.6 (b) shows *J-V* characteristics of InAs/ $AlAs_{0.16}Sb_{0.84}$ MQW structure with 10 nm barriers under solar illumination at 1 Sun (AM 1.5). In reverse bias J_{SC} saturates, which indicates that all photogenerated carriers are extracted from the sample under these conditions. In the reverse bias regime, the maximum photocurrent is $\sim 1.5\, mA/cm^2$ and stable after $\sim -0.25\, mV$. However, within the PV regime rather than following the ideal response (dashed line) the curvature displays an inflection point, with zero extracted current at $V \sim 0.25$ V. By further increasing the forward bias voltage, the majority current density increases and the normal *J-V* response of a diode is observed. The origin of this perturbation behavior in the PV regime is shown in Figure 6.7, where a schematic of a QW structure with the carrier (electrons) distribution confined within the potential well is shown. [23, 24]

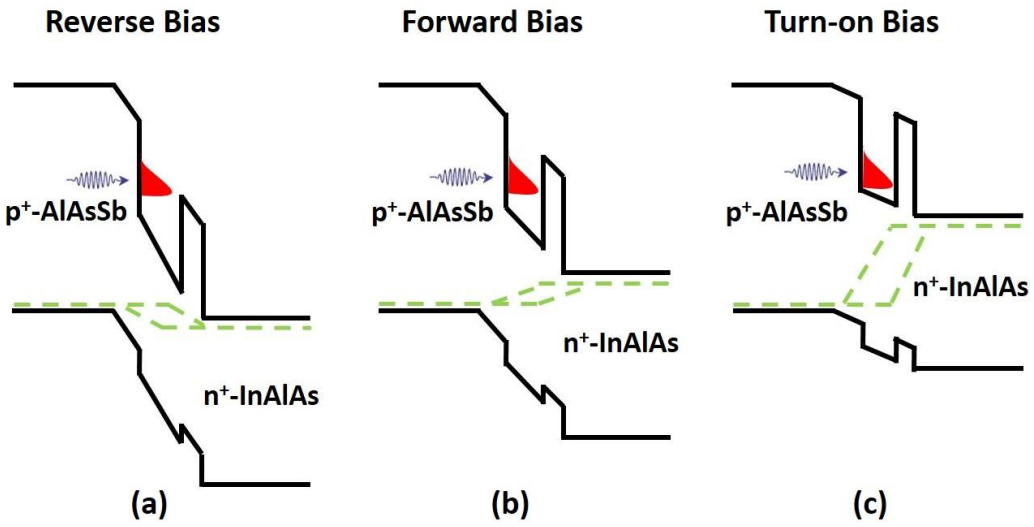

Figure 6. 7. Schematics of a quantum well within the intrinsic region of a p-i-n structure at (a) reverse, (b) forward, and (c) turn-on biases.

Figure 6.7 (a) shows the band bending of a QW structure under reverse bias, which creates large band bending and a decreased barrier due to the high internal electric field. In this condition, photogenerated carriers (electrons) may tunnel through the barrier material and reach the n-region. [22] As a result (especially for a narrow i-region and/or larger values, the case here) in reverse bias, photogenerated carriers may tunnel from the QW increasing the carrier extraction.

However, under low forward bias (see Figure 6.7 (b)) the amount of internal field is reduced therefore, the confinement of photogenerated carriers (electrons) increases. Under these conditions, fewer carriers tunnel through the barrier material, and most of the carriers remain confined within the QW region. This is the condition at which the inflection point is observed in the *J-V* curve. The existence of an inflection point is important, because at this condition it is possible to study the electrical properties of the hot carriers in the system, while the radiative recombination of photogenerated carriers within the QW provides information about the temperature of the carriers in the active region of the device. [23, 24] Figure 6.7 (c) shows a schematic of the band energy diagram for the MQW structure at a turn-on voltage (flat band conditions), when the majority carriers can freely flow across the junction and the diode is "on". Here, the majority current dominates the operation of the device and the system no longer operates as a solar cell.

Several other interesting properties are observed in the temperature dependent behavior of the *J-V* characteristics, shown in Figure 6.6. Increasing the lattice temperature from 77 K (black line) to 200 K (magenta line) results in a reduction in open circuit voltage (V_{OC}). This reduction in V_{OC} is (somewhat) correlated with the

shrinkage of the band gap energy as the lattice temperature increases. [25, 26, 27] However, simultaneously the lattice temperature also decreases the short circuit current density (J_{SC}). This behavior is not typical for group III-V solar cells and implies an increase of the dark saturated current (J_0) in the system with increasing temperature. [26, 28] Moreover, it is evident that increasing the lattice temperature also significantly reduces the strength of the inflection point and the quality of the diode characteristics in the system. This indicates that increasing the lattice temperature not only facilitates the escape of confined carriers within the QW, but enables direct tunneling across the junction; thus, increasing the leakage current and removing the rectification properties of the p-i-n diode.

Figure 6.8 shows temperature dependent *J-V* characteristics of the InAs/$AlAs_{0.16}Sb_{0.84}$ MQW structure with 2 nm barriers. The temperature dependent dark *J-V* curves of the sample are shown in Figure 6.8 (a). It is evident that by increasing the lattice temperature that the turn-on voltage of the *J-V* shifts to much lower values. In addition, there is significant leakage current at reverse bias, which increases dramatically at elevated lattice temperatures. This effect increases significantly as compared to the sample with 10 nm barriers (see Figure 6.7). This further supports the hypothesis: that direct tunneling limits the performance of these devices – since, having thinner barriers would certainly enhance leakage, as is the case here.

In Figure 6.8 (b) shows the temperature dependent *J-V* for the InAs/$AlAs_{0.16}Sb_{0.84}$ MQW structure with 2 nm barriers under 1 Sun (AM 1.5) illumination. At low temperature (77 K – red) there is evidence of an inflection point in forward bias.

However, this effect is not as strong as that observed for the MQW structure with a thicker barrier (10 nm – see Figure 6.6 (b)).

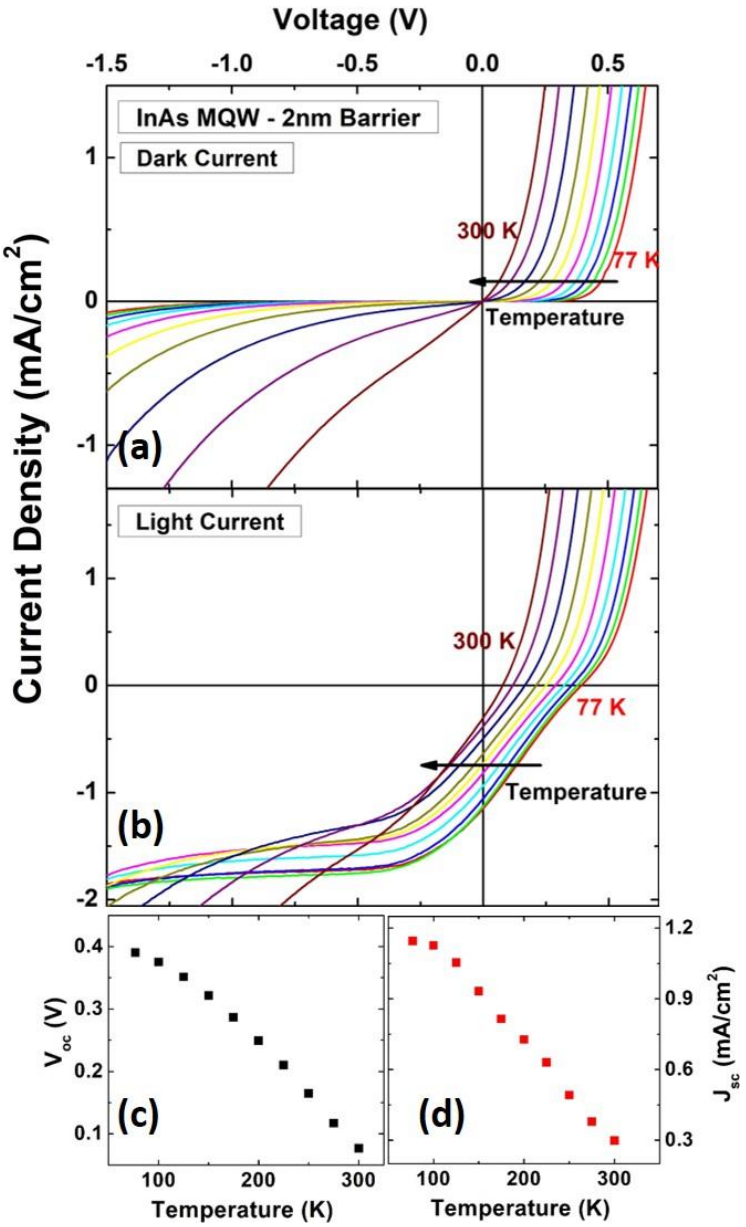

Figure 6. 8. Temperature dependent (a) dark and (b) light J-V curves of 2 nm barrier thick InAs MQW structure from 77 K to 300 K. (c) Open circuit voltage (V_{OC}) as a function of lattice temperature. (d) Short circuit current density (J_{SC}) as a function of lattice temperature.

The less pronounced inflection point for the thinner barriers is (once more) expected, since the probability for carrier penetration through the barrier material is greater in the sample with 2 nm barriers; increasing the lattice temperature results in a total removal of the inflection point in the light *J-V* response, while the leakage current increases significantly. The origin of this behavior is again attributed to tunneling of confined electrons from the QW region into the valence band of the p^+-AlAsSb material.

Figure 6.8 (c) shows V_{OC} versus lattice temperature for the InAs/AlAsSb QW with 2 nm barriers. As the lattice temperature increases, V_{OC} decreases, which is attributed to the dual effects of the reduction of the band gap energy and an increase in the dark current with increasing temperature. [26]

Figure 6.8 (d) shows temperature dependent behavior J_{SC} for the MQW structure with 2 nm barriers. Increasing the lattice temperature results in a reduction in J_{SC}. This behavior is atypical since, the band gap energy reduces as the lattice temperature increases, which increases the absorption of low energy photons. [26] As such, an increase in J_{SC} is expected with increasing lattice temperature, as more of the solar spectrum is harnessed. However, Figure 6.8 (c) shows the opposite trend (i.e. reduction in short circuit current density), which is presumably related to an increase in dark current (J_0) with lattice temperature – the dark current floods the photocurrent.

Figure 6.9 shows temperature dependent *J-V* characteristics of InAs/$AlAs_{0.16}Sb_{0.84}$ QW structure with 5 nm barriers. Figure 6.9 (a) shows temperature dependent *J-V* characteristics in the dark. The turn on voltage once more shifts to lower values with increasing lattice temperature. The amount of leakage current also increases at elevated temperatures, as the leakage current increases.

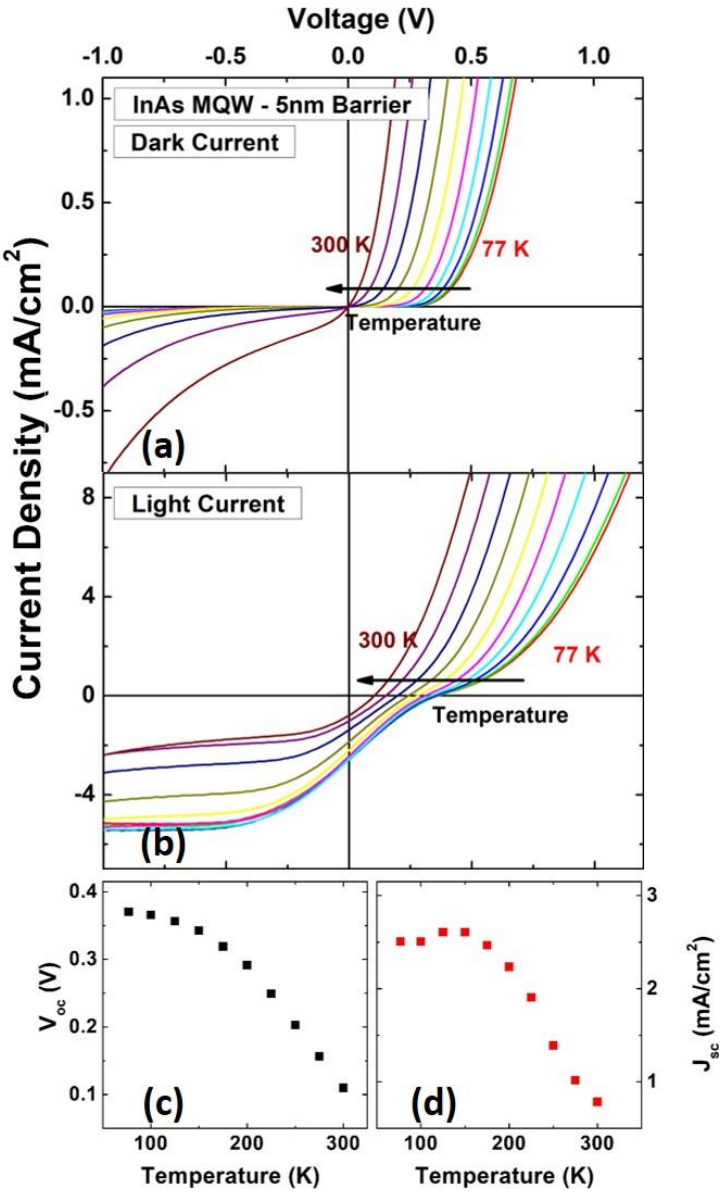

Figure 6. 9. (a) Dark and (b) light J-V curves of 5 nm barrier thick MQW structure for various lattice temperatures between 77 K and 300 K. (c) Open circuit voltage (V_{OC}) against lattice temperature. (d) Short circuit current density (J_{SC}) as a function of lattice temperature.

Figure 6.9 (b) shows temperature dependent *J-V* characteristics under 1-sun (AM 1.5). Under high reverse bias (V< -0.5V) the extracted photocurrent is constant. However, as

the bias voltage increases, an inflection point is again observed in the forward bias region, below the device turn on voltage. Increasing the lattice temperature removes the inflection point as expected, as the photogenerated electrons tunnel through the barrier, along with a decrease in J_{SC} above 150 K. Indeed, similar behavior was observed for both the InAs QWs with 2 nm and 10 nm barriers. The effects and hypothesis for this behavior are well supported by previous measurement of those samples. A comparison between the *J-V* characteristics of the three devices with 2 nm, 5 nm, and 10 nm $AlAs_{0.16}Sb_{0.84}$ (barriers) at 77 K shows the inflection point at forward bias region is more pronounced for the thickest barrier (10 nm) (compare the relative behavior in Figure 6.6 (b), Figure 6.8 (b), and Figure 6.9 (b)). This is expected because as the thickness of the QW barrier is larger: fewer photogenerated electrons will escape the deep QW.

Figure 6.9 (c) shows temperature dependent behavior of V_{OC} for the MQW structure with 5 nm barriers. The V_{OC} drops as the lattice temperature increases, a similar behavior to what has been observed for the two other MQW structures (2 nm and 10 nm barriers). The reduction of V_{OC} is therefore (again) attributed to a combination of both the temperature dependent change in the band gap and an increase in the dark leakage current (J_0) as a function of lattice temperature in these architectures. [25, 29] Figure 6.9 (d) shows the temperature dependence of the J_{SC} for the 5 nm barrier structure under 1-sun illumination. The J_{SC} does not change significantly up to $\sim$ 150 K, and then decreases by increasing temperature. The reduction of J_{SC} (as a function of lattice temperature) is consistent with that observed for the two other MQW structures. The *flattening* of J_{SC} up to 150 K is due to a competition between an increasing contribution

associated with shrinkage of band gap and an increase in dark saturation current (tunneling) at elevated temperatures.

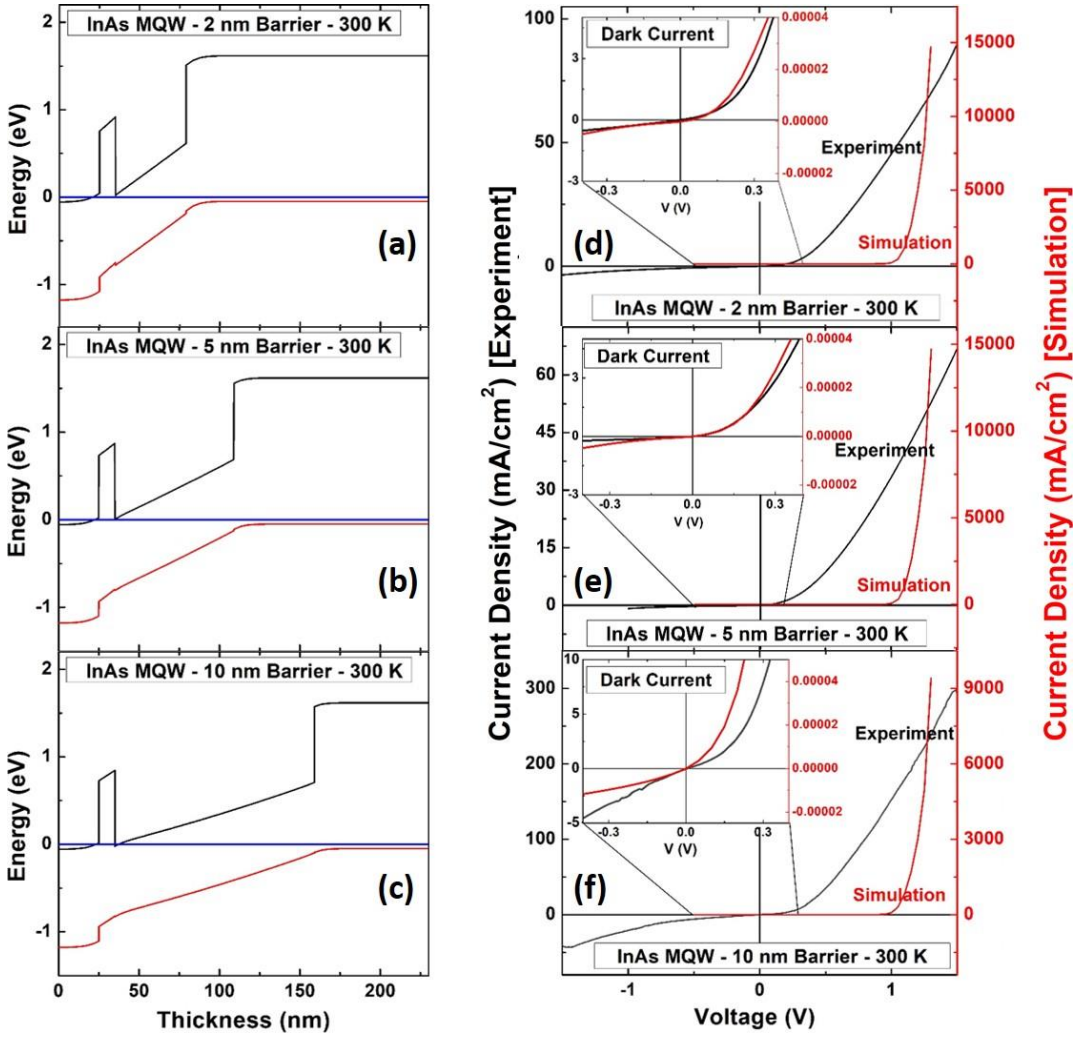

Figure 6. 10. Band diagram of the InAs MQW with (a) 2nm, (b) 5 nm, and (c) 10 nm barriers. The solid black, red, and blue lines show the position of the conduction band, valence band, and Fermi level, respectively. Dark current density J-V characteristics of (d) 2 nm, (e) 5 nm, and (f) 10 nm barrier thickness InAs MQW structures showing the comparison between experiments (black lines) and simulations (red lines). Insets in the figure show expanded views of the J-V characteristics between -0.4 V to 0.4 V.

To further understand the nature of the *J-V* characteristics from the initial InAs MQW devices with different barrier thicknesses, simulations were performed using NRL MultiBands® and the results compared with the experimental data.

Figure 6.10 shows the band diagram for the InAs/$AlAs_{0.16}Sb_{0.84}$ MQW devices with (a) 2 nm, (b) 5 nm, and (c) 10 nm barriers, respectively. The Fermi levels at equilibrium in these structures are displayed in blue. For these simulations, the MQW region is considered and shown as *one* large well in the individual band diagrams with effective band gaps and properties calculated by NRL MultiBands®.

Figure 6.10 also shows comparisons of the experimental and simulated dark *J-V* data for the (d) 2 nm, (e) 5 nm, and (f) 10 nm structures, respectively. It is clear that there is significant leakage current at reverse bias in all the MQW structures. As shown in the insets to Figure(s) 6.10 (d), (e), and (f), leakage current is evident in reverse bias for both the experimental (black) and simulated (red) results. As discussed, the origin of the leakage current for these samples is likely due to tunneling effects, which occurs across the active region of the MQW structures. This tunneling is facilitated by quantum tunneling by the conduction band electrons from the n-region into the valence band of the p-doped material. This effect is similar to Zener-type effects, which are more probable for highly doped p-n junctions with narrow depletion widths. [30, 31] The amount of turn-on voltage predicted by the model is much larger than that observed in experiment. This is attributed to the ideality of the material parameters and offsets inferred in the simulation, which do not reflect completely either the experimental inhomogeneities or tunneling processes. [32]

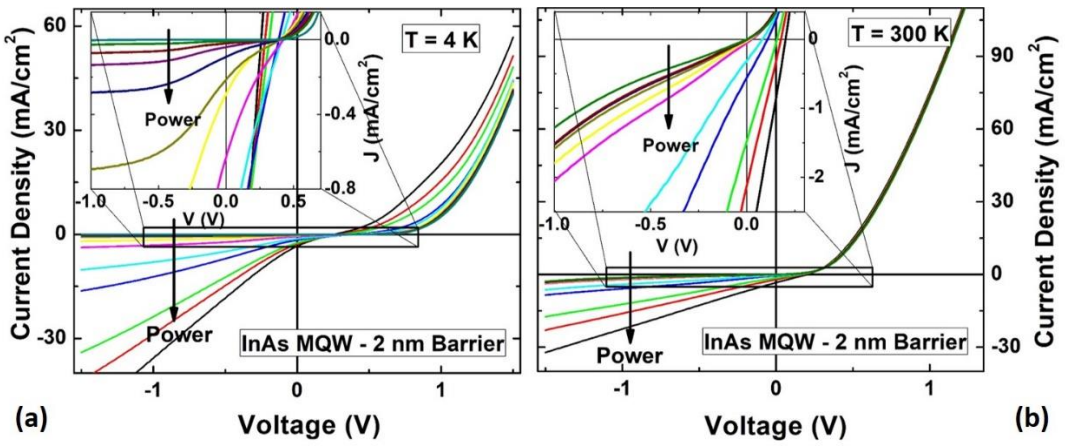

Figure 6. 11. Excitation power dependent J-V characteristics of 2 nm barrier thick InAs MQW structure at (a) 4 K and (b) 300 K. Insets in both panels show the expanded view of low excitation powers J-V curves for the MQW structure.

Figure 6.11 shows the excitation power dependence (using a monochromatic diode laser (1064 nm)) of the InAs/AlAsSb MQW device with 2 nm barriers at (a) 4 K and (b) 300 K, respectively. The insets in Figures 6.11 (a) and (b) show a "zoomed-in" region for the *J-V* characteristics (around $V \approx 0$ and $J_{SC} \approx 0$). As shown in the inset of Figure 6.11 (a), at low excitation powers inflection points due to the localization of photogenerated carriers (electrons) are evident. However, as the excitation power increases the inflection point becomes smaller and at very high excitation powers it is removed completely. In addition, it is also observed that at low excitation, the *J-V* curve in reverse bias saturates, which is indicative of a low leakage current. However as excitation power increases, the *J-V* curves show a large leakage current in reverse bias (see black and red in Figure 6.11 (a)). Similar behavior is observed for all the MQW structures studied. Previously the temperature dependent *J-V* characteristics for the

samples displayed increasing leakage current in reverse bias region with increasing temperature. Hence, there is a correlation between the increased lattice temperature (thermal population of the carriers) and the excitation power: under both conditions, the carrier distribution within InAs QWs increases and facilitates tunneling of localized electrons from the QWs.

Figure 6.11 (b) shows excitation power dependent behavior of the MQW structure with 2 nm barriers at 300 K. No inflection point is observed in the *J-V* characteristics of the sample in the forward bias region. Moreover, the amount of leakage current in reverse bias is large. Similar behavior has been observed for all other MQW structures (different barrier thicknesses). The origin of this behavior is currently under further investigation, but (again) it seems to be related to the thin active region and associated high field across the intrinsic region.

To study hot carriers in the system, we performed a similar investigation to Hirst, *et al.*, [23] where localized photogenerated electrons within shallow InGaAs QW were studied as a function of excitation power at low temperatures. It is expected that when the excitation power increases, the hot carrier population within the quantum well increases and therefore the photogenerated hot carriers can escape from the QW due to their lower confined energy. It is possible therefore, to evaluate the hot carrier behavior when the doped p-i-n MQW devices are under bias particularly, at the inflection point. At this condition, both the photogenerated hot carrier temperature and extracted current from the MQW structure can be measured by using a combination of photoluminescence and *J-V*. Thus, any effects related to the hot carrier temperature can be correlated to the electrical response of the device.

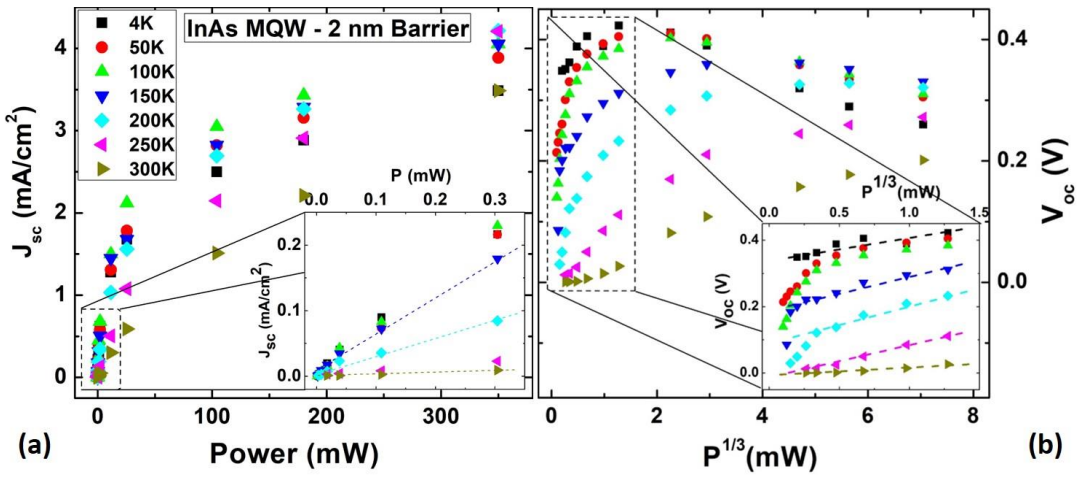

Figure 6. 12. (a) Extracted short circuit current density (J_{SC}) from J-V characteristics of 2 nm barrier thick MQW structure as a function of excitation power for various lattice temperatures. Inset shows the expanded view for low excitation powers. Dash lines in the inset are indicative of linear dependence between J_{SC} and P at low excitation powers. (b) Extracted open circuit voltage (V_{OC}) from J-V characteristics of 2 nm barrier thick MQW structure versus $P^{1/3}$. Inset in this figure shows the expanded view of the graph at the range of excitation powers where a linear dependence (which are shown by colored dashed lines) between V_{OC} and $P^{1/3}$ is observed.

Figure 6.12 (a) shows J_{SC} versus excitation power for various lattice temperatures for the InAs $AlAs_{0.16}Sb_{0.84}$ MQW with 2 nm barriers. With increasing excitation power, the J_{SC} increases. The inset of Figure 6.12 (a) highlights the behavior at low excitation powers. At low excitation power, there is a linear dependence on J_{SC}. This indicates that at lower powers the percentage of photogenerated carriers, which can escape is constant. This behavior is observed for all lattice temperatures. However with increasing the excitation power, the linear dependence of J_{SC} is removed and begins to saturate as

fewer photogenerated carriers are extracted. The origin of this behavior is *tentatively* attributed to the presence of a non-radiative process such as Shockley-Reed-Hall (SHR) and/or Auger recombination, which are dominant at higher excitation powers; although, this requires further investigation.

Figure 6.12 (b) shows the excitation dependent V_{OC} of MQW structure with a 2 nm barrier versus $P^{1/3}$ between 4 K and 300 K. The inset of Figure 6.12 (b) shows that there is a linear dependence (shown by colored dashed lines) of V_{OC} with $P^{1/3}$ at low powers. This linear dependence between V_{OC} and $P^{1/3}$ is indicative of the blueshift that results with increasing power from transitions created at the interface of the type-II MQW (see discussion in Chapter 4.3.1). In Figure 6.12 (b) it is also evident that by increasing the excitation power V_{OC} increases. For temperatures below 250 K there is a noticeable drop in V_{OC} at higher excitation powers. This effect becomes more pronounced as the temperature decreases; at 4 K the threshold power is only ~ 2 mW. This reduction in V_{OC} (at higher excitation powers) is related to an increase in the dark saturation current (J_0) with increased excitation and the subsequent increased leakage via tunneling of carriers localized in the MQWs.

Figure 6.13 shows the temperature dependent concentrated *J-V* behavior for the InAs/AlAsSb MQW with 2 nm barriers at (a) 2 × AM 1.5 (2 Suns) and (b) 22 × AM 1.5 (22 Suns). At 2 Suns, there is an obvious inflection point due to the barrier effect (see Figure 6.13 (a)). However as the lattice temperature is increased, this inflection point becomes less pronounced and a large leakage current is observed in reverse bias. At higher suns concentration (22 Suns, see Figure 6.13 (b)), there is no significant shift in the V_{OC} between 77 K and 300 K, while the *J-V* characteristics show large leakage

currents in reverse bias, even at low temperatures. Similar behavior was observed with monochromatic excitation laser (1064 nm) indicating that the high intensity excitation of these concentration measurements facilitates significant leakage in the devices.

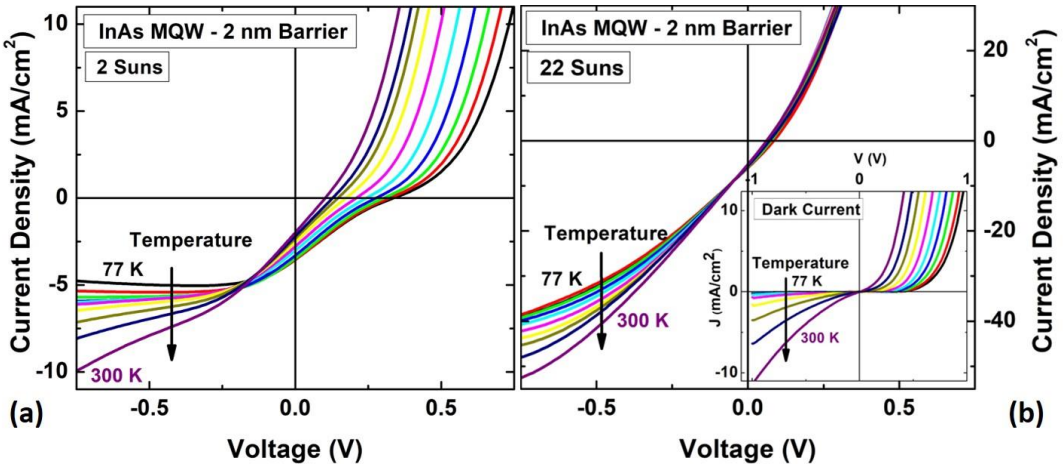

Figure 6. 13. Temperature dependent J-V characteristics of 2 nm barrier thick MQW structure at (a) 2 Suns (AM 1.5) and (b) concentrated (22 Suns) conditions. Inset in panel (b) shows dark J-V characteristics of 2 nm barrier MQW structure.

Figure 6.14 shows *J-V* characteristics of the MQW (2 nm) at (a) 77 K and (b) 300 K under various solar concentrations. In Figure 6.14 (a) at 2 suns (black line), the *J-V* characteristic displays an inflection point in forward bias and full photogenerated carrier extraction at $V < -0.25$ V. As the illumination increases, J_{SC} increases, as expected. However, V_{OC} shifts towards lower values. This behavior is evident for all solar concentrations, except at the highest concentration (cyan line) where both V_{OC} and J_{SC} shift to zero. Figure 6.14 (b) shows the *J-V* characteristics of InAs/AlAsSb MQW with the 2 nm barriers at 300 K. It is evident that at room temperature V_{OC} decreases with increasing concentration. However, the J_{SC} increases at higher concentrations (except

for the highest illumination). Figure 6.14 (c) shows the change in V_{OC} versus solar concentration for the MQW structure with 2 nm barriers at 77 K (black squares) and 300 K (red circles), respectively. It is observed that increasing the concentration causes the V_{OC} to drop for both lattice temperatures (77 K and 300 K). As has been discussed, this large drop in V_{OC} values is correlated with an increase in leakage current or enhanced dark current across the junction. [32]

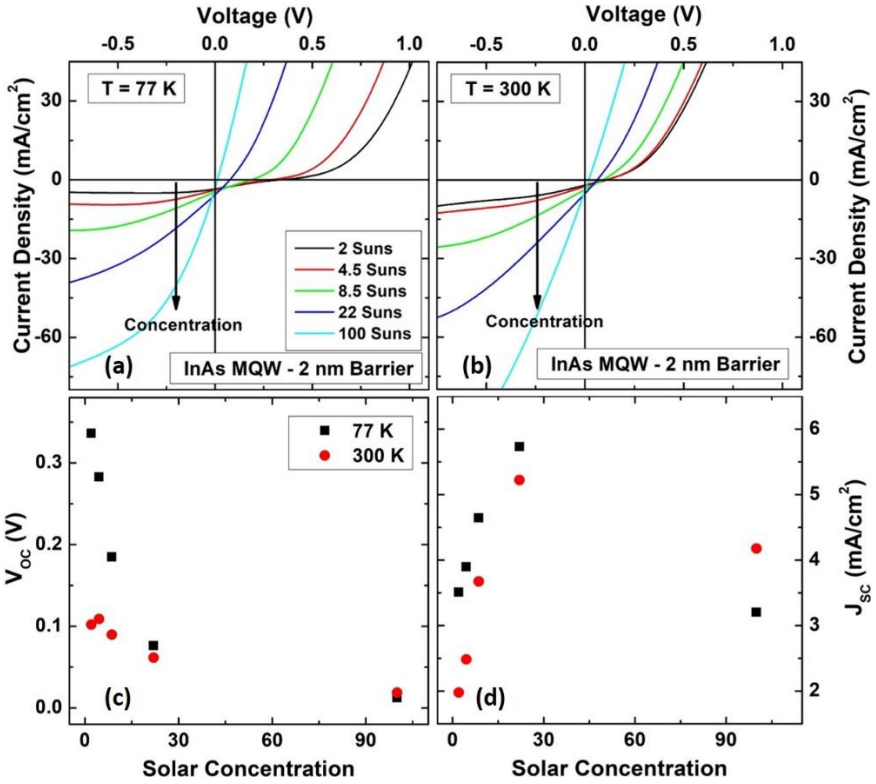

Figure 6. 14. J-V characteristic of 2 nm barrier thick MQW structure at various solar concentrations at (a) 77 K and (b) 300 K. Extracted V_{OC} and J_{SC} of the MQW structure are shown in panels (c) and (d), respectively.

Figure 6.14 (d) shows J_{SC} versus solar concentration at 77 K and 300 K, extracted from the data in panels (a) and (b), respectively. By increasing the concentration level,

J_{SC} increases up to a maximum value. However, at very high excitation powers a drop in J_{SC} is observed. The origin of this behavior is similar to behavior observed in several samples. Recent simulations suggest that this is related to high temperature and/or excitation induced tunneling (i.e., breakdown of the junction), which results in the loss of rectification of the diode. New designs with thick blocking barriers support this hypothesis.

6.5. External quantum efficiency (EQE) characterizations of InAs/AlAs$_x$Sb$_{1-x}$ MQW diodes

Figure 6.15 (a), (b), and (c) show a comparison of the external quantum efficiencies (EQEs) of the InAs/AlAsSb MQW diodes with 2 nm, 5 nm, and 10 nm barriers at 80 K, respectively. The red dashed lines in the graphs are a guide-to-the-eye to allow correlation amongst various features in the samples. Figure 6.15 (d), (e) and (f) show the associated band energy diagrams of the MQW structures at 80 K. Also shown in the band diagrams of the samples are all possible optical transitions that may occur in these systems. Although the difference in barrier thickness changes the amount of total confinement within the QWs, it is still possible qualitatively to compare the optical transitions (which is observable in EQE graphs) in these three devices.

The transition (E1) at ~ 0.85 eV, is close to the simulated spatially indirect transition across the QW ground state. This transition is observed as a shoulder in EQE and its position varies slightly for each MQW sample as expected due to the difference in barrier thicknesses; the energy of the QW ground state transition is slightly lower when the barrier thickness increases. [33]

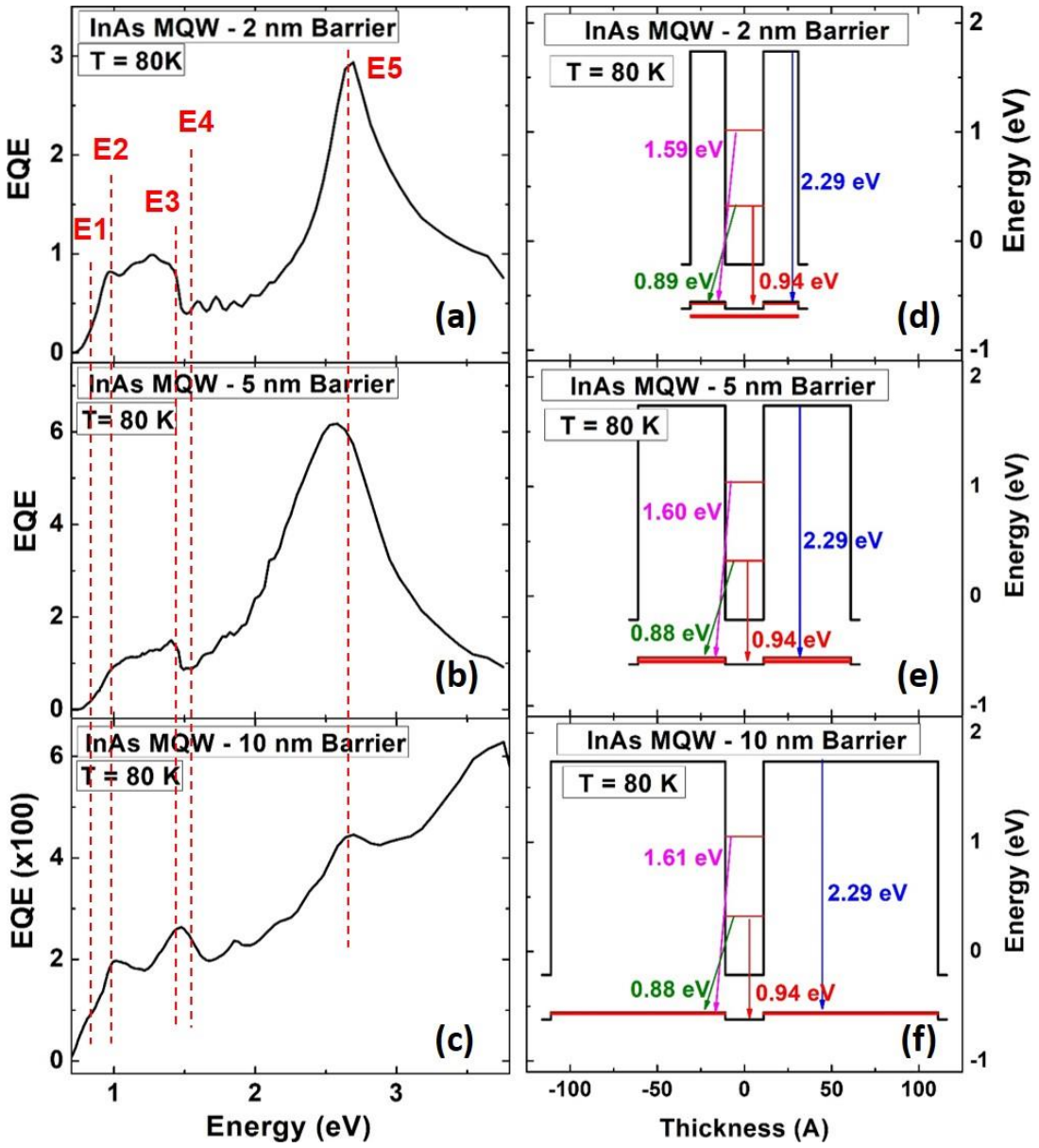

Figure 6. 15. External quantum efficiency (EQE) of MQW structures with 2 nm (a), 5 nm (b), and 10 nm (c) barrier thicknesses at 80 K. Red dash lines show where some features are in EQE graphs. (d)-(f) show band energy diagrams of 2 nm, 5 nm, and 10 nm barrier thick InAs/AlAsSb QW structure at 80 K, respectively.

The lowest energy spatially indirect transition for the QW structures is close to the simulated result for this transition (e1-hh1) at 80 K, which is ~ 0.88 eV (see the green arrows in Figure(s) 6.15 (d-f)). In addition, it is evident that the spatially indirect transition for all the MQW structures does not change significantly, despite the difference in barrier thickness (0.88 $\pm$ 0.01 eV).

The transition (E2) at ~ 0.95 eV is attributed to the direct transition of the InAs QW at 80 K. This energy is consistent with that determined from NRL MultiBands® at ~ 0.94 eV (red line). The transition (E3) at 1.40 eV is associated with absorption in the n^+-InAlAs layer. While (E4) at ~ 1.50 eV (seen as a valley in experimental EQE of 2 nm and 5 nm barrier thickness samples shown in Figure(s) 6.15 (a-c)) is related to absorption in the semi-insulating (SI) GaAs substrate. This feature is absent in the sample with the 10 nm barriers since this device was grown on p^+-InAs.

The fifth transition (E5) at ~ 2.65 eV is related to absorption in the p^+-AlAsSb buffer layer. The absorption peak at this energy is significant for all samples and reflects the relative thickness (therefore absorption) of this material in all the devices. There are slight shifts in the respective peak positions when comparing the individual samples. This is attributed to the existence of strain in the system, which varies from sample to sample. The transition calculated for the AlAsSb barrier occurs at ~ 2.29 eV at 80 K (blue line) as shown in Figure 6.15 (d)-(f). This somewhat less than that observed experimentally (see Figure 6.15 (a)-(c)). The origin of the difference between experiment and simulation is still under investigation, but likely reflects inhomogeneity in the system and/or coupling between direct/indirect or higher order valleys in the system.

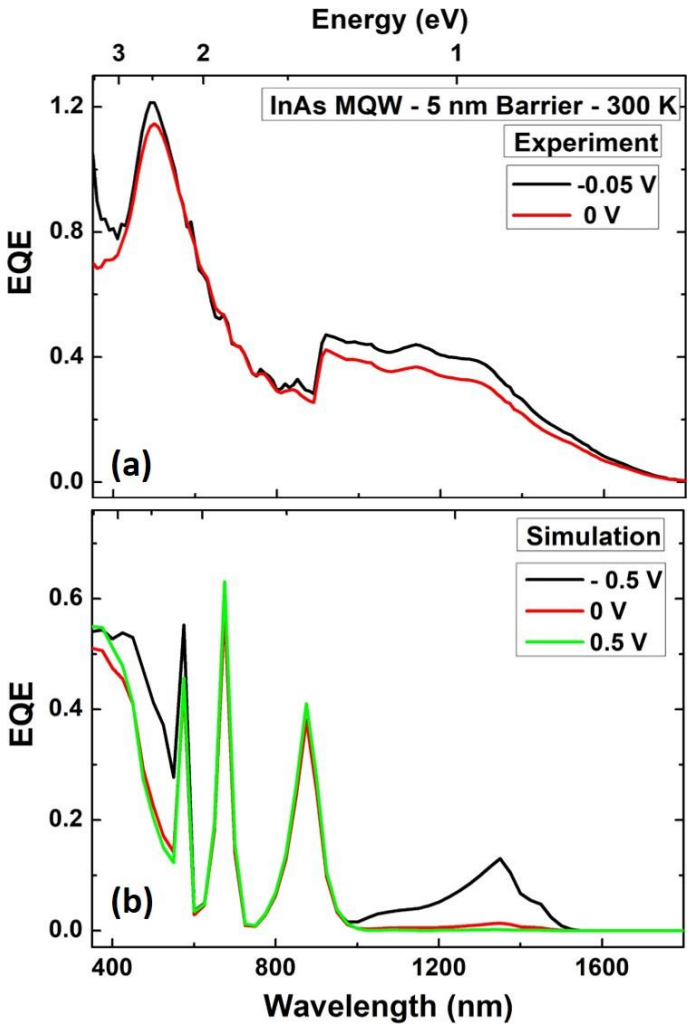

Figure 6. 16. (a) Experimental and (b) simulation results of bias dependent EQE at 300 K for 5 nm barrier thick InAs MQW structure.

Figure 6.16 (a) shows *bias dependent* EQE of InAs/AlAsSb for a MQW device with 5 nm barriers at 300 K over the range -0.05 V to 0 V. It is evident that by increasing the bias voltage from reverse to 0 V, the EQE decreases. In this MQW device, the reduction in applied reverse voltage will reduce tunneling effects. As a result, less localized carriers can escape through the barrier material into n-doped region. Figure 6.16 (b)

shows simulation results of bias dependent behavior of the QW structure at three biases (-0.5 V, 0 V, and 0.5 V). It is evident that the EQE peaks due to the QW region (both direct transition at 1348 nm or 0.91 eV, and the spatially indirect transition at 1460 nm or 0.85 eV) reduce by increasing the bias from -0.5 V to 0.5 V. This trend is consistent with the one observed experimentally: the competition between majority and minority carrier transport and photogenerated carrier confinement in the MQWs.

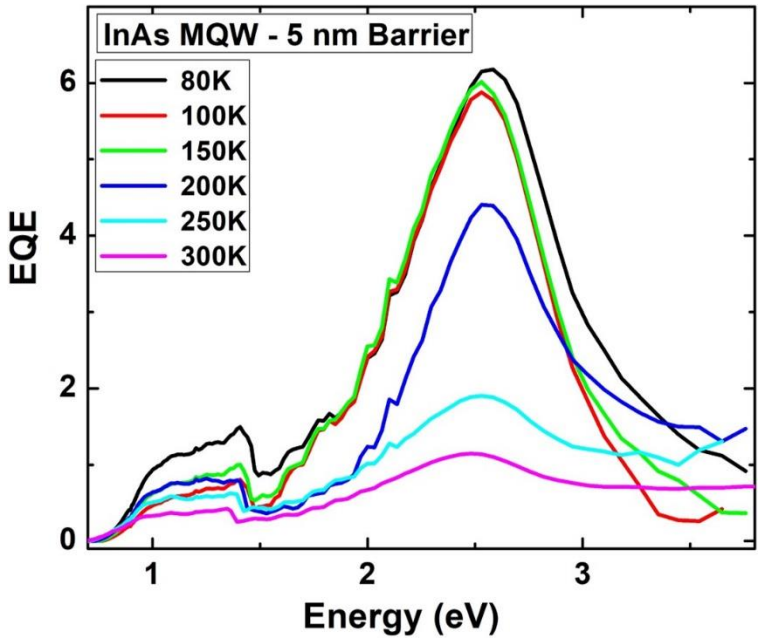

Figure 6. 17. Temperature dependent EQE behavior for 5 nm barrier thick InAs MQW structure.

Figure 6.17 shows temperature dependent EQE for the InAs MQW with 5 nm barriers. It is evident that increasing the lattice temperature (T > 150 K) results in a reduction in absolute EQE. Similar behavior is observed for all three MQW structures with increasing lattice temperature. This effect is consistent with that observed for temperature dependent *J-V* where the minority carrier extraction is overwhelmed by the

dark leakage current at higher temperatures. Moreover, the fact that the EQE of 5 nm barrier MQW samples does not change significantly below ~ 150 K also reflects the effect observed in the light J-V for this sample's characteristics (see Figure 6.9 (d)) – where no considerable drop is observed for J_{SC} up to 150 K, prior to significant leakage across the device.

Conclusion

In this chapter, the optical and electrical properties of several InAs/$AlAs_{0.16}Sb_{0.84}$ MQW p-i-n diodes with three different barrier thicknesses (2 nm, 5 nm, and 10 nm) were assessed to evaluate possible hot carrier effects in their optoelectronic properties. It is observed that at low temperature and excitation power (both monochromatic and solar illumination) inflection points are evident in the current density-voltage characteristics of all MQW structures – the effect of which increases as barrier thickness increases (2nm to 10 nm). This behavior is attributed to strong localization of the photogenerated carriers in the deep InAs/AlAsSb MQWs in the active region of the pin diode. However as the excitation power and lattice temperature are increase, this inflection point is reduced indicating a significant decrease in carrier confinement and direct tunneling across the intrinsic region of the device. This is evidenced by the fact that at high excitation powers (as well as elevated lattice temperatures) large dark leakage current is observed. Moreover, bias-dependent external quantum efficiency (EQE) measurements of the MQW structures and as a function of lattice temperature have been measured, as well as simulated. The simulations qualitatively reproduce the experiment very well, producing several well defined optical transitions in the system.

These results indicate that the thickness of the active region in the devices must be increased and/or the implementation of blocking layers is required to prevent dark leakage currents degrading the performance of these systems. A new set of devices are now under investigation and will be reported soon.

References

[1] Shockley, William, and Hans J. Queisser. "Detailed balance limit of efficiency of p-n junction solar cells." Journal of applied physics 32, no. 3 (1961): 510-519.

[2] Ross, Robert T., and Arthur J. Nozik. "Efficiency of hot-carrier solar energy converters." Journal of Applied Physics 53, no. 5 (1982): 3813-3818.

[3] Green, Martin A. "Third generation photovoltaics: Ultra-high conversion efficiency at low cost." Progress in Photovoltaics: Research and Applications 9, no. 2 (2001): 123-135.

[4] Conibeer, Gavin, Nicholas Ekins-Daukes, Jean-François Guillemoles, Dirk Kőnig, Eun-Chel Cho, Chu-Wei Jiang, Santosh Shrestha, and Martin Green. "Progress on hot carrier cells." Solar Energy Materials and Solar Cells 93, no. 6-7 (2009): 713-719.

[5] Le Bris, A., L. Lombez, S. Laribi, G. Boissier, P. Christol, and J-F. Guillemoles. "Thermalisation rate study of GaSb-based heterostructures by continuous wave photoluminescence and their potential as hot carrier solar cell absorbers." Energy & Environmental Science 5, no. 3 (2012): 6225-6232.

[6] Hirst, Louise C., Hiromasa Fujii, Yunpeng Wang, Masakazu Sugiyama, and Nicholas J. Ekins-Daukes. "Hot carriers in quantum wells for photovoltaic efficiency enhancement." IEEE Journal of Photovoltaics 4, no. 1 (2014): 244-252.

[7] Dimmock, James AR, Stephen Day, Matthias Kauer, Katherine Smith, and Jon Heffernan. "Demonstration of a hot-carrier photovoltaic cell." Progress in Photovoltaics: Research and Applications 22, no. 2 (2014): 151-160.

[8] Conibeer, G. J., C-W. Jiang, D. König, S. Shrestha, T. Walsh, and M. A. Green. "Selective energy contacts for hot carrier solar cells." Thin Solid Films 516, no. 20 (2008): 6968-6973.

[9] Esmaielpour, Hamidreza, Vincent R. Whiteside, Jinfeng Tang, Sangeetha Vijeyaragunathan, Tetsuya D. Mishima, Shayne Cairns, Michael B. Santos, Bin Wang, and Ian R. Sellers. "Suppression of phonon-mediated hot carrier relaxation in type-II InAs/AlAsxSb1− x quantum wells: a practical route to hot carrier solar cells." Progress in Photovoltaics: Research and Applications 24, no. 5 (2016): 591-599.

[10] Tang, J., V. R. Whiteside, H. Esmaielpour, S. Vijeyaragunathan, T. D. Mishima, M. B. Santos, and I. R. Sellers. "Effects of localization on hot carriers in InAs/$AlAs_xSb_{1-x}$ quantum wells." Applied Physics Letters 106, no. 6 (2015): 061902.

[11] Conibeer, Gavin, Robert Patterson, Lunmei Huang, Jean-Francois Guillemoles, Dirk Kőnig, Santosh Shrestha, and Martin A. Green. "Modelling of hot carrier solar cell absorbers." Solar energy materials and solar cells 94, no. 9 (2010): 1516-1521.

[12] König, Dirk, K. Casalenuovo, Y. Takeda, G. Conibeer, J. F. Guillemoles, R. Patterson, L. M. Huang, and M. A. Green. "Hot carrier solar cells: Principles,

materials and design." Physica E: Low-dimensional Systems and Nanostructures 42, no. 10 (2010): 2862-2866.

[13] Yao, Yao, Dirk König, and Martin Green. "Investigation of boron antimonide as hot carrier absorber material." Solar Energy Materials and Solar Cells 111 (2013): 123-126.

[14] Conibeer, Gavin, Santosh Shrestha, Shujuan Huang, Robert Patterson, Hongze Xia, Yu Feng, Pengfei Zhang *et al.* "Hot carrier solar cell absorber prerequisites and candidate material systems." Solar Energy Materials and Solar Cells 135 (2015): 124-129.

[15] König, D., Y. Takeda, and B. Puthen-Veettil. "Technology-compatible hot carrier solar cell with energy selective hot carrier absorber and carrier-selective contacts." Applied Physics Letters 101, no. 15 (2012): 153901.

[16] Esmaielpour, Hamidreza, Vincent R. Whiteside, Herath P. Piyathilaka, Sangeetha Vijeyaragunathan, Bin Wang, Echo Adcock-Smith, Kenneth P. Roberts *et al.* "Enhanced hot electron lifetimes in quantum wells with inhibited phonon coupling." Scientific reports 8, no. 1 (2018): 12473.

[17] Shah, Jagdeep. "Hot carriers in quasi-2-D polar semiconductors." IEEE Journal of Quantum electronics 22, no. 9 (1986): 1728-1743.

[18] Lumb, Matthew P., Igor Vurgaftman, Chaffra A. Affouda, Jerry R. Meyer, Edward H. Aifer, and Robert J. Walters. "Quantum wells and superlattices for III-V photovoltaics and photodetectors." In Next Generation (Nano) Photonic and Cell

Technologies for Solar Energy Conversion III, vol. 8471, p. 84710A. International Society for Optics and Photonics, 2012.

[19] Villemain, E., S. Gaillard, M. Rolland, and A. Joullie. "Characterization of ohmic contacts on n-and p-type GaSb." Materials Science and Engineering: B 20, no. 1-2 (1993): 162-164.

[20] Baca, A. G., F. Ren, J. C. Zolper, R. D. Briggs, and S. J. Pearton. "A survey of ohmic contacts to III-V compound semiconductors." Thin Solid Films 308 (1997): 599-606.

[21] Hölzl, Josef, and Franz K. Schulte. "Work function of metals." In Solid Surface Physics, pp. 1-150. Springer, Berlin, Heidelberg, 1979.

[22] Fair, Richard B., and Hayden W. Wivell. "Zener and avalanche breakdown in As-implanted low-voltage Si np junctions." IEEE Transactions on Electron Devices 23, no. 5 (1976): 512-518.

[23] Hirst, L. C., R. J. Walters, M. F. Führer, and N. J. Ekins-Daukes. "Experimental demonstration of hot-carrier photo-current in an InGaAs quantum well solar cell." Applied Physics Letters 104, no. 23 (2014): 231115.

[24] Esmaielpour, H., V. R. Whiteside, H. P. Piyathilaka, S. Vijeyaragunathan, B. Wang, K. P. Roberts, T. D. Mishima *et al.* "Control of hot carrier thermalization in type-II quantum wells: a route to practical hot carrier solar cells." In 2018 IEEE 7th World Conference on Photovoltaic Energy Conversion (WCPEC) (A Joint Conference of 45th IEEE PVSC, 28th PVSEC & 34th EU PVSEC), pp. 3682-3684. IEEE, 2018.

[25] Löper, P., D. Pysch, A. Richter, M. Hermle, S. Janz, M. Zacharias, and S. W. Glunz. "Analysis of the temperature dependence of the open-circuit voltage." Energy Procedia 27 (2012): 135-142.

[26] Singh, Priyanka, and N. Mr Ravindra. "Temperature dependence of solar cell performance—an analysis." Solar Energy Materials and Solar Cells 101 (2012): 36-45.

[27] Cotfas, Daniel Tudor, Petru Adrian Cotfas, and Octavian Mihai Machidon. "Study of Temperature Coefficients for Parameters of Photovoltaic Cells." International Journal of Photoenergy (2018).

[28] Cheng, Yang, "Quantum Dots for Photovoltaic Applications." Doctoral Dissertation, University of Oklahoma, 2017.

[29] Cheng, Y., M. D. C. Whitaker, R. Makkia, S. Cocklin, V. R. Whiteside, L. A. Bumm, E. Adcock-Smith, K. P. Roberts, P. Hari, and I. R. Sellers. "Role of Defects and Surface States in the Carrier Transport and Nonlinearity of the Diode Characteristics in PbS/ZnO Quantum Dot Solar Cells." ACS applied materials & interfaces 9, no. 15 (2017): 13269-13277.

[30] Hayden, Oliver, Ritesh Agarwal, and Charles M. Lieber. "Nanoscale avalanche photodiodes for highly sensitive and spatially resolved photon detection." Nature materials 5, no. 5 (2006): 352.

[31] Tian, Bozhi, Xiaolin Zheng, Thomas J. Kempa, Ying Fang, Nanfang Yu, Guihua Yu, Jinlin Huang, and Charles M. Lieber. "Coaxial silicon nanowires as solar cells and nanoelectronic power sources." nature 449, no. 7164 (2007): 885.

[32] Nelson, Jenny. The physics of solar cells. World Scientific Publishing Company, 2003.

[33] Zettili, Nouredine. "Quantum mechanics: concepts and applications." (2003).

Chapter **7**

Interface properties and non-idealities in InGaAsP and InP quantum wells encapsulated in AlInAs

7.1. Introduction

The $In_xGa_{1-x}As_{1-y}P_y/In_zAl_{1-z}As$ system has been developed for several applications including lasers, photodetectors, and optoelectronic devices. [1, 2, 3] Here, the InGaAsP quantum well (QW) system has been discussed previously (Chapter 4) to study the effects of excited state transitions and photoluminescence (PL) linewidth broadening on the determination of carrier temperature in hot carrier absorbers. This system has the advantage that a large range of band gaps can be realized through changing the composition of phosphorous (P) in the structure. At y = 0.6, a transition from a type-I to type-II band alignment occurs, the valence band is 'degenerate' at that composition. [4] This design is analogous to the InAs/AlAsSb system presented previously, which has been studied as a candidate system for hot carrier absorber applications. [5, 6, 7] As such, the $In_xGa_{1-x}As_{1-y}P_y/In_zAl_{1-z}As$ system provides a further test bed for the potential of the validity of physical characteristics of type-II systems for hot carrier applications.

The InGaAsP QW investigated is lattice matched with InP, and as such an InP cap layer is typically grown on top of the structure to serve as an isolation layer to avoid oxidation of the upper InAlAs layer. However, as has already been discussed the interface between localized states that form between InP and InAlAs add features to the PL spectrum emitted from the sample. In addition, these unintentional states that form

at the interface can have different properties depending on in what order the materials are grown: InP binary on InAlAs ternary, or vice-versa (InAlAs on InP). [8, 9] As a convention in order to distinguish these two interface configurations, the interface created between an InAlAs ternary material on top of an InP binary material is referred to as the *normal interface* and the interface created between an InP binary material grown on top of an InAlAs ternary an *inverted interface*. [8, 9, 10] It is expected optical transitions or recombination at these two interfaces (normal and inverted interfaces) should be similar. However, for this particular structure (InP/ InAlAs) the quality of the inverted interface can be (again) affected by localized states at the interface. [9] At the inverted interface, ternary layers of $InAs_xP_{1-x}$ on the order of a few monolayers are created due to an exchange between As and P atoms at the interface. This is associated with the difference in (larger) sticking coefficient of As compared with P [10] or as a result of the blockage of absorption sites by As elements during growth. [11] The transition created at this interface has an energy that is less than that of both InP and InAlAs compounds. [8, 9, 10, 11, 12] However, it is possible the emission from this inverted interface overlaps with the emission from the InGaAsP QW, which is the case here degrading the quality (or purity) of the QW emission. [12]

To investigate the effects of InP cap layer on the performance of the sample, an as-grown sample, which includes the typical InP cap layer is compared to one that has had the InP cap removed.

7.2. Experimental results: Sample structure and optical properties

The $In_{0.812}Ga_{0.188}As_{0.4}P_{0.6}/In_{0.52}Al_{0.48}As$ QW structure is grown on a p-type InP substrate at 580 ℃ by metal-organic chemical vapor deposition (MOCVD). After the deposition of a thick InGaAs buffer layer, a 200 nm InAlAs barrier material was deposited in preparation for the active region. The active layer comprises a single InGaAsP QW (20 nm) layer that is overgrown by a 200 nm InAlAs barrier layer. The structure is completed with a thin layer of InP cap (10 nm) to isolate the Al-containing layer.

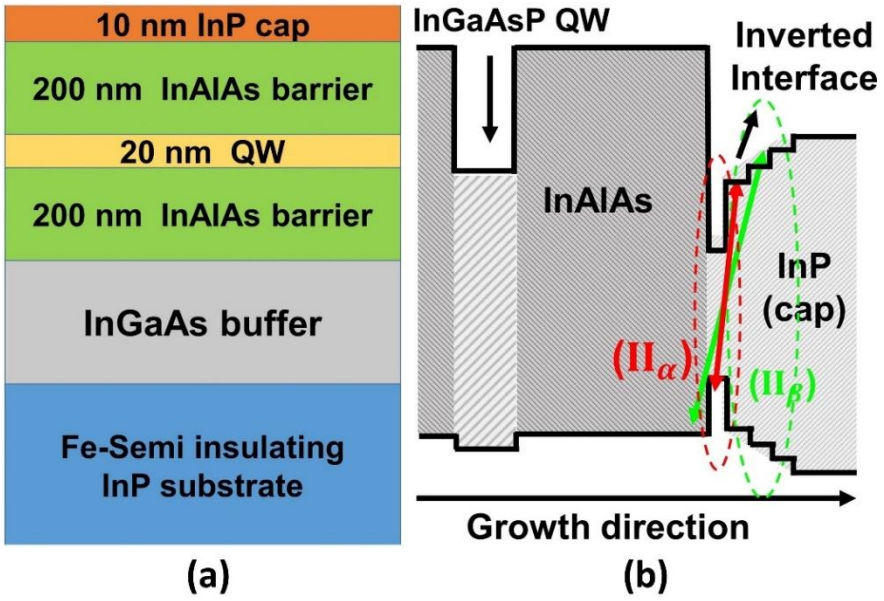

Figure 7. 1. (a) Schematic and (b) band energy diagram of InGaAsP/InAlAs single quantum well structure. [Reproduced from: *Esmaielpour, H., et al. "The effect of an InP cap layer on the photoluminescence of an InGaAsP/InAlAs quantum well heterostructure." Journal of Applied Physics 121, no. 23 (2017): 235301.*] [12]

Figure 7.1 shows the schematic (a) and band energy diagram (b) of InGaAsP QW. The band energy diagram of the QW structure shows an illustration of the graded layers of the order of a few monolayers. In addition, there are two further transitions at the inverted interface shown by red (II_α) and green (II_β), respectively.

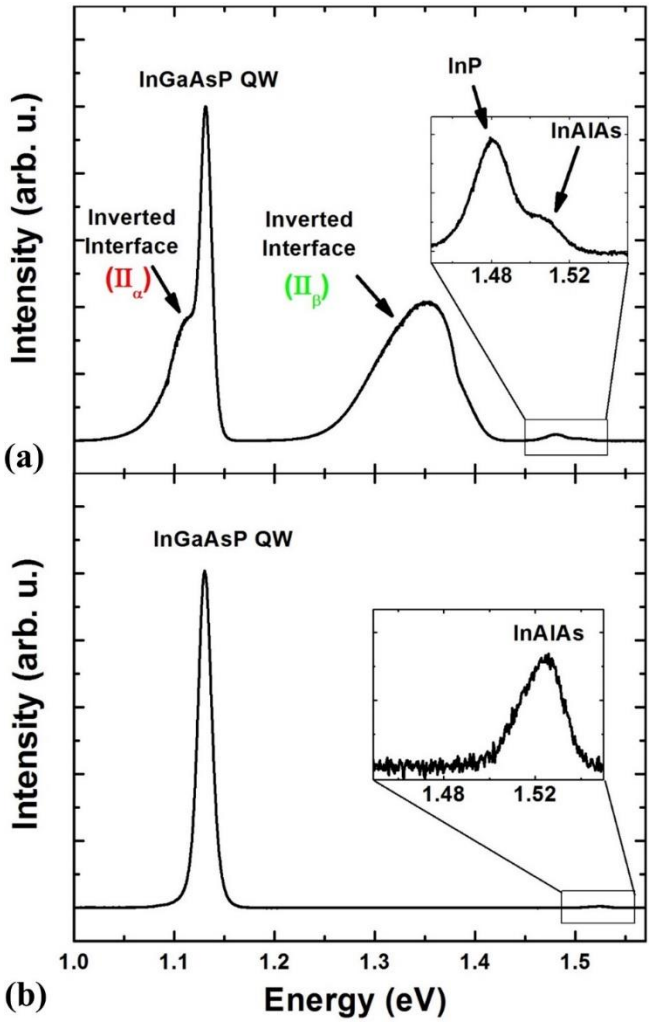

Figure 7. 2. PL spectra of InGaAsP QW with (a) and without (b) InP cap layer at 4 K. [Reproduced from: *Esmaielpour, H., et al. "The effect of an InP cap layer on the photoluminescence of an InGaAsP/InAlAs quantum well heterostructure." Journal of Applied Physics 121, no. 23 (2017): 235301*.] [12]

Figure 7.2 shows PL spectra of the QW structure at 4 K with (a) and without (b) the InP cap layer. A comparison between panel (a) and (b) shows that removing the cap layer results in the removal of some features evident in the full structure (i.e., with the InP cap in place). The removal of several features when the cap is removed indicates that these features are due to transitions at the inverted interface between the InP cap and InAlAs barrier. However, despite these changes before and after etching the sample, the transition associated with the QW (at 1.13 eV) remains intact and unchanged upon removing the InP cap. In Figure 7.2 (a) there is, however, a shoulder on the low energy side of the PL in the region of the QW (1.11 eV), which is attributed to the inverted interface transition (II_{α}). This is an example of how the transition due to the localized states at the interface can affect the spectral quality of the emission from the QW. This transition is not well understood, although Vignaud *et al.* [13] proposes its origin as due to the creation of a thin InAs layer (~ a few monolayer) that forms with the ternary ($InAs_xP_{1-x}$) graded layers at the inverted interface. This InAs thin layer has a type-I band gap, while the interface between the InP and InAlAs is type-II in nature. [8] In Figure 7.2 (a) there is also a feature at 1.35 eV in the PL spectrum, which is related to a second transition (II_{β}) at the inverted interface. This feature has been observed previously [9, 10, 11] and is associated with a transition from the graded $InAs_xP_{1-x}$ monolayers at the inverted interface. Finally, emission due to the InP cap is also evident in Figure 7.2 (a) at 1.48 eV. In the as-grown sample the transition due to InAlAs is observed as a shoulder on the high-energy side of the PL spectrum due to the InP cap layer (see inset to Figure 7.2 (a)). Likewise, the structure at 1.52 eV in Figure 7.2 (b) is related to the InAlAs

barrier, which along with the emission from the InGaAsP QW completes the very simple emission spectrum for the cap free sample.

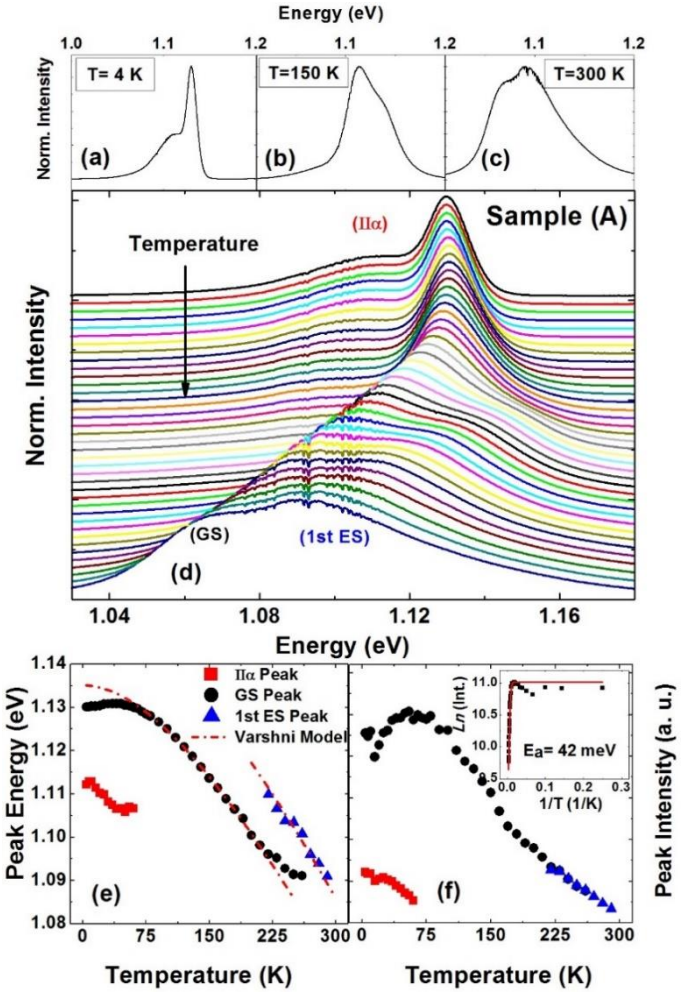

Figure 7. 3. (a) As-grown InGaAsP QW PL spectrum at 4 K (a), 150 K (b) and 300 K (c). Temperature dependent PL spectra at temperatures between 4 K and 300 K. (e) Peak energy versus lattice temperature. Red, black and blue colors represent the inverted interface (II_α), the ground state QW and the first excited state transitions, respectively. (f) Peak intensity for individual transition in system against lattice temperature. Inset in this panel shows the result of Arrhenius plot for the data in panel (f). [Reproduced from: *Esmaielpour, H., et al. "The effect of an InP cap layer on the photoluminescence of an InGaAsP/InAlAs quantum well heterostructure." Journal of Applied Physics 121, no. 23 (2017): 235301*.] [12]

Figure 7.3 shows the temperature dependent PL spectra of the as-grown InGaAsP QW. The QW ground-state transition energy occurs at 1.13 eV at 4.2 K (see Figure 7.3 (a)). In addition, a feature is also evident on the low energy side of the InGaAsP PL (1.11 eV), which is due to the contribution of the inverted interface. Increasing the lattice temperature (panel (b)) reduces the contribution of the localized states at the interface. On the other hand, a shoulder due to the occupation of 1st excited state becomes apparent and increases still further at 300 K (panel (c)). Figure 7.3 (d) shows the full temperature dependent PL spectra of the as-grown QW between 4 K and 300 K. There is a clear redshift in the PL peak position as temperature increases. In addition, the shape of PL spectrum changes with increasing temperature (see panels (a) to (c)). At lower temperatures, the features associated with the localized states at the AlInAs/InP interface are observed on the low energy side of PL spectra, but lose intensity as *T* approaches 75 K. Above 150 K, a feature due to the first excited state in the InGaAsP QW is observed and increases at elevated lattice temperatures. The energy separation between the ground state and first excited state transitions is close to the value determined by NRL MultiBands® (~ 36 meV).

Figure 7.3 (e) shows peak energy versus lattice temperature for all three features observed in the temperature dependent PL spectra. The temperature dependent behavior of inverted interface (II_α) shows a redshift with increasing temperature up to 75 K, above which it no longer contributes to the PL. The InGaAsP QW transitions from the ground and first excited state are shown as solid black circles and solid blue triangles, respectively. The red dashed line is the Varshni fit for this temperature dependent data. Both ground state and first excited state transitions show redshifts with increasing

temperature, which is consistent with the thermal expansion of the crystal structure. The empirical Varshni model follows: [14]

$$E(T) = E_0 - \frac{\alpha T^2}{\beta + T}, \tag{7.1}$$

where α and β are constant parameters related to material properties of the semiconductor, E_0 band gap at 0 K, and T the lattice temperature. By fitting the experimental results for the ground state transition (black dots) with the Varshni equation (Equation 7.1), α and β are determined to be $4.8 \times 10^{-4}\ eV/K$ and $360\ K$, respectively. These results are comparable with those found for the same material and reported in the literature. [15, 16] The extracted band gap values at T = 0 K, for the ground and first excited state transitions are 1.135 eV and 1.151 eV, respectively.

Figure 7.3 (e) shows at low temperatures < 50 K, the change of peak energy does not match the Varshni fit due to the existence of localized states in the system. Localized states created in the system have energy levels below the semiconductor band gap and recombination of carriers from these states create PL spectra with peak energies lower than the energy of the fundamental band gaps. As the temperature increases carriers can escape from these localized states and the PL shifts to energies associated with the semiconductor band edge.

The change of peak intensities due to localized states (solid red squares), ground state (solid black circles), and first excited state (blue triangles) transitions versus lattice temperature are shown in Figure 7.3 (f). The intensity due to localized states decreases with increasing lattice temperature. This is further evidence that as the temperature increases the contribution of the localized states decreases (at the inverted interface

between InP cap and InAlAs barrier) and carriers redistribute to the band edges. Further evidence for the transfer of carriers from the localized states to the QW is an increase in the PL intensity of the QW up to 75 K, as the localized state emission quenches. The reason for the increase in peak intensity between 15 K < T < 75 K is once more attributed to the thermal redistribution of charges from localized states into the ground state of the QW. Above 75 K, the PL intensity quenches due to the increase in the contribution of non-radiative recombination mechanisms at elevated temperature.

To investigate the temperature dependent behavior of the peak intensity of the QW transition, an Arrhenius fitting is applied on experimental results using the following equation: [17]

$$I(T) = \frac{I(0)}{1+A\exp(-E_a/k_BT)}, \tag{7.2}$$

where $I(T)$ is temperature dependent peak intensity, A is a constant, E_a is the activation energy, and $I(0)$ is the peak intensity at 0 K. The Arrhenius plot of the ground state transition is shown in the inset to Figure 7.3 (f). This model is applied for temperatures above 75 K, where a reduction in peak intensity is observed. At low temperatures (T < 75 K), it is not possible to apply Equation 7.2 due to non-idealities in the system. An activation energy of 42 meV is extracted from this analysis, which is consistent with the energy separation between the ground and first excited states in the QW ($\sim$ 36 meV) as predicted by NRL MultiBands®. [18]

Figure 7.4 shows temperature dependent behavior of InGaAsP QW structure with the InP cap removed. Figure 7.4 (a) shows the QW PL spectrum at 4 K, which (as expected) does not show any transition due to the inverted interface at low energy. As the lattice

temperature increases (see Figure 7.4 (b) and (c)) a shoulder becomes evident on the high-energy side of PL spectra, which is associated with the excited state transition. The PL at 300 K (Figure 7.4 (c)) also shows a low energy contribution of the InGaAs buffer layer. Figure 7.4 (d) shows the temperature dependent PL between 4.2 K and 300 K. The extracted peak energies versus temperature from these data are shown in Figure 7.4 (e). The red dashed line in this figure represents the result of fitting with the Varshni equation (Equation 7.1). The extracted constants for this cap-less sample (α, β, E_0) are consistent with those determined for the as-grown sample (with InP cap), which indicates that the temperature dependent behavior of the QW peak energy is independent of the InP cap. At low temperatures – despite the removal of the InP cap – there is a deviation from the Varshni-dependence and evidence of an "s-shape" associated with non-idealities in the system. Since interface states due to the InP/AlInAs system are absent in this sample, the presence of localized states in the QW PL are attributed to alloy fluctuations in the InGaAsP, which is not unusual in ternary and quaternary materials having been observed in several other systems including AlAsSb and GaInNAs.

Figure 7.4 (f) shows the change of peak intensity versus temperature for the "cap-less" InGaAsP QW. The PL intensity quenches monotonically as temperature increases and it is possible to perform an Arrhenius fit of the full temperature range (see inset of Figure 7.4 (f)). However, three activation energies are required to adequately fit the data. The first activation energy is ~ 0.58 meV (or 6.8 K), which is associated with the minima in the "s-shape" behavior below 15 K.

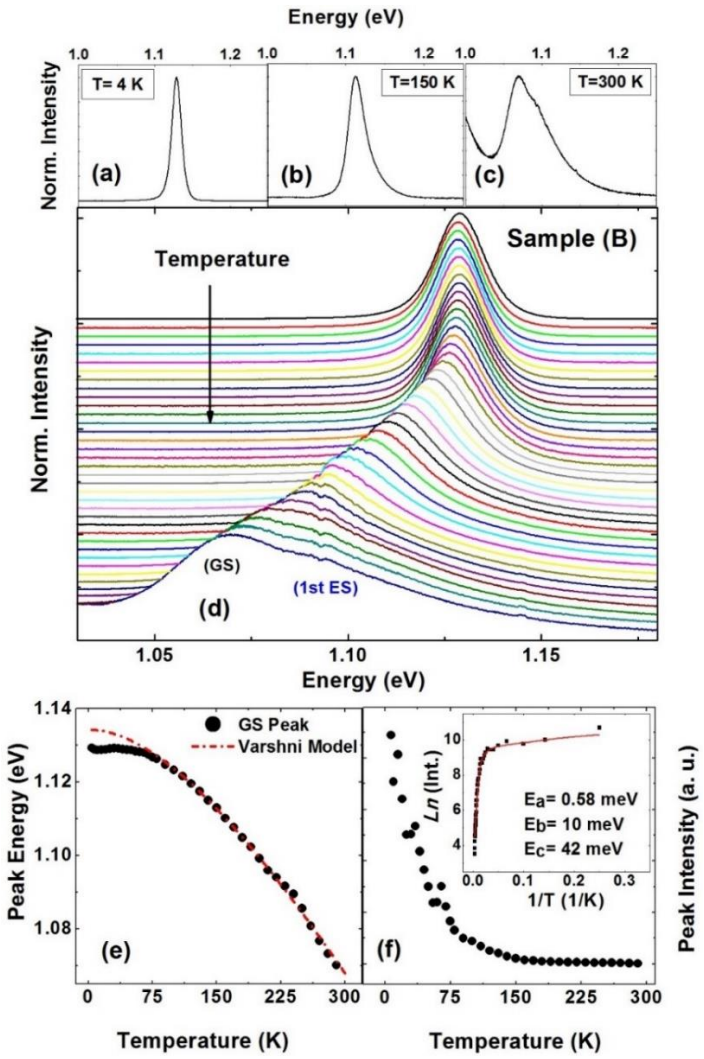

Figure 7. 4. PL spectrum for *cap-less* InGaAsP QW at 4 K (a), 150 K (b) and 300 K (c). (d) Temperature dependent PL spectra for various lattice temperatures between 4 K and 300 K. (e) Peak energy versus lattice temperature for the ground state QW transition. Dashed line shows Varshni fitting with the experimental result. (f) Peak intensity versus lattice temperature for the ground state QW transition. Inset of panel (f) shows the result of Arrhenius plot for the experimental results. [Reproduced from: *Esmaielpour, H., et al. "The effect of an InP cap layer on the photoluminescence of an InGaAsP/InAlAs quantum well heterostructure." Journal of Applied Physics 121, no. 23 (2017): 235301.*] [12]

The second activation energy is ~ 10 meV, which is attributed impurity binding energy. Finally, the third extracted activation energy is found to be ~ 42 meV, which is the same value extracted for capped sample described above. This final energy is consistent with the energy separation between ground and first excited state in the QW. The similarity between extracted activation energy (42meV) for both samples (with and without InP cap layer) indicates – once more – that the occupation of excited states mechanism is independent of InP cap layer.

Figure 7.5 shows power dependent PL spectroscopy of both samples at 4.2 K and 300 K. The power dependent behavior of the as-grown sample at 4.2 K is shown in Figure 7.5 (a). At the highest excitation power (black line in Figure 7.5 (a)) emission from the QW dominates, also, there is a low energy feature associated with recombination at localized states at the inverted interface (II_α). As power is reduced, the contribution of the QW decreases and (II_α) dominates the PL spectrum. The inset of Figure 7.5 (a) shows the power dependence of the peak energies for both the QW ground state (solid black circles) and (II_α (solid red squares) versus $P^{1/3}$. The linear relationship between the QW peak energy and $P^{1/3}$ confirms the type-II band alignment for the QW.

Interestingly, the inverted interface transition also follows a type-II band alignment behavior, although it was expected this transition to have a type-I band alignment (see the inset of Figure 7.5 (a)). [13] As proposed by Vignaud *et al.*, [13] the inverted interface transition (II_α) is perhaps associated with the formation of a thin layer (~ a few monolayers) of InAs at the interface between the InP cap and the InAlAs barrier.

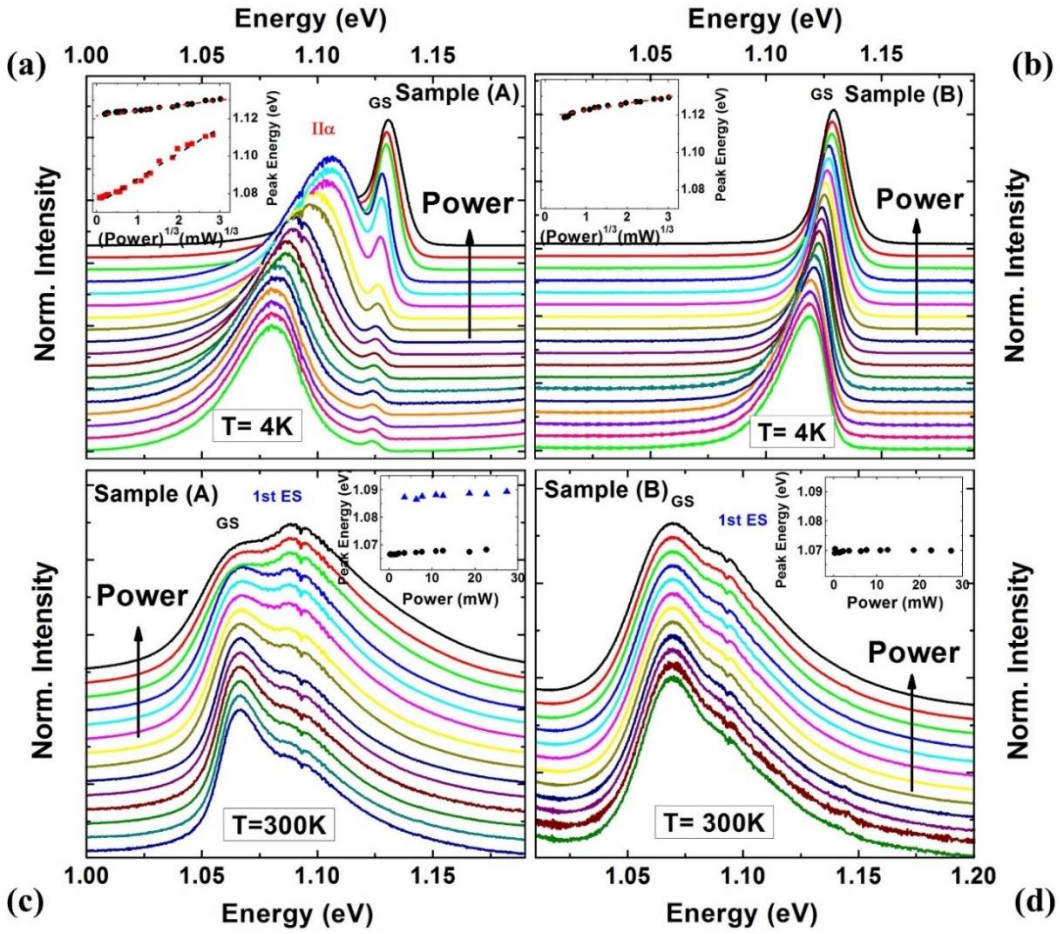

Figure 7. 5. (a) and (b) excitation power dependent PL spectroscopy for as-grown (sample A) and *cap-less* (sample B) InGaAsP QW structure at 4 K. Insets in both panels (a) and (b) show peak energy versus $P^{1/3}$. Black and red colors in inset of panel (a) represent the ground state QW and the inverted interface transitions (II_{α}). (c) and (d) excitation power dependent PL spectroscopy for as-grown (sample A) and *cap-less* (sample B) at 300 K. Insets in panels (c) and (d) show the results of peak energy versus excitation power. Black and blue colors represent transitions associated with the ground state and the first excited state transitions. [Reproduced from: *Esmaielpour, H., et al. "The effect of an InP cap layer on the photoluminescence of an InGaAsP/InAlAs quantum well heterostructure." Journal of Applied Physics 121, no. 23 (2017): 235301*.] [12]

As shown in the schematic of the sample at the inverted interface region (see Figure 7.1 (b)), this thin layer of InAs would be type-I in nature. Since II_α follows a $P^{1/3}$ dependence here (see inset to Figure 7.5 (a)), it is likely the origin and composition of this layer is much more complex than predicted – so that, alloy fluctuations and/or impurities contribute to II_α. [12, 19] This is supported by the fact that there is a linear dependence between the peak energy of II_α and the logarithm of excitation power. This behavior is typically related to the spatially separated carriers due to alloy fluctuations in the system. [9]

Figure 7.5 (b) shows power dependent PL spectra of cap-less sample at 4.2 K. At the highest power the PL spectrum is symmetric, however, as the excitation power decreases PL spectrum reveals the presence of an Urbach tail related to localized states on the low energy side of the emission spectrum, which again is attributed to alloy fluctuations in the InGaAsP and/or at the QW/AlInAs interface. [20] The inset to Figure 7.5 (b) confirms the type-II band alignment of the system. The power dependent PL spectra of the InGaAsP QW with InP cap layer at 300 K are shown in Figure 7.5 (c). No evidence of the inverted interface transition is observed on the low energy side of PL spectrum at 300 K. In addition, it is observed that the change in the peak positions of both the ground state and first excited state transitions are small (see the inset to Figure 7.5 (c)). The InGaAsP QW has a quasi-type-II band alignment, therefore the photogenerated holes can escape from the small confinement in valence band easily as the temperature increases. When delocalized, the radiative efficiency increases since the system is effectively in the quasi-type-I regime. This reduces the $P^{1/3}$ dependence observed at lower temperatures. As a result, there is little change in peak energies for

both transitions (ground state and first excited state) versus excitation power at 300 K (see inset of Figure 7.5 (c)). Figure 7.5 (d) shows the power dependent PL of the cap-less QW at 300 K. The first excited state is observed as a shoulder on the high-energy tail of power dependent PL associated with the ground state of the QW. [12, 19]

7.3. Excitation power photoluminescence (PL) spectroscopy of InGaAsP and InP single quantum wells

Figure 7.6 (a) and (b) show PL spectra at 4 K for both InGaAsP and InP single quantum well samples, respectively, grown upon an n-type InP substrate. The insets of these two panels show the band energy diagrams of both samples at 300 K calculated using NRL MultiBands®. In Figure 7.6 (a) there are two peaks at 1.11 eV and 1.13 eV, which are related to the inverted interface (II_{α}) and the QW transitions, respectively; an in-depth discussion about these transitions have been discussed in Section 7.2. The peak at 1.35 eV is related to a second transition at the inverted interface (II_{β}) created between the InP cap and InAlAs barrier materials. The features at 1.48 eV and 1.51 eV are associated with InP cap and InAlAs barrier, respectively.

Figure 7.6 (b) shows the PL spectrum of the InP QW structure at 4 K. The band energy diagram of the sample is shown in inset to this figure. The InP QW band energy diagram indicates that the ground state energy level is at $\sim$ 1.225 eV at 300 K. However, the experimental transition for the ground state of the InP QW is at a lower value of $\sim$ 1.118 eV at 300 K, which reflects the complexity and non-idealities or the experimental system relative to the idealized case/parameters used in the simulation.

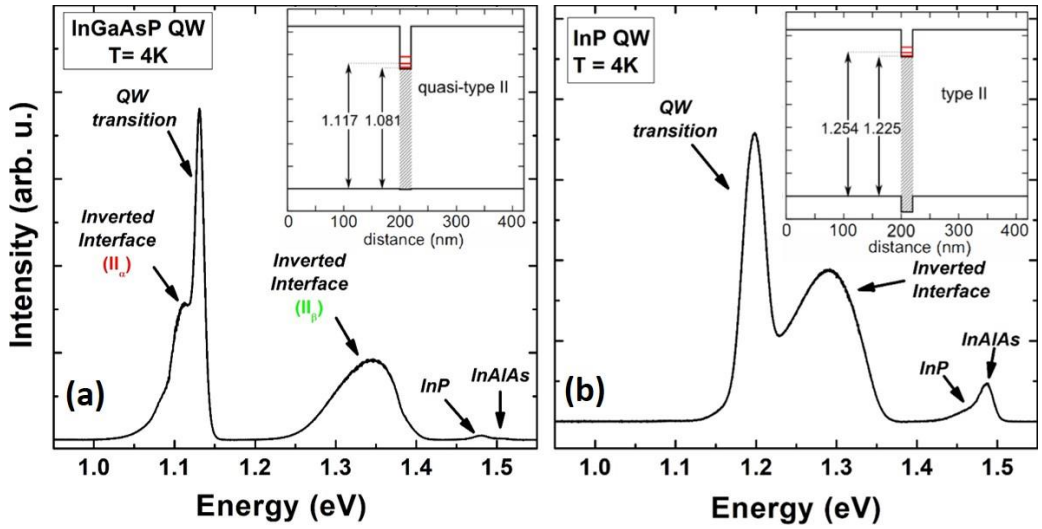

Figure 7. 6. PL spectra of (a) InGaAsP and (b) InP single quantum well structures at 4 K. Insets in each panel show the associated band energy diagram of the quantum well structures in each panel.

The feature at 1.3 eV in Figure 7.6 (b) is attributed to the inverted interface transition between the InP cap and the InAlAs barrier materials, as this transition is unlikely related to the occupation of excited states since its energy separation is of the order of 100 meV (which is considerably larger than that determined by simulation (~ 30 meV)). Moreover, the transition this 1.3 eV transition is only present at low temperatures, quenching at higher temperatures. This behavior is opposite of what it is expected for occupation of excited states because the probability of excited state transition increases as carriers receive more thermal energy. [19] The features at 1.46 eV and 1.49 eV are related to the InP cap and InAlAs barrier material, respectively. The transitions related to cap and barrier materials occur at values lower than the InGaAsP QW. This is attributed to the subtleties of the growth conditions, strain introduced into the system, and/or clustering of the group III-elements (Al, In). [9, 11]

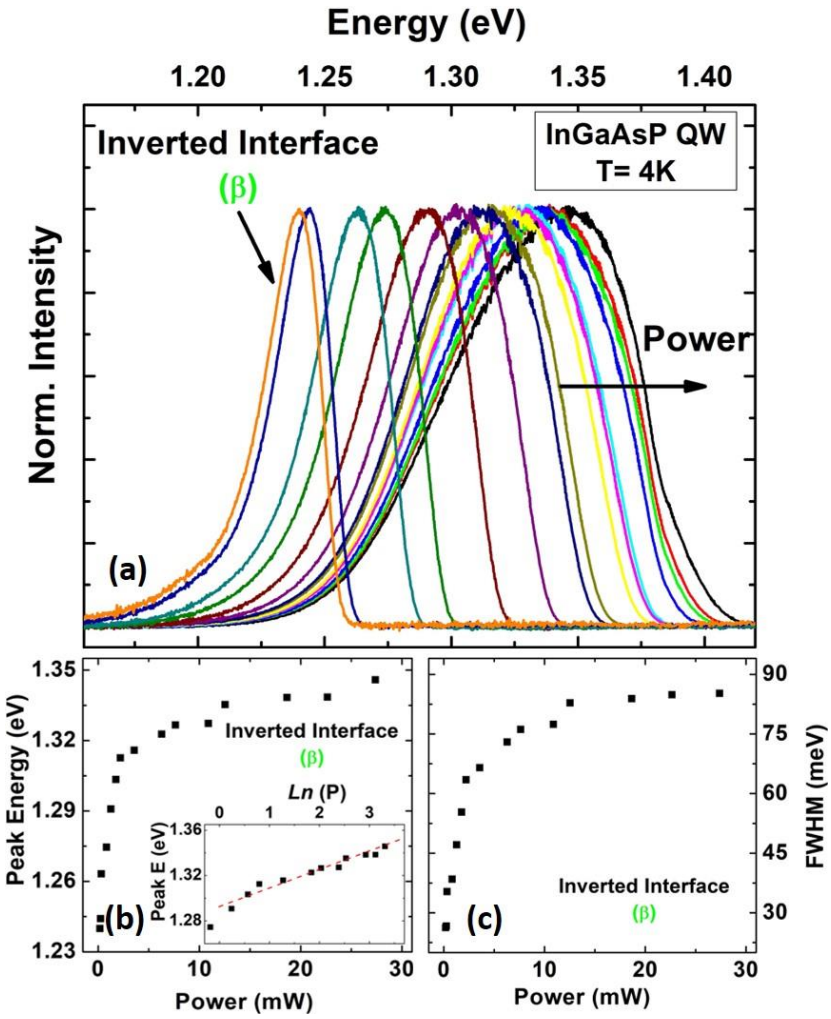

Figure 7. 7. (a) Normalized PL spectra of the InGaAsP QW structure associated with the inverted interface (II_β) transition at 4 K for various excitation powers. (b) Peak energy as a function of excitation power extracted from PL spectra in panel (a). Inset of panel (b) shows peak energy versus natural logarithm of excitation power. (c) Line-width broadening of PL spectra in panel (a) versus excitation power.

The transitions due to the inverted interface (at 1.11 eV) and the InGaAsP QW ground state (at 1.13 eV) have been discussed comprehensively in Section 7.2. Here, the power dependent PL of a second inverted interface transition in the capped InGaAsP QW

structure observed at 1.35 eV is evaluated at 4 K (see Figure 7.7). As discussed, these inverted interfaces are created when a binary material (InP) is grown on top of a ternary material (InAlAs). In these systems, the relative larger sticking coefficient of As than P, coupled with As-P exchange at the interface, result in graded monolayers of $InAs_xP_{1-x}$, which form a so-called inverted interface between InP and InAlAs layers. This results in the absence of an abrupt normal interface between the InAlAs ternary and the upper InP binary material. [9, 10, 11, 12]

Figure 7.7 (b) shows the change of peak energy versus excitation power. With increasing power, considerable change in peak energy and shape from β is apparent. There is also an abrupt change in the peak energy at low excitation powers (before $\sim$ 2.5 mW); thereafter the effect of excitation power on the peak energy slows. The inset of Figure 7.7 (b) shows the linear dependence of the peak energy of β as a function of natural logarithm of the excitation power. The origin of this behavior is associated with indirect transitions at the inverted interface. In general, for indirect transition in real space, the transition probability is determined by the square of momentum matrix element ($\left|\left\langle \Psi_i^e(k_\parallel)\middle|e.grad\middle|\Psi_j^{hh}(k_\parallel)\right\rangle\right|^2$) multiplied by the square of electron and hole wave packet overlap integral ($\left|\left\langle \Psi_i^e(k_\parallel)\middle|\Psi_j^{hh}(k_\parallel)\right\rangle\right|^2$) multiplied by the electron and hole occupation probability. In this situation, the electron-hole wavefunction overlap changes exponentially ($\left|\left\langle \Psi_i^e(k_\parallel)\middle|\Psi_j^{hh}(k_\parallel)\right\rangle\right|^2 \approx e^{-d/c_0}, c_0 = Const.$), with spatial separation *d*. Therefore, the transition probability at the interface reduces exponentially with distance *d*. In the case of an inverted interface, which is not abrupt (unlike a normal interface), the wavefunction overlap term becomes dominant. Consequently, saturation at the largest separation occurs first. As reported by Böhrer *et al.* [9] the excitation

dependence of the peak PL energy for localized emission at a graded interface follows the exponential behavior ($P \propto e^{E}$). [8, 9]

Figure 7.7 (c) shows the excitation dependent linewidth broadening of the PL spectra of β shown in Figure 7.7 (a). The FWHM increases with excitation power, and (approximately) saturates at higher intensities. This broadening reflects the inhomogeneity of the system and several competing transitions and levels at the inverted interface (see Figure 7.6 (b)).

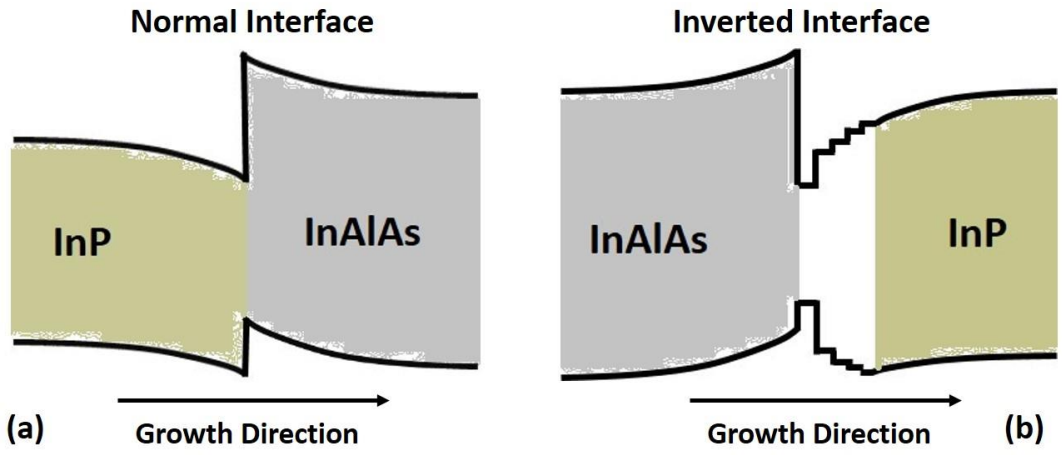

Figure 7. 8. Schematics of band bending at normal (a) and inverted (b) interfaces.

Although the materials involved at both the normal interface (InAlAs ternary on InP binary materials) and inverted interface (InP binary on InAlAs ternary materials) are the same, these two interfaces do not have the same optical transitions. One of the main differences between these two structures is related to the existence of graded monolayers of an $InAs_xP_{1-x}$ ternary (or $In_xAl_{1-x}As_yP_{1-y}$ quaternary) at the inverted interface. [9, 11] These extra layers increase the recombination energy at the inverted interface while the normal interface is abrupt with strong band bending due to Coulomb interactions. As a

result, the energy due to the inverted interface transition occurs at higher values than that of the normal interface. [9, 10] The schematics of band energy diagram at normal and inverted interfaces are shown in Figure 7.8 (a) and (b), respectively.

Figure 7.9 shows power dependent study of the InP QW structure at 4.2 K. Figure 7.9 (a) shows the normalized PL spectra of the ground state transition of the InP QW and the inverted interface transition at 4.2 K. The inset in Figure 7.9 (a) shows a magnified region of the normalized spectra for the region around the inverted interface transition. Both peaks in Figure 7.9 (a) are blue-shifted with increased excitation power. In addition, at lower excitation power an additional feature on low energy side of the QW PL spectrum is evident, whose contribution becomes negligible with increasing power. This lower energy feature is attributed to Urbach processes that are saturated at elevated powers.

The excitation dependence of the peak energies extracted from the PL shown in Figure 7.9 (a) are shown in Figure 7.9 (b) and (c), respectively. Although the peak energy of both transitions change in a similar manner with excitation power, their origin is somewhat different. The inset of Figure 7.9 (b) shows the peak energy change of the ground state transition versus $P^{1/3}$. The linear dependence shown in inset is indicative of a pure type-II band alignment transition at interface. The inset of Figure 7.9 (c) shows the change of peak energy transition due to the inverted interface versus natural logarithm of excitation power. This transition has a linear dependence between peak energy and $\ln(P)$, which is indicative of indirect transition due to localized states at the inverted interface.

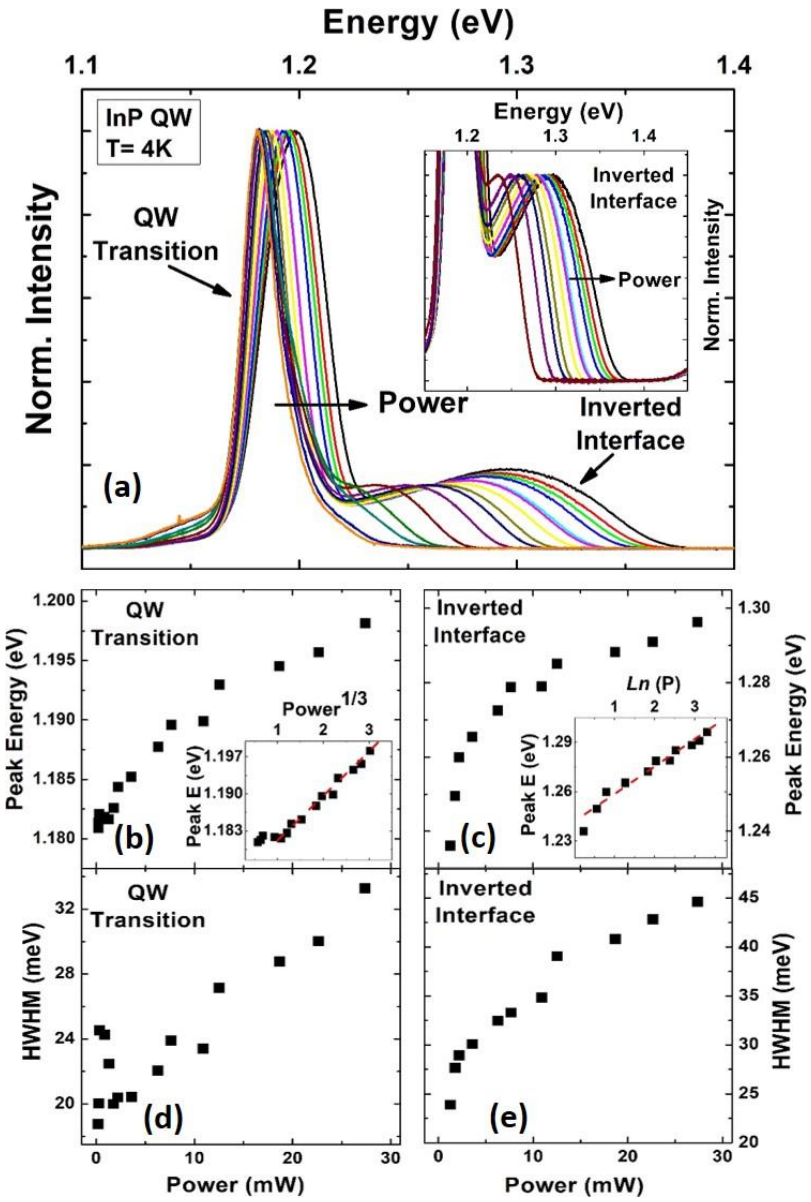

Figure 7. 9. (a) Normalized PL spectra of InP QW at 4 K at various excitation powers. Inset in panel (a) shows the zoom-in region of the inverted interface transition for various excitation powers. (b) and (c) Peak energy versus excitation power for the ground state QW and the inverted interface transitions. Insets in panels (b) and (c) show the QW peak energy versus ($P^{1/3}$) and the peak energy of the inverted interface transition versus *Ln*(P), respectively. (d) and (e) Line-width broadening as a function of excitation power for the ground state QW and the inverted interface transitions, respectively.

As the excitation power increases, the linewidth of both transitions become larger and no saturation is observed (see Figure(s) 7.9). To quantitatively investigate the linewidth broadening of both transitions within the convoluted PL spectra, the half width at half maximum (HWHM) of the low energy side of the ground state transition and the high energy side of the inverted interface transition are considered, as shown in Figure 7.9 (d) and (e), respectively. By comparing the linewidth broadening of inverted interface transitions emitted from InGaAsP QW (Figure 7.7 (c)) and InP QW (Figure 7.9 (e)), it is evident that the linewidth broadening in InGaAsP QW saturates at lower excitation density than the InP. This suggests the density of states for localized states at the inverted interface in the InGaAsP QW structures is lower than that in the InP QW sample.

Figure 7.10 (a) shows normalized power dependent PL spectra of InGaAsP QW at 4 K, which shows no change in shape and/or peak position the transitions related to the InP cap at 1.48 eV or the InAlAs barrier material at 1.51 eV. This power independent behavior for peak energy is consistent with the type-I nature of these transitions. Moreover as expected, there is also no change in the peak positions of InP cap (1.46 eV) and InAlAs barrier (1.49 eV) in InP QW sample (Figure 7.10 (b)) for the same reason.

Figure 7.10 (c) and (d) show the FWHM of the convoluted PL spectrum of InAlAs and InP cap transitions for both samples. It is observed that the linewidth stays the same for a wide range of powers, which is indicative of high quality materials. [10] However, an increase in the PL linewidth of the InP QW is observed for lower powers, as shown in Figure 7.10 (d). This is the result of the small increase in the contribution of low energy InP cap layer at low excitation powers as compared to the InAlAs transition.

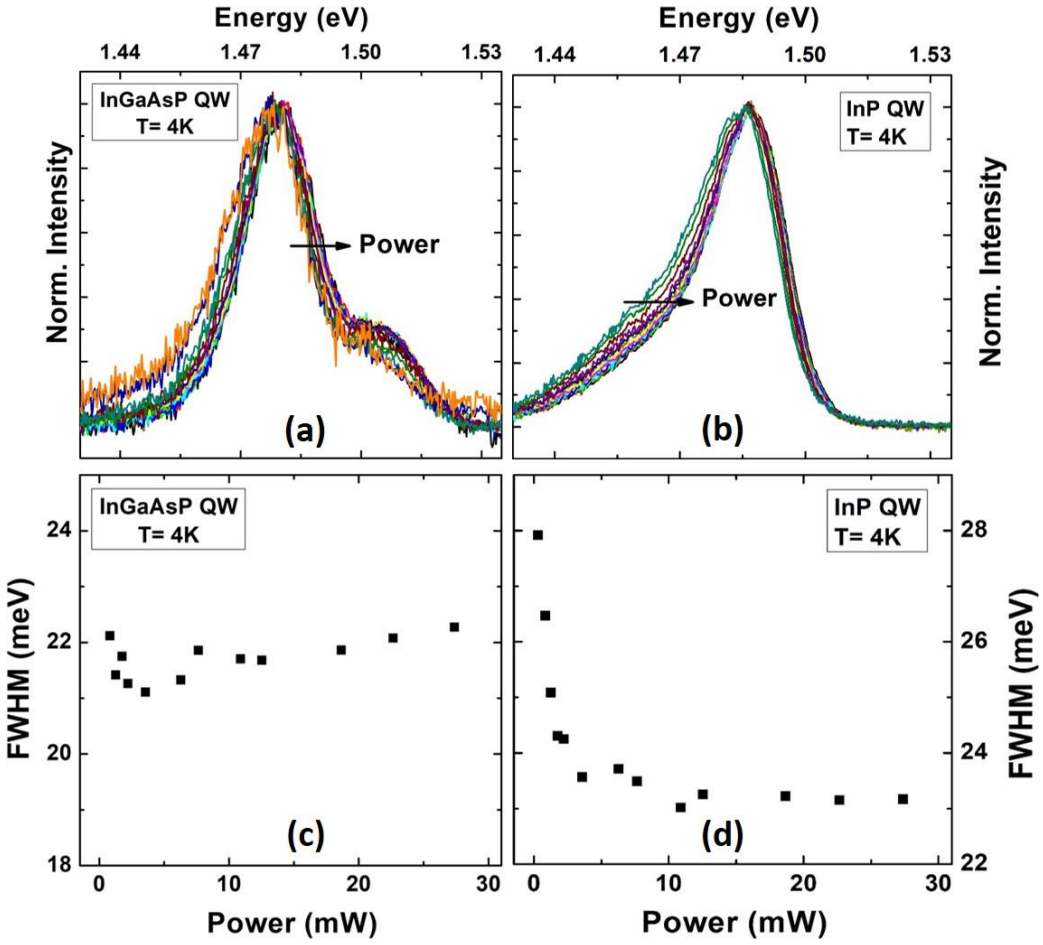

Figure 7. 10. (a) Normalized PL spectra of InGaAsP QW sample due to the transition at InAlAs and InP cap materials at 4 K. (b) Normalized PL spectra of InP QW sample focused on the region due to InAlAs transition at 4 K temperature. (c) and (d) Full width at half maximum of the PL spectra as a function of excitation intensity for InGaAsP QW and InP QW sample, respectively.

7.4. Polarized photoluminescence (PL) spectroscopy of the quantum well structures

Figure 7.11 (a) shows polarized PL spectra of InGaAsP QW structure at 4 K excited at the highest power (OD00) of the He-Cd laser (442 nm). The black and red plots

represent two different PL polarizations probed when a linear polarizer is placed parallel and perpendicular to the [011] direction, as defined by the growth direction of the sample.

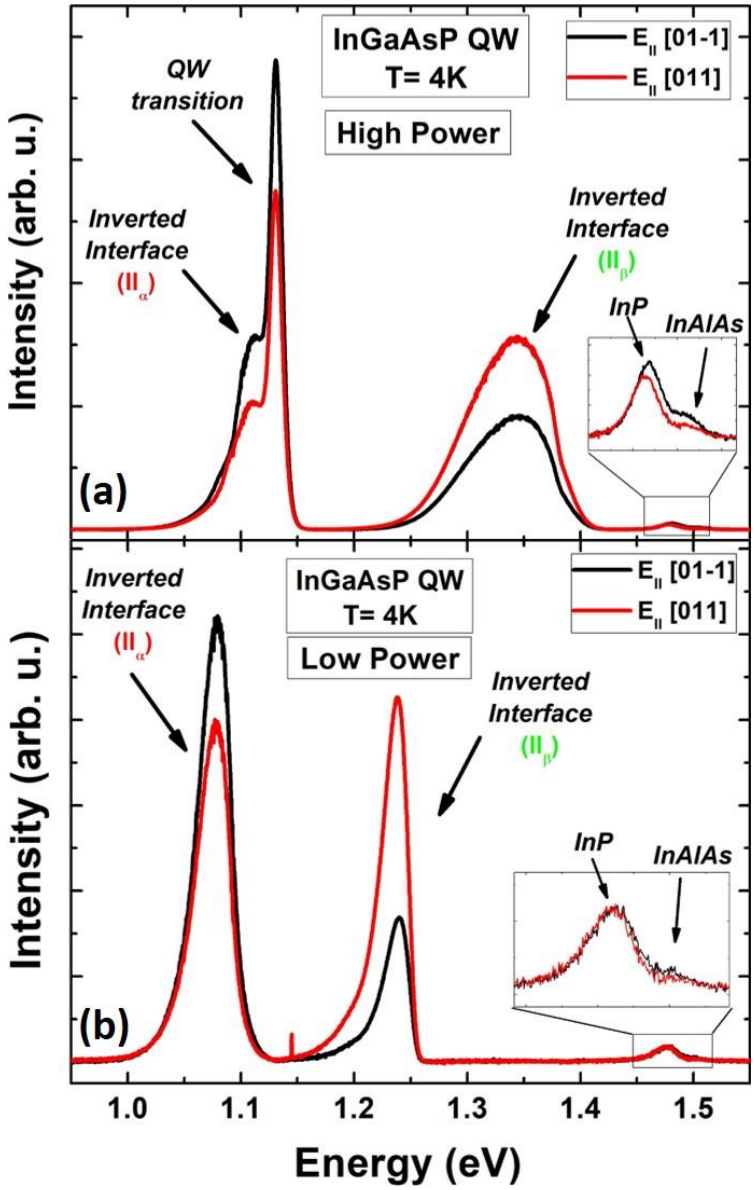

Figure 7. 11. (a) and (b) Low temperature (4 K) polarized PL spectra of InGaAsP QW for two different excitation powers. Black and red colors represent two perpendicular orientations of the polarizer aligned with [011] and [01 − 1] directions, respectively.

As seen in Figure 7.11 (a), there is a change in intensity for the InGaAsP QW, InP cap, InAlAs barrier, and the inverted interface (II_α and II_β) transitions with rotation of the polarizer. Figure 7.11 (b) is a similar measurement on the same sample but for low excitation power (OD300). Under these conditions, the peak associated with the ground state QW is absent from the spectrum. However, there is still emission and polarization dependent behavior in the PL from both the inverted interface transitions (II_α and II_β). When considering the feature at higher power related to the InP and InAlAs, there are clear differences at low and high powers. At low power (see Figure 7.11 (b)) no polarization is evident. However, at higher powers (see Figure 7.11 (a)) a small polarization is evident in both transitions. This power dependent behavior of the InP and AlInAs transition is unusual and not fully understood. However, there appears to be effects due to compositional mixing and/or strain affecting the behavior of the InP and AlInAs, which requires further analysis.

The origin of polarized PL spectrum is probably due to the splitting of states in the valence band. [21, 22, 23] This effect is enhanced in heterostructures due to quantum confinement and strain, when the degeneracy of the valence band states is lifted. [24] Under compression or tensile strain the energy separation increases, and sub-band energy levels in the valence band move farther from the conduction band. [21] Therefore, optical transitions from the conduction band to higher order energy levels in the valence band become limited. The suppression of the conduction band to the light hole state is observed in InGaAs/GaAs QW, where the compressive strain caused a shift in the light hole sub-band in energy further from the conduction band. [22] In a larger valence band splitting, the suppression of transitions to higher order energy levels in the

valence becomes stronger and more polarization effect is detected in the emitted PL signal. However, by increasing lattice temperature the thermal hole distribution between the sub-band levels in the valence band becomes larger and transitions from multiple valence band states to the conduction band becomes more probable. This effect results a reduction in the polarization degree in the emitted PL spectrum as a function temperature. [21]

To understand the origin of the polarization dependence of the QW and inverted transitions, the orientation of the structure must be understood. A schematic of a tetrahedral crystal lattice structure for InP/InAlAs/InP compounds is depicted in Figure 7.12 (a). The shaded planes represent those planes containing InAs-like bonds. In type-II heterostructures, the perturbation due to local biaxial strain can remove the degeneracy of heavy hole states. Therefore, two sublevels due to excitonic dipoles can arise along the [011] and $[01\bar{1}]$ crystallographic directions. These two orientations are orthogonal to the (100) growth direction of the substrate. Figure 7.12 (a) illustrates the projections of [011] and $[01\bar{1}]$ directions on the (100) plane, which are the normal and inverted interface polarization directions, respectively.

Figure 7.12 (b) shows the peak intensity for the different features of the PL spectrum as a function of transmission orientation of the polarizer. The peak intensity of the inverted interface (II_α) and the QW transitions (are shown in solid black circles and solid red squares, respectively) rotate in phase to one another. However, the PL intensity from the inverted interface (II_β) rotates 90° out of phase form both the QW and II_α. This phase shift is due to the orthogonality of the InAs planes at the different InP/InAlAs

interfaces. Similar behavior in the polarization dependence of inverted interface transitions is also observed when assessing the low power PL (see 7.11(b)).

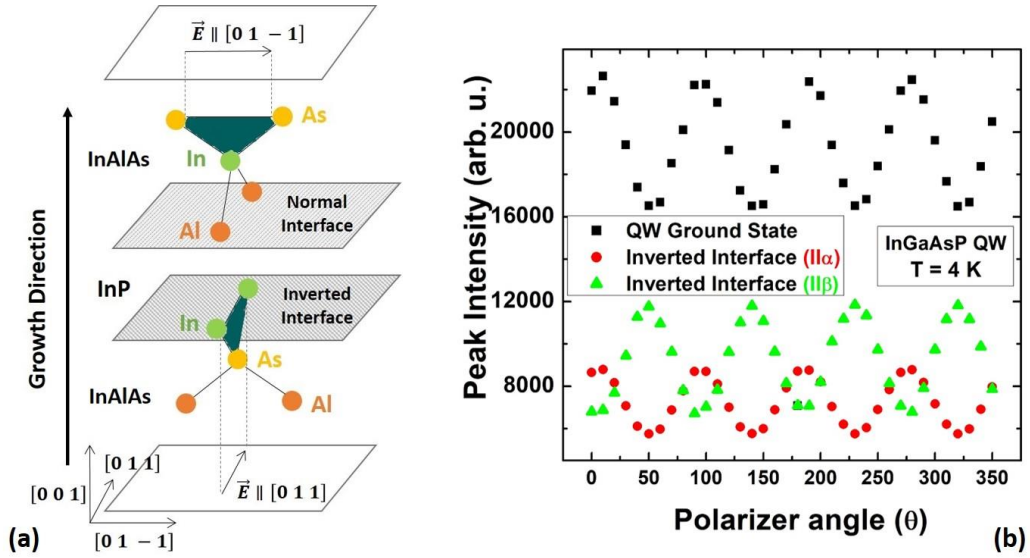

Figure 7. 12. (a) Tetrahedral crystal lattice structure for InP/InAlAs, which creates normal and inverted interface transitions. InAs planes, which are responsible for graded layers at the interface are shaded. These planes are aligned in two orthogonal planes ([011] and [01-1]). (Bohrer, *et al.* [9]) (b) Peak intensity of the PL spectrum of InGaAsP QW sample against the transmission direction of the polarizer for the QW and the inverted interface (II_α and II_β) transitions shown by different colors. It is seen that the polarization of the inverted interface (II_α) and the QW transitions are orthogonal to the polarization direction of the inverted interface (II_β).

The relative intensity of the PL from the two orthogonal orientations of the polarizer is indicative of a change in the degree of polarization for different excitation powers. The degree of linear polarization for the system is given by: $P = (I_\perp - I_\parallel)/(I_\perp + I_\parallel)$, where $I_\perp$ and $I_\parallel$ represent the intensity of the parallel and perpendicular directions of the

emitted PL, respectively. The degree of optical polarization, P with the various transitions in the PL spectra is shown in Figure 7.13. Figure 7.13 (a) shows P for the inverted interface (II_α) as a function of intensity at 4.2 K. As the excitation power increase, so does the degree of optical polarization.

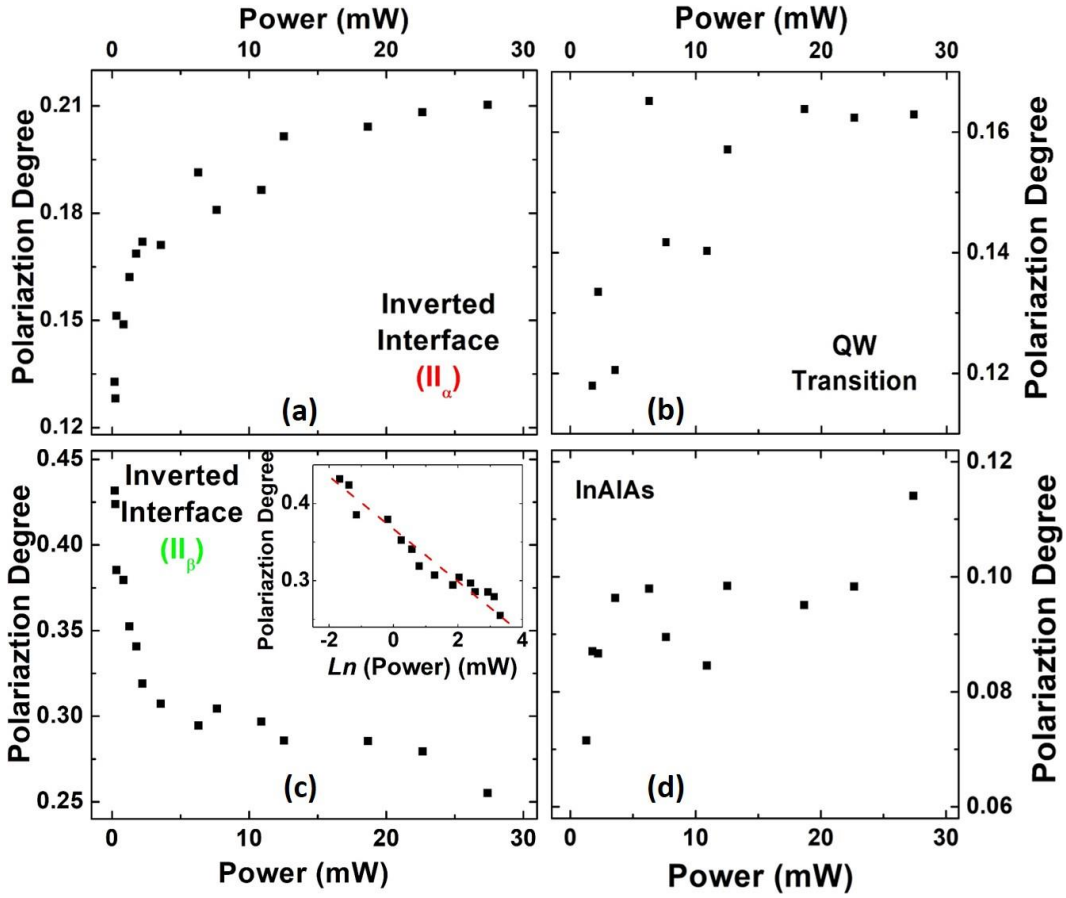

Figure 7. 13. Polarization degree of the InGaAsP QW structure for (a) the inverted interface (II_α), (b) the QW, (c) the inverted interface (II_β) and (d) InAlAs transitions as a function of excitation power. Inset in panel (c) shows the linear behavior of polarization degree versus natural logarithm of excitation power.

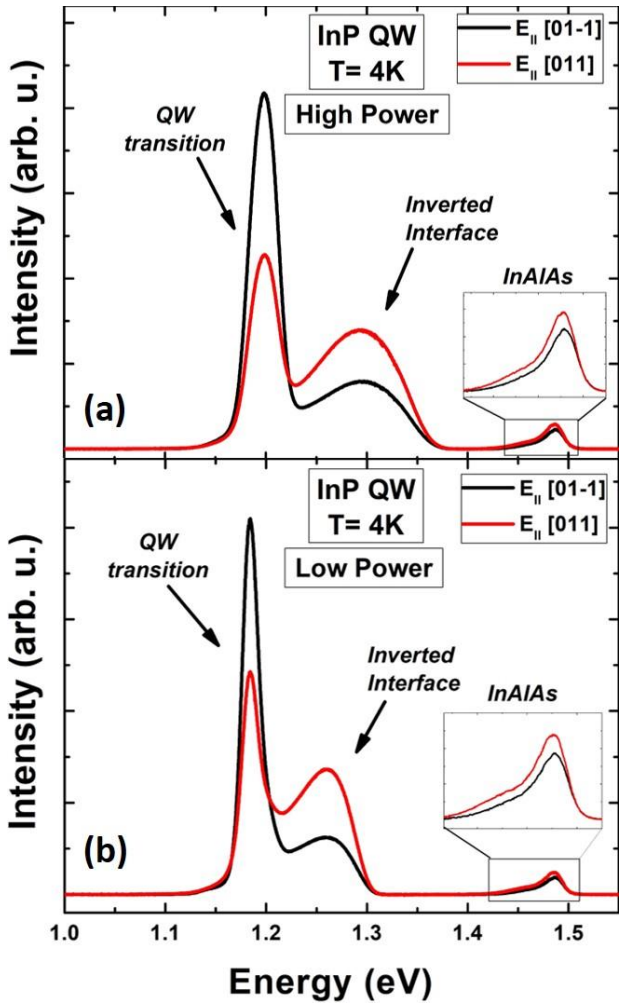

Figure 7. 14. (a) and (b) Low temperature (4 K) polarized PL spectra of InP QW for two different excitation intensities (OD00, and OD100). Black and red solid lines show PL spectra measured at two orthogonal orientations of polarizer transmission.

Figure 7.13 (b) shows the excitation dependent degree of optical polarization for the QW. Although this feature does show evidence of linear polarization, this effect is small. The change in the degree of optical polarization for the inverted interface II_β is shown in Figure 7.13 (c). Again, this transition shows a negligible polarization. However, the small effect that does occur results in a decrease in polarization with excitation power.

The inset of Figure 7.13 (c) shows that this effect also has a linear dependence with the natural logarithm of excitation power. Although this trend is unusual, since the effect is small, extra measurements and confirmation of the behavior are required before further physical descriptions of this process can be considered. Finally, the excitation dependent PL polarization of the InAlAs material is shown in Figure 7.13 (d). The effect on this transition is negligible, with any changes in polarization within the error of the measurements.

Figure 7.14 (a) and (b) show polarized PL spectra of InP QW at 4 K for two different excitation powers. Black and red solid lines show how the PL spectrum changes when the transmission direction of the polarizer rotates by 90^{o} degrees. Similar to the one observed previously for the InGaAsP QW sample, the PL spectrum is elliptically polarized and polarizations of the QW and inverted interface transitions are out of phase.

The change in linear polarization degree for the features in the InP QW spectrum is shown in Figure 7.15. It is seen that the polarization degree for the ground state QW transition increases by excitation power (Figure 7.15 (a)), and it saturates quickly. The same behavior was already observed for the polarization degree of the inverted interface (II_{α}) and QW transitions for the InGaAsP QW sample. However, the saturation in the polarization degree of the QW transition for InP QW structure occurs at lower power values compared with the inverted interface (II_{α}) and QW transitions for the InGaAsP QW.

Figure 7.15 (b) shows the polarization degree of inverted interface decreases by increasing excitation power. This behavior has an opposite trend with the one observed for the QW transition. The inset of this panel shows a linear change of polarization

degree as a function of natural logarithm of excitation power (there is no theoretical equation describing the linear dependence between polarization degree and natural logarithm of excitation). Similar behavior is observed for the inverted interface (II_β) transition in InGaAsP QW sample, see inset of Figure 7.13 (c). Figure 7.15 (c) shows the polarization behavior of InP and InAlAs transitions, which does not show a strong dependence to excitation power.

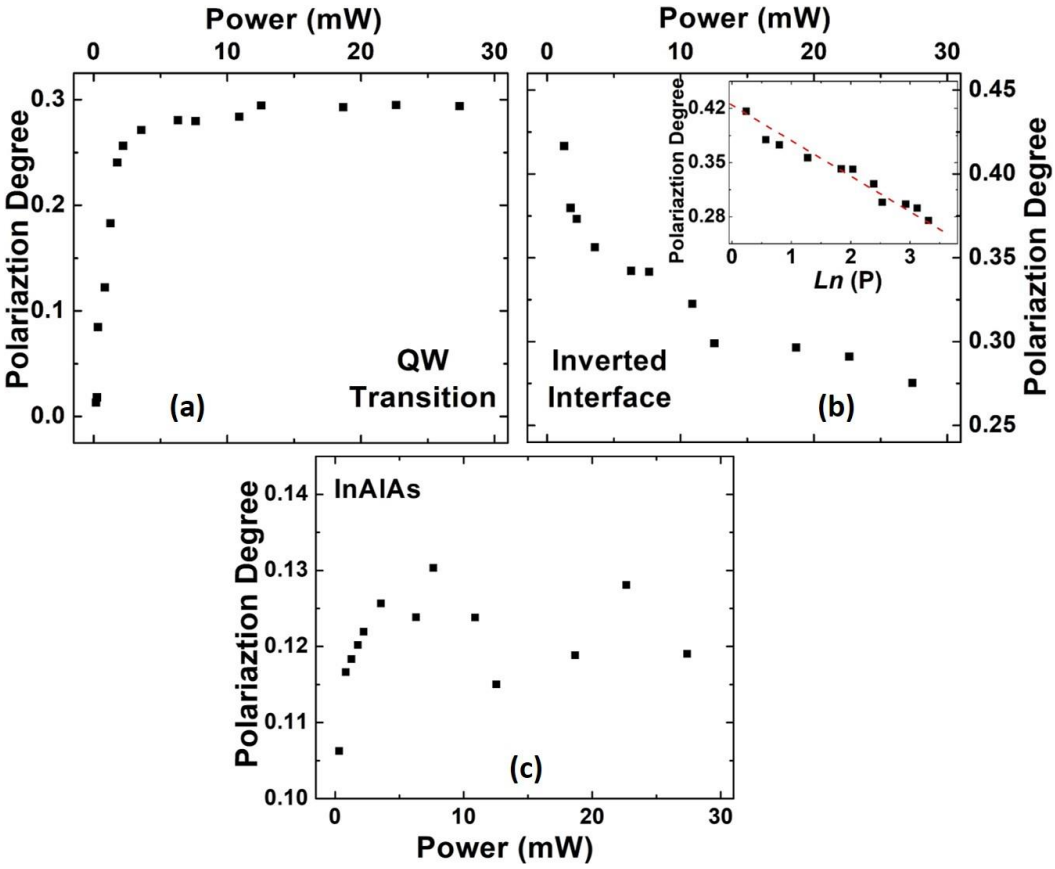

Figure 7. 15. Low temperature polarization degree of (a) the QW (1st peak), (b) the inverted interface (2nd peak) and (c) InAlAs transitions of InP QW structure. Inset of panel (b) shows the linear dependence of polarization degree for the inverted interface transition versus natural logarithm of power.

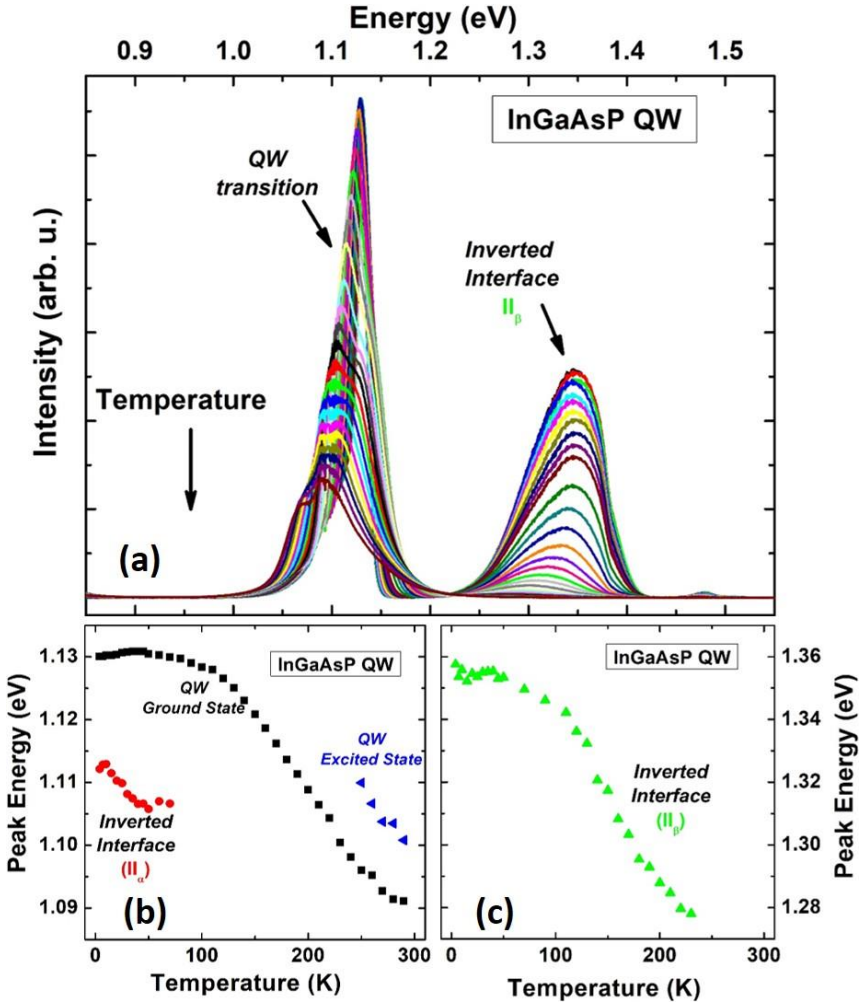

Figure 7. 16. (a) Temperature dependent PL spectra of InGaAsP QW structure. (b) and (c) Peak energy versus lattice temperature for the inverted interface (II_α) (red circles), the QW ground state (black squares), the first excited state (blue triangles) and the inverted interface (green triangles) transitions, respectively.

So far, excitation power dependent spectroscopy of the InGaAsP QW and InP QW samples at 4 K have been presented. Figure 7.16 shows PL spectra of InGaAsP QW at various lattice temperatures between 4 K and 300 K. The expected redshift of the band gap are observed according to the Varshni equation for all transitions. The peak shifts

associated with II_α and II_β are also affected by the thermal population of photogenerated carriers in localized states at these inverted interfaces.

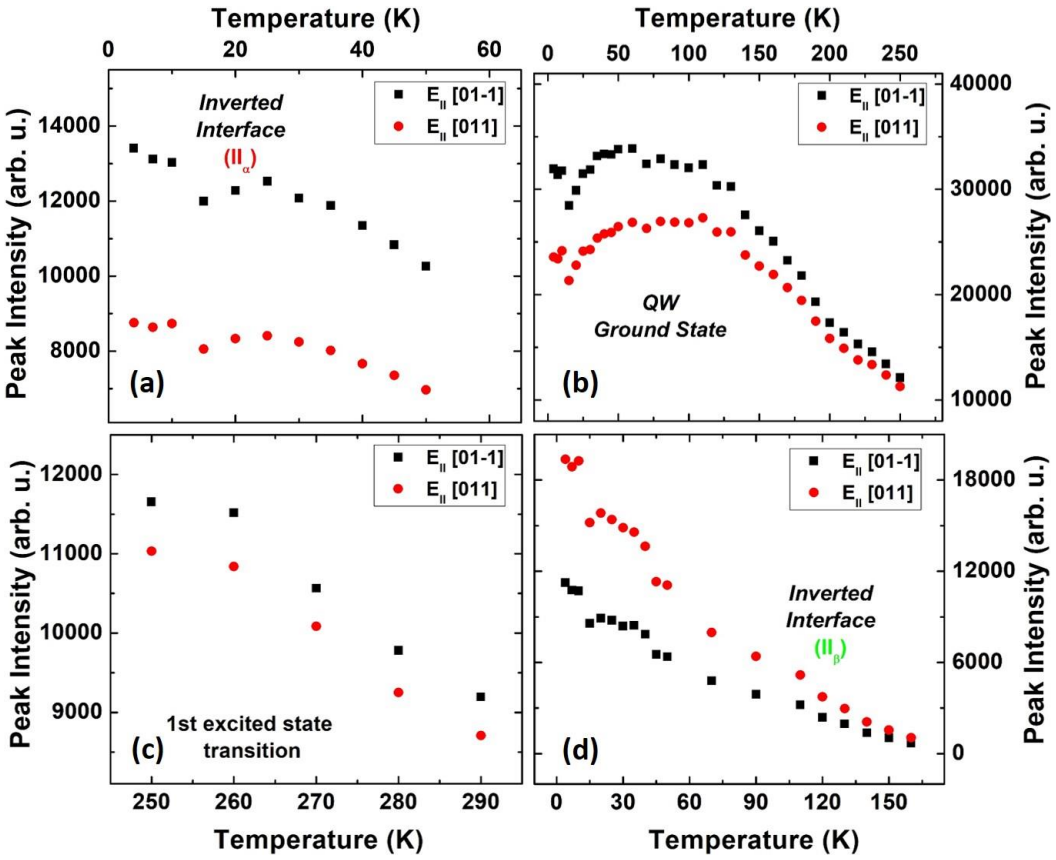

Figure 7. 17. (a)-(d) Peak intensity versus lattice temperature for the inverted interface (II_α) , the QW ground state, the first excited state, and the inverted interface (II_β) transitions of the InGaAsP QW sample extracted from temperature dependent PL spectra (see Figure 7.16 (a)). Black and red dots represent the PL peak intensities for two perpendicular directions of the polarizer transmission.

Figure 7.17 shows the change of PL peak intensity for InGaAsP QW as a function of lattice temperature for the two perpendicular orientations of the linear polarizer. The solid black squares and solid red circles represent the PL peak intensities aligned along

the [00-1] and [011] directions, respectively. The difference in peak intensities for two polarizations becomes smaller as temperature increases; especially for the ground state QW (Figure 7.17 (b)) and the inverted interface (II_β) transition (Figure 7.17 (d)). The physical explanation for this behavior is under investigation – however, this behavior indicates that by increasing lattice temperature the polarization of optical transitions in InGaAsP QW reduces, see Figure 7.18.

The difference in peak intensity for first excited state transition is shown in Figure 7.17 (c), it shows the relative difference between two peak intensities is constant over the temperature range studied. Figure 7.17 also shows that II_β transition is out of phase with all other transitions, at all temperatures. Moreover, when the orientation of the polarizer is aligned along the $[01-1]$ direction, the intensity of the ground state, first excited state and the II_α (inverted interface) transitions are maximized; while, the intensity of the II_β inverted interface is minimized.

Figure 7.18 shows the temperature dependent degree of optical polarization for the various transitions evident in the InGaAsP QW. As shown in Figure 7.17, the degree of optical polarization for all features is reduced with increasing lattice temperature, except for the first excited state, which shows a small and constant degree of optical polarization. The amount of change in polarization degree of the ground state QW transition is 73 %, 10% for II_α, and 28 % for II_β. The large and decreasing polarization of the QW and II_β imply the linear polarization of these samples is related to preferential orientation along the [00-1] plane, which suffers from thermal redistribution and mixing of the linear contributions at higher temperatures.

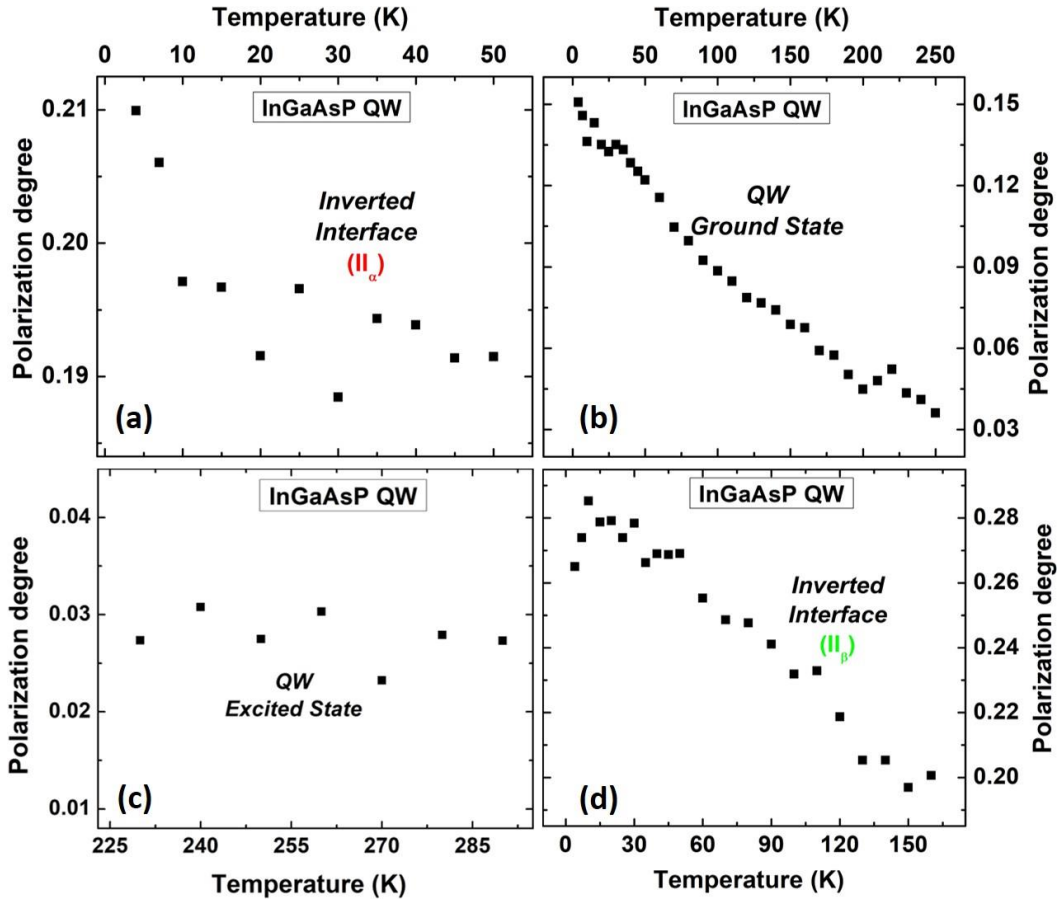

Figure 7. 18. Polarization degree as a function of lattice temperature for (a) the inverted interface (II_α), (b) the QW ground state, (c) the first excited state and (d) the inverted interface (II_β) transitions for InGaAsP QW structure.

Figure 7.19 shows temperature dependent PL spectra of the InP QW between 4 K and 300 K. The GS PL from this QW is evident at ~ 1.2 eV. A transition that has been attributed to an additional layer formed by a few monolayers of graded $InAs_xP_{1-x}$ at InP/AlInAs interface is also evident ~ 1.3 eV. At low temperatures, the ground state and inverted interface peaks are distinct; as the temperature increases, they become more convoluted due to the thermally mediated redshift and broadening of both peaks. Above 140 K, the contribution of the feature related to the $InAs_xP_{1-x}$ is quenched and its

contribution is therefore negligible. The peak located at 1.48 eV is associated with the InAlAs barrier and InP cap.

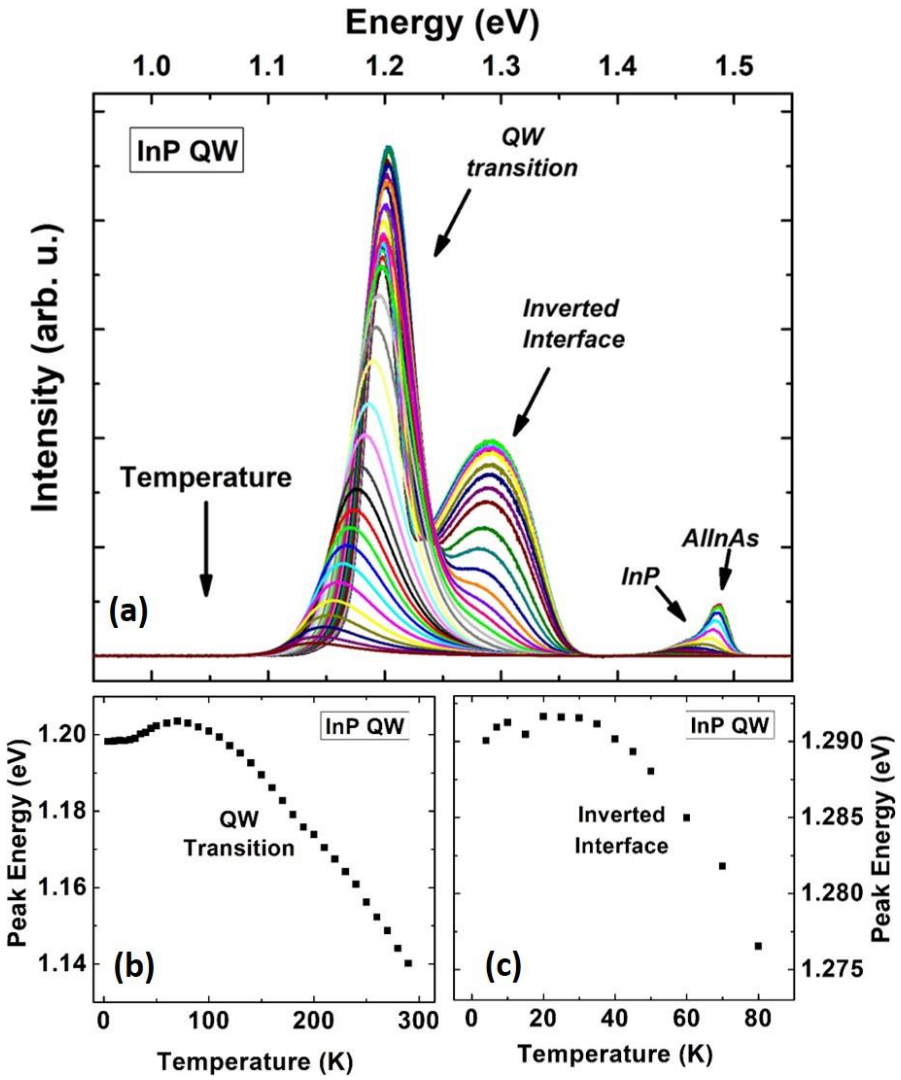

Figure 7. 19. (a) Temperature dependent PL spectra of InP QW at temperatures between 4K and 300K. (b) and (c) Peak energy versus lattice temperature for the QW ground state and the inverted interface transitions, respectively.

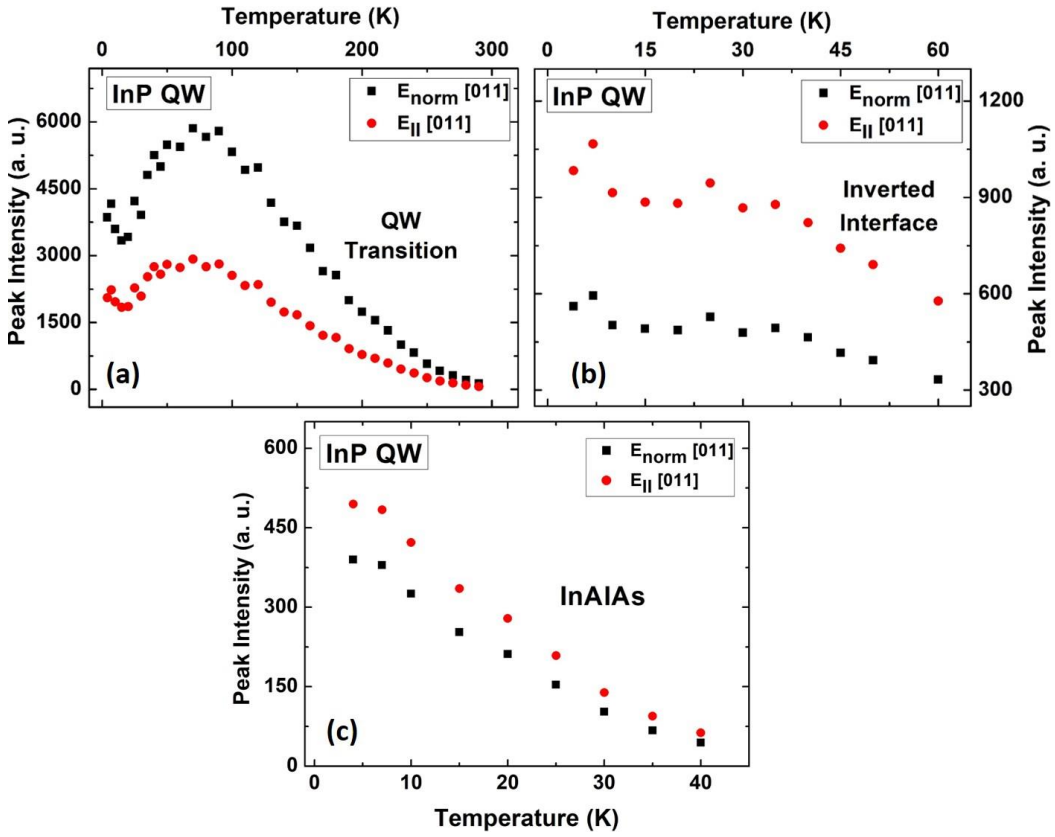

Figure 7. 20. Peak intensity of InP QW structure as a function of temperature for (a) the QW ground state, (b) the inverted interface and (c) InAlAs transitions, respectively. Black and red dots are associated with peak intensities when polarizer transmission is aligned with $[01-1]$ and [011], respectively.

Figure 7.20 shows the temperature dependent degree of optical polarization for the InP QW between 4 K and 300 K. The solid black squares and solid red circles represent the intensity associated with two perpendicular polarizations, respectively. In Figure 7.20 (a), the peak intensity associated with the ground state of the QW increases up to 75 K (for both orientations) and then it drops due to increase in non-radiative processes. The initial increase in peak intensity of the ground state QW transition is associated with

thermal redistribution of photogenerated charges at the localized states within the inverted interface and their diffusion into the QW region.

Figure 7.20 (b) and (c) show the change of peak intensities for the inverted interface and InAlAs transitions as a function of lattice temperature, respectively. It is observed that the peak intensity quenches for both transitions. However for the inverted interface, there is a slight increase (or flattening) around 30 K, prior to further quenching of the PL. This increase (or flattening) in peak intensity of the inverted interface is consistent with the change in peak intensity of the QW transition (the QW peak intensity drops up to 20 K, followed by an increase up to about 80 K); this effect confirms the correlation between peak intensity change of the ground state QW and inverted interface transitions due to thermal redistribution.

Figure 7.21 shows the change in degree of optical polarization (*P*) degree as a function of lattice temperature for all optical transitions in InP QW. In Figure 7.21 (a) the *P* of the QW increases with increasing lattice temperature. This behavior indicates that at elevated temperatures the polarization of the PL from the ground state of the QW transition is stronger than at low temperatures – the inverse behavior is observed for the InGaAsP QW. The origin of this behavior is currently under further investigation to determine if these properties are a function of the non-idealities of the samples or are intrinsic to these systems. One hypothesis for the increase of polarization as a function of lattice temperature can be attributed to larger separation of the sub-band states in the valence band due to the local biaxial strain. [9] At this condition, when occupation of higher order sub-band levels in the valence band is limited, the optical transition (PL) from the conduction band to the holes in the lowest valence band state has the same

polarization as the valence band state. In addition, by increasing the hole distribution in the lowest energy level in the valence band at elevated temperatures the emitted PL becomes more polarized with the same polarization as the occupied sub-band state in the valence band. [21, 24]

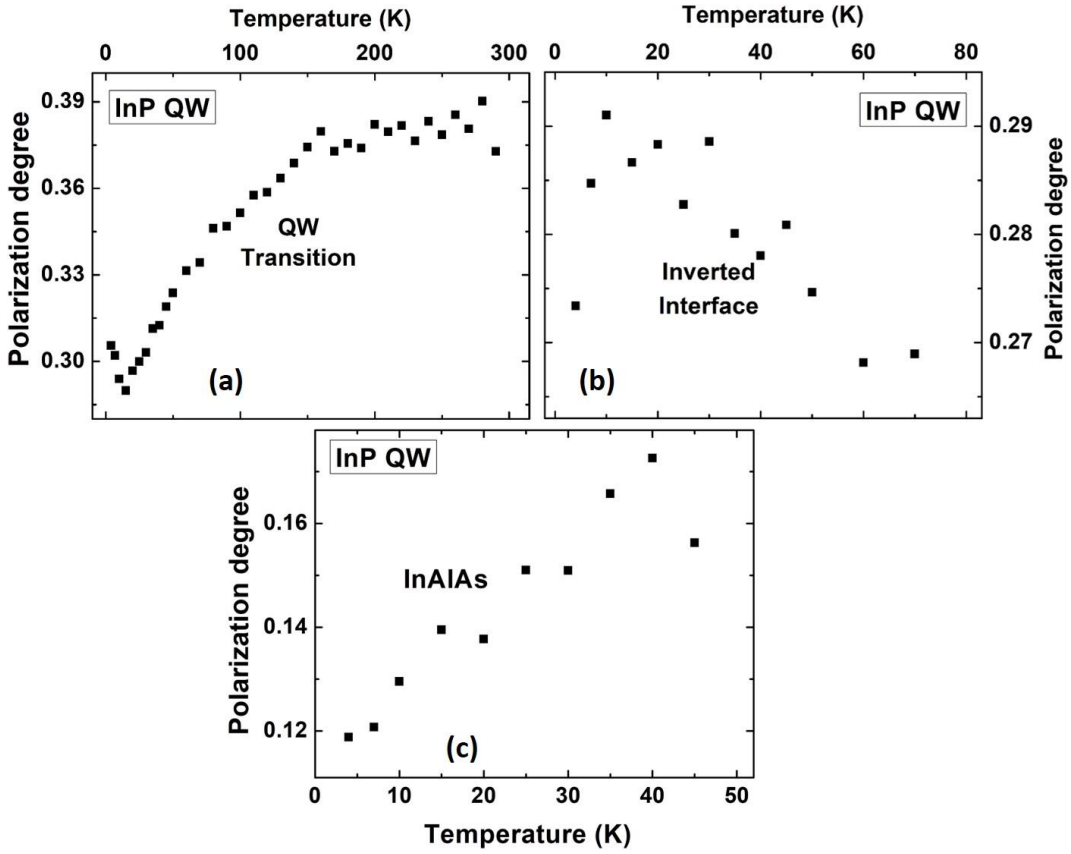

Figure 7. 21. Polarization degree versus lattice temperature for (a) the QW ground state, (b) the inverted interface and (c) InAlAs transitions in InP QW sample.

Figure 7.21 (b) and (c) show temperature dependent *P* for the inverted interface and InAlAs transitions, respectively. There is a slight decrease in *P* for the inverted interface with increasing temperature as the photogenerated carriers escape localized states. [21] Similar behavior is observed for the inverted interface of InGaAsP QW, as shown in

Figure 7.18 (d). A slight increase in the polarization for InAlAs transition is observed in Figure 7.21 (c), which is similar to the behavior of the InP QW (see Figure 7.21 (a)).

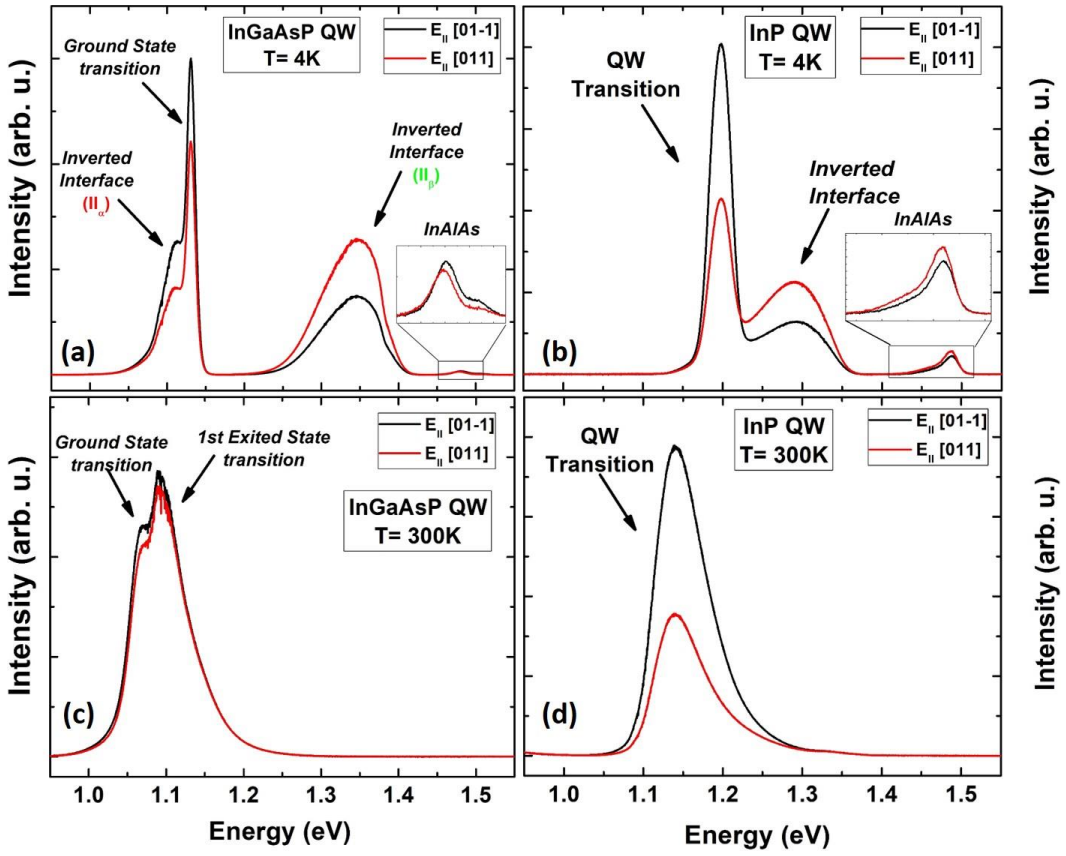

Figure 7. 22. (a) and (c) Comparison between two perpendicular polarizations (shown by red and black lines) for InGaAsP QW at 4K and 300K, respectively. (b) and (d) Comparison between two perpendicular polarizations for InP QW at 4K and 300K, respectively. It can be seen that as temperature increases, polarization effect for InGaAsP QW decreases, and at room temperature, the PL spectrum has a negligible polarization effect. However, the polarization of the emitted PL spectrum of InP QW increases by increasing lattice temperature and it shows strong polarization behavior at 300K.

Figure 7.22 shows a comparison of the PL for the two perpendicular polarizations at 4.2 K and 300 K for both the InGaAsP QW (a) and (c), respectively; and the InP QW (b) and (d), respectively. For the InGaAsP QW at 4.2 K (panel (a)), there is a distinct difference in the two PL spectra for the two perpendicular polarizations as shown in black and red, respectively. However at room temperature (c), this difference is significantly reduced. Figure 7.22 (b) and (d) show the comparison between two polarizations for the InP QW at 4K and 300 K, respectively. There is strong polarization at both low and higher temperatures for this QW.

Again, the strength and orientation of the polarization dependence of the InP versus InGaAsP QW are under further investigation, both theoretically and with magneto-optical spectroscopy. In these systems, the origin of polarization has been investigated to determine and confirm the nature of inverted interfaces in the systems, which (as have been discussed) have strong polarization dependencies. On closer inspection of the spectra in Figure 7.22, there is some evidence that the coupling between the inverted interfaces and the QWs – particularly in the case of the InP QW – may somehow contribute to the polarization dependence of the QW emission. This will be further studied and reported elsewhere.

Conclusion

In conclusion, the effects of interface transitions that result in InP and InGaAsP systems when encapsulated in InAlAs have been studied comprehensively using photoluminescence spectroscopy. It is observed that there are two additional optical transitions that arise in these systems due to the inverted interface (II_α and II_β) that is

particularly prevalent when the samples are capped with InP. The inverted interface transition in InP QWs at 4.2 K (II_α at 1.11 eV) is very close to the optical transition from the ground state of the QW (at 1.13 eV), which serves to broaden the full width at half maximum (FWHM) of the QW PL spectrum. By increasing the lattice temperature and/or excitation power, the inverted interface transition (especially II_α) is reduced; at room temperature no evidence of such interface transitions are observed. This is attributed to the redistribution of photogenerated carriers at higher temperatures that escape from the localized states and diffuse into the QW region.

In the second part of this chapter, polarization dependent PL was performed on both the InP and InGaAsP QW structures to confirm the origin of the interface transitions. Temperature dependent optical polarization was observed in both the InP and InGaAsP QWs. The orientation of the polarized PL for the inverted interface transition (II_β) was perpendicular to polarization of the second inverted interface transition (II_α), and the QW transition; this is due to the orthogonality of planes at the interfaces where photogenerated carriers were accumulated. Temperature dependent PL spectroscopy of *InGaAsP QW* structures showed a *decrease* in the degree of optical polarization with *increasing temperature*, while the *InP QW* displayed a *stronger degree of optical polarization* at *elevated temperatures*. The origin of this unusual temperature dependence of the optical polarization for the InP QWs is currently under further investigations and will be presented elsewhere.

References

[1] Kagawa, Toshiaki, Yuichi Kawamura, and Hidetoshi Iwamura. "A wide-bandwidth low-noise InGaAsP-InAlAs superlattice avalanche photodiode with a flip-chip structure for wavelengths of 1.3 and 1.55 μm." IEEE journal of quantum electronics 29, no. 5 (1993): 1387-1392.

[2] Kawamura, Yuichi, and Takuya Shono. "Absorption Change Induced by Electric Field of an InGaAsP/InAlAs/InP Asymmetric Quantum Well Structure Gown on InP Substrates." Japanese Journal of Applied Physics 50, no. 2R (2011): 020201.

[3] Coldren, Larry A., Scott W. Corzine, and Milan L. Mashanovitch. Diode lasers and photonic integrated circuits. Vol. 218. John Wiley & Sons, 2012.

[4] Kawamura, Yuichi, and Hidetoshi Iwamura. "InGaAsP/InAlAs type I/type II multiple quantum well structures grown by gas source molecular beam epitaxy." Journal of crystal growth 150 (1995): 597-601.

[5] Tang, J., V. R. Whiteside, H. Esmaielpour, S. Vijeyaragunathan, T. D. Mishima, M. B. Santos, and I. R. Sellers. "Effects of localization on hot carriers in InAs/$AlAs_xSb_{1-x}$ quantum wells." Applied Physics Letters 106, no. 6 (2015): 061902.

[6] Esmaielpour, Hamidreza, Vincent R. Whiteside, Jinfeng Tang, Sangeetha Vijeyaragunathan, Tetsuya D. Mishima, Shayne Cairns, Michael B. Santos, Bin Wang, and Ian R. Sellers. "Suppression of phonon-mediated hot carrier relaxation in type-II InAs/$AlAs_xSb_{1-x}$ quantum wells: a practical route to hot carrier solar

cells." Progress in Photovoltaics: Research and Applications 24, no. 5 (2016): 591-599.

[7] Hirst, Louise C., Michael K. Yakes, Chaffra A. Affouda, Christopher G. Bailey, Joseph G. Tischler, Hamidreza Esmaielpour, Vincent R. Whiteside *et al.* "Hot-carrier effects in type II heterostructures." In 2015 IEEE 42nd Photovoltaic Specialist Conference (PVSC), pp. 1-3. IEEE, 2015.

[8] Vignaud, D., X. Wallart, F. Mollot, and B. Sermage. "Photoluminescence study of the interface in type II InAlAs–InP heterostructures." Journal of applied physics 84, no. 4 (1998): 2138-2145.

[9] Böhrer, J., A. Krost, R. Heitz, F. Heinrichsdorff, L. Eckey, D. Bimberg, and H. Cerva. "Interface inequivalence of the InP/InAlAs/InP staggered double heterostructure grown by metalorganic chemical vapor deposition." Applied Physics Letters 68, no. 8 (1996): 1072-1074.

[10] Benyattou, T., M. A. Garcia, S. Moneger, A. Tabata, M. Sacilotti, P. Abraham, Y. Monteil, and R. Landers. "Optical characterization of InP/InAlAs/InP interfaces grown by MOVPE." Applied surface science 63, no. 1-4 (1993): 197-201.

[11] Hellara, J., K. Borgi, H. Maaref, V. Souliere, and Y. Monteil. "Optical properties of InP/InAlAs/InP grown by MOCVD on (100) substrates: influence of V/III molar ratio." Materials Science and Engineering: C 21, no. 1-2 (2002): 231-236.

[12] Esmaielpour, Hamidreza, Vincent R. Whiteside, Louise C. Hirst, Joseph G. Tischler, Robert J. Walters, and Ian R. Sellers. "The effect of an InP cap layer on

the photoluminescence of an $In_xGa_{1-x}As_{1-y}P_y/In_zAl_{1-z}As$ quantum well heterostructure." Journal of Applied Physics 121, no. 23 (2017): 235301.

[13] Vignaud, D., X. Wallart, and F. Mollot. "InAlAs/InP heterostructures: Influence of a thin InAs layer at the interface." Journal of applied physics 76, no. 4 (1994): 2324-2329.

[14] Varshni, Yatendra Pal. "Temperature dependence of the energy gap in semiconductors." physica 34, no. 1 (1967): 149-154.

[15] Raisky, O. Y., W. B. Wang, R. R. Alfano, C. L. Reynolds, Jr, and V. Swaminathan. "Investigation of photoluminescence and photocurrent in InGaAsP/InP strained multiple quantum well heterostructures." Journal of applied physics 81, no. 1 (1997): 394-399.

[16] Temkin, H., V. G. Keramidas, M. A. Pollack, and W. R. Wagner. "Temperature dependence of photoluminescence of n-InGaAsP." Journal of applied Physics 52, no. 3 (1981): 1574-1578.

[17] Hugues, M., B. Damilano, J-Y. Duboz, and J. Massies. "Exciton dissociation and hole escape in the thermal photoluminescence quenching of (Ga, In)(N, As) quantum wells." Physical Review B 75, no. 11 (2007): 115337.

[18] Lumb, Matthew P., Igor Vurgaftman, Chaffra A. Affouda, Jerry R. Meyer, Edward H. Aifer, and Robert J. Walters. "Quantum wells and superlattices for III-V photovoltaics and photodetectors." In Next Generation (Nano) Photonic and Cell Technologies for Solar Energy Conversion III, vol. 8471, p. 84710A. International Society for Optics and Photonics, 2012.

[19] Esmaielpour, Hamidreza, Vincent R. Whiteside, Louise C. Hirst, Joseph G. Tischler, Chase T. Ellis, Matthew P. Lumb, David V. Forbes, Robert J. Walters, and Ian R. Sellers. "Effect of occupation of the excited states and phonon broadening on the determination of the hot carrier temperature from continuous wave photoluminescence in InGaAsP quantum well absorbers." Progress in Photovoltaics: Research and Applications 25, no. 9 (2017): 782-790.

[20] Gogineni, Chaturvedi, Nathaniel A. Riordan, Shane R. Johnson, Xianfeng Lu, and Tom Tiedje. "Disorder and the Urbach edge in dilute bismide GaAsBi." Applied Physics Letters 103, no. 4 (2013): 041110.

[21] Liuolia, Vytautas, Saulius Marcinkevičius, You-Da Lin, Hiroaki Ohta, Steven P. DenBaars, and Shuji Nakamura. "Dynamics of polarized photoluminescence in m-plane InGaN/GaN quantum wells." Journal of Applied Physics 108, no. 2 (2010): 023101.

[22] Adams, J. G. J., W. Elder, P. N. Stavrinou, J. S. Roberts, M. Gonzalez, J. G. Tischler, R. J. Walters *et al.* "Experimental measurement of restricted radiative emission in quantum well solar cells." In Photovoltaic Specialists Conference (PVSC), 2010 35th IEEE, pp. 000001-000005. IEEE, 2010.

[23] Lavallard, P., C. Gourdon, and R_ Planel. "Interface induced anisotropic splitting of exciton states in GaAsAlAs short period superlattices." Superlattices and microstructures 12, no. 3 (1992): 321-325.

[24] Masui, Hisashi, Hisashi Yamada, Kenji Iso, Shuji Nakamura, and Steven P. DenBaars. "Optical polarization characteristics of m-oriented InGaN/GaN light-

emitting diodes with various indium compositions in single-quantum-well structure." Journal of Physics D: Applied Physics 41, no. 22 (2008): 225104.

Chapter **8**

Optical Spectroscopy of 2D and 3D Hybrid Lead Halide Perovskites

8.1. Introduction

Recently, hybrid lead halide perovskites have attracted a considerable interest for photovoltaic applications. [1, 2, 3] These materials have shown outstanding properties as solar cell absorbers such as: large absorption coefficients in the range of the maximum visible spectrum, low production costs, high power conversion efficiency, simple fabrication processes, and the capability of being deposited on flexible substrates. [3, 4, 5] In addition, the band gap of these materials is closely matched to the peak of the solar spectrum, which coupled with their low exciton binding energies and long diffusion lengths make them exciting systems for utility-scale PV. [5, 6, 7, 8] An important consideration regarding these materials and their applications to photovoltaic (PV) technology (particularly, hot carrier solar cells) is to study the interaction of electrons (or holes) with phonons in the system. [5, 6, 9, 10, 11] Slow carrier cooling rates have been observed in these systems however, the origin of this interesting behavior remains poorly understood.

Hybrid lead halide perovskite systems take a basic ABX_3 structure, as shown in Figure 8.1. In this description "A" refers to (typically) an organic cation such as methylammonium (MA^+, $CH_3NH_3^+$), "B" is a divalent metal cation (Pb^{2+} or Sn^{2+}) and "X" is a halide anion e.g., Br^- or I^-. [1, 9, 12] By changing the composition of the

constituent materials, the electrical and optical properties of the structure can be controlled. One compound, which has attracted much research activity, is the perovskite system methylammonium lead triiodide – $MAPbI_3$. Although this structure suffers degradation in atmospheric conditions, it has produced solar cell efficiencies in excess of 20%. [13] However, to facilitate the practical implementation of these systems, the stability and moisture resistance of these systems must be improved.

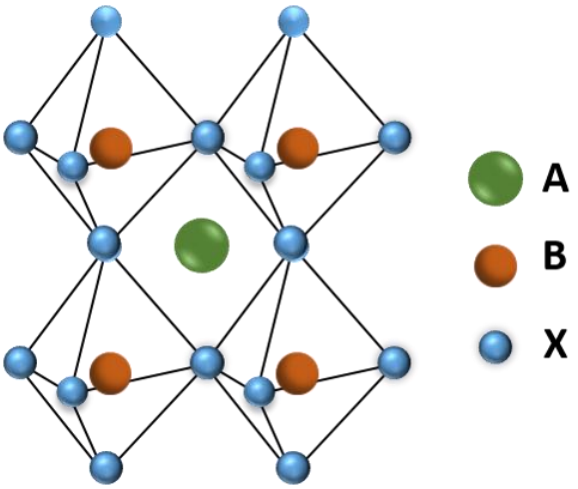

Figure 8. 1. Schematic of a perovskite crystal structure. "A" is a large cation molecule like methylammonium (MA^+), "B" a smaller cation like Pb^{2+}, and "X" a halogen ion like I^- or Br^-.

Improvements in stability of the structure has been shown when the inorganic cation MA^+ is replace with alternative molecules such as Formamidinium (FA^+) (more common), as well as n-butylammonium (BA^+). In the case of BA^+, this substitution results in the formation of a 2D family of $(BA)_2(MA)_{n-1}Pb_nI_{3n+1}$ ($(CH_3(CH_2)_3NH_3)_2(CH_3NH_3)_{n-1}$ Pb_nI_{3n+1}) perovskites. These so-called Ruddlesden-Popper 2D perovskites can be visualized by slicing the 3D structure and arranging them along the (110) plane. [14] For the n = 1 compound, the BA^+ cations substitute

completely with the MA^+ cations and as the "*n*" value increases, the MA^+ cation contribution to the structure increases, increasing the thickness in the out of plane direction. When "*n*" is a large value ($n \rightarrow \infty$), the structure reverts to *bulk* 3D $MAPbI_3$. [14, 15]

As discussed, one of the main issues with $MAPbI_3$ is its instability when exposed to humid environments. However, in the case of $(BA)_2(MA)_{n-1}Pb_nI_{3n+1}$ these 2D perovskites have very good moisture-resistance properties and it has been reported that their properties are unchanged, even after two months of operation under laboratory conditions (40% humidity). [14] This effect is attributed to the hydrophobic nature of the BA^+ cations and their well-oriented dense structure. As a result of these features direct contact of the perovskite with water molecules in the ambient environment is limited and the structure is stable for a longer period of time than the bulk systems.[14]

In this study, four different perovskite structures ($n = 1, 2, 4$, and ∞) were investigated. For simplicity, instead of writing the full chemical formulas of the compounds, abbreviations will be utilized hereafter: PbI_4 is used for the single-layer ($n = 1$), Pb_2I_7 for the two-layer ($n = 2$), Pb_4I_{13} for the four-layer ($n = 4$), and PbI_3 for the 3D ($n \rightarrow \infty$) perovskite structure.

8.2. Experimental results and discussions

8.2.1. Photoluminescence and Transmission Spectroscopy of the Perovskite Structures

Continuous wave power and temperature dependent PL spectroscopy are performed on the samples using a He-Cd (442 nm) laser. The samples are kept under vacuum and the temperature is controlled by a Janis closed cycle cryostat, which operates from 4 K to 300 K. The emitted PL signals are dispersed using a Princeton Instrument 2560i spectrometer and detected with an air cooled Si-detector.

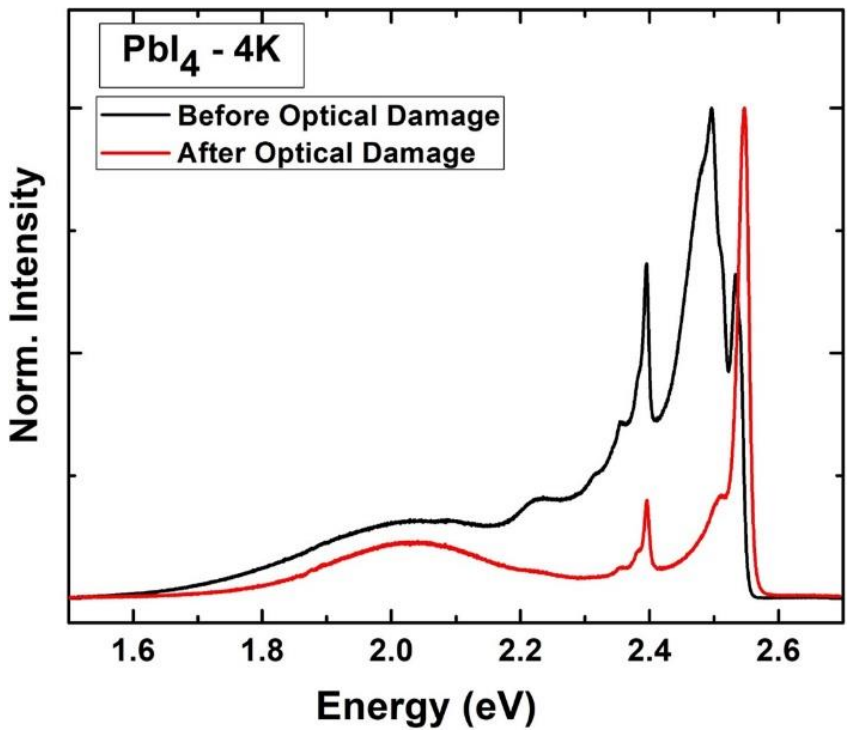

Figure 8. 2. The comparison of PL spectra of the one-layer (n = 1, PbI_4) 2D perovskite at 4 K before and after optical damage by a He-Cd laser.

One important aspect regarding the optical properties of perovskite samples is to make sure there is no irreversible and catastrophic phase change due to local thermal heating during laser excitation. Permanently optical altering by laser illumination can occur due to accumulative heating through absorption in the perovskite film. This results in the decomposition of the perovskite, which is irreversible and significantly degrades the optical and electrical properties of the structure.

Figure 8.2 shows PL spectra before (black) and after (red) optical damage in PbI_4 (n=1) due to parasitic heating with the He-Cd laser. The emitted PL spectra of the sample before and after exposure are clearly different, which is associated with irreversible changes in the structure upon high power laser excitation. As a result, the first step in performing a systematic investigation of such systems is to determine the range of the excitation powers, under which irreversible changes the perovskite structures are avoided.

Figure 8.3 shows the PL spectra at 300 K for four samples (n = 1, 2, 4, and ∞) measured at laser fluences below the decomposition limit described above. It is observed that by reducing the amount of MA^+ cation in the system the band gap energy of the system shifts to higher values as the perovskite transitions from a 3D to 2D structure. This is related to the increase in quantum confinement associated with reducing the dimensionality of the perovskite layers. [14, 15, 16] In addition, it is observed at n = 1 that the PL spectrum has a narrow full width at half maximum (FWHM). By increasing the "n" value, the FWHM increases and additional features arise around the main peak. This effect is associated with additional (unintentional

formation of) incomplete layers within the system with transition energies between 2.4 eV (PbI_2) and 1.5 eV (PbI_3). [14, 17]

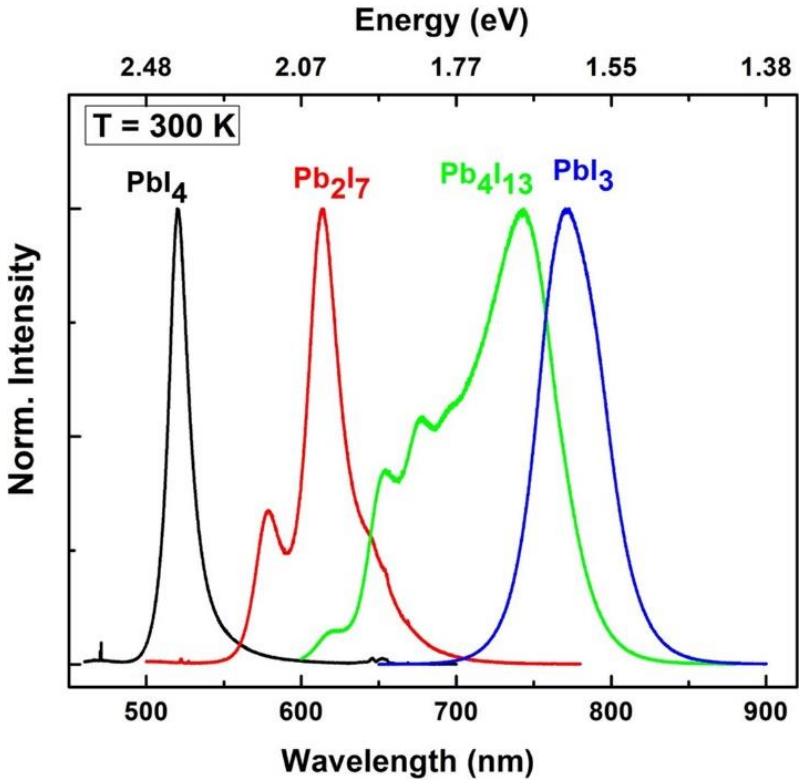

Figure 8. 3. PL spectra of 2D (n = 1 (black), 2 (red), 4 (green)) and 3D (n → ∞ (blue)) perovskite samples at 300 K.

Figure 8.4 shows temperature dependent behavior of the 2D (*n* = 1, 2, and 4) and 3D perovskite samples. These figures show XYZ plots (color plots) of the PL spectra of the samples where X (horizontal axis) is lattice temperature, Y (vertical axis) is the magnitude of photon energy for the emitted PL, and Z (out of plane axis) is the normalized intensity. In the scale bar above the main panels, the dark blue color is low intensity (close to zero) and dark red is the maximum value for the normalized intensity. It is observed that the peak energy of the samples increases (or stabilizes) when

increasing the lattice temperature. This behavior, as reported by several groups, [5, 18] is associated with an out-of-phase band edge stabilization of these compounds when the lattice temperature increases. This is in contrast to the more typical semiconductor behavior where the peak energy of the PL spectra is redshifted with increasing lattice temperature due to thermal expansion of the lattice. [19]

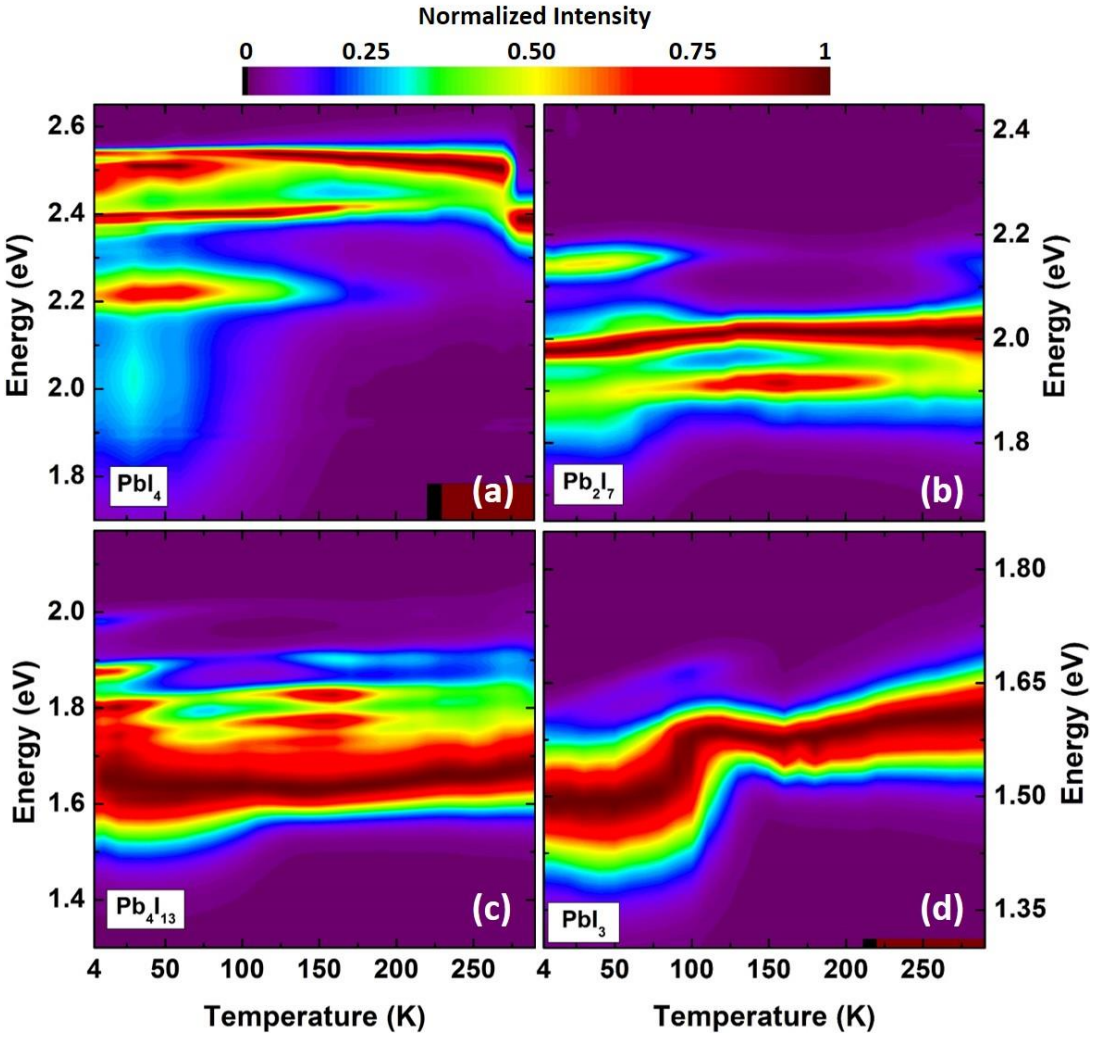

Figure 8. 4. Temperature dependent normalized PL spectra for 2D (n = 1 (a), 2 (b), 4 (c)) and 3D (n → ∞ (d)) perovskite samples. This graph shows how the PL peak energy of the each sample changes from 4 K to 300 K.

Figure 8.4 (d) shows PL spectra of the 3D (PbI_3) perovskite as a function of temperature. At low temperatures, the PL spectrum is broad with multiple competing features. This is indicative of the existence of inclusions from opposing phases of the perovskite and localized states in the structure, which create multiple optical transitions within the system. [5] The origin of this behavior in $MAPbI_3$ is associated with the phase changes and the inherent instability of the material. $MAPbI_3$ has an orthorhombic structure at low temperatures (T < 130 K -160 K), which transforms to a tetragonal structure up to ~ 330 K. [5, 18] During the phase change, localized states are created, which trap photogenerated charges and/or excitons. It has been observed that when MA^+ is substituted with FA^+, less broadening of the PL spectrum occurs. [5] As such, it is not considered that the broadening of the PL spectrum due to inhomogeneities is an intrinsic property of perovskite materials.

As the lattice temperature is increased above 150 K, the PL spectrum of the PbI_3 also broadens (see Figure 8.4(d)). This PL linewidth is associated with a number of scattering mechanisms in the system, a comprehensive discussion concerning linewidth broadening is provided at the end of this chapter. [20, 21] Figure 8.4 (a) shows the normalized temperature dependent PL of the $n = 1$ (PbI_4) 2D perovskite from 4 K to 300 K. At low temperatures ($T < 130$ K), the PL spectrum is broad, which is associated with the optical transitions of trapped carriers at the localized states in the system. As the lattice temperature increases, the contribution of these states becomes less significant as photogenerated carriers gain enough thermal energy to escape from these states. [22, 23, 24] Moreover, it is seen by increasing lattice temperature the peak energy does not significantly shift energetically for the 2D system ($n = 1$) (see Figure 8.4 (a)). However

at 280 K, there is an abrupt shift in the peak energy to a lower energy. The origin of this effect is associated with an "orthorhombic to orthorhombic" phase transition. [25] That is, during the phase change the crystal structure does not change phase state, but the orientation of the organic molecules with respect to the organic layers rotate, which causes a change in (affects) the optical gap. A hysteresis behavior is observed for this transition, the peak shift occurs at 280 K as the sample is heating up, and reverts back to around 230 K as the sample cools down. This behavior is related to the existence of a metastable state in the crystal structure, which is effective in the range of 230 K – 280 K. [20]

The normalized temperature dependent PL for the two-layer (n = 2) (Pb_2I_7) 2D perovskite is shown in Figure 8.4 (b). At low temperatures the PL spectrum of the sample is broad and as the lattice temperature increases (up to ~ 100 K) this broadening reduces; however, thereafter an additional feature appears on the low energy side of the PL with a separation from the main peak of ~ 100 meV. The origin of this additional feature (which lasts up to room temperature) has been attributed to mixed phases and the existence of thicker regions in the 2D perovskite ($n > 2$); i.e., through the non-ideal formation of the $n = 2$ layer during synthesis. [14] Finally, the temperature dependent PL for the four-layer ($n = 4$) (Pb_4I_{13}) 2D perovskite is shown in Figure 8.4 (c). The emitted PL of this compound is very broad with multiple optical transitions even at 300 K. This is once more associated with the contribution (or contamination) of other *n*-layers within the system, which create intermediate layers stabilized by surface effects in the thin perovskite structure. [14, 15]

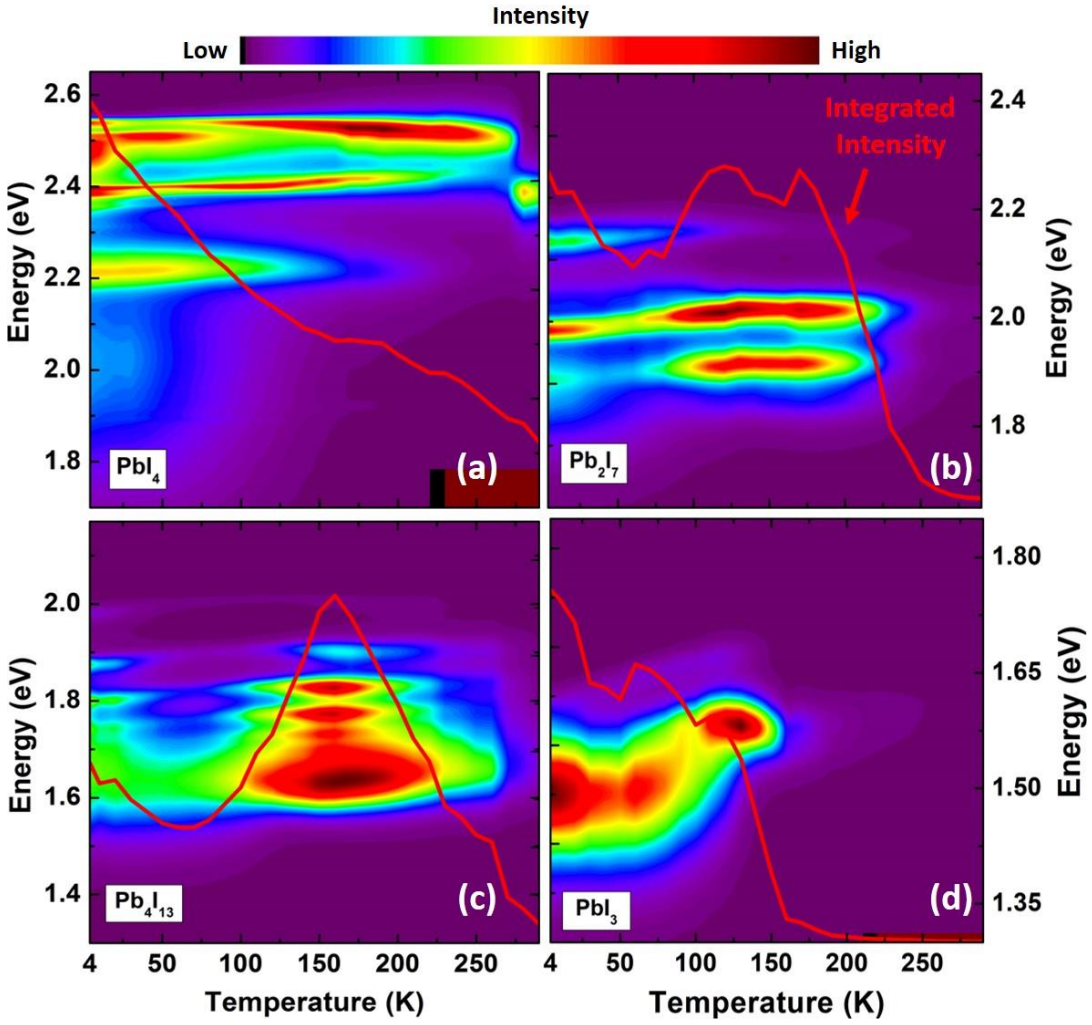

Figure 8. 5. Temperature dependent PL spectra for 2D (n = 1 (a), 2 (b), 4 (c)) and 3D (n → ∞ (d)) perovskite samples. This graph shows how the PL intensity of the each sample changes from 4 K to 300 K. Solid red line shows *integrated* PL intensity as a function of lattice temperature.

Figure 8.5 shows the radiative recombination intensity of the samples in the range 4K to 300 K. Figure 8.5 also shows comparative plots of the PL intensities at various lattice temperatures. Figure 8.5 (a) shows the change of the PL intensity for the *n* = 1 (PbI_4)

2D perovskite. At low temperatures (T < 50 K), the optical transitions between 2.4 eV and 2.5 eV have the highest PL intensity. As the lattice temperature increases above 50 K, the feature at 2.53 eV increases in magnitude. In addition, in the range 150 K to 200 K – where the PL intensity at 2.4 eV quenches – the PL transition at 2.53 eV becomes dominant – producing the highest intensity observed for this transition. This thermal redistribution of photogenerated carriers occurs as they escape from localized states to then occupy alternative optical transitions and the fundamental bands of the system. [22] Increasing the lattice temperature above 200 K causes the PL intensity to decrease. This effect is generally related to an increase in non-radiative recombination with increasing temperature, which results in a reduction in the rate of radiative recombination efficiency. [22, 26, 27]

The temperature dependent PL intensity for the n = 2 (Pb_2I_7) 2D perovskite is shown in Figure 8.5 (b) from 4 K to 300 K. It is evident that increasing the lattice temperature increases the peak PL intensity between 75 K and 200 K. This indicates that at low temperatures, photogenerated carriers are trapped at localized states or inclusions and radiative recombination occurs at these states at low temperature. In addition, the *integrated* intensity does not change considerably at low temperatures, which is indicative of thermal redistribution in the system. However, as the temperature increases the carriers escape from the localized states and recombine radiatively in a smaller subset of states. As such, the peak PL intensity at these energies increases at these intermediate temperatures. [22, 28]

Figure 8.5 (c) shows the temperature dependent behavior of the PL intensity for the (n = 4) (Pb_4I_{13}) 2D perovskite. At low temperatures the PL intensity is low, similar to

that of the other 2D perovskites discussed (n = 1, 2). As the temperature increases, the *integrated* PL and peak intensity of the $n = 4$ sample increase. As has been discussed, the PL spectrum for the four-layer 2D perovskite is broad, which is attributed to inhomogeneity in the structure and the presence of a number of competing 2D contributions ($n = 1$, $n = 2$, $n = 3$ etc.). [14] Above 200 K, the PL intensity quenches, which is associated with an increase in non-radiative recombination processes [22] and indicates significant inclusions and/or structural inhomogeneities in this particular sample. Similar behavior is also observed in the *integrated* PL intensity for the $n = 4$ sample.

The temperature dependent PL intensity of the 3D (PbI_3) perovskite sample is shown in Figure 8.5 (d). At low temperatures ($T < 30$ K), the PL intensity is strong and dominated by a transition at 1.48 eV. Increasing the temperature to 120 K (while retaining the orthorhombic – prior to any phase transition) results in a reduction in the PL intensity. As discussed, the crystal structure of the $MAPbI_3$ changes from an orthorhombic to tetragonal phase at ~ 130 K – 160 K. As the temperature approaches this phase transition, an increase in the contribution of inclusions from the different (competing) phases occurs, which serves to quench the PL. Therefore, the contribution of non-radiative recombination increases, subsequently reducing the efficiency of the PL. [22] As shown in Figure 8.5 (d) the PL intensity drops up to 120 K, which is further evidence for the increasing the rate of non-radiative recombination. Although the PL peak intensity is at its maximum at 140 K, it is evident that the *integrated* PL intensity also drops, which also further supports the increased role of non-radiative recombination processes.

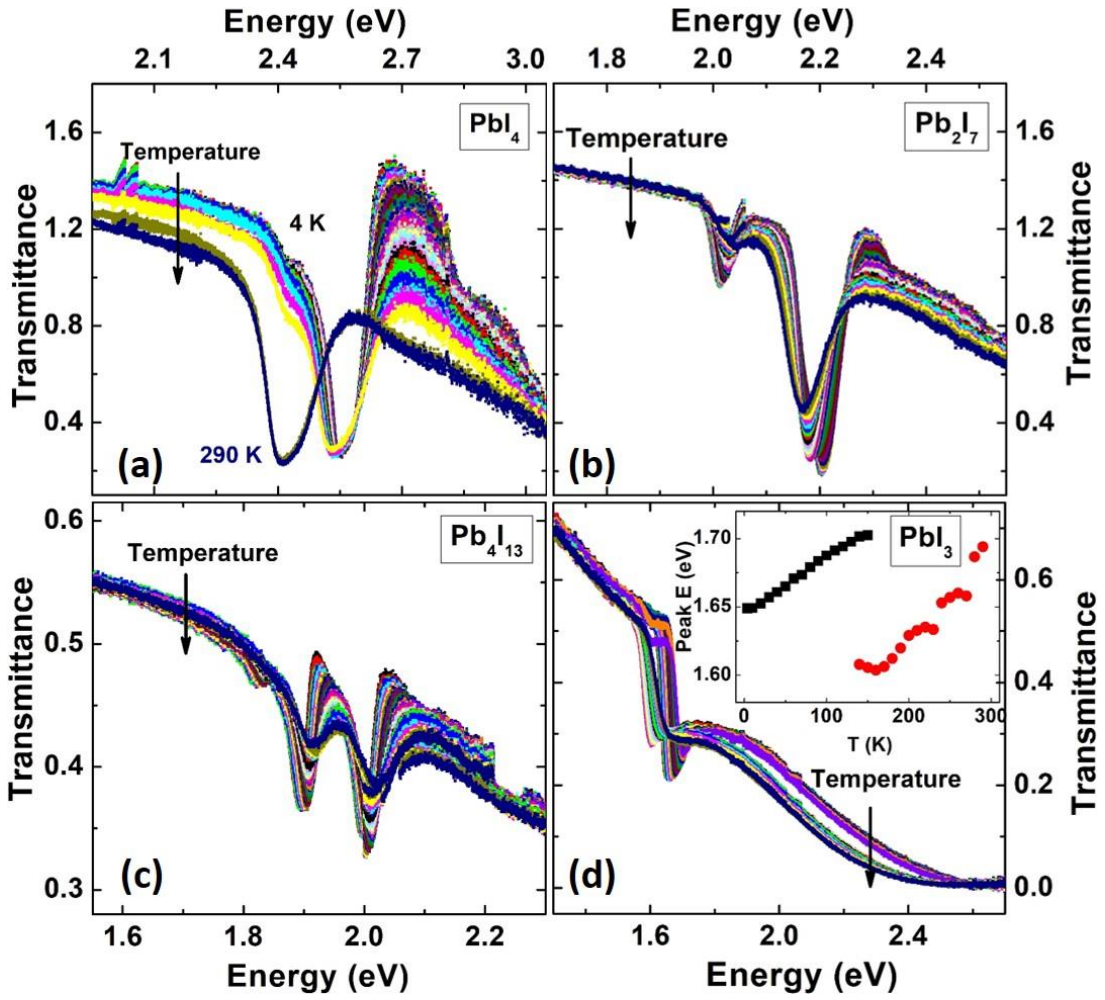

Figure 8. 6. Temperature dependent transmission spectroscopy for 2D (n = 1 (a), 2 (b), 4 (c)) and 3D (n → ∞ (d)) perovskite samples. The inset in panel (d) shows the change of the optical absorption energy value versus lattice temperature.

Figure 8.6 shows transmission spectroscopy of the 2D and 3D perovskite samples at various lattice temperatures. Transmission provides information regarding the major optical transitions in the system. For this measurement, a broad white light source is passed through the sample and the transmitted light is recorded. By normalizing the

transmitted light with a reference, it is possible to determine at what wavelengths optical absorption occurs.

Figure 8.6 (a) shows temperature dependent transmission spectra for the n = 1 (PbI_4) 2D perovskite. A large valley is evident at 4.2 K, which does not shift significantly with lattice temperatures up to ~ 270 K. At 280 K, however, an abrupt change is observed in the transmission profile, which is consistent with the shift in the peak energy observed in the complementary PL for n =1 at the same temperature (see Figure 8.4 (a). The temperature dependent transmission for the n = 2 (Pb_2I_7) 2D perovskite is shown in Figure 8.6 (b). At low temperatures, there is a strong absorption feature at 2.15 eV, which blueshift with increasing temperature. This behavior is also consistent with the blueshift observed for the peak energy of the PL (see Figure 8.4 (b)) for this sample. In addition, another peak is also evident at a lower energy in the transmission (absorption) (~ 2 eV), which becomes significant above ~ 100 K. This transition is associated with the inhomogeneity of the film and the contribution of additional (unintentionally) thicker 2D regions (domains) in the perovskite layer. [15]

Figure 8.6 (c) shows the temperature dependent behavior of the n = 4 (Pb_4I_{13}) sample from 4 K to 300 K. Here, there are three absorption features at low temperatures. As the temperature increases, the transition associated with the lowest absorption feature becomes negligible. As is shown in Figure 8.4 (c), a broad PL spectrum is observed for this n = 4 sample from 4 K to 300 K. Moreover, in Figure 8.6 (c) it is also evident that while the dominant (strongest) absorption peaks are associated with higher energy levels, the peak of the PL is associated with the lower energy transition, as shown in Figure 8.5 (c). This behavior is related to the fact that the PL is dominated by the lowest

energy transition in the system and the transfer of photogenerated carriers to the lower energy transitions, while transmission (or absorption) reflects the interaction strength – or density of states of the respective transition. The temperature dependent transmission for the 3D (PbI_3) $MAPbI_3$ perovskite is shown in Figure 8.6 (d). With increasing temperature, there is a slight shift in the transitions to higher energy up to 130 K. Above this temperature, the absorption peaks experience an abrupt shift to a lower energy due to the phase change from orthorhombic to tetragonal in the system. [5, 18]

Figure 8.7 shows a comparison of the transmission and PL spectra at several lattice temperatures (4 K, 150 K, and 300 K) for the 3D (PbI_3) and n = 1 (PbI_4) 2D perovskite samples. A resonance in a transmission (or absorption) spectrum represents the energy value of the onset of interband absorption. However, the peak value in a PL spectrum is indicative of the position of the lowest energy optical transition. An offset between the band-to-band absorption and peak PL intensity occurs in the presence of localized states and/or excitonic resonances results in a Stokes shift, which represents the binding (or depth) of the lower energy PL transitions. [29]

Figure 8.7 (a), (b), and (c) show a comparison between PL (black) and transmission (red) spectra of the 3D (PbI_3) perovskite sample at 4 K, 150 K, and 300 K, respectively. It is evident in all of these plots that the positions of the transitions in the absorption are at higher energies than the features in the PL spectra. The difference between the interband absorption and optical transition peaks is again attributed to the existence of localized states and/or excitonic transitions in the system. [29] In addition, it is observed that at 150 K there are two strong transitions in the transmission spectra (see red spectra in Figure 8.7 (b)), which are attributed to absorption from mixed crystal phases (both

orthorhombic and tetragonal) in the perovskite structure. At this condition, the peak of the PL spectrum is matched with the lowest energy value for the transmission spectrum at 150 K. This effect is related to the transfer of photogenerated carriers to the lowest energy in the system; i.e., the relaxed tetragonal ground state.

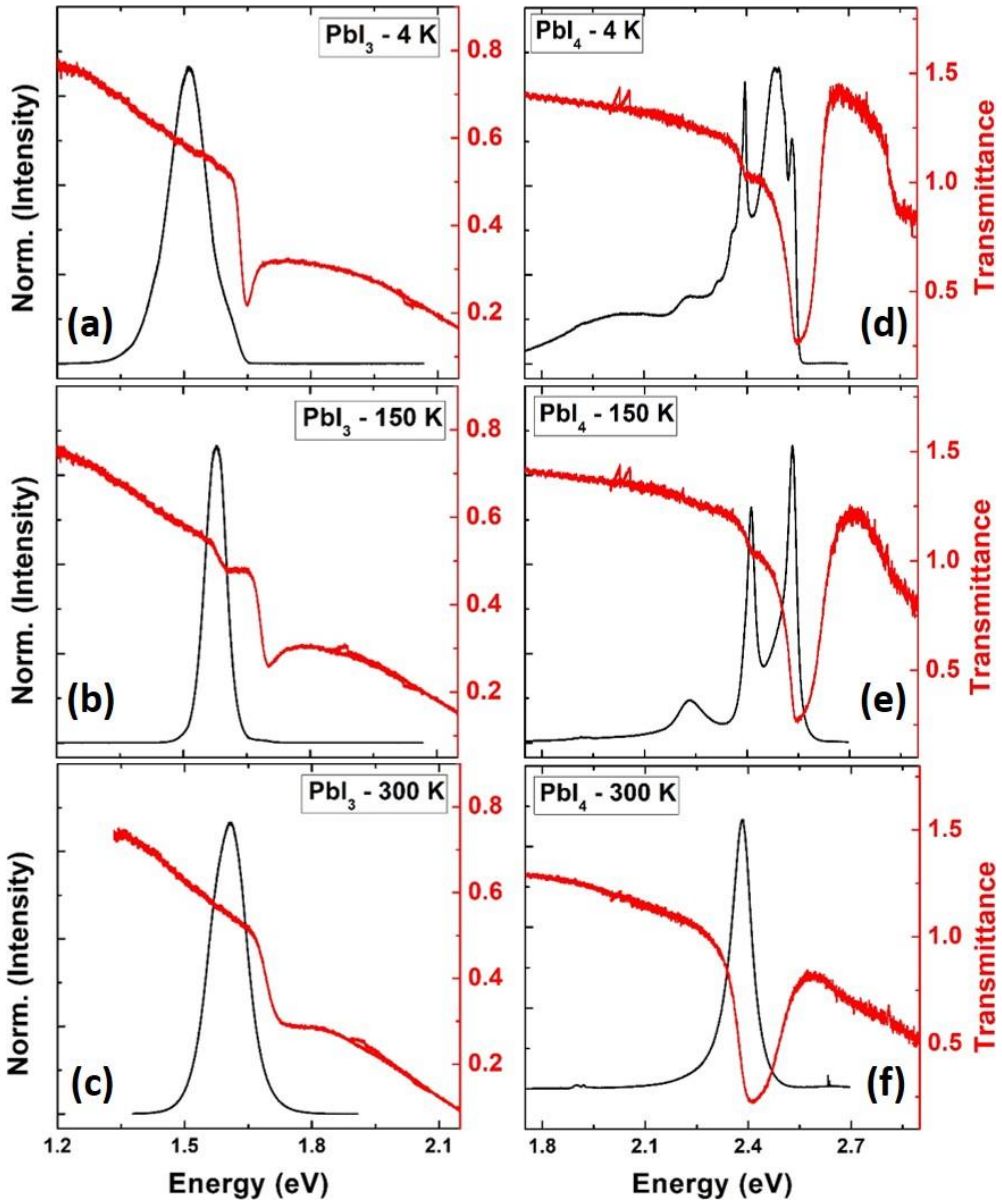

Figure 8. 7. The comparison between PL (black) and transmission spectra (red) of the 3D (PbI_3) and one-layer (n=1) (PbI_4) 2D perovskite samples at various lattice temperatures.

Comparison plots between the PL (black) and the transmission (red) spectra at 4.2 K, 150 K, and 300 K for the 2D (PbI_4) perovskite sample are shown in Figure 8.7 (d), (e), and (f), respectively. At low temperature (4 K), there are two transitions in the absorption for the 2D (PbI_4) perovskite sample; however, there are multiple optical transitions observed in the PL spectrum (see Figure 8.7 (d)). The origins of these multiple features in the PL are (again) related to excitons and localized states in the system. By increasing the temperature, the broadening of each optical transition in the PL spectra reduces (see Figure 8.7 (e) and (f)). This is likely due to the thermally mediated escape of the photogenerated carriers from localized states to shallower energy levels closer to the band gap transitions. At 300 K, there is only one feature evident in the transmission spectrum, see Figure 8.7 (f), which is matched with the peak energy value of the PL spectrum.

8.2.2. Photoluminescence line-width broadening analysis

As has been discussed, a potential advantage of the perovskites is their slow carrier cooling rates, which is interesting for potential hot carrier solar cell applications. In general, utilizing a structure with a slow thermalization process will enhance the power conversion efficiency of a solar cell if the hot carriers can be extracted efficiently. One method to study hot carrier properties of an absorber is to investigate its excitation. As has been discussed extensively in this thesis, power dependent PL spectroscopy can be used to investigate the presence of hot carriers in semiconductor structures, such effects are enhanced in low-dimensional systems (e.g., quantum wells (QWs) and quantum dots (QDs)) due to subtle interactions of confined photogenerated hot carriers and phonons in these systems. [30, 31]

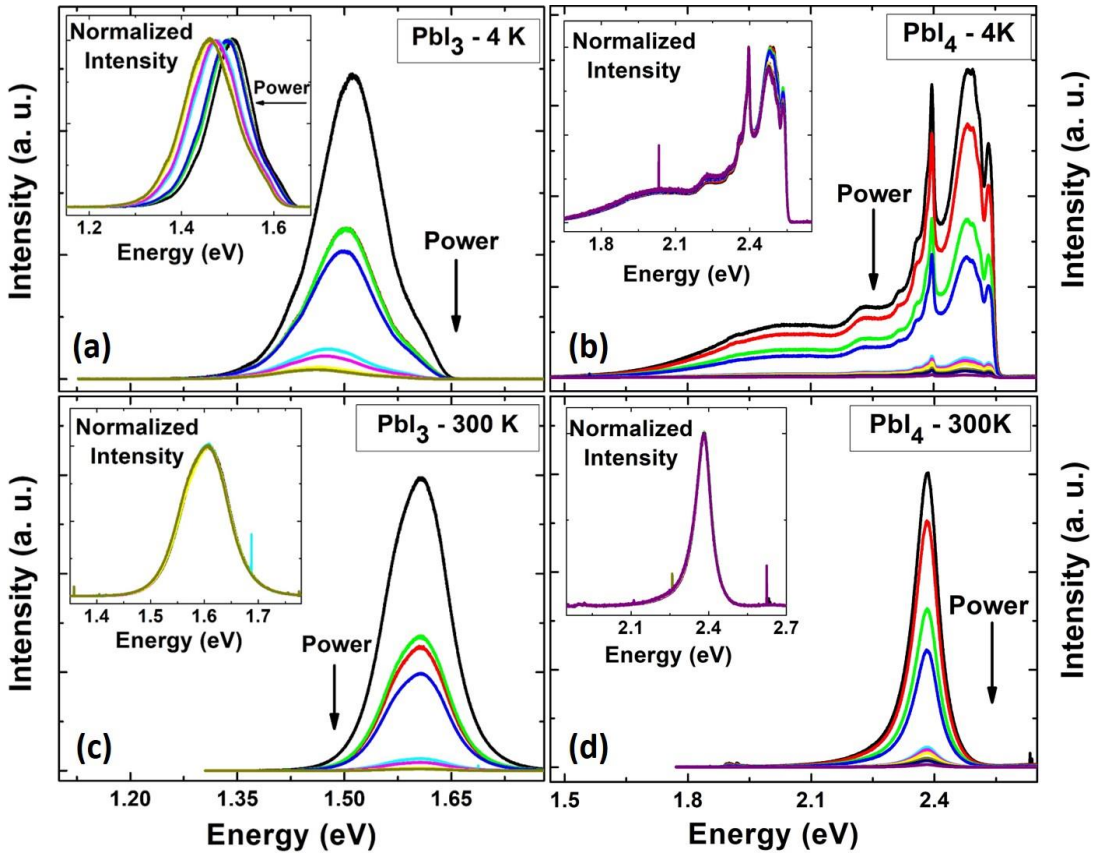

Figure 8. 8. Excitation power dependent PL spectroscopy of the 3D (PbI_3) and 2D (PbI_4) perovskite samples at 4 K and 300 K. (a) and (c) show the PL spectra of the PbI_3 sample at 4 K and 300 K, respectively. (b) and (d) show the PL spectra of the PbI_4 sample at 4 K and 300 K, respectively.

Evidence of hot carrier effects is typically observed via the broadening to the high-energy tail of the emitted PL spectrum. The extracted slope from the high-energy PL has a relationship with the carrier temperature. [32, 33, 34, 35] Therefore, such analysis might be applied to investigate the properties of hot carriers in the perovskite systems. Figure 8.8 shows the excitation power dependent behavior of the 3D (Figure 8.8 (a) and (c)) and n=1 (PbI_4) 2D (Figure 8.8 (b) and (d)) perovskite samples at 4 K and 300 K,

respectively. These two samples were selected in order to compare the effects of carrier confinement in the presence of hot carriers in 2D and 3D structures.

Figure 8.8 (a) shows the excitation power dependent behavior of the 3D perovskite sample at 4.2 K. A blueshift is observed in the peak energy as a function of excitation power. As shown in Figure 8.7 (a), the optical transition at 4.2 K occurs at a lower energy than the dominant transition in absorption spectrum. The origin of this effect is related to filling of localized states as a function of excitation power. [36] The power dependent normalized PL intensity of the sample at 4.2 K (shown in the inset of Figure 8.8 (a)) does not show any significant high energy broadening, which suggests the system is effectively in equilibrium. One possible reason for the absence of hot carriers in the systems is the need for high excitation powers (as observed in traditional inorganic systems [32]) to stimulate hot carriers effects. Here, it is likely that the excitation power utilized for the measurements (in order to avoid any laser damage to the sample) is below the threshold required for hot carrier generation in the material. As expected, the excitation dependent PL at 300 K (see Figure 8.8 (c)) also does not show any evidence of hot carrier effects.

Figure 8.8 (b) shows excitation power dependence of the n = 1 2D perovskite at 4.2 K. Multiple optical transitions are observed in this system with increasing excitation power at low temperature. As is also evident in Figure 8.8 (b), the PL intensity also quenches significantly when the excitation power is reduced. Moreover, the normalized PL spectra also overlay each other with no evidence of broadening on the high energy tail of the PL (see the inset to Figure 8.8 (b)). Figure 8.8 (d) shows the power dependent behavior of the n = 1 2D perovskite at 300 K. An overlay of the normalized PL spectra

at various powers (see the inset of Figure 8.8 (d)) further indicates that the carriers are at thermal equilibrium with lattice and that no hot carrier effect are evident.

Despite the absence of significant hot carrier effects in the perovskite samples, considerable thermal broadening is observed in the temperature dependent PL (See Figure 8.4). Therefore, it is helpful to study the electron-phonon interactions in the system via temperature dependent PL linewidth broadening analysis. The PL linewidth broadening as function of temperature is given by: [21]

$$\Gamma_{tot}(T) = \Gamma_0 + \Gamma_{LA}T + \frac{\Gamma_{LO}}{[exp(h\omega_{LO}/k_BT)-1]} + \Gamma_{imp}exp\left[-\frac{E_B}{k_BT}\right]. \quad (8.1)$$

In the above equation, Γ_0, Γ_{LA}, Γ_{LO} and Γ_{imp} are linewidth broadening due to the temperature independence inhomogeneous broadening at 0 K, acoustic (LA) phonons, optical (LO) phonons, and ionized impurities scattering mechanisms, respectively. The energy of LO-phonons and ionized impurities in the system are denoted $h\omega_{LO}$ and E_B, respectively. [21, 37]

Figure 8.9 (a) shows the PL spectra of the 3D perovskite sample at various lattice temperatures. It is observed that at low temperatures (T < 130 K) that the PL spectra are broad with the contribution of several competing transitions. Although above 130 K the PL spectra of the 3D perovskite narrows (compared with lower lattice temperatures), there remains evidence of a transition on the low energy tail of the PL spectra, which is attributed to an Urbach contribution via defects and/or impurities in the system. [5] It is also evident that the $MAPbI_3$ PL spectrum further broadens as the temperature of the lattice increases. The quantitative linewidth broadening of the sample (as a function of

lattice temperature) is shown in Figure 8.9 (b). Below 130 K the PL linewidth does not follow any systematic trends. However, at T > 130 K there is a linear dependence in the full width at half maximum (FWHM) with lattice temperature.

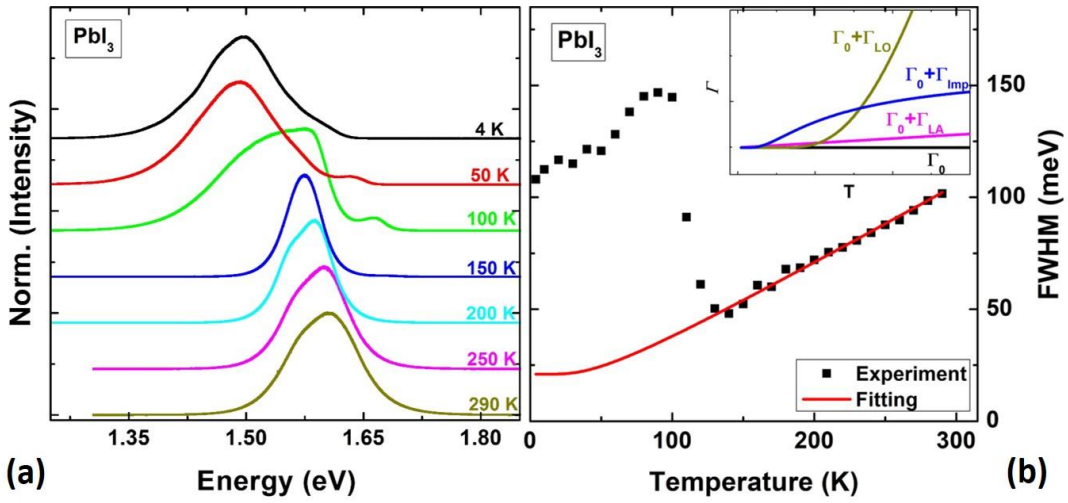

Figure 8. 9. (a) PL spectra of the 3D (PbI_3) perovskite sample at various lattice temperatures. (b) Full width at half maximum (FWHM) of the PL spectra of the PbI_3 sample (black dots) and a fitting on the data (red line) as a function of lattice temperature. The inset in the figure shows an example of how each term in Equation 8.1 contributes to the broadening of the PL line-width.

By fitting the PL linewidth broadening to Equation 8.1 it is possible to determine the contribution of the various different scattering mechanisms in the system. The inset to Figure 8.9 (b) shows an example of how each scattering mechanism contribute the PL linewidth as a function of lattice temperature. The linewidth broadening due to acoustic (LA) phonons changes linearly with temperature and the energy contribution of these phonons is small; also, their effect is more prominent at lower temperatures due to the limited contribution of LO phonons at low temperature. The contribution of ionized

impurities is larger at low temperatures, but stabilizes (see the inset of Figure 8.9 (b)) as the temperature increases. At elevated temperatures the PL broadening is dominated by longitudinal optical (LO) phonons, which is expected for polar semiconductors. The strength of the LO-phonon contribution is determined by the Fröhlich coupling coefficient, which can be extracted by fitting the LO-phonon scattering term for charge carrier-LO phonon interactions in the system (see Table 8.1). [5]

Figure 8.9 (b) shows that the temperature dependence of the FWHM of the 3D (PbI_3) perovskite does not show systematic behavior over the full temperature range; there is a large reduction in the FWHM above 90 K. However, above 130 K a linear dependence of the linewidth broadening may be inferred, broadening in this region has been considered appropriate in the literature [5, 38] since $MAPbI_3$ is much more homogeneous and stable in the this (tetragonal) regime. As such, Equation 8.1 is fit to the higher temperature range (as shown in Figure 8.9 (b)) and the individual contributions of each scattering mechanism extracted. In this system ($MAPbI_3$) it is evident that at elevated temperatures, the PL broadening is determined almost solely by exciton-LO phonon coupling.

As discussed by Herz *et al*., [5] a linear dependence of the linewidth broadening implies ionized impurities significantly contribute to the broadening in $MAPbI_3$. This is consistent with the fitting shown in Figure 8.9 (b). Therefore, the origin of the linear dependence of the FWHM is attributed to one of two effects: 1) acoustic (LA) phonon scattering; and 2) optical (LO) phonon scattering, which both have a linear temperature dependence at elevated temperatures. However, the reported values for the strength of exciton-acoustic phonon coupling for organic materials is in the order of $\mu eV/K$, which

only contribute a few meV to PL linewidth at 300 K. So, the contribution of acoustic phonons is neglected here since the experimental linewidth exceeds 100 meV. [5, 20, 39] As such, LO-phonon scattering is determined to dominate the linewidth broadening in these perovskite systems. [5, 20] The extracted broadening contributions extracted from the experimental fits to Equation 8.1 for the 3D perovskite are provided in Table (8.1) and shown as the red line in Figure 8.9 (b).

Table 8. 1. Extracted fitting parameters for the 3D (PbI_3) perovskite.

$\boldsymbol{\Gamma_0}$ $(\boldsymbol{meV})$ $(\boldsymbol{FWHM})$	$\boldsymbol{E_{LO}}$ *(meV)*	$\boldsymbol{\Gamma_{LO}}$ $(\boldsymbol{meV})$
21	*11.5*	*47.5 ± 1.0*

The extracted values for the inhomogeneous broadening, LO-phonon energy, and the strength of carrier-phonon Fröhlich coupling consistent with to those reported in the literature. [5]

Figure 8.10 (a) shows the PL spectra of the *n* =1 PbI_4 2D perovskite at various lattice temperatures. It is evident that there are multiple competing optical transitions at low temperatures.

To study the PL linewidth broadening in lieu of contributions from these low temperature excitonic resonances, the half-width-at-half-maximum (HWHM) is considered on the high energy tail of the PL spectrum of the high energy transition (see the red dotted rectangle in Figure 8.10 (a)), which matches the band-to-band (band edge) transition extracted in the absorption spectrum at the same temperature (see Figure 8.7(d)). The HWHM is considered to eliminate the details of the low energy resonance and investigate the properties of the 2D film. The extracted HWHM is shown in Figure

8.10 (b) as solid black squares and the fit to Equation 8.1 shown in red. It is evident that by increasing the lattice temperature significant linewidth broadening occurs in the *n* =1 layer (even before phase transition at 280 K).

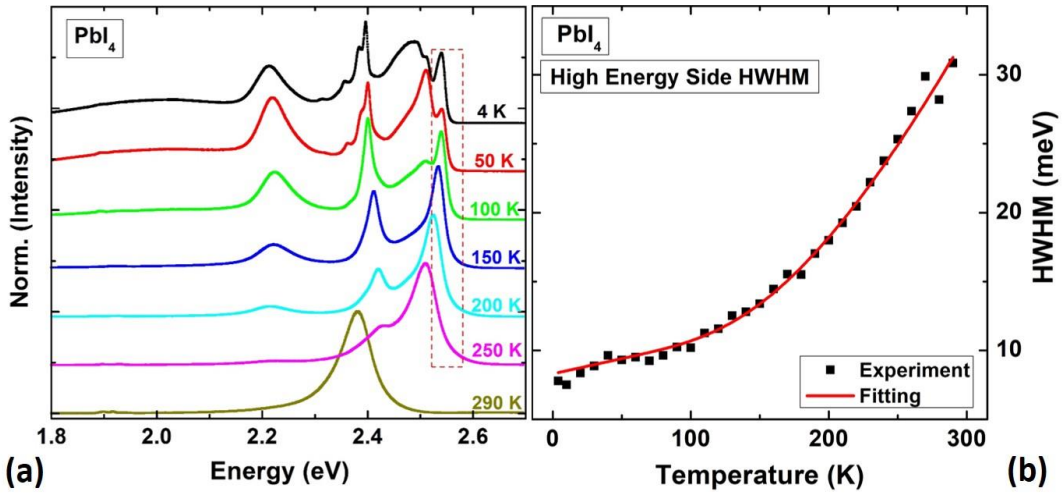

Figure 8. 10. (a) PL spectra of the PbI_4 2D perovskite at various lattice temperatures. The dashed rectangle shows the region where the HWHM of the PL spectra is investigated. (b) HWHM of the emitted PL (black dots) and the fitting (red line).

According to Equation 8.1 such rapid broadening suggest that the contribution of LO phonon coupling is significant. Fitting Equation 8.1 to the experimental data for the *n* = 1 2D perovskite allows the various scattering contributions to be assessed. Although care must be taken in this analysis due to the contribution/effects of mixed phases and localized states in the low temperature PL, this analysis is considered valid since only the high energy transition is assessed here (which is consistent with the band edge absorption).

Table 8. 2. Extracted fitting parameters for the one-layer (PbI_4) 2D perovskite.

Γ_0 (meV) $(HWHM)$	Γ_{LA} (meV/K)	E_{LO} *(meV)*	Γ_{LO} (meV)
8.3	*0.022 ± 0.002*	*57.4 ± 1.1*	*148.4 ± 7.1*

Table 8.2 shows the parameters extracted using Equation 8.1 from the fit (red line) to the experimental data (see Figure 8.10 (b). A small contribution due to LA-phonon scattering is evident at low temperatures, but this is insignificant when the contribution of the LO-phonons and the strength of carrier-LO phonon Fröhlich coupling parameter are considered; they are approximately five and three times greater than those extracted in the bulk $MAPbI_3$ perovskite, respectively (see Table 8.2).

This comparison between the extracted information from one-layer 2D and 3D perovskite samples shows the strength of carrier-LO phonon Fröhlich coupling and LO-phonon energy increases for 2D perovskites with respect to their bulk counterparts. [20] Although the origin of this behavior is still under investigation, these preliminary results indicate that much stronger carrier-carrier and carrier-phonon interactions occur in 2D perovskites. For example, the exciton binding energy is an order of magnitude less in 3D perovskite to 2D perovskite. [40, 41] Values as high as 370 meV – 490 meV have been reported for the exciton binding energy in the $BAPbI_4$ perovskites, which are larger than those reported for the 3D system. [42]

Conclusion

Continuous wave excitation power and temperature dependent photoluminescence and transmission spectroscopy of hybrid lead halide 2D (n = 1, 2, 4) and 3D ($n \rightarrow \infty$) perovskite samples have been performed. A blueshift of the peak energy as a function

of lattice temperature is observed for all samples, which is attributed to relaxation of the perovskite band edges at elevated lattice temperatures. Excitation power dependent spectroscopy does not reveal direct evidence for the presence of hot carrier effects, which may indicate fast thermalization processes over the range of studied powers. Temperature dependent PL linewidth broadening analysis was performed to investigate the contribution of the different scattering mechanisms and carrier-phonon interactions in 2D ($n = 1$) and 3D ($n \rightarrow \infty$) perovskites. It is observed that by reducing the dimensions of the sample (3D to 2D), both the optical phonon mode and the strength of carrier-LO phonon coupling increase significantly.

References

[1] Green, Martin A., Anita Ho-Baillie, and Henry J. Snaith. "The emergence of perovskite solar cells." Nature photonics 8, no. 7 (2014): 506.

[2] Niu, Guangda, Xudong Guo, and Liduo Wang. "Review of recent progress in chemical stability of perovskite solar cells." Journal of Materials Chemistry A 3, no. 17 (2015): 8970-8980.

[3] Snaith, Henry J. "Perovskites: the emergence of a new era for low-cost, high-efficiency solar cells." The Journal of Physical Chemistry Letters 4, no. 21 (2013): 3623-3630.

[4] Yang, Woon Seok, Jun Hong Noh, Nam Joong Jeon, Young Chan Kim, Seungchan Ryu, Jangwon Seo, and Sang Il Seok. "High-performance photovoltaic perovskite layers fabricated through intramolecular exchange." Science 348, no. 6240 (2015): 1234-1237.

[5] Wright, Adam D., Carla Verdi, Rebecca L. Milot, Giles E. Eperon, Miguel A. Pérez-Osorio, Henry J. Snaith, Feliciano Giustino, Michael B. Johnston, and Laura M. Herz. "Electron–phonon coupling in hybrid lead halide perovskites." Nature communications 7 (2016): 11755.

[6] Stranks, Samuel D., Giles E. Eperon, Giulia Grancini, Christopher Menelaou, Marcelo JP Alcocer, Tomas Leijtens, Laura M. Herz, Annamaria Petrozza, and Henry J. Snaith. "Electron-hole diffusion lengths exceeding 1 micrometer in an organometal trihalide perovskite absorber." Science 342, no. 6156 (2013): 341-344.

[7] Wehrenfennig, Christian, Giles E. Eperon, Michael B. Johnston, Henry J. Snaith, and Laura M. Herz. "High charge carrier mobilities and lifetimes in organolead trihalide perovskites." Advanced materials 26, no. 10 (2014): 1584-1589.

[8] D'Innocenzo, Valerio, Giulia Grancini, Marcelo JP Alcocer, Ajay Ram Srimath Kandada, Samuel D. Stranks, Michael M. Lee, Guglielmo Lanzani, Henry J. Snaith, and Annamaria Petrozza. "Excitons versus free charges in organo-lead tri-halide perovskites." Nature communications 5 (2014): 3586.

[9] Herz, Laura M. "Charge-carrier dynamics in organic-inorganic metal halide perovskites." Annual review of physical chemistry 67 (2016): 65-89.

[10] Yang, Ye, David P. Ostrowski, Ryan M. France, Kai Zhu, Jao Van De Lagemaat, Joseph M. Luther, and Matthew C. Beard. "Observation of a hot-phonon bottleneck in lead-iodide perovskites." Nature Photonics 10, no. 1 (2016): 53-59.

[11] Yang, Jianfeng, Xiaoming Wen, Hongze Xia, Rui Sheng, Qingshan Ma, Jincheol Kim, Patrick Tapping *et al.* "Acoustic-optical phonon up-conversion and hot-phonon bottleneck in lead-halide perovskites." Nature communications 8 (2017): 14120.

[12] Wu, Kewei, Ashok Bera, Chun Ma, Yuanmin Du, Yang Yang, Liang Li, and Tom Wu. "Temperature-dependent excitonic photoluminescence of hybrid organometal halide perovskite films." Physical Chemistry Chemical Physics 16, no. 41 (2014): 22476-22481.

[13] https://www.nrel.gov/pv/assets/pdfs/pv-efficiencies-07-17-2018.pdf

[14] Cao, Duyen H., Constantinos C. Stoumpos, Omar K. Farha, Joseph T. Hupp, and Mercouri G. Kanatzidis. "2D homologous perovskites as light-absorbing materials for solar cell applications." Journal of the American Chemical Society 137, no. 24 (2015): 7843-7850.

[15] Chen, Shan, and Gaoquan Shi. "Two-Dimensional Materials for Halide Perovskite-Based Optoelectronic Devices." Advanced Materials 29, no. 24 (2017): 1605448.

[16] Straus, Daniel B., and Cherie R. Kagan. "Electrons, excitons, and phonons in two-dimensional hybrid perovskites: connecting structural, optical, and electronic properties." The journal of physical chemistry letters 9, no. 6 (2018): 1434-1447.

[17] Cao, Duyen H., Constantinos C. Stoumpos, Christos D. Malliakas, Michael J. Katz, Omar K. Farha, Joseph T. Hupp, and Mercouri G. Kanatzidis. "Remnant PbI2, an unforeseen necessity in high-efficiency hybrid perovskite-based solar cells?." Apl Materials 2, no. 9 (2014): 091101.

[18] Frost, Jarvist M., Keith T. Butler, Federico Brivio, Christopher H. Hendon, Mark Van Schilfgaarde, and Aron Walsh. "Atomistic origins of high-performance in hybrid halide perovskite solar cells." Nano letters 14, no. 5 (2014): 2584-2590.

[19] Varshni, Yatendra Pal. "Temperature dependence of the energy gap in semiconductors." physica 34, no. 1 (1967): 149-154.

[20] Ni, Limeng, Uyen Huynh, Alexandre Cheminal, Tudor H. Thomas, Ravichandran Shivanna, Ture F. Hinrichsen, Shahab Ahmad, Aditya Sadhanala, and Akshay Rao. "Real-Time Observation of Exciton–Phonon Coupling Dynamics in Self-

Assembled Hybrid Perovskite Quantum Wells." ACS nano 11, no. 11 (2017): 10834-10843.

[21] Lee, Johnson, Emil S. Koteles, and M. O. Vassell. "Luminescence linewidths of excitons in GaAs quantum wells below 150 K." Physical Review B 33, no. 8 (1986): 5512.

[22] Liu, Zhiqiang, Yang Huang, Xiaoyan Yi, Binglei Fu, Guodong Yuan, Junxi Wang, Jinmin Li, and Yong Zhang. "Analysis of photoluminescence thermal quenching: guidance for the design of highly effective p-type doping of nitrides." Scientific reports 6 (2016): 32033.

[23] Li, Q., S. J. Xu, W. C. Cheng, M. H. Xie, S. Y. Tong, C. M. Che, and H. Yang. "Thermal redistribution of localized excitons and its effect on the luminescence band in InGaN ternary alloys." Applied Physics Letters 79, no. 12 (2001): 1810-1812.

[24] Esmaielpour, Hamidreza, Vincent R. Whiteside, Louise C. Hirst, Joseph G. Tischler, Robert J. Walters, and Ian R. Sellers. "The effect of an InP cap layer on the photoluminescence of an $In_xGa_{1-x}As_{1-y}P_y/In_zAl_{1-z}As$ quantum well heterostructure." Journal of Applied Physics 121, no. 23 (2017): 235301.

[25] Billing, David G., and Andreas Lemmerer. "Synthesis, characterization and phase transitions in the inorganic–organic layered perovskite-type hybrids [(CnH2n+ 1NH3) 2PbI4], n= 4, 5 and 6." Acta Crystallographica Section B 63, no. 5 (2007): 735-747.

[26] Diab, Hiba, Gaëlle Trippé-Allard, Ferdinand Lédée, Khaoula Jemli, Christèle Vilar, Guillaume Bouchez, Vincent LR Jacques *et al.* "Excitonic Emission in

Organic-Inorganic Lead Iodide Perovskite single crystals." arXiv preprint arXiv:1606.01729 (2016).

[27] Huang, Jiani, Thang B. Hoang, and Maiken H. Mikkelsen. "Probing the origin of excitonic states in monolayer WSe 2." Scientific reports 6 (2016): 22414.

[28] Nuytten, Thomas, Manus Hayne, Bhavtosh Bansal, H. Y. Liu, Mark Hopkinson, and Victor V. Moshchalkov. "Charge separation and temperature-induced carrier migration in Ga 1− x In x N y As 1− y multiple quantum wells." Physical Review B 84, no. 4 (2011): 045302.

[29] Silver, Scott, Jun Yin, Hong Li, Jean-Luc Brédas, and Antoine Kahn. "Characterization of the Valence and Conduction Band Levels of n= 1 2D Perovskites: A Combined Experimental and Theoretical Investigation." Advanced Energy Materials (2018): 1703468.

[30] Conibeer, Gavin, Santosh Shrestha, Shujuan Huang, Robert Patterson, Hongze Xia, Yu Feng, Pengfei Zhang *et al.* "Hot carrier solar cell absorber prerequisites and candidate material systems." Solar Energy Materials and Solar Cells 135 (2015): 124-129.

[31] Esmaielpour, Hamidreza, Vincent R. Whiteside, Herath P. Piyathilaka, Sangeetha Vijeyaragunathan, Bin Wang, Echo Adcock-Smith, Kenneth P. Roberts *et al.* "Enhanced hot electron lifetimes in quantum wells with inhibited phonon coupling." Scientific reports 8, no. 1 (2018): 12473.

[32] Shah, Jagdeep. "Hot carriers in quasi-2-D polar semiconductors." IEEE Journal of Quantum electronics 22, no. 9 (1986): 1728-1743.

[33] Le Bris, A., L. Lombez, S. Laribi, G. Boissier, P. Christol, and J-F. Guillemoles. "Thermalisation rate study of GaSb-based heterostructures by continuous wave photoluminescence and their potential as hot carrier solar cell absorbers." Energy & Environmental Science 5, no. 3 (2012): 6225-6232.

[34] Hirst, Louise C., Hiromasa Fujii, Yunpeng Wang, Masakazu Sugiyama, and Nicholas J. Ekins-Daukes. "Hot carriers in quantum wells for photovoltaic efficiency enhancement." IEEE Journal of Photovoltaics 4, no. 1 (2014): 244-252.

[35] Esmaielpour, Hamidreza, Vincent R. Whiteside, Jinfeng Tang, Sangeetha Vijeyaragunathan, Tetsuya D. Mishima, Shayne Cairns, Michael B. Santos, Bin Wang, and Ian R. Sellers. "Suppression of phonon-mediated hot carrier relaxation in type-II InAs/AlAsxSb1− x quantum wells: a practical route to hot carrier solar cells." Progress in Photovoltaics: Research and Applications 24, no. 5 (2016): 591-599.

[36] Zhao, Zhexin, Ramesh B. Laghumavarapu, Paul J. Simmonds, Haiming Ji, Baolai Liang, and Diana L. Huffaker. "Photoluminescence study of the effect of strain compensation on InAs/AlAsSb quantum dots." Journal of Crystal Growth 425 (2015): 312-315.

[37] Veliadis, J. V. D., J. B. Khurgin, Y. J. Ding, A. G. Cui, and D. S. Katzer. "Investigation of the photoluminescence-linewidth broadening in periodic multiple narrow asymmetric coupled quantum wells." Physical Review B 50, no. 7 (1994): 4463.

[38] Milot, Rebecca L., Giles E. Eperon, Henry J. Snaith, Michael B. Johnston, and Laura M. Herz. "Temperature-dependent charge-carrier dynamics in CH3NH3PbI3 perovskite thin films." Advanced Functional Materials 25, no. 39 (2015): 6218-6227.

[39] Gauthron, K., J. S. Lauret, L. Doyennette, G. Lanty, A. Al Choueiry, S. J. Zhang, A. Brehier *et al.* "Optical spectroscopy of two-dimensional layered (C6H5C2H4-NH3) 2-PbI4 perovskite." Optics express 18, no. 6 (2010): 5912-5919.

[40] Hong, X., T. Ishihara, and A. V. Nurmikko. "Dielectric confinement effect on excitons in PbI 4-based layered semiconductors." Physical Review B 45, no. 12 (1992): 6961.

[41] Ishihara, T., X. Hong, J. Ding, and A. V. Nurmikko. "Dielectric confinement effect for exciton and biexciton states in PbI4-based two-dimensional semiconductor structures." Surface science 267, no. 1-3 (1992): 323-326.

[42] Yaffe, Omer, Alexey Chernikov, Zachariah M. Norman, Yu Zhong, Ajanthkrishna Velauthapillai, Arend van Der Zande, Jonathan S. Owen, and Tony F. Heinz. "Excitons in ultrathin organic-inorganic perovskite crystals." Physical Review B 92, no. 4 (2015): 045414.

Conclusion

In this thesis, InAs/AlAsSb MQW structures have been comprehensively investigated for their potential for applications in hot carrier solar cells. Continuous wave power and temperature dependent photoluminescence spectroscopy show evidence of robust hot carrier effects, even at elevated lattice temperatures. This behavior is attributed to the creation of a strong phonon-bottleneck in the type-II MQW structures, several unique properties of this system are considered to contribute to this effect. These include an increased lifetime of hot electrons in the QW due to the spatial separation of the photogenerated carriers, and a phonon mismatch between the InAs quantum wells and the AlAsSb barriers, which inhibits heat transfer from the system.

In evaluating the hot carrier dynamics in QWs, a detailed analysis of the extraction and determination of the carrier temperature using CW photoluminescence is presented. Three complementary approaches are performed to evaluate the applicability of each method. These methods are derived from Planck's radiation law, they are: 1) a simple linear fitting of the high energy tail of natural logarithm of the PL spectrum; 2) fitting the whole PL spectrum using an equilibrium generalized Planck formulation; and 3) applying a more advanced non-equilibrium generalized Planck formulation to fit the PL. By comparing the results from these three methods, similar results were determined in all three cases for the InAs MQWs confirming the validity of the analysis for the MQWs assessed. This is important since high energy broadening of the PL can arise due to occupation of the quantum-confined states in the QWs and/or subtleties due to the band structure.

To further understand the influence of state filling and PL linewidth broadening on evaluating the hot carrier temperature in QWs, a comprehensive study of the optical properties of a high-quality state of the art InGaAsP QW structure was performed. It is observed that at high excitation powers, as well as elevated lattice temperatures, occupation of excited states (state filling) results in the screening of the hot carrier temperature and a larger *extracted* value than the actual physical carrier temperature of the system. As such, care must be taken when considering the simple Planck-based analysis of QW systems.

To study the dynamics of photogenerated hot carriers in the InAs MQW structure, ultrafast transient absorption spectroscopy at various lattice temperatures were performed. It was observed that there are three dominant recombination mechanisms in the samples studied. A fast recombination process that is associated with localized states, quenches with increasing lattice temperature. On the other hand, two slower recombination processes due to type-II band-band transitions become stronger at elevated temperatures. These results are consistent with the observations from CW PL spectroscopy that a transition from type-I-like to type-II recombination behavior occurs above 100 K; while, a transition from type-II to so-called quasi type-II behavior – where the holes are delocalized – is observed at elevated lattice temperatures. As a result of these measurements, it is determined that the carrier lifetime at elevated temperatures is longer than that at lower temperatures.

DFT calculations support experimental observations of a phonon mismatch in the system, which is proposed to inhibit hot carrier relaxation in these QWs. Specifically, DFT calculations indicate that there is a large phononic gap for the barrier material

(AlAsSb), which suppresses the dominant hot carrier thermalization mechanism (Klemens effect) in the barriers; this provides an impedance mismatch and inhibited thermal conductivity at the QW interface. Therefore, it is proposed that acoustic phonons and heat accumulate in the QWs, facilitating reabsorption of acoustic and optical phonons with the subsequent creation of a stabilized hot carrier population.

Optical spectroscopy of the effects of an InP capping layer on the emission of InGaAsP QW structures is also investigated. It is shown that the interface created between InP cap layer on top of InAlAs barrier material (the so-called inverted interface) adds features to the emitted PL spectra of the QW, which reduce the purity of the emission of these systems. As the lattice temperature is increased, the effects of the inverted interface transitions become negligible due to the saturation of the localized states at the interface. These transitions are also shown to have a strong polarization dependence. The origin of these transitions and their relationship to the InP cap is confirmed by removing the capping layer with wet etching, which is shown to eliminate the contribution of interface states in the QW spectrum.

In addition to optical spectroscopy and fundamental analysis of QW systems, p-i-n diodes with different InAs MQW structures have been fabricated to investigate the behavior of photogenerated hot carriers in the device architectures. Current-voltage (*J-V*) analysis of the QW p-i-n diodes show evidence of strong confinement in these deep QWs that induce inflection points in the light *J-V* response of the system. However, strong leakage and direct tunneling are observed with increasing temperature and/or excitation power limiting the ability to unambiguously investigate hot carriers in the devices. NRL MultiBands® simulations confirm that the leakage current arises due to

the high electric field and large band bending in the active region. The combination of which facilitates Zener or avalanche-like breakdown at higher temperature or under more intense excitation powers. New device architectures to circumvent these issues are now underway.

The majority of this PhD dissertation has been focused on the optical spectroscopy of hot carrier properties of MQW structures that have type-II band alignment. Recently, electrical characterizations of InAs MQW p-i-n diodes have also begun. Several avenues are open for investigation based on the results previously described. For example: the role of AlAsSb barrier and its poor thermal transport (phonon properties), how significant is type-II band alignment in sustaining hot carrier populations, what is the origin of strong leakage current in reverse bias in device structures, as well as, assessing the barrier to transport as clearly seen by the lack of V_{OC} in the J-V characteristics.

In order to pursue these avenues several designs have been proposed. To investigate comprehensively the origin of the leakage current at reverse bias, simulations indicate that the first barrier thickness is critical. Therefore, a series of samples with different barrier thicknesses have now been grown by Dr. Santos' group at OU. In addition to having direct comparisons of hot carrier properties in systems with different band alignments, several p-i-n MQW structures with type-I, type-II, and a degenerate valence band with InAlAs barrier materials have also been provided by Rochester Institute of Technology.

Finally, continuous wave excitation power and temperature dependent photoluminescence and transmission spectroscopy of hybrid lead halide 2D and 3D $MAPbI_3$ perovskite samples have also been investigated in this thesis. It was observed

that the band gap energies of the 2D structures are larger than their 3D counterpart due to quantum confinement effects in these systems. In addition, the exciton-LO phonon energy and the strength of their coupling are significantly larger for 2D structures, when compared with the bulk $MAPbI_3$.

The main focus of the research described here, was on utilizing nanostructures with a type-II band alignment for applications as the absorber in hot carrier solar cells. In the last few decades, the activity in hot carriers for photovoltaics has been predominantly theoretical however recently, designing hot carrier solar cells utilizing quantum confinement effects in nanostructures has attracted a lot of interest experimentally. Despite considerable progress in the field with several of these works showing proof of principle evidence of hot carrier effects in devices, these works have typically involved very high excitation powers and/or operation at low temperatures – conditions that are unrealistic for practical solar cells. However, in the work presented in this thesis the type-II systems proposed have been shown to display experimental evidence of robust hot carrier effects at elevated lattice temperatures and under low(er) irradiation levels (< 1000 Suns). These results are significant since they represent conditions consistent with commercial concentrator PV system (where hot carrier solar cell would undoubtedly be used), and as such offer a genuine route towards the realization of practical hot carrier solar cells. That being said, considerable challenges still exist with further work required with regards to optimizing light absorption in thin hot carrier absorbers, as well as, to utilize energy selective contacts for efficient hot carrier extraction.

Appendix A

Determination of absorbed power in quantum well structures

Determination of absorbed power in a sample is important for optical spectroscopy and solar cell applications. To determine the amount of wavelength (λ) dependent reflection and transmission for a structure, one practical technique is to utilize transfer matrix analysis, as described by Petterson. [1] To calculate absorbed power, it is required to find the electric field, $\bar{E}_j(x)$ as a function of distance (x) along the growth direction in the multilayer structure. For a homogenous and isotropic material with parallel plane interfaces, it is possible to describe light propagation through the material using 2×2 matrices. [1, 2]

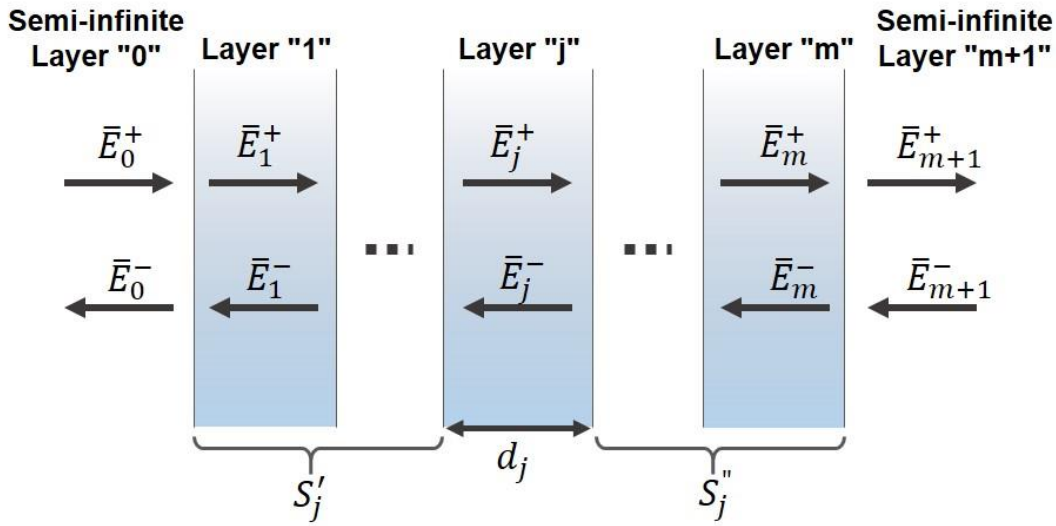

Figure A. 1. Schematic of a multilayer structure embedded between two semi-infinite layers (J=0 and J = m+1).

To calculate the electric field in a system, it is assumed the structure consists of "j" individual layers, (j = 1, 2…, m) with thicknesses of "d_j" is embedded between two semi-infinite layers (j = 0 and j = m + 1), as shown in Figure A.1. In addition, it is assumed each layer has a wavelength dependent complex index of refraction equal to $\bar{n}_j(\lambda) = n_j(\lambda) + i \cdot k_j(\lambda)$, where n_j and k_j are real and imaginary refractive indices.

The electric field at any point in the structure is defined by two components, $\bar{E}_0^+$ and $\bar{E}_0^-$, propagating along positive and negative *x* directions, respectively. At an interface between two layers (j and k), an interface matrix (I_{jk}) describes the relation between electric fields in the left and right layers:

$$\begin{bmatrix} \bar{E}_j^+ \\ \bar{E}_j^- \end{bmatrix} = I_{jk} \begin{bmatrix} \bar{E}_k^+ \\ \bar{E}_k^- \end{bmatrix} = \begin{bmatrix} \frac{1}{t_{jk}} & \frac{r_{jk}}{t_{jk}} \\ \frac{r_{jk}}{t_{jk}} & \frac{1}{t_{jk}} \end{bmatrix} \begin{bmatrix} \bar{E}_k^+ \\ \bar{E}_k^- \end{bmatrix}, \tag{A.1}$$

where r_{jk} and t_{jk} are reflection and transmission coefficients, respectively, which are equal to:

$$t_{jk} = \frac{2\,\bar{n}_j}{\bar{n}_j + \bar{n}_k}, \tag{A.2}$$

$$r_{jk} = \frac{\bar{n}_j - \bar{n}_k}{\bar{n}_j + \bar{n}_k}. \tag{A.3}$$

Propagation of light through a media causes a change in its phase and intensity (it is being absorbed), which is described by a layer matrix L_j:

$$L_j = \begin{bmatrix} e^{-i\xi_j d_j} & 0 \\ 0 & e^{i\xi_j d_j} \end{bmatrix}, \tag{A.4}$$

where $\xi_j = (2\pi/\lambda)\bar{n}_j$. The electric fields within the first (j = 0) and the last (j = m + 1) semi-infinite layers are,

$$\begin{bmatrix} \bar{E}_0^+ \\ \bar{E}_0^- \end{bmatrix} = S \begin{bmatrix} \bar{E}_{m+1}^+ \\ \bar{E}_{m-1}^- \end{bmatrix}, \tag{A.5}$$

where the transfer matrix "*S*" is,

$$S = \begin{bmatrix} S_{11} & S_{12} \\ S_{21} & S_{22} \end{bmatrix} = \left(\prod_{n=1}^{m} I_{(n-1)n}\, L_n\right) \cdot I_{m(m+1)}. \tag{A.6}$$

As a result, the reflection coefficient is calculated by,

$$r = \frac{\bar{E}_0^-}{\bar{E}_0^+} = \frac{S_{21}}{S_{11}}, \tag{A.7}$$

and the transmission coefficient,

$$t = \frac{\bar{E}_{m+1}^+}{\bar{E}_0^+} = {S_{11}}^{-1}. \tag{A.8}$$

In order to determine the internal electric field in layer (j) of a multilayer structure, the transfer matrix is:

$$S = S_j^- L_j S_j^+, \tag{A.9}$$

where S_j^- and S_j^+ are:

$$S_j^- = \left(\prod_{n=1}^{j-1} I_{(n-1)n}\, L_n\right) \cdot I_{(j-1)j}, \tag{A.10}$$

and,

$$S_j^+ = \left(\prod_{n=j+1}^{m} I_{(n-1)n}\, L_n\right) \cdot I_{m(m+1)}. \tag{A.11}$$

As a result, electric fields propagating to negative ($\bar{E}_j^-$) and positive ($\bar{E}_j^+$) directions at a distance (x) in layer (j) are:

$$\frac{\bar{E}_j^+}{\bar{E}_0^+} = t_j^+ = \frac{\frac{1}{S_{j11}^-}}{1+\frac{S_{j12}^- S_{j21}^+}{S_{j11}^- S_{j11}^+} e^{i2\xi_j d_j}}, \tag{A.12}$$

and,

$$\frac{\bar{E}_j^-}{\bar{E}_0^+} = t_j^- = t_j^+ \frac{S_{j21}^+}{S_{j11}^+} e^{i2\xi_j d_j}. \tag{A.13}$$

Therefore, the total electric field in layer (j) is the superposition of electric fields propagating to negative and positive directions at a distance (x), which is:

$$\bar{E}_j(x) = \bar{E}_j^+(x) + \bar{E}_j^-(x) = \left(t_j^+ e^{i\xi_j x} - t_j^- e^{-i\xi_j x}\right)\bar{E}_0^+. \tag{A.14}$$

Finally, the amount of time averaged absorbed power in layer (j) as a function of distance (x) is,

$$Q_j(x) = \frac{4\pi c \varepsilon_0 k_j n_j}{2\lambda} \left|\bar{E}_j(x)\right|^2, \tag{A.15}$$

where c and ε_0 are speed of light and permittivity for free space, respectively. In addition, the distance (x) in an individual layer (j) changes from 0 to d_j, ($0 \le x \le d_j$). Via this analysis it is possible to calculate the amount of light absorption in a sample at a given wavelength (λ).

References

[1] Pettersson, Leif AA, Lucimara S. Roman, and Olle Inganäs. "Modeling photocurrent action spectra of photovoltaic devices based on organic thin films." Journal of Applied Physics 86, no. 1 (1999): 487-496.

[2] Peumans, Peter, Aharon Yakimov, and Stephen R. Forrest. "Small molecular weight organic thin-film photodetectors and solar cells." Journal of Applied Physics 93, no. 7 (2003): 3693.

Appendix B

Determination of Laser beam radius

To calculate absorbed power density, it is required to determine the laser spot size on a sample. In this thesis, the lasers utilized for optical and electrical characterizations have Gaussian beam shapes. Electric fields (E_s) for these lasers have radially symmetrical distributions, which are described by,

$$E_s = E_0 \exp\left(-\frac{r^2}{\omega_0^2}\right), \tag{B.1}$$

where E_0, r, and ω_0 are: the electric field at ($r = 0$), the distance from the center, and the beam radius, respectively. Therefore, the intensity of a Gaussian beam is,

$$I_s = \mu\, E_0 E_0{}^{*} \exp\left(-\frac{2r^2}{\omega_0^2}\right) = I_0 \exp\left(-\frac{2r^2}{\omega_0^2}\right), \tag{B.2}$$

where μ and I_0 are vacuum permeability and maximum beam intensity, respectively. Unlike circular beams, Gaussian beams do not have any boundaries in order to be used as a characteristic for defining their dimensions. Therefore, there are some definitions for defining their beam sizes. Figure B.1 shows the change of intensity in Equation B.2 of a Gaussian beam versus distance from its center. It is evident that intensity drops as it moves away from the center.

As shown in Figure B.1, there are two useful concepts for Gaussian beams: 1) beam radius, and 2) full width at half maximum (FWHM). The beam radius (ω_0), which defines the beam spot size, is the distance where the beam intensity drops by $1/e^2$ or 0.135 of its maximum intensity. At a distance twice the beam radius ($2\omega_0$), the intensity

decreases to 0.0003 of maximum intensity, which is approximately zero. The FWHM of a Gaussian beam occurs when the intensity is half of the maximum intensity (beam intensity at the center). The relationship between FWHM and beam radius is $r_{FWHM} = 0.59\ \omega_0$.

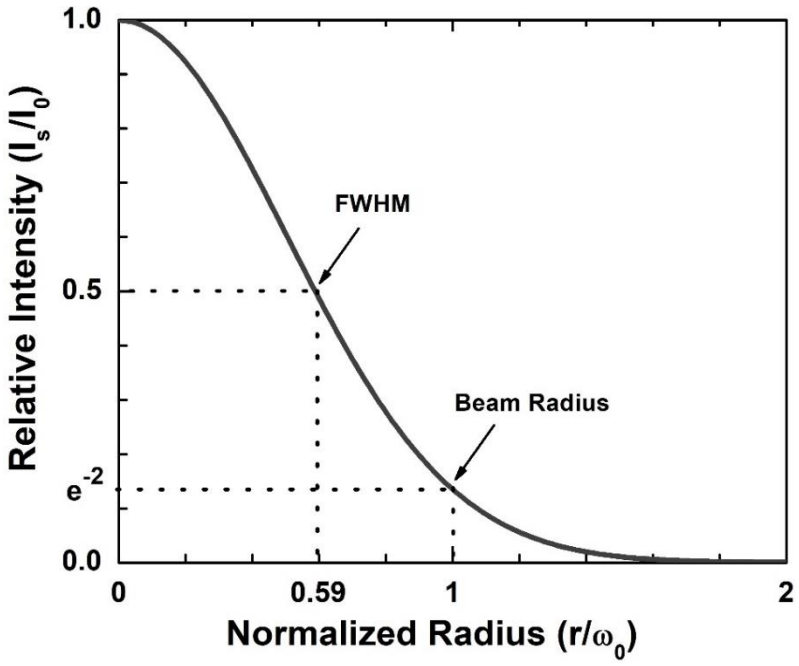

Figure B. 1. Relative intensity of a Gaussian beam versus normalized radius.

Here the beam radius is measured using pinholes, which move across the beam and the change in intensity is recorded with a photodetector (Newport 818-UV). The schematic of the experimental setup is shown in Figure B.2.

In this experiment, the Gaussian beam illuminated from a He-Cd laser (442 nm) is concentrated on a sample via an objective lens (M Plan Apo NIR 100X). It is possible to determine the spot size of the laser focused by the objective lens via a pinhole experiment. The numerical aperture (N.A.) of the objective lens is 0.50 and its working

distance is 12.0 mm. The numerical aperture is a dimensionless number, which represents the ability of the lens to focus light; in other words, a sample with larger N.A. has more capability to gather light at a fixed distance and to resolve fine features of a specimen. The numerical aperture is given by:

$$N.A. = n \cdot \sin\theta, \tag{B.3}$$

where n and θ are the index of refraction and the half-angle of the maximum cone of light that exits the objective lens. The working distance is the distance from the objective lens to the sample when it is in focus. The result of the experiment is shown in Figure B.3.

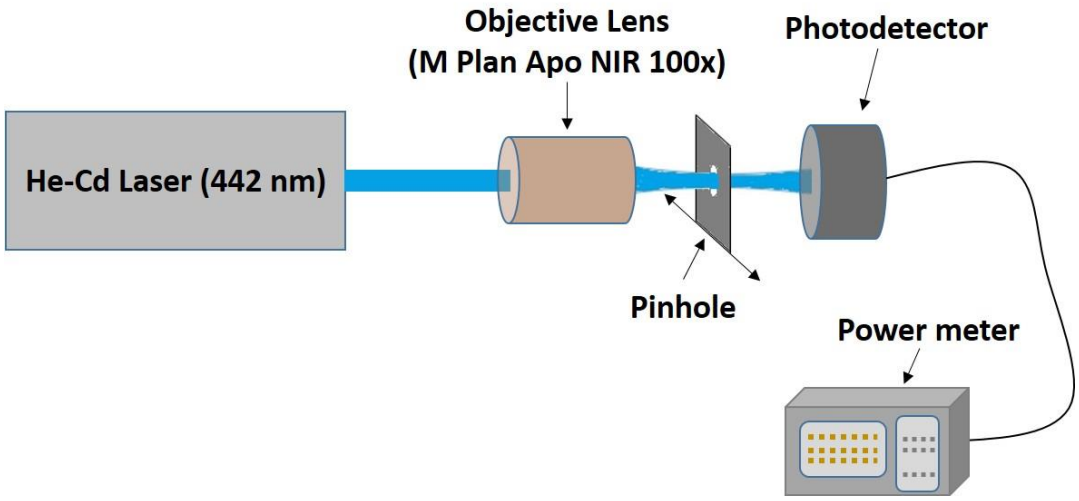

Figure B. 2. Experimental setup for determination of Laser beam radius.

In Figure B.3, the change in intensity is plotted as a function of distance away from the center. The black and red lines represent experimental and a Gaussian fitting data.

Therefore, it is possible to determine the beam radius, where the maximum intensity drops by $1/e^2$. The calculated beam radius (ω_0) at the focal point is 1.05 μm.

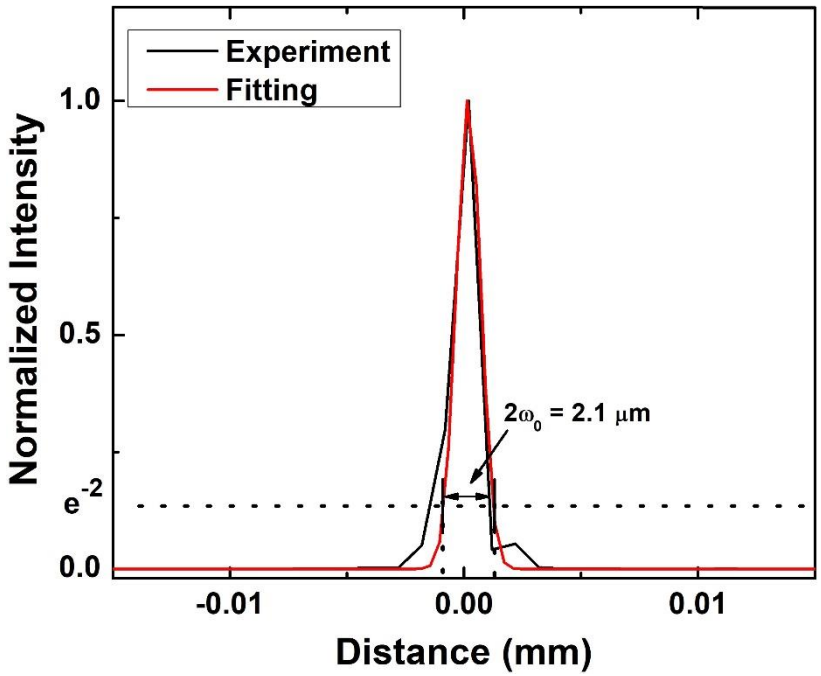

Figure B. 3. Experimental (red) and theoretical (Gaussian fitting; black) of normalized intensity as a function of the pinhole displacement.

List of Publications

Peer-reviewed Journal Papers

J1. Hamidreza Esmaielpour, Vincent R. Whiteside, Herath P. Piyathilaka, Sangeetha Vijeyaragunathan, Bin Wang, Echo Adcock-Smith, Kenneth P. Roberts, Tetsuya D Mishima, Michael B Santos, Alan D Bristow, Ian R Sellers, "*Enhanced hot electron lifetimes in quantum wells with inhibited phonon coupling.*" Scientific reports 8, no. 1 (2018): 12473.

J2. Vincent R. Whiteside, Brenden A. Magill, Matthew P. Lumb, **Hamidreza Esmaielpour**, Michael A. Meeker, Rathsara RHH Mudiyanselage, Adrien Messager, S Vijeyaragunathan, Tetsuya D Mishima, Michael B Santos, Igor Vurgaftman, Giti A Khodaparast, Ian R Sellers, "*Valence band states in an InAs/AlAsSb multi-quantum well hot carrier absorber*." Semiconductor Science and Technology (2018).

J3. Hamidreza Esmaielpour, Vincent R. Whiteside, Louise C. Hirst, Joseph G. Tischler, Chase T. Ellis, Matthew P. Lumb, David V. Forbes, Robert J. Walters, and Ian R. Sellers. "*Effect of occupation of the excited states and phonon broadening on the determination of the hot carrier temperature from continuous wave photoluminescence in InGaAsP quantum well absorbers*." Progress in Photovoltaics: Research and Applications 25, no. 9 (2017): 782-790.

J4. Hamidreza Esmaielpour, Vincent R. Whiteside, Louise C. Hirst, Joseph G. Tischler, Robert J. Walters, and Ian R. Sellers. "*The effect of an InP cap layer on the*

photoluminescence of an $In_xGa_{1-x}As_{1-y}P_y/In_zAl_{1-z}As$ quantum well heterostructure." Journal of Applied Physics 121, no. 23 (2017): 235301.

J5. Hamidreza Esmaielpour, Vincent R. Whiteside, Jinfeng Tang, Sangeetha Vijeyaragunathan, Tetsuya D. Mishima, Shayne Cairns, Michael B. Santos, Bin Wang, and Ian R. Sellers. "*Suppression of phonon-mediated hot carrier relaxation in type-II InAs/AlAsxSb1− x quantum wells: a practical route to hot carrier solar cells*." Progress in Photovoltaics: Research and Applications 24, no. 5 (2016): 591-599.

J6. Tang, J., V. R. Whiteside, **H. Esmaielpour**, S. Vijeyaragunathan, T. D. Mishima, M. B. Santos, and I. R. Sellers. "*Effects of localization on hot carriers in InAs/AlAs x Sb1–x quantum wells*." Applied Physics Letters 106, no. 6 (2015): 061902.

Peer-reviewed Conferences

C1. H. Esmaielpour, V. R. Whiteside, H. P. Piyathilaka, S. Vijeyaragunathan, B. Wang, K. P. Roberts, T. D. Mishima, M. P. Lumb, M. B. Santos, A. D. Bristow, and I. R. Sellers, "*Control of hot carrier thermalization in type-II quantum wells: a route to practical hot carrier solar cells*", In 2018 IEEE 7th World Conference on Photovoltaic Energy Conversion (WCPEC)(A Joint Conference of 45th IEEE PVSC, 28th PVSEC & 34th EU PVSEC), pp. 3682-3684. IEEE, 2018.

C2. H. Esmaielpour, V. R. Whiteside, H. P. Piyathilaka, S. Vijeyaragunathan, B. Wang, K. P. Roberts, T. D. Mishima, M. P. Lumb, M. B. Santos, A. D. Bristow, and I. R. Sellers, "*Inhibited Hot-Carrier Cooling in Type-II InAs/AlAsSb Quantum Wells: Controlled Decoupling of Electron-Phonon Relaxation*," Compound Semiconductor

Week (CSW), The 45th International Symposium on Compound Semiconductors (ISCS) And The 30th International Conference on Indium Phosphide And Related Materials (IPRM), Boston, MA, 2018.

C3. Hamidreza Esmaielpour, Vincent R. Whiteside, Louise C. Hirst, Joseph G. Tischler, Robert J. Walters, and Ian R. Sellers. "*The effect of excited state occupation and phonon broadening in the determination of the non-equilibrium hot-carrier temperature in InGaAsP quantum-well absorbers* (Conference Presentation)." In Physics, Simulation, and Photonic Engineering of Photovoltaic Devices VII, vol. 10527, p. 1052706. International Society for Optics and Photonics (SPIE), 2018.

C4. Alan D. Bristow, Herath P. Piyathilaka, **Hamidreza Esmaielpour**, Vincent R. Whiteside, Michael B. Santos, and Ian R. Sellers. "*Hot-carrier dynamics in type-II semiconductor quantum wells* (Conference Presentation)." In Ultrafast Phenomena and Nanophotonics XXII, vol. 10530, p. 105300U. International Society for Optics and Photonics (SPIE), 2018.

C5. H. Esmaielpour, J. Tang, V. R. Whiteside, S. Vijeyaragunathan, T. D. Mishima, M. B. Santos, B. Wang, and I. R. Sellers, "*Type-II quantum well absorbers: candidate systems for hot carrier solar cells*", Material Research Society (MRS), Phoenix, AZ, 2017.

C6. V. R. Whiteside, **H. Esmaielpour**, J. Tang, S. Vijeyaragunathan, T.D. Mishima, M. B. Santos, B. Wang, R. Q. Yang, and I. R. Sellers, "*Evidence of suppressed hot carrier relaxation in type-II InAs/AlAs$_x$Sb$_{1-x}$ quantum wells*." SPIE Optics+ Photonics for Sustainable Energy. International Society for Optics and Photonics, 2016.

C7. J. Tang, V. R. Whiteside, **H. Esmaielpour**, S. Vijeyaragunathan, T. D. Mishima, M. B. Santos, and I. R. Sellers, "*Evidence of hot carriers at elevated temperatures in InAs/AlAs$_{0.84}$Sb$_{0.16}$ quantum wells*." SPIE OPTO. International Society for Optics and Photonics, 2015.

C8. L. C. Hirst, M. K. Yakes, C. A. Affouda, C. G. Baile, J. G. Tischler, **H. Esmaielpour**, V. R. Whiteside, I. R. Sellers, M. P. Lumb, D. V. Forbes, R. J. Walters, "*Hot-carrier effects in type II heterostructures*." Photovoltaic Specialist Conference (PVSC), 2015 IEEE 42nd. IEEE, 2015.

Conferences and Symposiums

C9. H. Esmaielpour, V. R. Whiteside, H. P. Piyathilaka, S. Vijeyaragunathan, B. Wang, K. P. Roberts, T. D. Mishima, M. P. Lumb, M. B. Santos, A. D. Bristow, and I. R. Sellers, "*Methods to control heat losses in systems developed for practical hot carrier solar cells*." Photovoltaic Oklahoma Research and Institute (PVOKRI) Symposium, Oklahoma State University, Stillwater, OK, 2018.

C10. H. Esmaielpour, V. R. Whiteside, L. C. Hirst, D. V. Forbes, R. J. Walters, and I. R. Sellers, "*Power and temperature dependent photoluminescence investigation of the linear polarization at normal and inverted interface transitions in InP/InAlAs and InGaAsP/InAlAs QW structures*", American Physical Society (APS), New Orleans, 2017.

C11. H. Esmaielpour, J. Tang, V. R. Whiteside, S. Vijeyaragunathan, T. D. Mishima, M. B. Santos, B. Wang, and I. R. Sellers, "*Type-II quantum well absorbers: a candidate system for hot carrier solar cells*." Oklahoma NASA Energy and Materials Symposium. University of Tulsa, Tulsa, OK, 2017.

C12. H. Esmaielpour, J. Tang, V. R. Whiteside, S. Vijeyaragunathan, T. D. Mishima, M. B. Santos, and I. R. Sellers, "*Accurate determination of the temperature dependent thermalization coefficient (Q) in InAs/AlAsSb quantum wells*." APS Meeting Abstracts. Vol. 1. 2015.

C13. H. Esmaielpour, J. Tang, V. R. Whiteside, S. Vijeyaragunathan, T. D. Mishima, M. B. Santos, B. Wang, and I. R. Sellers, "*Reduced thermal losses in InAs/AlAs$_x$Sb$_{1-x}$ quantum wells: A candidate system for practical hot carrier solar cells*." Oklahoma NASA Energy and Materials Symposium. University of Tulsa, Tulsa, OK, 2016.